

# Development of a Regional Sediment Mobility Model for Submerged Archaeological Sites

Justin K. Dix  
David O. Lambkin  
Pierre W. Cazenave

School of Ocean and Earth Science,  
University of Southampton,  
National Oceanography Center, Southampton.

Funded by English Heritage through the Aggregate Levy Sustainability Fund, project number 5224.



**National Oceanography  
Centre, Southampton**  
UNIVERSITY OF SOUTHAMPTON AND  
NATURAL ENVIRONMENT RESEARCH COUNCIL



**RESOURCE MANAGEMENT ASSOCIATION**



This report is the final summary document from the project:

## Development of a Regional Sediment Mobility Model for Submerged Archaeological Sites

The project was kindly funded by English Heritage through the Aggregate Levy Sustainability Fund (ALSF project number 5224).

The data and sub-reports contained in this report are part of publications in preparation. Data are therefore presented here on the understanding that they will not be used explicitly in any publications without the prior consent of the project members and proper acknowledgement.

Once agreed, any use of data should be acknowledged using the section title and the following report reference:

Dix, J.K., Lambkin, D.O. and Cazenave, P.W. (2007) ' *Development of a Regional Sediment Mobility Model for Submerged Archaeological Sites*'. English Heritage ALSF project no. 5524. School of Ocean and Earth Science, University of Southampton, U.K. 156pp.

Whilst every effort was made to ensure the accuracy and integrity of the data and information contained in this report, the project does not provide any explicit guarantee of accuracy. As such, the data and any analyses based upon it should be interpreted with appropriate consideration for this.

For further information regarding the data, please contact us on:

Dr Justin Dix - [jkd@noc.soton.ac.uk](mailto:jkd@noc.soton.ac.uk)

Dr David Lambkin - [dlambkin@abpmer.co.uk](mailto:dlambkin@abpmer.co.uk)

School of Ocean and Earth Science,  
National Oceanography Centre, Southampton,  
European Way,  
Southampton.  
SO14 3ZH

tel: 02380 593057

fax: 02380 593057

## Executive Summary

An understanding of the dynamics of underwater archaeological sites has been a primary research aim of marine archaeologists for the last four decades. To develop a viable sediment dynamic model for artefact based sites is crucial both in terms of site formation process study; a priori archaeological investigation; and latterly the effective management of marine sites to ensure their future stability.

Previous ALSF project work by Dix *et al.* (2007) did review, identify and study the process that govern the accumulation or erosion of sediments from around shipwreck sites. Understanding such local processes and their physical result (up to a few tens or hundreds of meters from the site) is of benefit to many diverse and large user-groups, including:

- Heritage managers, *undertaking site preservation works.*
- Archaeologists, *interpreting geophysical data and predicting dispersal of artefacts.*
- Marine ecologists, *prediction of local habits.*
- The dredging industry, *interpreting the sedimentary environment and enabling efficient design of exclusion zones.*
- Marine engineers, *understanding generic local response of the seabed to the introduction of three-dimensional structures.*

These previous site specific studies have highlighted the need for information about the temporal and spatial variance in the input rates of sediments from outside of the site, controlled by processes occurring at a regional scale. In this project we apply one of the leading commercial numerical hydrodynamic modelling products, DHI's MIKE 21 software, to the development of regional scale models of seabed sedimentation and erosion. The results provide a means to estimate or predict the tidal and sedimentary environment at a regional scale which may then be used, either in its own right or in conjunction with site specific work, to further enhance the understanding and effectiveness of the user groups described above.

The model provides results at a resolution of approximately 5km over the whole of the English Channel and southern North Sea. The information produced by the model includes:

- Orientation of the tidal axis
- Residual tidal flow direction and magnitude
- Residual sediment transport direction and magnitude
- Magnitude and asymmetry of sediment transport
- Tendency towards regional-scale net bed accumulation or erosion.

On the basis of all results, regions of the English Channel and the English coastline (5-20km offshore) can be categorised according to the predicted strength of sediment mobility (the average strength of sediment transport) and the asymmetry of that transport. Conceptual models are proposed to allow extension of the predicted environmental conditions to predicting wreck site response and the conditions of debris dispersal. The model demonstrated that temporal variability is present in the system at semi-diurnal (half-daily), spring-neap (two-weekly) and equinoxal (six-monthly) timescales. However, the model also suggests that variability is generally confined to the magnitude of the response; the direction (e.g. of residual transport) or sign (erosion or accumulation) of response is consistent over time.

The relative results describe the outline shape of present day major sand body accumulations in the English Channel; however, insufficient data regarding distribution of grain size and the thickness of sediment layers was available at the scale of the English Channel, to quantitatively define or predict the boundaries. The model considers only tidal forcing (the dominant factor in water depths deeper than 20m); therefore, results from shallower depth regions (generalised here as within 5km of the coastline) are excluded from the interpretation.

The model was designed and calibrated using a variety of, but limited number and coverage of data sets from the field; it was identified that large scale calibration would be improved by

the collection of dedicated data for this purpose in offshore locations throughout the English Channel. It was also demonstrated, through the application of more detailed input data in two smaller sub-areas, that the accuracy and usefulness of the model results for license region sized areas may be improved in future studies by the provision of more detailed data, as it becomes available (e.g. as is collected during Environmental Assessment).

# Contents

<b>1. Introduction.....</b>	<b>1</b>
1.1 Background.....	1
1.2 Aims and Objectives.....	1
1.2.1. Aims.....	1
1.2.2. Objectives .....	2
<b>2. Background .....</b>	<b>5</b>
2.1 Tidal Regime .....	5
2.2 Wave Climate .....	7
2.3 Sediment Distribution.....	9
2.4 Sediment Transport.....	13
2.4.1. Bedload Transport.....	13
2.4.2. Suspended load transport .....	17
2.5 The Hastings Shingle Bank Sub-area. ....	17
2.6 The Eastern Channel License Sub-area .....	20
<b>3. Design and calibration of the numerical model.....</b>	<b>21</b>
3.1 Hydrodynamic module parameters and choices. ....	21
3.1.1. Domain.....	21
3.1.2. Bathymetry.....	21
3.1.3. Solution technique.....	22
3.1.4. Flood and dry .....	22
3.1.5. Eddy viscosity.....	23
3.1.6. Bed resistance .....	23
3.1.7. Coriolis forcing.....	23
3.1.8. Wind forcing .....	23
3.1.9. Ice coverage .....	23
3.1.10. Tidal potential.....	23
3.1.11. Precipitation – Evaporation .....	24
3.1.12. Wave radiation.....	24
3.1.13. Sources.....	24
3.1.14. Boundary conditions.....	24
3.1.15. Initial conditions.....	24
3.1.16. Decoupling.....	24
3.2 Sand transport module parameters and choices.....	25
3.2.1. Model definition.....	25
3.2.2. Time parameters.....	26
3.2.3. Sediment properties.....	26
3.2.4. Bed resistance .....	26
3.2.5. Dispersion .....	26
3.2.6. Sources.....	27
3.2.7. Initial conditions .....	27
3.2.8. Morphology.....	27
3.3 Calibration .....	27

3.3.1.	Calibration data availability and summary .....	27
3.3.1.1.	Large-scale spatial data.....	27
3.3.1.2.	Point time-series data.....	28
3.3.1.3.	Tidal elevation.....	29
3.3.1.4.	Current speed and direction .....	30
3.3.2.	Calibration methods.....	30
3.3.2.1.	Large-scale spatial data.....	30
3.3.2.2.	Point time-series data.....	30
3.3.3.	Calibration results.....	31
3.3.3.1.	Open boundaries .....	31
3.3.3.2.	Land boundaries.....	33
3.3.3.3.	Mesh resolution – English Channel .....	33
3.3.3.4.	Mesh resolution – Nested subregions .....	40
3.3.4.	Solution technique.....	44
3.3.5.	Bed roughness.....	45
3.3.6.	Eddy viscosity.....	54
3.3.7.	Decoupled timestep.....	54
3.4	Summary and final choice of model setup.....	56

## **4. Results of the numerical model ..... 59**

4.1	Results of the hydrodynamic model .....	61
4.1.1.	Tidal axis orientation .....	61
4.1.2.	Residual flow field analysis.....	62
4.2	Results of the sediment dynamics model.....	68
4.2.1.	The English Channel.....	68
4.2.1.1.	Residual sediment transport analysis .....	68
4.2.1.2.	Local sediment mobility and transport asymmetry .....	74
4.2.1.3.	Residual bedload transport inferred from tidal current data .....	76
4.2.1.4.	Residual suspended load transport inferred from tidal current data.....	78
4.2.1.5.	Bed level change .....	78
4.2.2.	Summary .....	82
4.3	Comparison with the nested subareas.....	83
4.3.1.	Hastings Shingle Bank.....	83
4.3.1.1.	Comparison with flow data.....	83
4.3.1.2.	Comparison with regional bathymetry.....	83
4.3.1.3.	Comparison with predicted bed level change .....	86
4.3.1.4.	Comparison with distribution of sediment grain size .....	87
4.3.2.	Area 473E .....	89
4.3.2.1.	Comparison with regional bathymetry.....	89
4.3.2.2.	Comparison with predicted bed level change .....	92
4.3.3.	Summary .....	93

## **5. Distribution and variability of regional scale sediment mobility..... 95**

5.1	Distribution of present day sediment transport patterns .....	95
5.2	Predicting regions likely to experience future changes in local sediment mobility and/or transport asymmetry.....	99
5.3	Predicting regions likely to experience future net bed level change.....	99

<b>6. Desktop evaluation of the impact to archaeological sites caused by changes in local sediment mobility. ....</b>	<b>102</b>
6.1 Changes to the seabed potentially caused by marine aggregate dredging .....	102
6.1.1. Gravel extraction.....	102
6.1.2. Sand extraction.....	103
6.2 The potential impact of regional scale net seabed erosion/accretion on archaeological sites.....	104
6.3 Spatial and temporal scales of variability in sediment mobility and site response	110
<b>7. Dissemination .....</b>	<b>112</b>
<b>8. References.....</b>	<b>113</b>
<b>9. Appendix A – Basic variables in MIKE .....</b>	<b>117</b>
9.1 Method.....	117
9.2 Results .....	117
9.2.1. Bathymetry.....	117
9.2.2. Bed Roughness.....	118
9.2.3. Eddy viscosity.....	120
9.2.4. Wind.....	121
9.2.5. Obstacles.....	122
9.3 Summary and conclusions.....	122
<b>10. Appendix B – Optimising Mesh Design in MIKE</b>	<b>123</b>
<b>FM</b>	
10.1 Rationale.....	123
10.2 Introduction .....	123
10.3 Parametric sensitivity testing.....	124
10.3.1. Effect of local water depth.....	125
10.3.2. Effect of local velocity magnitude.....	126
10.3.3. Effect of element size .....	127
10.3.4. Effect of the chosen maximum allowable CFL number .....	127
10.4 The distribution of $\Delta x$ and $\Delta t$ in a mesh of ‘uniform’ element area.....	128
10.4.1. Relating $\Delta x$ to the area of triangular flexible mesh elements .....	128
10.4.1.1. Testing methodology.....	128
10.4.2. Raw meshes and the effect of mesh smoothening .....	129
10.4.2.1. No Smoothening .....	129
10.4.2.2. With Smoothening .....	132
10.4.3. Complex domains .....	132
10.5 Choice of vertex spacing for describing boundaries and structures .....	133
10.6 Refining a mesh using local water depth.....	135
10.6.1. The refine mesh tool in MIKE zero.....	135
10.6.1.1. Basic functionality and best practice.....	135

10.6.1.2.	Optimisation of the refine mesh procedure.....	140
10.6.1.3.	Effect of mesh resolution on tidal propagation rates.....	141
10.6.2.	Manual mesh refinement .....	143
10.7	Dealing with individual small elements .....	144
10.8	Summary of findings.....	146
10.8.1.	Summary of sensitivity studies.....	146
10.8.2.	Summary of uniform mesh studies.....	146
10.8.3.	Summary of mesh refinement studies.....	147
10.8.4.	Fixing local problems .....	148
10.9	Choosing the appropriate mesh resolution .....	148

**11. Appendix C – A Review of the Bed Roughness Variable in MIKE21fm HD and ST Modules ..... 150**



# **1. Introduction**

## **1.1 Background**

An understanding of the dynamics of underwater archaeological sites has been a primary research aim of marine archaeologists for the last four decades. To develop a viable sediment dynamic model for artifact based sites is crucial both in terms of site formation process study; a priori archaeological investigation; and latterly the effective management of marine sites to ensure their future stability.

Conceptual models (e.g. Muckleroy, 1977; Ward et al., 1991) based on single or multi-site archaeological investigations have been published but unfortunately seldom used. More recently Dix and co-workers (building on a project by Dix & Saunders (Saunders, 2005)) have, as part of the EH funded Round 2 ALSF programme (Project 3365), been investigating, through in situ measurement and calibrated tank experiments, site dynamic models for individual archaeological sites. Although this work has been with the specific emphasis of looking at the potential impacts of upstream bed lowering by aggregate dredging, it has elucidated significant information on the processes controlling sedimentation and erosion on the site scale.

However, as both these laboratory and in situ approaches are ideal for looking at individual sites of interest (for instance protected wreck sites), they could not be regarded as a cost or time efficient approach to looking at large numbers of archaeological sites in regional assessment areas. The previous site specific studies also highlighted the need for information about the temporal variance in the input rates of sediments from outside of the site, controlled by processes occurring at a regional scale. Depending upon the location of the site within the region, spatial variation might also be important. The conclusion is therefore, that a large scale numerical modelling approach is required to provide this additional information.

In this project we apply one of the leading commercial numerical hydrodynamic modelling products, DHI's MIKE 21 software, to the development of regional scale models of seabed sedimentation and erosion and thence to predict the potential impacts on submerged archaeological sites.

The MIKE 21 package is capable of modelling bedload and suspended load transport of sediments under combined wave and tidal current flows. Depending on the input parameters available, the model is able to provide sediment transport predictions from the 5-10 m to the kilometre scale. With this information it is possible to identify areas with potential for net erosion or deposition, the sediment transport pathways within the region and how these conditions may change with time and/or input parameters (e.g. change conditions due to nearby dredging activity, or more regional scale climate change). Having established the regional sediment dynamics of the system, individual archaeological sites in the area can then be placed in their greater sediment and hydro-dynamic contexts. Finally, the relationships being established between the regional sediment regime and site specific sediment dynamics as part of 3365 should enable at least first order predictions of the potential environmental threats posed to archaeological resources.

## **1.2 Aims and Objectives**

### **1.2.1. Aims**

The primary aims of this project were:

- To use MIKE 21 to characterize the seabed dynamics of regional scale aggregate licence areas and thus investigate the potential threats to exposed submerged archaeology.
- To compare model outputs with field data including: time lapse swath bathymetry, side scan sonar surveys, grab and core data, video data and in situ sediment tracer experiments being carried out by the RMA and ECA,
- To compare these (regional) licence scale models with a model developed from lower resolution datasets for the entire Eastern English Channel. This latter model will be integrated with the statistical analysis of shipwreck databases being undertaken as part of the AMAP1 project proposed by Bournemouth University.

All of these aims were achieved, through the successful completion of the objectives listed below.

### 1.2.2. Objectives

The overall project aims were realised through a series of objectives, subdivided into four phases:

*Phase 1:* Production of a calibrated numerical model to describe the hydro- and sediment-dynamics of regions used for marine aggregate dredging.

**Objective 1** – Review and synthesise extant oceanographic, bathymetric and archaeological knowledge of a first case study region with extensive extant *in situ* data. Much of this work has been completed as part of Project 3365.

**Objective 2** – Through consultation with other experienced users of the MIKE 21 software, set up a correctly functioning numerical model to simulate the hydro-dynamics of the first study region.

**Objective 3** – Undertake sensitivity testing of the hydro-dynamic model to simulate the effect of potential variation in the quality or resolution of input data for the first study region.

**Objective 4** – Through consultation with other experienced users of the MIKE 21 software, set up a correctly functioning numerical model to simulate the sediment-dynamics of the first study region.

**Objective 5** – Undertake sensitivity testing of the sediment-dynamic model to simulate the effect of potential variation in the quality or resolution of input data for the first study region.

**Objective 6** – Review and synthesise extant oceanographic, bathymetric and archaeological knowledge of a second case study region with less extensive extant *in situ* data. Much of this work has been completed as part of Project 3365.

**Objective 7** – Through consultation with other experienced users of the MIKE 21 software, set up a correctly functioning numerical model to simulate the hydro-dynamics of the second study region.

**Objective 8** – Undertake sensitivity testing of the hydro-dynamic model to simulate the effect of potential variation in the quality or resolution of input data for the second study region.

**Objective 9** – Through consultation with other experienced users of the MIKE 21 software, set up a correctly functioning numerical model to simulate the sediment-dynamics of the second study region.

**Objective 10** – Undertake sensitivity testing of the sediment-dynamic model to simulate the effect of potential variation in the quality or resolution of input data for the second study region.

**Objective 11** – Compare and evaluate the results of the sensitivity testing from the two study areas to produce recommendations for data requirements and for the general construction of such numerical models.

Literature and data reviews were undertaken for the two sites (Hastings Shingle Bank and Area 473E) being modelled in more detail (**Objectives 1 and 6**) which may be found in Section 2. These models were typically built and interpreted in the context of results from the more extensive English Channel model, developed in Phase 3. Once sufficient data were accumulated, hydro- and sediment-dynamics models were designed for these two areas (**Objectives 2, 4, 7 and 9**, described in Section 3). Sensitivity testing of the models (**Objectives 3, 5, 8 and 10**) was then undertaken as part of the model design and calibration process, the results of which are described in Section 3.3. Rather than explicit recommendations for data requirements and for the general construction of models (**Objective 11**), the philosophy of model sensitivity testing is explored and appropriate values are presented for the model setup used here, in Section 3.3, however, it was also found that similar models using different configurations may have different data accuracy requirements and sensitivity testing should be undertaken for the specific model design on each occasion.

*Phase 2: Implications of spatially and temporally varying regional scale hydro- and sediment-dynamics for the stability of archaeological sites.*

**Objective 12** – Interpret the results from the calibrated models in Phase 1 to produce maps of sediment transport pathways and magnitude, quantifiably identifying areas likely to experience net sedimentation or erosion.

**Objective 13** – Investigate the potential effects of altering the spatial patterning of sediment mobility (e.g. potentially due to nearby marine aggregate dredging).

**Objective 14** – Investigate the potential effects of altering the patterning of sediment mobility over variable temporal scales (e.g. potentially due to nearby marine aggregate dredging; natural variations in tidal flows over spring-neap, seasonal and annual time scales; effect of climate change).

**Objective 15** – Desktop evaluation of the impact of predicted regional scale net seabed erosion/sedimentation on archaeological sites in the study areas. Site specific processes are represented by the results of the previously completed Project 3365.

Results contributing to **Objective 12** (maps of sediment transport pathways and magnitude) may be found in Section 4. **Objectives 13, 14 & 15** (the effects on the sedimentary environment and archaeological sites of temporal and/or spatial variability in the predicted parameters) are more conceptual in nature due to the shear range of possible scenarios and are therefore dealt with as a desktop study of potential effects in Section 5 and 6, rather than as specific, quantitative modelling studies.

*Phase 3: Large-scale assessment of long-term risk to archaeological sites in the English Channel.*

**Objective 16** – Review and synthesise extant oceanographic, bathymetric and archaeological knowledge of the English Channel at coarse resolution. Part of this work has already been completed as part of Project 3365.

**Objective 17** – Create a numerical model simulating hydro- and sediment-dynamics in the English Channel at coarse resolution (determined by the spatial resolution of the extant bathymetric and hydro-dynamic data).

**Objective 18** – Combine and evaluate the English Channel model output with extant data to identify, broadly, regions of high/medium/low sediment mobility with implications for expected wreck site character. Suggest, broadly, areas with potential for significant additional bed erosion or accretion in response to predicted long term changes in environmental conditions.

A review of literature concerning the marine environment of the English Channel was undertaken (**Objective 16**) and may be found in Section 2. Hydro- and sediment-dynamic models of the English Channel were designed, calibrated and sensitivity tested (**Objective 17**) in Section 3.3; a discussion of the results (**Objective 18**) may be found in Section 4. Information from the literature review provided valuable context and information when considering the setup of the numerical models and during the interpretation of the results.

#### *Phase 4: Dissemination*

**Objective 19** – The outputs from this project will include: a final report for both EH, the RMA and the ECA; presentations at National and International conferences – in particular we wish to present at the 2007 AGU conference; submission of peer-reviewed scientific publications; data and interpretations for the AMAP1 project proposed by Bournemouth University; and core material for the EU component of the EU-funded MACHU project. Finally, where possible the data and outputs from this project will be stored on NOC databases and made available where possible. As with Project 3365 and its variation order, where the data is owned by either the RMA or the ECA, permission for its use must be sought from these bodies.

Throughout the project, interaction was sought by the project members with other researchers, stakeholders and data end-users. This resulted in a number of dissemination opportunities arising and the project was also able to provide direct support to two other (same round) ALSF projects. A review of all dissemination activities carried out as part of the present study (Objective 19) may be found in Section 7.

## **2. Background**

This Section presents an overview of previously published literature describing the geology, sediments and oceanography of the English Channel. Additional sections describe the same for the two smaller regional study areas – the Hastings Shingle Bank and the eastern Channel license areas, containing the Area 473E license.

### **2.1 Tidal Regime**

Water movement in the English Channel is dominantly tidal in water depths exceeding 30m (e.g. Harris et al., 1995, Newell et al., 1998); the primary forcing is provided by the semi-diurnal lunar (M2) tidal constituent (Anthony, 2002). Typical tidal ranges in the Channel are of the order 6-10m (Larsonneur et al., 1982), but are also as large as 15m in the central southern part of the English Channel, near to the Channel Islands and the Baie du Mont-Saint-Michel (east of the Cotentin peninsula);. The distribution of co-range and co-phase lines for the M2 constituent is shown in Figure 1. In the English Channel, the tide propagates from the Atlantic eastwards, rotating around a virtual amphidromic point north of Poole Bay. In the southern North Sea, the tidal wave rotates anticlockwise around the centrally located amphidrome. In both basins, tidal range increases with distance from the amphidrome.

Peak tidal current speeds vary significantly both along the length and across the breadth of the Channel. Higher peak flows are associated with larger tidal ranges in Figure 1 but are also locally modified by flow interaction with constrictions and headlands (e.g. the Cotentin Peninsula). Maximum velocities of  $2\text{ms}^{-1}$  are observed off the northern point of the Cotentin Peninsula and decrease generally with distance to the east and west; velocities are also significantly decreased within semi-enclosed coastal bays (e.g. Lyme Bay, Start Bay). In addition to observed tidal currents, similar patterns have also been reported as a result of numerical modelling studies, e.g. Pingree (1980), Mauvais (1991) and Grochowski et al. (1993a&b), using the results of Salomon and Breton (1991).

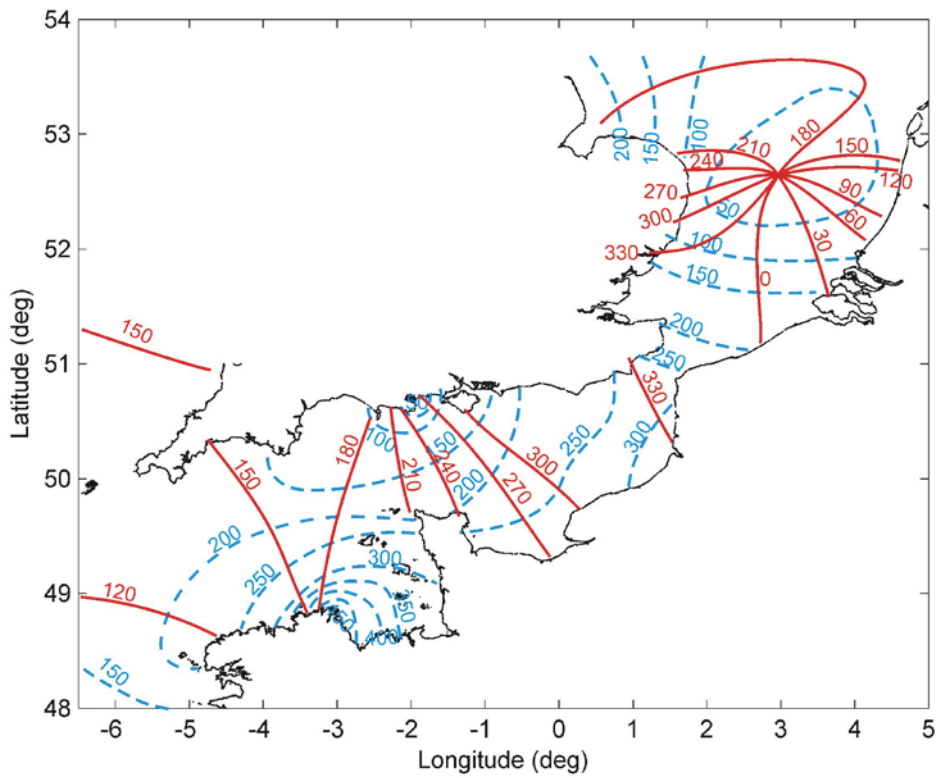


Figure 1. Co-range (blue [cm]) and co-phase (red [degrees]) contours of the M2 tidal constituent in the English Channel and southern North Sea. After Howarth (1990).

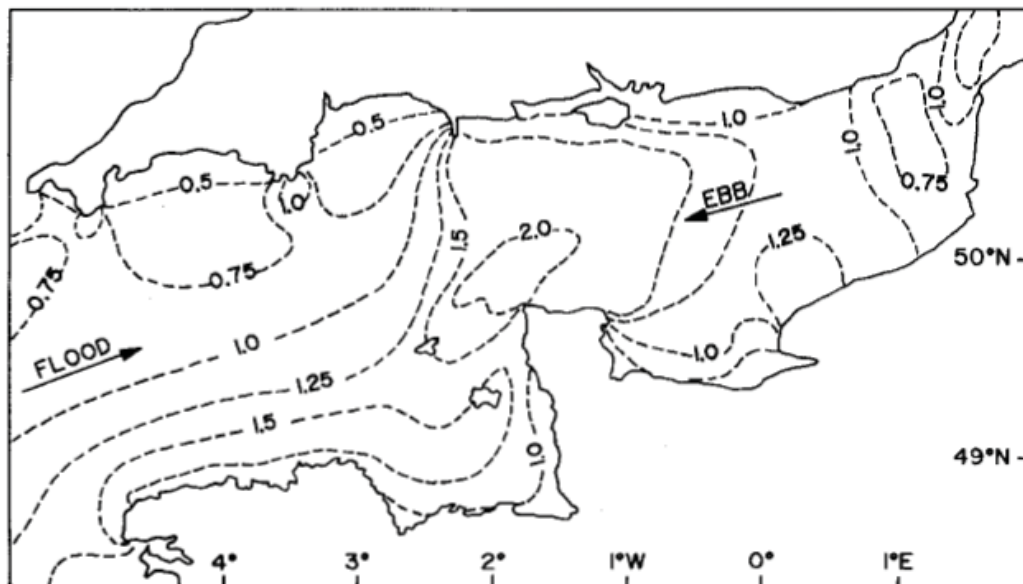


Figure 2 Peak near surface tidal current speed ( $\text{ms}^{-1}$ ) from Grochowski et al. (1993a).

Using a combination of field observations and numerical modelling, Pingree (1980) suggests that tidal oscillations in the western Channel manifest as a progressive wave (high

water corresponds approximately to peak tidal flows) whilst in the eastern Channel they manifest as a standing oscillation (high water corresponds approximately to slack water conditions). The maximum shear stress produced by the tide may be determined from such maps of peak tidal current speed in conjunction with information regarding the bathymetry; maximum bottom shear stress distribution was also calculated analytically using the distribution of the M2 and M4 tidal constituents by Harris *et al.* (1995)

In addition to semidiurnal asymmetry in tidal velocity, longer-term residual tidal circulation in the Eastern English Channel has been described by several authors either using numerical models (e.g. Pingree, 1980; Stride, 1981; Mauvais, 1991 (Figure 3); or Grochowski *et al.*, 1993a). Results from the various studies agree that there is a recirculation in the western Channel, entering eastwards along the French coast, then north towards Start Point, then westwards along the British coast. Eastwards of this line, there is generally eastwards residual flow along the long axis of the Channel to the Dover Straits. More complex circulation patterns are found closer to the coasts, particularly in the Central English Channel associated with large scale flow interaction with the Cotentin Peninsula, Channel Islands, the Isle of Wight and other significant headlands. The results of Mauvais (1991) show residual flow in a northeast direction through the Dover Straits. A more detailed numerical modelling study by Sentchkev and Korentenko (2005) using a Lagrangian particle tracking approach suggests that the rate and direction of residual transport in the Dover Straits over spring-neap timescales is described as: slow in an onshore direction on the British side; at a medium rate towards the north east centrally; and as rapid and towards the north east on the French side. It was also reported that the rate and direction of residual transport may be different when considering only spring or neap cycles independently.

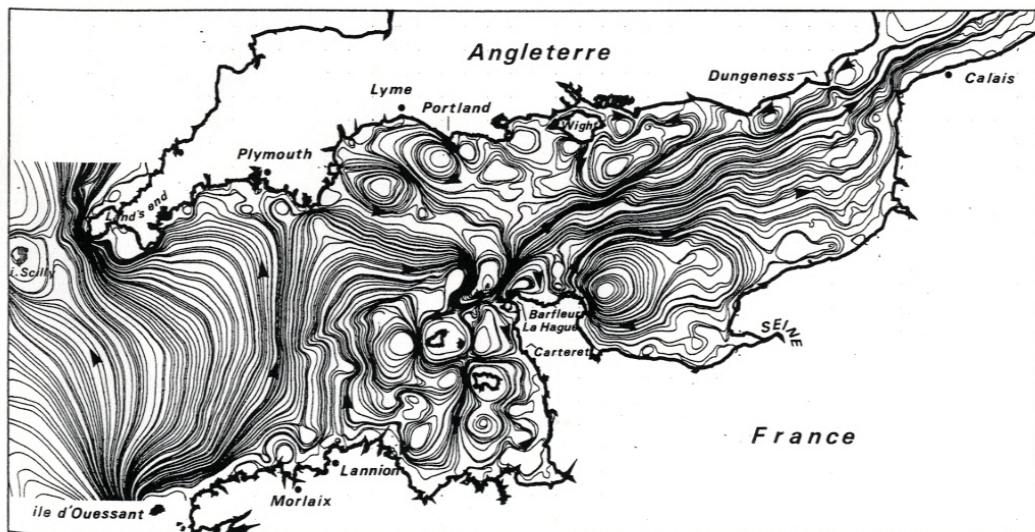


Figure 3 Long-term circulation in the English Channel (Mauvais, 1991)

## 2.2 Wave Climate

The largest wave heights observed in the eastern English Channel approach from directions of  $\sim 240^\circ$  (storm driven waves and swell from the Atlantic) and  $40\text{-}50^\circ$  (storm and wind driven waves from the North Sea and Dover Straits). Waves from  $240^\circ$  are more frequent than those arriving from any other angle and have on average higher wave heights and longer wave periods (Posford Haskoning, 2002). Typical wave heights in eastern and central parts of the English Channel were described by Grochowski and Collins (1994) as

0.6m and 0.75m in water depths of 29m and 66m, respectively. In a study by Crickmore *et al.* (1972) wave periods during a field study approximately 10km offshore of Worthing were typically in the range 6-10s.

Wave climate has also been investigated in terms of the typical orbital velocities induced at the bed. Crickmore, *et al.* (1972) undertook a study to determine the maximum orbital velocities between the 10-25m depth contours. Wave periods of 6-10s and wave heights of 3.05m and 6.10m were observed during the study. The predicted near-bed orbital velocities in 25m water depth are within the range  $\sim 0.25\text{ms}^{-1}$ - $0.9\text{ms}^{-1}$ . In a separate study by Draper (1967), orbital velocities of  $0.9\text{ms}^{-1}$  and  $0.25\text{ms}^{-1}$  were observed at 30m water depth for <1% and  $\sim 30\%$  of the year respectively.

In water depths of greater than 10m, due to attenuation of orbital velocity with depth, erosion and transport resulting from wind and wave action is generally small compared to tidally induced material flow (Mauvais, 1991). Wave driven sand transport has been highlighted in numerous studies to be of significant importance locally, but therefore only in shallow coastal regions of the shelf sea.

Combined wave-current action may result in sediment transport where the local tidal flow alone would be insufficient (Bagnold, 1963); the direction of sediment transport then depends upon the relative strength, direction and asymmetry of the two component flows. Symmetrical wave induced orbital flow at the seabed (typically in deeper water) increase the resuspension rate of sediment, which is then transported in the direction of the current; in shallower water, streaming or asymmetry in the wave velocity will add a additional component of transport in the direction of wave propagation.

Based on an assumed distribution of sediment and a statistical representation of wave action in the English Channel, the percentage of time per year during which the median grain size and median sand size fractions are disturbed by wave action was numerically estimated from the depth-dependent near-bed currents by Grochowski and Collins (1994). Results for median grain size material and the mean sand fraction grain size are shown in Figure 4. Inshore regions of less than 10m water depth were excluded from the study due to the complexity of waves in such shallow water. The Figure shows that the majority of the seabed is unaffected by wave action, especially in deeper, central locations. The median grain size is typically undisturbed by wave action for more than 99% of the year, except in Lyme Bay and along the French coast adjacent to the Channel Islands (undisturbed for only 60-80% of the year) where the seabed is muddy and therefore more easily mobile. The mean grain size (typically smaller and therefore more mobile than the median) is still typically undisturbed for more than 95% of the year, again except in regions of fine grained sediment.

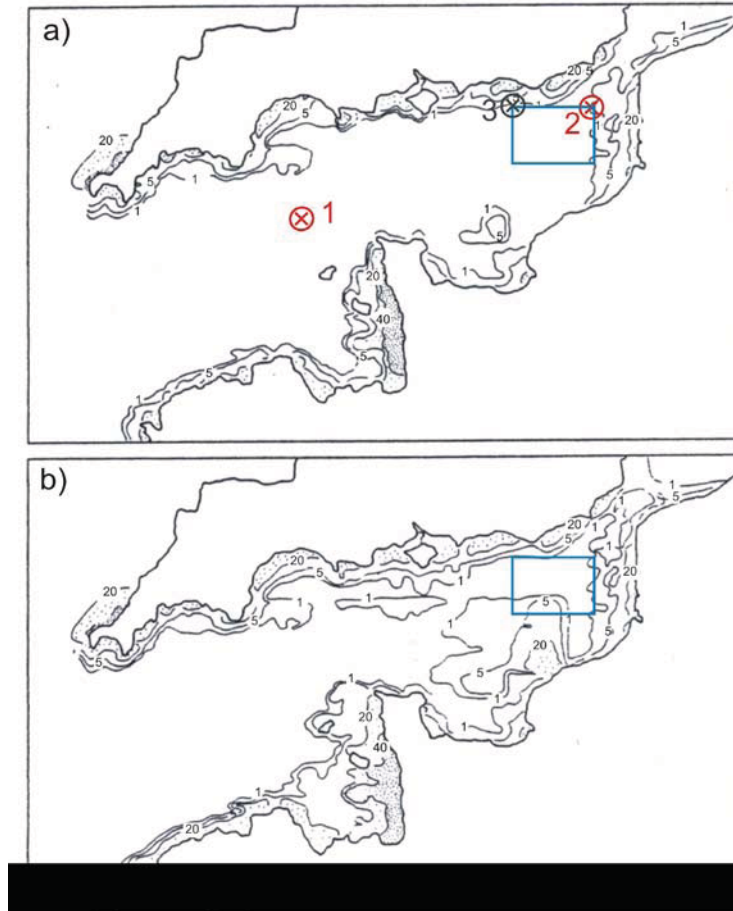


Figure 4 Percentage of time during the year for which (a) the median grain size and (b) sand are disturbed by wave activity (from Grochowski and Collins, 1994). Red markers indicate the locations of the wave conditions identified by Grochowski and Collins (1994); marker (3) indicates the location of wave period identified by Crickmore *et al.*, (1972). The blue box indicates the general location of the eastern Channel license areas.

### 2.3 Sediment Distribution

The present day distribution of seabed sediments in the English Channel and southern North Sea is the result of ongoing sediment redistribution according to the large scale patterns of tidal forcing described above, following the Holocene marine transgression from the end of the last glacial period 10 – 12ka BP.

Figure 5 shows a generalised curve of relative sea level rise during the Holocene in the North Sea region. Initial increases in water depth due to continental shelf flooding allow for greater sediment mobility due to the stronger, shallower tidal flows (Stride *et al.*, 1982). As water levels increased, the tide became less energetic and coarser sediments became progressively less mobile. Sea level rise over the last 2000 years has been only slight in comparison and projected sea level rise in the next 100 years (<1m) is not particularly significant in comparison to overall change throughout the Holocene.

The sediment cover in the English Channel can be separated into two subsets: an immobile lag deposit consisting of coarse grained (10-60mm) flint clasts and a finer (0.15-0.5mm), mature quartz clasts layer. The lag sediments were deposited before the Holocene transgression, and are generally overlain by the finer quartz clasts. The lag sediments are immobile under the present tidal regime (Hamblin *et al.*, 1992).

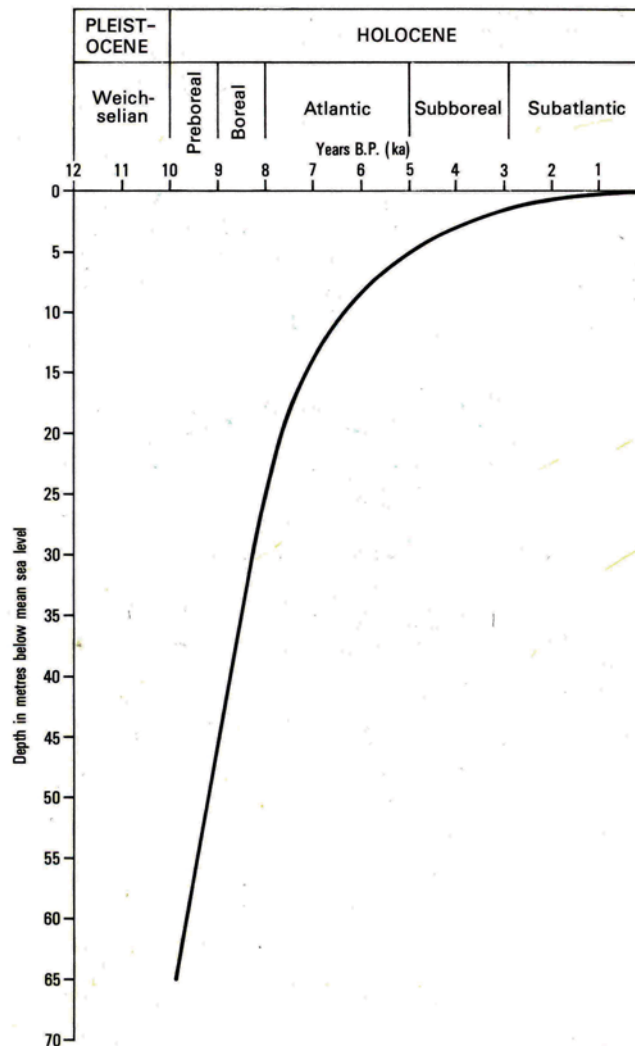


**Figure 5 Generalised curve of relative sea level during the Holocene in the North Sea region (Cameron *et al.*, 1992)**

The marine transgression was followed by a period of more stable hydrodynamics. Finer material is presently being introduced to the system from the seabed through erosion of the existing material and from coastal erosion; fluvial sediment input to the coastal environment occurs locally but is limited in volume due to high deposition rates in estuaries (Hamblin *et al.* 1992).

The fine sediment veneer (where present) is being actively transported and modified under today's tidal regime; areas of coarser sediment are generally the lag deposit which has had the finer fractions winnowed away, leaving only the older, coarser material deposited during the transgression (Hamblin *et al.* 1992).

The distribution of sediment facies in the English Channel has been described in various publications, studies and institutional reports. A variety of quantitative spatial information and detailed geological history of subregions of the English Channel are presented in British Geological Survey publications, e.g. Evans (1990), Pantin, (1991), Hamblin *et al.* (1992) and Cameron *et al.* (1992). However, only data to the British national boundary, i.e. only half of the Channel width, are reported. Other whole channel sediment facies distribution maps have been presented e.g. by Vaslet (1978) or Larssonneur *et al.* (1982). The former also subdivided sand facies broadly by grain size; this was used by later authors to estimate the mean or median grain size distribution of the sand fraction over the

area. Of the limited number of studies reporting the detailed distribution of quantitative measures, such as mean grain diameter of the sand fraction or similar, over large areas; the extent, detail and terminology incorporated into each chart tends to vary, making direct comparison difficult and resulting in apparent disagreement as to a ‘true’ distribution. However, most studies agree that:

- The central English Channel between the Isle of Wight and the Cotentin Peninsula is associated with the coarsest material (Figure 7) (Grochowski *et al.*, 1993a).
- Mean grain size decreases to the east of the central Channel with a relatively uniform north-south distribution except for more significant fining in the low-velocity embayments on the French coast.
- Local coarsening is observed east of Beachy Head, towards and into the Dover Straits from medium sands (diameter 0.5-0.25mm) to coarse sands (1-2mm). Seabed type in the Dover Straits is highly variable in character.
- Mean grain size decreases to the west of the central Channel. Local fining is observed within low-velocity coastal embayments (e.g. Lyme Bay). There is a general coarsening of sediments southward towards the French coast.

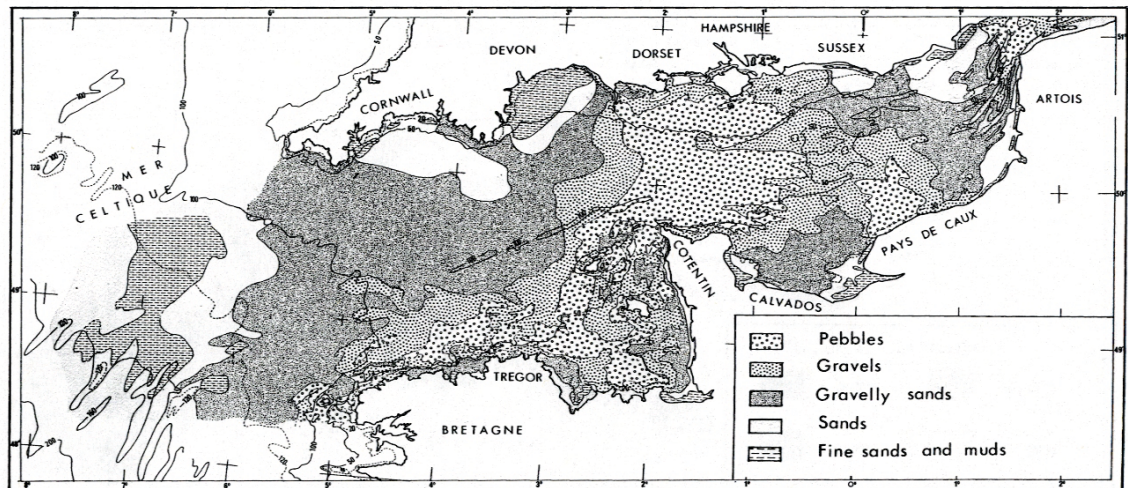


**Figure 6** Distribution of seabed sediment facies in the English Channel according to Larsonneur *et al.* (1982)

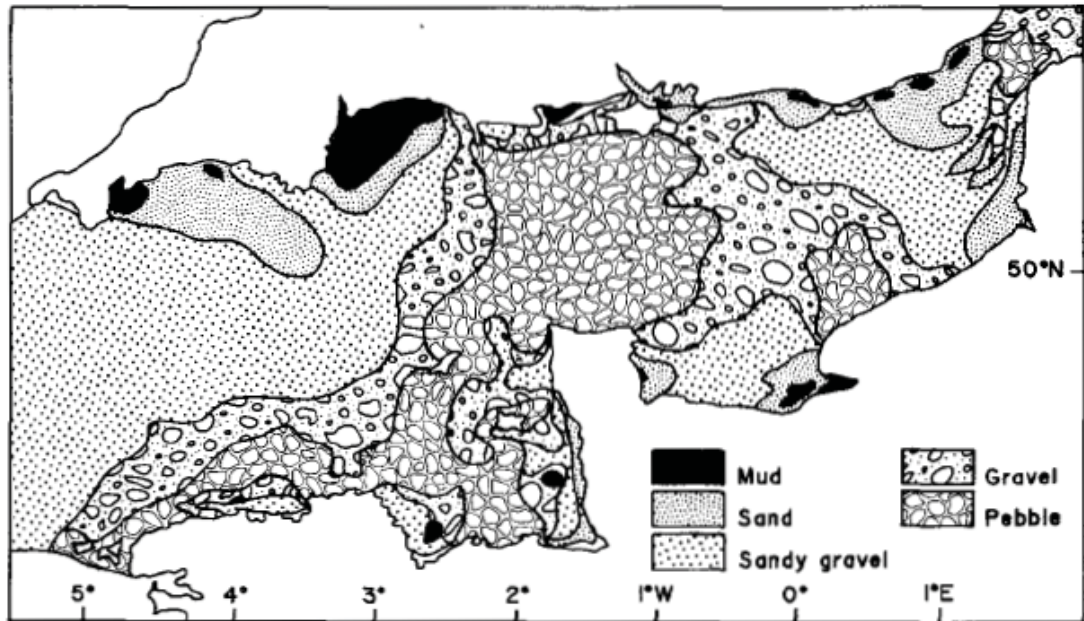


**Figure 7** Distribution of seabed sediment facies in the English Channel according to Grochowski *et al.* (1993a), after Vaslet *et al.* (1978).

Apparent disagreement in the literature is mainly found in areas of increased complexity. In the Dover Straits, Larsonneur *et al.* (1982), Beck *et al.* (1991) and Grochowski *et al.* (1993a) all report a broad range of sediment types, from coarse (pebbles and gravels) offshore to fine (muds) onshore; whereas, Hamblin *et al.* (1992) working at a lower resolution describe a more uniform mixture of grainsizes from sands and gravelly sands offshore to muddy sands onshore. The actual spatial distribution of the localised patches of sediment also unaccountably varies between the various authors. The highest resolution study of sediment distribution in the Dover Straits comes from Beck *et al.* (1991).

Particular emphasis has been placed on the distribution of sand bodies and sand waves within the English Channel and southern North Sea by a number of studies (e.g. Kenyon and Stride, 1970; Johnson *et al.* 1982; Beck *et al.*, 1991). Sand accumulations are thought to be indicative of depositional sedimentary environments and long-term sink areas. Linear sand bars are orientated subparallel to the tidal axis whilst the crest orientation of sand waves is perpendicular to the tidal axis and (semi-diurnal) sediment transport direction so long as the bed is known to be actively transported (Rubin and Ikeda, 1990; Rubin and Hunter, 1987). Figure 8 shows the distribution of sand waves around the British Isles, the same distribution was later presented by Beck *et al.* (1991).



**Figure 8** The distribution of sand waves around the British Isles, based on widespread sonograph coverage and echosounder profiles (from Johnson *et al.* 1982).

Although a great deal of complexity is observed in the distribution and sorting of modern sediments, sediments are being moved gradually towards an equilibrium distribution. One such distribution was proposed by Stride *et al.*, 1981 and is shown in Figure 9.

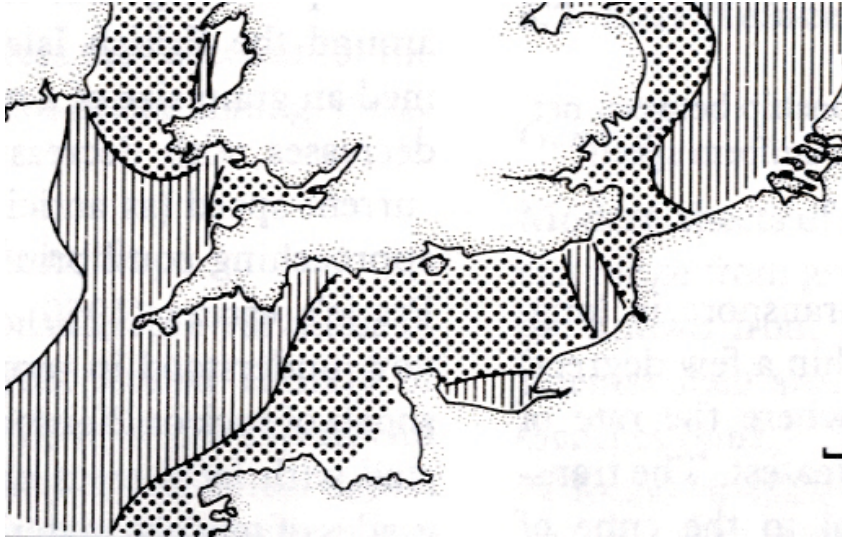


**Figure 9. The proposed equilibrium distribution of sands and muds in the English Channel, based upon the present day distribution of tidal forcing and patterns of sediment transport inferred from geophysical data, by Stride *et al.* (1982). Key: dotted – exposed gravel; hatched – sand accumulation; white – mud accumulation.**

The thickness of sediment bodies overlying hard rock substrata in the central and eastern part of the English Channel (in British territorial waters) was described by Hamblin *et al.* (1992). Over the majority of the English Channel, sediment thickness is less than 0.5m; areas of thicker sediment cover correlate also with the areas of finer sediments, principally in the Dover Strait. Sediment deposit thickness increases towards the east from the central Channel and close to the French coast north of Somme. Hamblin *et al.* (1992) report that in regions east of Beachy Head to the Dover Straits, sediment thicknesses are greater than 5m (exceeding 30m in places).

West of Beachy Head, sediments in British territorial waters of the Channel are reported as moderately sorted; localised regions may be less (poorly) or better (moderately well) sorted. Sediments are reported as being well sorted adjacent to Beachy Head and in larger regions towards the approaches to the Dover Straits. There is strong spatial variation (both better and poorer sorting) in the narrow parts of the Dover Straits constriction.

## 2.4 Sediment Transport

### 2.4.1. Bedload Transport

Sediment transport in the English Channel follows patterns formed by the actual and residual effects of tidal and wave forcing; patterns of sediment movement can therefore vary between offshore and nearshore regions. Excluding regions significantly affected by wave action, patterns of bedload transport have been previously proposed on the basis of results from field or numerical modelling studies, e.g. Pingree (1980), Johnson *et al.* (1982), Grochowski *et al.* (1993a), Harris *et al.* (1995) or Anthony (2002). Where included, previous studies generally agree that in water depths greater than 20-30m, tidal forcing is dominant, whereas in shallower water, wave action is of increasing importance.

The earliest maps of sediment transport pathways (Figure 10) were based on interpretation of bedform alignment and asymmetry by Kenyon and Stride (1970), Stride *et al.* (1982) and were presented as the best available information up to 12 years later in a review paper by Johnson *et al.* (1982). This map included a number of features reproduced in some form in almost all subsequent studies, namely:

- A bedload parting zone in the central English Channel
- A convergence zone in the Dover Straits
- A second bedload parting zone in the southern North Sea
- Westward transport in the western Channel with a secondary sink around the Channel Islands.
- Eastward transport in the eastern Channel
- Transport from the north and north-east into the Thames Estuary.



**Figure 10. Net sand transport directions on the continental shelf around the British Isles, based on IOS bedform data (Stride *et al.*, 1982).**

Still using interpretation of geophysical data, detail was improved at the Dover Straits by Kenyon *et al.* (1981) (Figure 11). These data along the French coast of the Dover Straits were reexamined by Beck *et al.* (1991) and augmented by local radioactive tracer experiments. Beck *et al.* suggested that sediment transport along the French coast of the Dover Straits is instead towards the North Sea (Figure 12). Beck *et al.* also make more explicit, the location of the convergence zone between the Dover Straits and the English Channel.

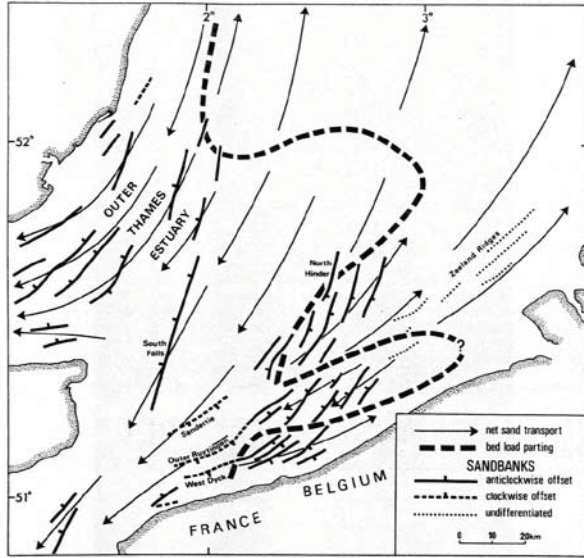


Figure 11. Bedload parting zone in the southern North Sea from Kenyon *et al.* (1981)

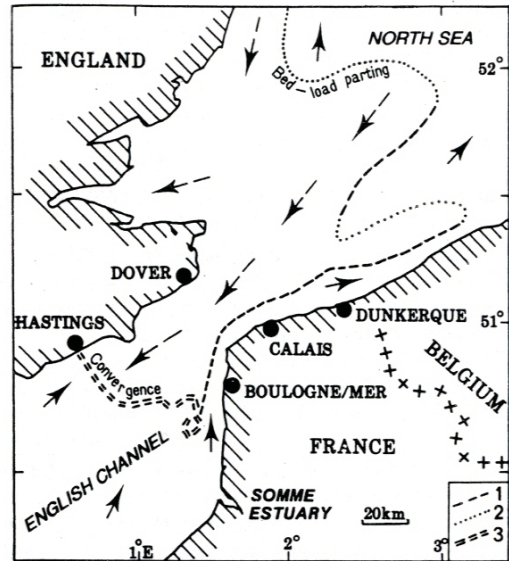


Figure 12. Bedload parting zone with additional detail along the French coastline by Beck *et al.* (1991)

More recent approaches have typically utilised numerical modelling tools. Grochowski *et al.* (1993a,b) applied a simple sediment transport model to hydrodynamic model predictions of tidal flow in the English Channel by Salomon and Breton (1991), thus estimating residual transport pathways (Figure 13). The same general features of transport were found although the location of the sediment convergence zone at the entrance to the Dover straits is somewhat different in alignment to that of Beck *et al.* (1991). The majority of sediment transport through the Straits is predicted to be from the North Sea to the English Channel, except for a narrow strip of north-easterly transport along the French coastline. Grochowski *et al.* provide a greater level of detail on the basis of the more detailed model results, moving the divergence zone in the central Channel slightly to the east and suggesting the presence of eddies associated with the Cotentin Peninsula.

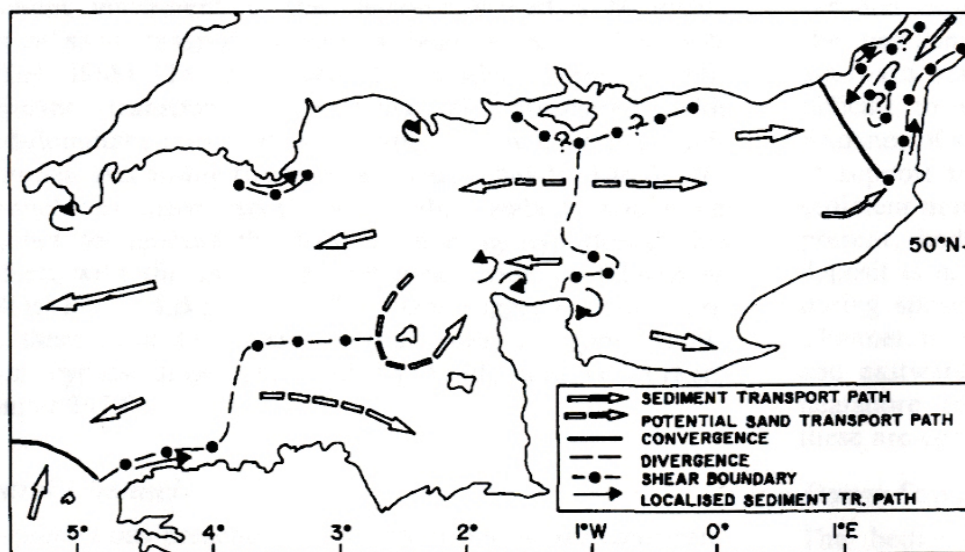


Figure 13. Residual sediment transport pathways in the English Channel. From Grochowski *et al.* (1993b)

In a slightly different approach, Harris *et al.* (1995) numerically modelled estimates of the spatial distribution of shear stress due to tidal flows at the seabed for all areas of the English Channel. Flows were simulated using the main (M2 and M4) tidal components; results showing the maximum bottom stress in all UK waters are displayed in Figure 14.

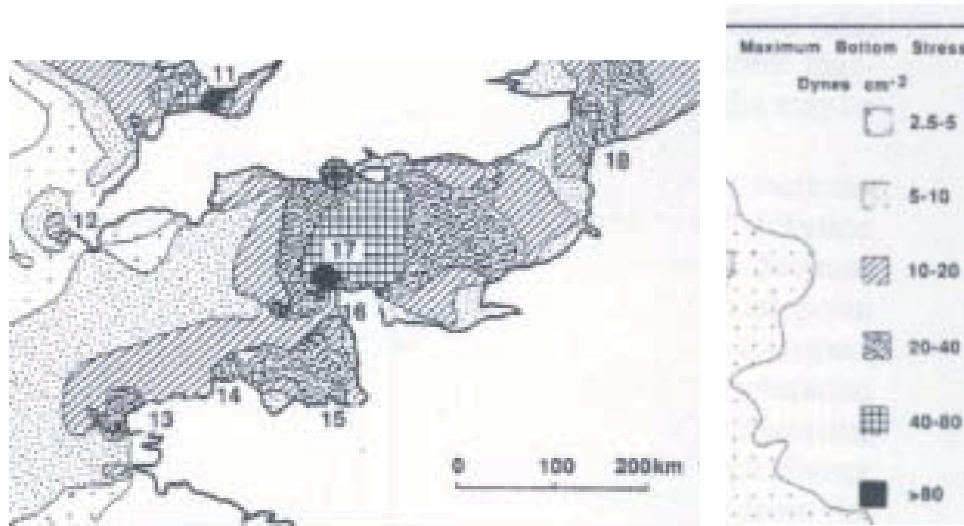


Figure 14. Numerically estimated maximum bottom stress as induced by M2 and M4 currents. Bottom stresses are calculated in Dynes.cm<sup>-2</sup> where 1 Dyne = 1×10<sup>-5</sup> Newtons. Positions of the amphidromal points are marked ⊕. From Harris *et al.* (1995).

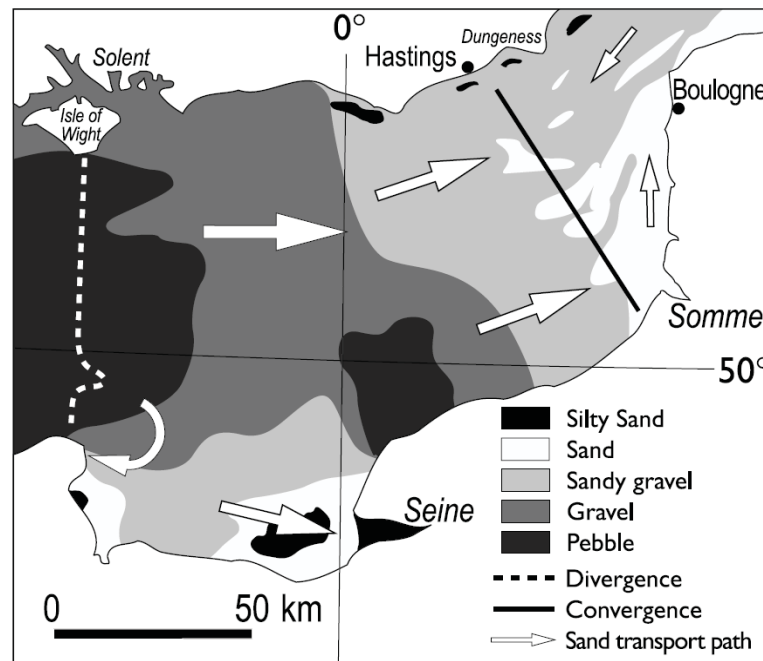


Figure 15 Distribution of seabed sediment facies in the English Channel according to Anthony (2002). Proposed sediment transport paths and convergence/divergence zones are indicated

### 2.4.2. Suspended load transport

The spatial distribution of suspended sediment concentration in the English Channel and southern North Sea has been investigated by various previous studies including Eisma and Kalf (1979 & 1987), Eisma and Iriou (1988), Postma (1990), Jones *et al.* (1994), Pohlman and Puls (1994), Prandle (1997), Velegrakis *et al.* (1997) and McManus and Lafite *et al.* (1999). The quantitative aspects of these reports are summarised in more detail in Dix *et al.* (2007). Suspended sediment transport is a passive advective process and therefore in the short term follows the tidal ellipse and in the long terms follows the direction of residual tidal flow; there will also be temporally variable contribution from meteorological effects (wind driven currents, waves, storm surges, etc). In terms of suspended sediment flux direction, the similarity of the estimated input and output values mean that the eastern English Channel is considered to be a bypass for fine grained suspended sediments passing through to the North Sea, rather than providing a significant source or sink (Velegrakis *et al.* 1999). Eddies induced by the longitudinal lateral shear boundary in the Dover Straits may act to locally deposit suspended material in this particular area (Grochowski *et al.* 1993b). No similar information was found regarding other areas of the English Channel.

## 2.5 The Hastings Shingle Bank Sub-area.

The Hastings Shingle Bank was formed in the late Holocene (~10-12ka BP) as a shallow water deposit (Hamblin *et al.* 1992). Sediments were sourced from soft Tertiary strata (sands) and also from Quaternary plateau gravels. As is the case in the English Channel in general, there are essentially two sediment types present: a coarse grained, immobile lag deposit; and a fine grained, mobile deposit. The lag deposit was laid down during the marine transgression at the end of the last glaciation where higher tidal flows allowed transport of coarser material. As sea levels continued to rise, energy available for sediment transport decreased, leaving a relict seabed of coarser material (Hamblin *et al.*, 1992). Since then, finer material has been mobilised by the lower flow speeds. Sediment and bathymetry distribution is partially controlled by a palaeo-cliff of thicker, coarse gravelly deposits occur (Hamblin *et al.* 1992). This is the principal controlling factor in the location of the Hastings Shingle Bank itself.

Sediment distribution in the environs of Hastings Shingle Bank is generally finer than that on the bank (Dix *et al.* 2007, Hamblin *et al.* 1992). Transport of the bank itself has been shown to be low to none (Dickson *et al.* 1973): a test dredge pit of 4m deep by 30m wide was dredged and monitored acoustically and with divers. Upon returning to the same area 6 months later, acoustic and diver data showed that there had been no net transport of the coarse grained material. Calculations on maximum grain size capable of being transported by regional flows suggested 3.1mm as the upper limit. Dickson and Lee (1973) have shown that the grains in the interstices of coarser beds experience 1% of the shear stress those on the surface experience, thus even the sediments between the grains of the lag deposit are not transported off the bank.

Draper (1967), Grochowski *et al.* (1993) and Reynaud *et al.* (2003) indicate that the dominant forcing on the seabed is tidal, and waves are likely to only play an occasional role in sediment transport.

Sedimentological and bedform distribution based on a number of zones (*Figure 16*) can be described as follows:

- The main shingle bank's long axis is orientated WSW-ENE (Zone A in *Figure 16*). Sediment cover on the bank is dominated by coarse grained material, which grain size analysis of 7 grab samples from the bank shows to have mean grain sizes of 20-60mm. The southern extent of the bank is visible on the sidescan sonar mosaic as a sharp boundary between the high backscatter of the bank, and the medium backscatter

of the small channel between the bank and the fine grained sediment region at the eastern end of the study area.

- The western end of the Shingle Bank (Zone A) is characterised by a number of flow parallel ribbons of exposed coarser grained lag material interleaved with medium grained plane beds. These bedforms extend up a gently sloping bed whose water depth changes from ~18-24m. This slope has a number of sinuous, steep (~1-4°) faced terraces leading up to the main bank. There is no discernible change in sediment cover associated with individual terraces.
- Overall, the bank is devoid of bedforms visible from the bathymetric map of the area.
- Water depths on the bank range from 13-20m below Chart Datum (Hastings). The bank falls away north to a slightly deeper region to the north down a gentle (<0.5°) slope. The southern extent of the bank (visible on the sidescan sonar mosaic as the line between the high backscatter of the bank and the medium backscatter of the small channel) is bounded by a much steeper slope (~3-4°). South and east of the bank, the sediments become finer grained, with the largest continuous area of fine grained material less than 500m from the eastern end of the bank.
- Similar ribbons of coarse grained material extend along the entire eastern side of the licence area into the medium grained material. Grain sized in the ribbons are comparable to those seen on the bank itself, whereas material further north east is consistently finer grained (<10mm). The boundary between the bank and the bed to the north east is of a similar definition to that seen between the bank and the south east. Ribbons such as these are indicative of high sediment transport rates in sediment starved regions (Stride *et al.* 1982).
- The area north east of the bank (Zone B in Figure 16) is distinguished by a gently (<0.5°) northerly sloping seabed. Sediment cover in this area is uniformly medium grained fining slightly in the most northerly section. The finest sediment cover (mean grain size <6mm) is associated with a number of large and very large 2D dunes. Typical wavelengths are 60-180m and amplitudes are 0.5-2m. The large and very large dunes have smaller parasitic bedforms superimposed on them; wavelengths are 10-12m and amplitudes 5-10cm.
- Zone C can be subdivided into two regions based on the water depth and the associated bedform variability. The shallow region (<20m depth) is characterised by a fine grained seabed formed into very large dunes (wavelengths ~200-250m, amplitudes ~2m), upon which are superimposed a number of large dunes (wavelengths 9-12m, amplitudes ~10cm). In the deeper region of Zone C, the sediment grain size is similar to the shallows, but the very large dunes are absent; only the large dunes are present.
- South of the bank, the sedimentology is largely dominated by a tongue of finer grained material (Zone C in Figure 16) extending from the shallow region east of the bank along the top of the slope and down into the deeper water. Either side of this finer material, the seabed sediments are medium grained and uniformly distributed. Variability in seabed type is a function of the bedforms expressed on the seabed.
- The southern region can be also subdivided into a sediment starved region (Zone D in Figure 16) and a sediment rich region (Zone E in Figure 16). Zone D is dominated by a large number of bedrock outcrops and relatively thin sediment cover. Energy is sapped from the water column by outcropped bedrock which would otherwise be available to transport material. This spatially variable energy distribution has formed a number of “dune trains”, where energy is funnelled between outcropping bedrock allowing localised sediment transport, which forms elongated trains of increasingly large (both wavelength and amplitude) bedforms. Conversely, Zone E appears sediment rich; large (100-175m wavelength and 0.5-2m) 3D dunes are dominant with

smaller parasitic 2D dunes (wavelengths of 2-10m and amplitude of 10-30cm).

- Zone D (sediment starved) in the south east shows the effect of the bank on the hydrodynamics through the changing dune axes; moving eastwards, the axes change from a 150° orientation to 140°
- The sediment rich southern region (Zone E) is also different from the east in the asymmetry of sediment transport, as inferred from dune profiles. Those dunes seen on the bed in the east, although sediment starved, appear to be actively transporting material; those in the west, however, are generally symmetrical, indicating no net sediment transport direction.
- Of note in Zone E, are a number of large, north orientated, strongly asymmetrical, very large dunes. The sidescan sonar mosaic of these features shows coarser ribbons on the lee slope of each dune.
- Zone F (Figure 16) is a uniformly medium grained (7mm – 25mm) with water depths of between 20-32m. It is dominated by medium 2D dunes (wavelengths of ~10m and amplitudes of 5-10cm), although there are some very large 3D dunes (wavelengths of 100-175m and amplitudes of 0.5-2m) with parasitic medium 2D dunes.

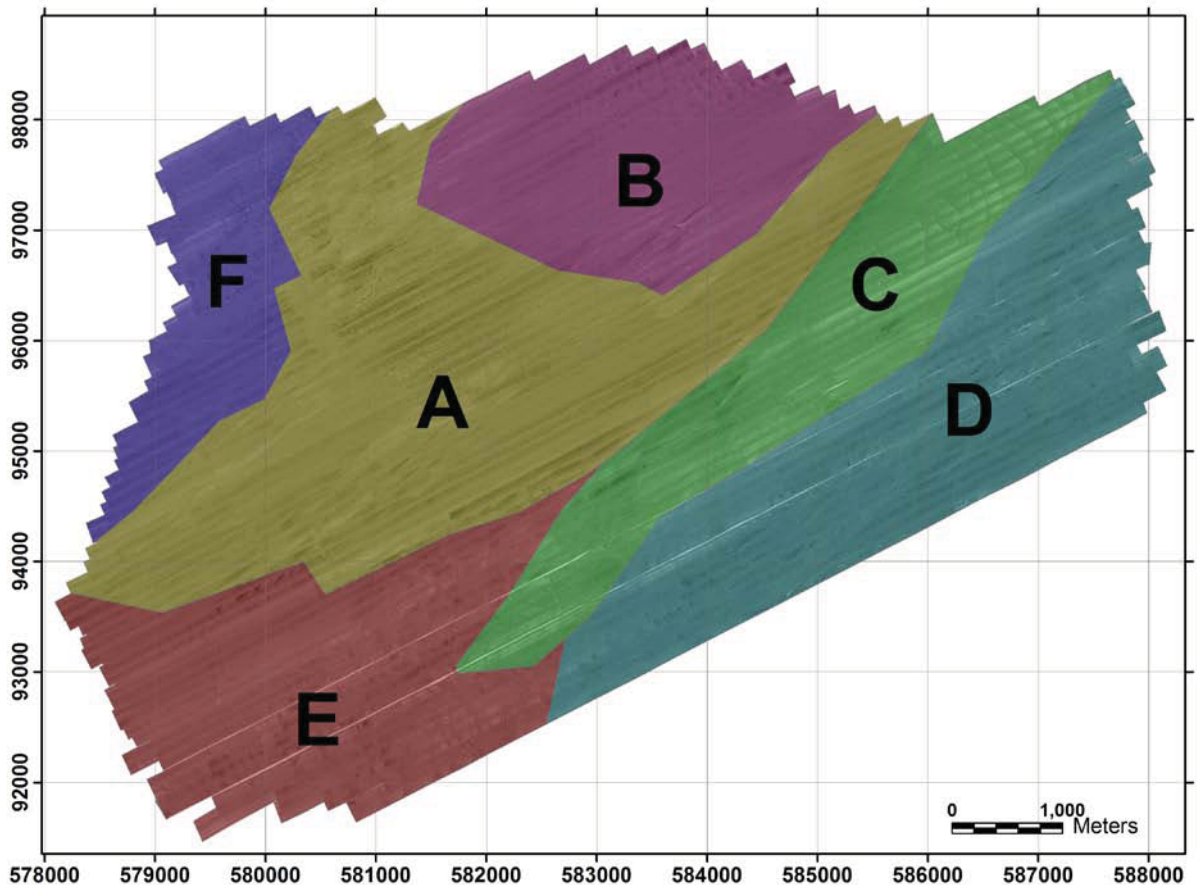
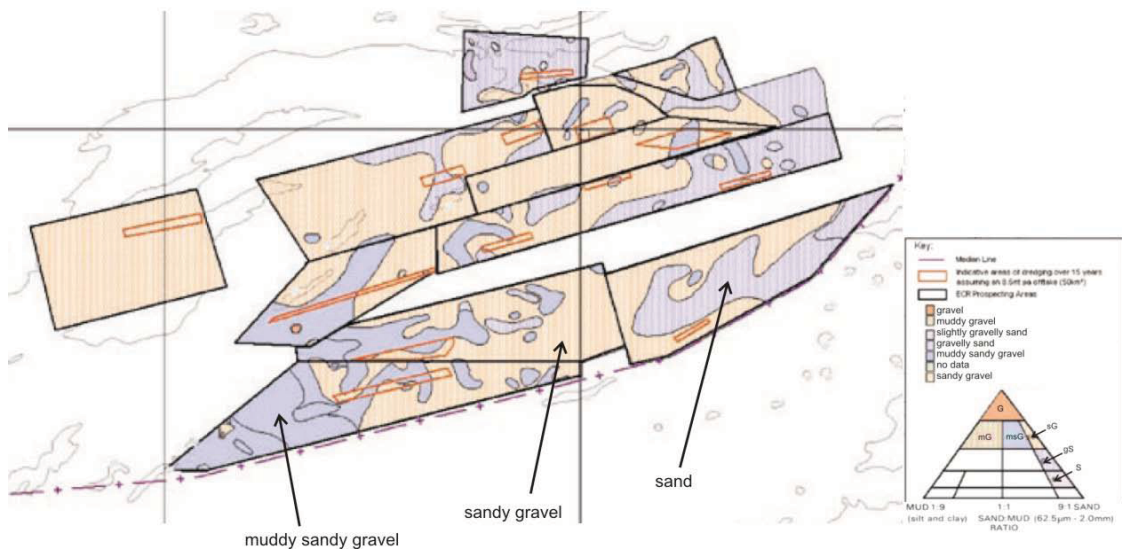


Figure 16 Zones of characteristic sediment cover. Axes in meters (Grid - Ordinance Survey of Great Britain).

## 2.6 The Eastern Channel License Sub-area

The east Channel license region (ECLR), containing Area 473E, is underlain mostly with stable Tertiary, Palaeogene bedrock (Smith *et al.*, 1975) comprising clays, sandy clays and silts, which tend not to penetrate the surface. Partly or wholly infilled palaeo-channels of mid-quaternary age are found in the region (Posford Haskoning, 2002). Overlying this, the surficial sedimentary layer is more complicated, varying in quantity and composition in an east-west direction due to spatial variation in tidal forcing outlined in Figure 2b. Figure 17 shows a sediment type distribution map of the ECLR, based on the top 40cm of numerous vibrocore samples collected in the region.



**Figure 17 Sediment distribution in the ECLR. Values represent the average of the top 40cm of numerous vibrocores collected in the region. Composition is based on the Folk classification, as shown (adapted from Posford Haskoning, 2002).**

Surface sediments vary in thickness between 5 and 10m in the ECLR, and mainly comprise a mixture of sand and 30% to 60% flint gravels. Sediments towards the east of the ECLR have a progressively higher carbonate shell content and decreasing median grain size (from 5-10mm in the west to <1mm in the east). A schematic west-east cross section through the ECLR (Figure 18) indicates an increase in abundance and depth of sand overlying the gravel towards the east. Sand waves of up to 11m high form in the far east of the region.

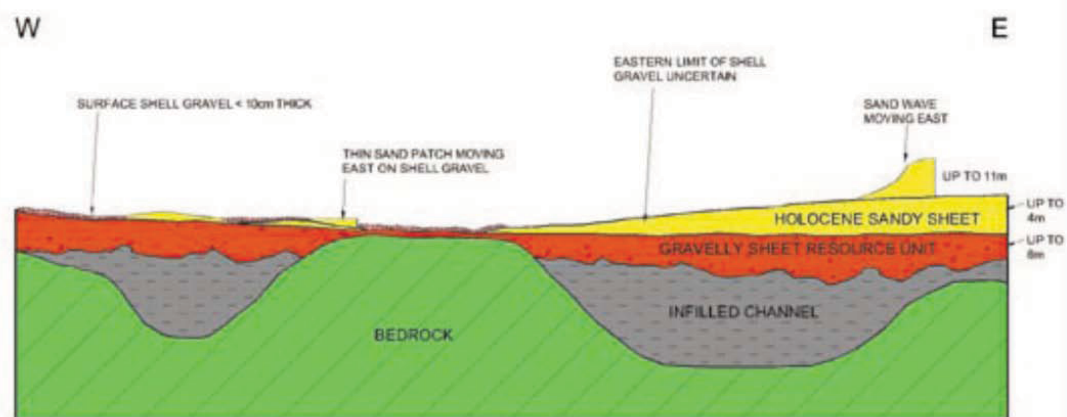


**Figure 18 Schematic cross section from west to east (left to right respectively) of sediments in the ECLR (Posford Haskoning, 2002).**

### **3. Design and calibration of the numerical model**

The MIKE software suit (2007 edition using service pack 1) was chosen for use in the present study. Specifically, the hydrodynamic module of the MIKE21 suite was used to model depth averaged hydrodynamic conditions (local water surface elevation, current speed and direction) using a flexible mesh (triangular elements). The sand transport module was also used to estimate the resulting transport patterns of non-cohesive sediments.

A number of inputs and choices must be made during the model setup in order to obtain the best possible estimate of the true result. In the hydrodynamic module, these include: the domain; solution technique; flood and dry; eddy viscosity; bed resistance; Coriolis forcing; wind forcing; ice coverage; tidal potential; precipitation/evaporation; wave radiation; sources; boundary conditions; and initial conditions. In the sand transport module, for a pure current forcing only, these include: model definition; time parameters; solution technique; sediment properties; bed resistance; dispersion; sources; initial conditions; and, morphology. The detailed meaning and effect of these parameter sets or choices are available in the appropriate MIKE software manuals but are also described below along with the choices made and in the context of the present study.

#### **3.1 Hydrodynamic module parameters and choices.**

##### **3.1.1. Domain**

The 'domain' collectively describes the shape and size of the body of water being modelled. The horizontal extent of the domain is delimited by the location of the open (sea) and closed (land) boundaries. Within these boundaries, a two-dimensional mesh is created which defines the locations and therefore the spatial resolution at which calculations are made, information is stored and results are produced. Each element and node in the mesh is also assigned a value for local water depth, collectively describing the bathymetry of the domain. The domain is created using the mesh generator tool in the MIKE zero interface.

##### **3.1.2. Bathymetry**

The bathymetry of the domain is the shape of the basin within which the flow is allowed to propagate. A different bathymetry effectively describes a different basin shape and will result in a different flow field, affecting the rate and direction of tidal propagation, with implications for local current speed, direction and derivative quantities such as bed shear stress and sediment transport. The degree of difference is a function of the extent and magnitude of the difference in both absolute (a very small difference everywhere or a large difference very locally may not affect the overall results significantly) and relative terms (the extent or magnitude of the difference must be significant compared to the domain size or the local water depth). The degree of difference is also likely to be controlled by the complexity of the flow in the region of modified bathymetry (flow associated with headlands, sandbanks, boundary constrictions, etc).

C-MAP was chosen as the main source of bathymetry data for the whole of the domain being modelled. Other potential sources included the ETOPO2 and GEBCO data sets but these are only available at a medium resolution (2 arc seconds = 3704m N/S x 2381m E/W); the former is derived from interpretation of altimetry data (with warnings about accuracy for shelf sea water depths) and the latter is derived from coarse digitisation of large scale admiralty chart data. The original sources of the C-MAP data are the various hydrographical offices of

the nations with coastal borders within the domain (i.e. UK, France, Belgium and The Netherlands); therefore, the data are considered to be of high quality. The source data vary in spatial density but are not artificially extrapolated prior to initial gridding in MIKE. The data are provided as local depth in meters, relative to the source chart datum (typically the height of mean low water springs in UK). Based on local time series measurements of tidal heights, a separate data set is also provided by C-MAP to convert from the source data datum to 'mean sea level' (the level about which the tide fluctuates, locally). These datum correction data are also interpolated over the extent of the source data and then applied to the source C-MAP bathymetry data.

The data are provided as irregular points which must be interpolated to the mesh. Both natural neighbour and linear interpolation methods with user adjustable coefficients are available in the MIKE mesh generator tool and may result in differences in the resulting bathymetry. The density of C-MAP data points decreases away from the coast and additional multi-beam swath bathymetry data were used to produce accurate bathymetric detail in the nested subregions.

Local water depth may vary naturally on daily, monthly or annual timescales due to local sediment erosion or accumulation. The magnitude of the vertical change in bed level can be in the order of centimetres to meters for small to medium bedforms and in the order of 1-10 meters for large dynamic sand waves or banks. Such changes do however tend to be part of a longer term fluctuation around a mean value.

No parts of the English Channel are reported in the literature to be experiencing long-term, persistent and significant (e.g.  $>0.5\text{m}$ ) sediment erosion or accretion. In most regions the maximum height of sediment accumulation is likely to be hydraulically controlled by the local current speed and sediment properties, i.e. accumulation reduces the water depth which increases current speed which increases erosion, producing an equilibrium water depth and therefore sediment thickness; the potential supply rate of mobile sediment to any given area is also finite. The maximum depth of erosion can also be hydraulically controlled but may also be limited by the presence of a bed rock or more resistant sediment base, or the development of an armoured layer in areas of poorly sorted (mixed) grain size.

In the recent geological past, sea level in the English Channel was significantly lower and varied greatly during the subsequent marine transgression to present day levels. In the near future, the report of the IPCC (2007) predicts that global mean sea levels may rise due to climate change by 0.18-0.59m by the year 2100. The additional effect of post glacial isostatic rebound (causing the south coast of the UK to subside by 0.5-1.0mm/yr) increases the predicted mean sea level rise in the English Channel by an additional 0.05-0.1m over the same period (Shennan and Horton, 2002).

### **3.1.3. Solution technique**

The fundamental equations controlling the model are inherently complex and may be individually formed of not just one but many parts that hone the result towards the 'true' value (the unique result of the full set of equations). The number of parts that must be used is not fixed and a smaller number may be used to obtain a close approximation of the true result whilst making fewer calculations. Models using these 'low order solutions' are therefore faster but potentially less accurate. High order solutions are technically more accurate but may increase run times by a factor of 2-4. Low and high order solutions produce results that are more similar when gradients in the model are small, i.e. smaller tidal range, flatter bathymetry, less interaction with the coastline, etc. A low order solution was used in the present study; this choice was recommended by the software providers DHI and was tested as part of the calibration procedure (see Section 3.3.3.5).

### **3.1.4. Flood and dry**

Flood and dry is the name given to a numerical tool within the model which aids in maintaining numerical stability. It is concerned with water movement over grid nodes in the inter-tidal zone, i.e. nodes that are not continuously submerged. Due to the scale of the mesh elements being used adjacent to the coastline (5000-7500m), the depth of these elements was representative of deeper water and therefore greater than the local tidal range, hence not posing any problems with drying. However, as a precaution against unforeseen problems from isolated shallow water elements in estuaries and as it does not significantly affect the model run time, this feature was activated.

### **3.1.5. Eddy viscosity**

Eddy viscosity is a parameter in the fundamental model equations controlling flow through the domain. It expresses the viscosity of the flow, in a horizontal plane, without the need to fully model fluid eddies that may be too small to be resolved by the computational mesh. Different parameterisations for eddy viscosity may be specified, including: the Smagorinski formulation [default]; no eddy viscosity; or constant eddy viscosity. The default formulation and coefficient was used. The coefficient value was tested as part of the calibration procedure (see Section 3.3.3.7).

### **3.1.6. Bed resistance**

Bed resistance is a parameter in the fundamental model equations controlling flow through the domain. Combined with flow speed, bed resistance describes the friction felt by the flow. Different parameterisations may be specified, including: Manning number [default]; Chezy number; or no friction. A uniform or a spatially variable value may be applied. The default formulation but with a modified uniform coefficient value was eventually used. The coefficient value was selected as part of the calibration procedure (see Section 3.3.3.6).

### **3.1.7. Coriolis forcing**

The Coriolis force is an additional acceleration force felt by objects as they move over the spinning Earth. In the northern hemisphere, it causes objects in motion (in this case, the flow of water) to be deflected to the right; the strength of this deflection is variable with latitude and is greatest at the poles, decreasing to zero at the equator. The Coriolis force is a parameter in the model equations controlling flow through the domain. As default, the Coriolis force is calculated separately for each node of the mesh using the known value of latitude, other choices include using a fixed value (suitable for small scale domains with only small variation in latitude) or no Coriolis force (not a realistic scenario). The default setting was used in the present study.

### **3.1.8. Wind forcing**

Wind blowing across the water surface will induce an additional current to that of the tide. The speed and direction of this secondary current is a function of the speed and direction, duration and length scale of the wind field acting upon the domain. No wind fields were applied as part of the present study.

### **3.1.9. Ice coverage**

Sea ice forms a solid barrier to the effects of wind stress locally and may occupy a large fraction of the water column. Where its distribution is known, it may be applied to the model. The typical absence of sea ice at the study latitude means that sea ice is not a consideration in the present study and this module was not used in the present study.

### **3.1.10. Tidal potential**

The tidal response of very large domain models, e.g. the Mediterranean or larger, are not simply driven by the changes in water level at the relatively small open boundaries, but by the gravitational effects of the sun and the moon which must be applied directly to the water body for a correct solution. The advice of the software suppliers, DHI, was that the English Channel does not require the application of tidal potential and so this correction was not applied in the present study.

#### **3.1.11. Precipitation – Evaporation**

The volume of isolated water bodies in environments with highly seasonal rainfall and/or strong evaporation potential may fluctuate significantly. Temporal variability in the spatial and temporal distribution of these may be required to obtain a realistic solution for such bodies of water. The depth of the English Channel is not significantly affected by local evaporation or precipitation and so this module was not used in the present study.

#### **3.1.12. Wave radiation**

Water waves propagating through the domain translate energy and momentum which may be described numerically as wave radiation stresses. These values vary spatially and temporally and must be calculated using another module in the MIKE software suite. These are then used in the purely tidal hydrodynamic model to yield the combined flow field. Due to the added complexity and the number of runs required to test, wave action was not included in the present study.

#### **3.1.13. Sources**

Significant inputs of water into the domain, e.g. large rivers, can alter local flow patterns from that driven purely by the tide. The regions of interest in the English Channel are located far from any significant such sources and so none were applied in the present study.

#### **3.1.14. Boundary conditions**

The tidal signal is introduced to the domain at the open boundaries as a variation in water surface elevation about the mean level. Time series of the tidal elevation profile along the open boundaries are obtained from the predictive ‘KMS’ model provided with the MIKE software. The hydrodynamic model then propagates this signal through the domain as a function of the other variables listed here.

The KMS global tide model data represents the major diurnal (K1, O1, P1 and Q1) and semidiurnal tidal constituents (M2, S2, N2 and K2) with a spatial resolution of  $0.25^\circ \times 0.25^\circ$  based on TOPEX/POSEIDON altimetry data. It is noted in the DHI help manual for MIKE 21 that the KMS model is applicable mainly in relatively deep water, e.g. depths greater than 20 meters. Because the KMS model includes only a finite number of tidal constituents, adequate distance must also be allowed between the open boundaries and the region of interest to allow higher harmonics to be developed, if they are considered important. For more information on the KMS model, see e.g. Ole Baltazar Andersen (1995).

#### **3.1.15. Initial conditions**

If an initial distribution of water surface elevation or current speed and direction is known, it may be applied, otherwise, an initial period of time is required by the model to reach an equilibrium state. No such information was available so the model was started from a state of uniform mean sea level (=0m) and current (=0ms<sup>-1</sup>).

#### **3.1.16. Decoupling**

By running a hydrodynamic model in decoupled mode, the most basic results of the model calculations are regularly saved which can be used at a later time to efficiently reconstruct the hydrodynamic flow field. The decoupled run files can be used directly by other modules (e.g. the sand transport module), to test many scenarios without the need to recalculate the hydrodynamic part every time.

## 3.2 Sand transport module parameters and choices.

### 3.2.1. Model definition

A choice may be made to model the equilibrium or non-equilibrium response of the sediment transport to the current. An equilibrium response assumes that the amount of sediment in transport is in equilibrium with the flow velocity and direction at each timestep. A non-equilibrium response is the more realistic of the two, where there is a lag between flow velocity and the response in suspended sediment concentration, e.g. sediment may remain in suspension (gradually settling out) for some time after the current speed has decreased below the threshold for suspension. The non-equilibrium mode was preferred but could not be used due to compatibility issues with lat/long projection meshes. Therefore the equilibrium mode was used in the present study.

A choice of sediment transport formulation can also be made. Choices include: Engelund and Hansen (1972); Engelund and Fredsøe (1976); van Rijn (1984); and (for bed load only) Meyer-Peter and Müller (1948). Comparisons of scenario predictions by the various formulae are presented in Soulsby (1997). At the time, all of the above relationships were considered suitable for the calculation of either bed, suspended or (through summation) total load transport. When calculating total load, the relatively simple approach of Engelund and Hansen (1972) is shown to compare closely (within 9%) to the more complicated approach of van Rijn (1984). Soulsby (1997) also notes that there is a factor 2 difference between calculations of total load made using the full range of formulae presented therein. The particular formulations listed above are not compared directly in the literature in terms of accuracy when predicting bedload or suspended load independently, therefore, in order to choose the equation with the lowest overall reported error in total sediment transport (the most important factor in long term sediment transport), the method of Engelund and Hansen (1972) was chosen for use in the final model. From the DHI scientific documentation for the ST module, the dimensionless rate of total-load transport  $\Phi_t$  is calculated as

$$\Phi_t = 0.1 \frac{C^2}{2g} \theta^{2.5}$$

with  $C$  = Chezy's number and

$$\Phi_t = \frac{q_t}{\sqrt{(s-1)gd^3}}$$

with  $q_t$  = the total-load sediment transport and  $g$  = gravitational acceleration. The dimensionless bed shear stress  $\theta$  is defined as

$$\theta = \frac{U_f^2}{(s-1)gd}$$

where  $U_f$  is the shear velocity related to total friction,  $d$  is the grain diameter and  $s$  is the relative density of the bed material. This formulation assumes that the dimensionless bed shear stress  $\theta$  is much larger than the Critical Shields Parameter for initiation of transport  $\theta_c$ . Therefore, the value of  $\theta_c$  specified by the user will not be applied if this formulation has been

chosen. Something similar applies to the gradation of the bed material, since Engelund & Hansen theory is based on the median grain size  $d_{50}$ .

### 3.2.2. Time parameters

The hydrodynamic part of the model may not reach equilibrium immediately, producing anomalously high current speeds at atypical directions locally. The start of sediment transport calculations may be manually delayed until it is assumed that an equilibrium state has been reached. The sediment transport may also be magnified here as a crude method of extrapolating long term morphological change.

### 3.2.3. Sediment properties

The porosity of the bed, the sediment grain diameter and density may be specified as variables in the sediment transport equations and are important in calculating morphological change. The default bed porosity (0.4) and sediment density ( $2650\text{kgm}^{-3}$ ) values were used as they represent a natural quartz sand bed with average packing and of average sorting (Soulsby, 1997). The choice of uniform grain diameter [63, 200, 500 &  $1000\mu\text{m}$ ] or a spatially varying value was a primary variable in the scenarios tested as part of the present study.

The spatially varying mean grain size was compiled using data from the various sources described in Section 2.3 and only represents the broad scale distribution of sediment type. The spatially variable grain size distribution used in the sediment transport model and when calculating spatially variable bed roughness is shown below.

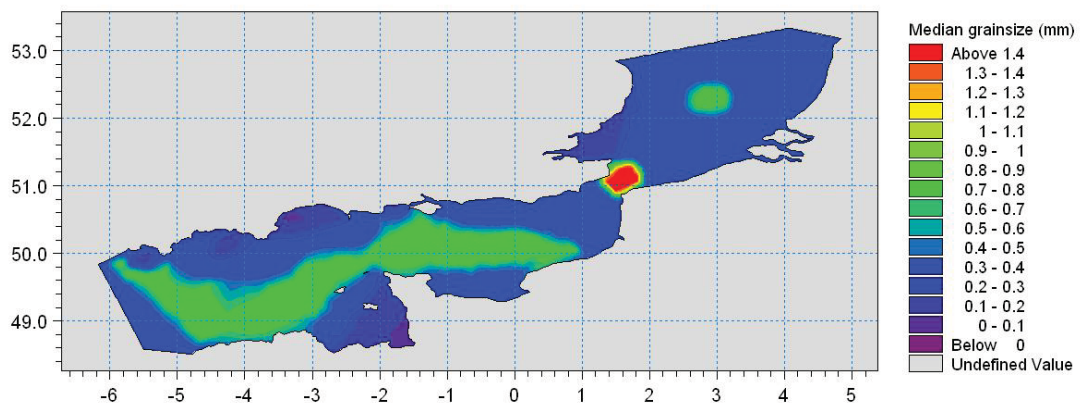


Figure 19. Distribution of variable mean grain size where used in the model.

### 3.2.4. Bed resistance

Sediment transport is a function of the force applied to the bed by the current which is in turn a function of the current speed and bed resistance. As in the hydrodynamic module, different parameterisations may be specified, including: Manning number [default]; Chezy number; or no friction. The choice of coefficient will affect the rate at which sediment will move through the domain but there was insufficient time and observed data available to undertake a sensitivity or calibration study for this parameter. Therefore, the default formulation and coefficient value ( $M=32$ ) were used.

### 3.2.5. Dispersion

Dispersion is a component part of the underlying equations and describes the rate at which sediment in transport is dispersed laterally by natural diffusion processes not resolved by the large scale flow patterns. Not available as a choice in decoupled mode.

### **3.2.6. Sources**

Significant inputs of sediment into the domain, e.g. fluvial sources, dredge spoil dumping or plumes, can alter local sediment transport budgets and related morphological patterns from that driven purely by the tide interacting with existing marine sediments. The regions of interest in the English Channel are located far from any such sources and so none are considered necessary in the present study; this option was not available as a choice in decoupled mode.

### **3.2.7. Initial conditions**

If an initial distribution of sediment transport or suspended sediment concentration is known, it may be applied, otherwise, an initial period of time is required by the model for an equilibrium to be reached. No such information was available and this option was not available as a choice in decoupled mode.

### **3.2.8. Morphology**

Spatial gradients in sediment transport result in morphological change, i.e. erosion or accumulation, which can affect the local depth and flow of water over the area. Coupled model runs, where both the hydrodynamics and sediment transport are calculated at each time step, can include morphological feedback where the bathymetry is updated by the sediment transport module for each timestep of the model. Decoupled model runs without morphological feedback were used in preference, firstly due to the complex distribution of sediments in the study region requiring multiple runs, secondly due to the implications for incorrect morphological feedback distorting the hydrodynamics, and thirdly due to the prohibitively long run times that would become necessary.

## **3.3 Calibration**

The intention of the calibration procedure is to tune the model so that the results it produces compare as closely as possible with previously observed or predicted data that have been collected or created in such a way that there is a higher degree of confidence in their accuracy than that of the un-calibrated model output. The actual coefficient values or the choice of inputs eventually used may not be the same as those thought to be 'ideal' from general theory or in comparison to those derived from the field. The need for such tuning occurs as numerical models, and the number, accuracy and resolution of the inputs into them, are inevitably a simplification of reality and this must be accounted for.

Confidence in the accuracy of the model is improved: 1) by having a closer fit between the predicted and calibration data sets; and 2) by using calibration data of higher accuracy or with less susceptibility to minor errors or issues of scale and time.

### **3.3.1. Calibration data availability and summary**

The data that were available for use in calibration included both time-independent large-scale spatial data and point time-series data.

#### **3.3.1.1. *Large-scale spatial data***

The available large-scale spatial data included figures and charts of the (predicted or interpolated) distribution of tidal co-range and co-phase lines in the domain. Co-range and co-phase data were obtained from a POL report (1990) for the O1, K1, N2, M2 and S2 tidal constituents, and from Admiralty Chart 5058 (1996) for the mean tide only. It was not possible due to time constraints in the present study, but it may be possible in the future, to create digital maps of the distribution of the K1, O1, P1, Q1, M2, S2, N2 and K2 constituents using the KMS model input data for quantitative comparison.

Other large scale spatial data sources describe the distribution of residual flow or sediment transport vectors. Figures describing generalised pathways of sediment transport in the southern North Sea and English Channel are available from various sources, principally using interpretation of sandy bedform orientation, e.g. Stride (1963), Kenyon and Stride (1970), Kenyon *et al.* (1981), Johnson *et al.* (1982), later augmented in the Dover Straits by a summary of radioactive tracer studies by Beck *et al.* (1991). Large scale residual flow patterns from numerical modelling studies were presented by Salomon and Breton (1991).

### 3.3.1.2. Point time-series data

A search was undertaken for all historical tidal elevation and current meter data available within the domain. The majority of data found was made available through the British Oceanographic Data Center (BODC) website. The distribution of all point series data is shown in Figure 20. There is a noticeable absence of data in deeper water in the whole of the English Channel; a higher density of data is available from the southern North Sea and Thames Estuary. Of the limited number of data sets available in the English Channel, three were used, namely: offshore points adjacent to the Isle of Wight; on the Owers bank; and on the Hastings Shingle Bank. The latter two represent data collected as part of round 2 ALSF project 3365. The line of data points between the Isle of Wight and Cherbourg were only recently added to the BODC website, have not undergone rigorous quality control and therefore were not used in the present study; it will however be extremely useful to reassess the suitability of these data for future calibration of similar models.

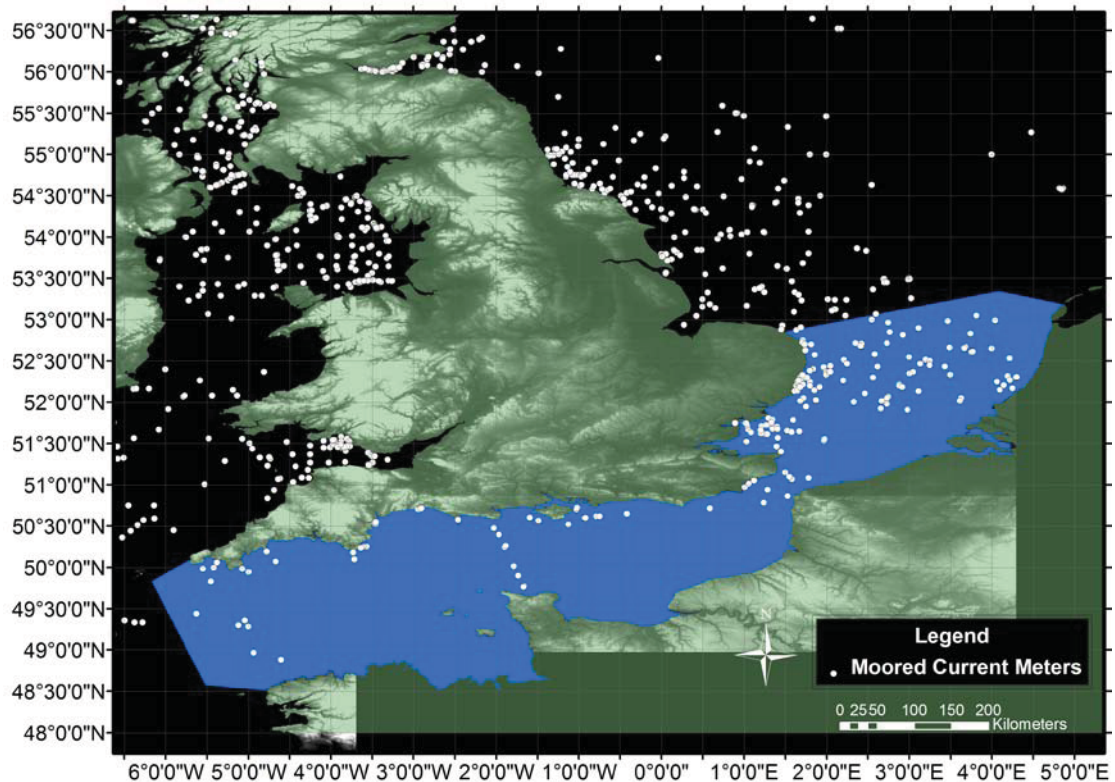


**Figure 20. Distribution of current meter data sets available from the British Oceanographic Data Center data base and previous fieldwork studies, near to the model domain.**

### 3.3.1.3. Tidal elevation

Tidal elevation measurements were only available at onshore sites (ports and harbours), the majority of which form the national tidal gauge network (Figure 21). These data are carefully quality controlled but are collected in relatively shallow water, making them susceptible to shallow water tidal effects and meteorological influences. These effects are typically then filtered from long time series through the process of tidal harmonic analysis and as such these data are used to construct the large-scale co-range and co-phase charts described above. However, these effects also make these data unsuitable for detailed (instantaneous) comparison with the lower spatial resolution data from the model, over short timescales, and were therefore not used for this purpose.

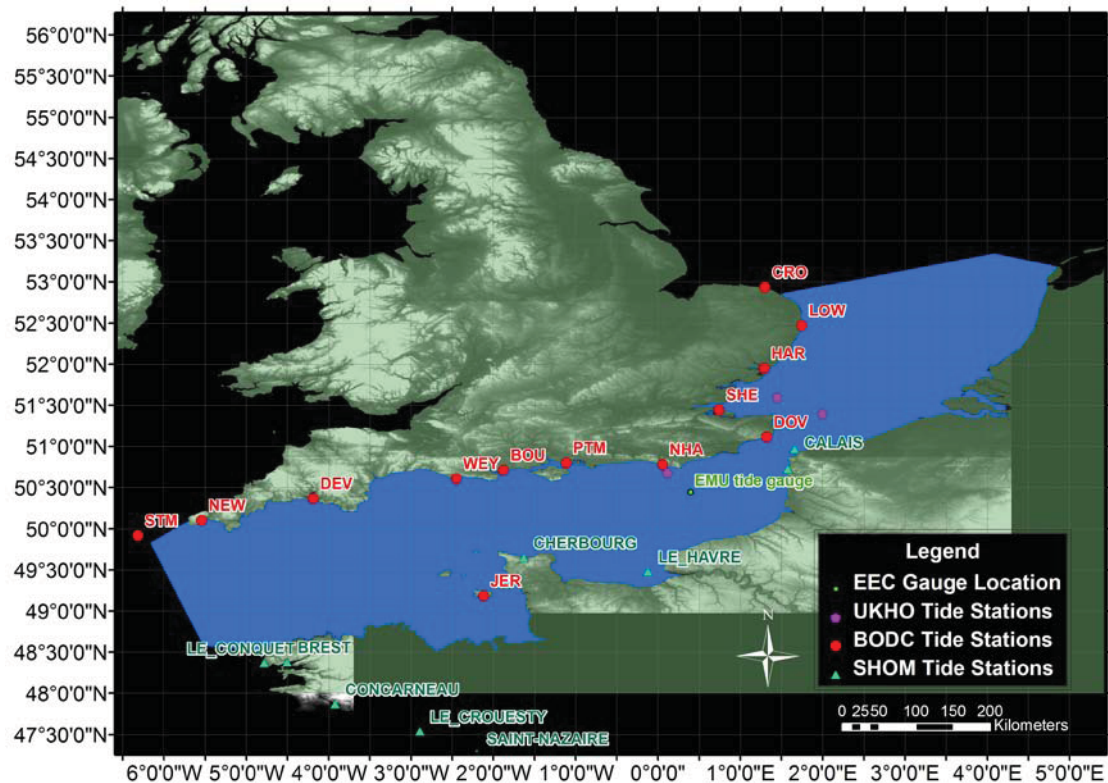


**Figure 21. The distribution of nationally operated tidal gauge network sites, near to the model domain.**

Tidal elevation time series from specific offshore locations in the middle of the domain may be obtained from the C-Map database, however, these data are predicted and only then on the basis of a small (unknown) number of constituents; the source data was not available. Similar predicted time series may be obtained from the KMS model, also used to provide tidal elevation input at the boundaries to the model. These time series are also based on a finite number of constituents (8) and so may not represent the ‘true’ or fully developed tidal signal.

Tidal elevation time series data sets are also available from two offshore sites. These data come from the two 30 day, multiple current meter deployments made during the summers of 2005 and 2006 as part of the ‘Modelling Exclusion Zones for Marine Aggregate Dredging’ ALSF project 3365. These data are used here for purposes of calibration but represent only two sites, covering only a small part of the domain and using equipment not specifically designed for the accurate measurement of water depth (quoted accuracy  $\pm 0.5\%$  of water column height, e.g. approximately  $\pm 15\text{cm}$  in 30m water depth).

#### **3.3.1.4. *Current speed and direction***

Observations of current speed and direction in the domain were more numerous but were concentrated in the North Sea / Thames Estuary and the outer part of the Western Approaches; a small number of observations were available from the Dover Straits and around the Isle of Wight. The data were typically collected using a variety of single point current meters deployed on subsurface moorings (near to the seabed), with the exception of the Hastings Shingle Bank and Owers Bank data sets which were collected as part of ALSF project 3365, using acoustic doppler current profiling devices. With the exception of the latter and the few records from close to the Isle of Wight, data sets were not available for most of the central eastern part and the majority of the western part of the English Channel.

To rationalise the number of model runs that had to be made for comparison with point data, the number of observed data sets was filtered and reduced. Thirty data sets were identified: a) that were overlapped in time; b) where the individual data sets covered a significant period of time (e.g. more than 14 days); c) that cover a wide range of locations; and d) that represented the full range of locations where data was available. These fell into seven temporal groups identified for use in calibration. The accuracy of the instruments making the measurements was not reported in all cases so in order to use the data it must be assumed that all data were collected with due regard for accuracy and quality control. Due to insufficient information about the individual mooring configurations, no adjustments were made to the reported current speeds, which are assumed herein to represent the depth mean value.

Point series data are particularly sensitive to meteorological effects as they are deployed for relatively short periods of time in comparison to the frequency of storm events and atmospheric pressure fluctuations, especially during winter months. The model however considers only the pure tidal contribution to currents and sediment transport.

### **3.3.2. Calibration methods**

#### **3.3.2.1. *Large-scale spatial data***

Due to issues of Copyright and the difficulty of obtaining the underlying data, the location of predicted co-range and co-phase lines were qualitatively (visually) compared with those previously published. It will be shown in the following sections that variation of certain input parameters, within the ranges tested, significantly affects the distribution of large scale spatial data. The fact that the results are so sensitive improves the accuracy of such a qualitative calibration, because the user does not have to make judgements based on only subtle differences.

#### **3.3.2.2. *Point time-series data***

Point time series of current speed and direction were also compared qualitatively with the observed data in the first instance to compare more subtle differences such as half tidal cycle shape and phase relationships. Point time-series of current speed and direction data were also quantitatively analysed as follows and as indicated in Figure 22:

1. The tidal elevation time series' are analysed for harmonic information allowing the current data to be divided approximately into individual half-tidal (identified as flood or ebb) cycles.
2. The peak current speed in each half-cycle is identified and the difference between the observed and predicted value is recorded.
3. The difference between the observed and predicted current direction at the point of peak velocity in each half cycle is recorded.

4. The difference between the observed and predicted current direction at the mid-point of each half cycle is also recorded.
5. Additional meta-information is also recorded against each half cycle value including flood or ebb, spring or neap and peak velocity magnitude.

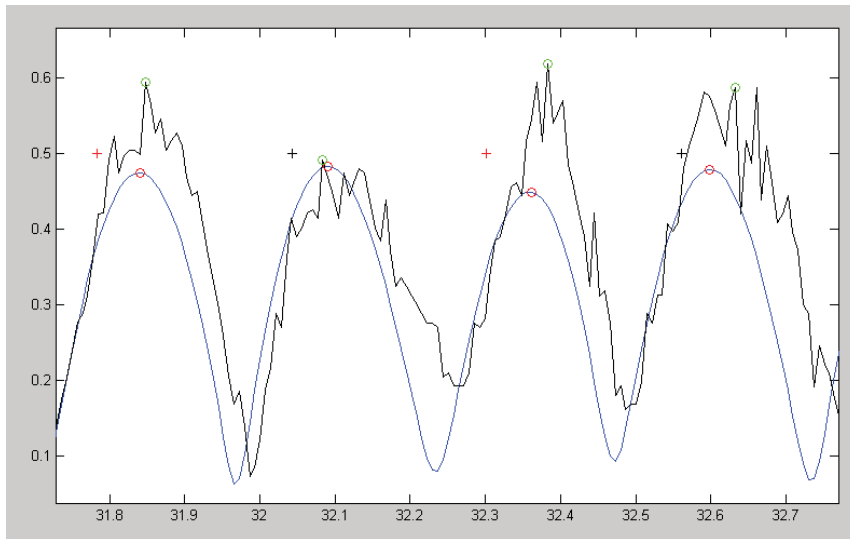


**Figure 22. Schematic description of the method for quantitative time series comparison.** Key: black line – observed tidal current speed; blue line – modelled current speed; red and green circles – peak current speeds in each half cycle.

Results from different scenarios (incrementally different parameter values) were compared either by:

- Plotting mean error values against the incrementally altered parameter value, observing the trend and finding the optimum value which minimises overall error (e.g. Figure 39). This method may be used in an objective quantitative manner and it represents the error for a whole time series as a single value.
- Plotting individual error values against the corresponding peak flow velocity as scatter data (e.g. Figure 37). Scatter data resulting from different parameter values are overlain and compared, allowing relative error to be viewed in the context of the current speed. The optimum value may then be semi-quantitatively chosen by minimising error in a certain subset of the data (e.g. all data with a peak velocity greater than the threshold of motion for a certain sand fraction).

Calibration of the model was undertaken by iteratively and systematically varying the values of the various model parameters in isolation. Parameters were only varied within the suggested ranges provided by DHI and entirely unrealistic scenarios (e.g. no bed resistance or eddy viscosity) were discounted from the outset. The literature was used where possible to establish the most likely ‘true’ or ‘best’ value for a parameter.

### 3.3.3. Calibration results

The following parameters, variables and choices were tested as part of a sensitivity study towards final calibration of the model: open boundary location; land boundary definition; mesh resolution; solution technique; bed roughness; eddy viscosity.

#### 3.3.3.1. Open boundaries

When choosing the location of open boundaries, the advice received from DHI was that open boundaries should avoid intersecting or interacting with complex tidal regions such as narrow constrictions or amphidromic systems. Therefore, 4 configurations of open boundary location were tested (shown in Figure 23); these boundaries coincide approximately with the location of previously published local co-phase lines (Admiralty Chart 5058, 1996).

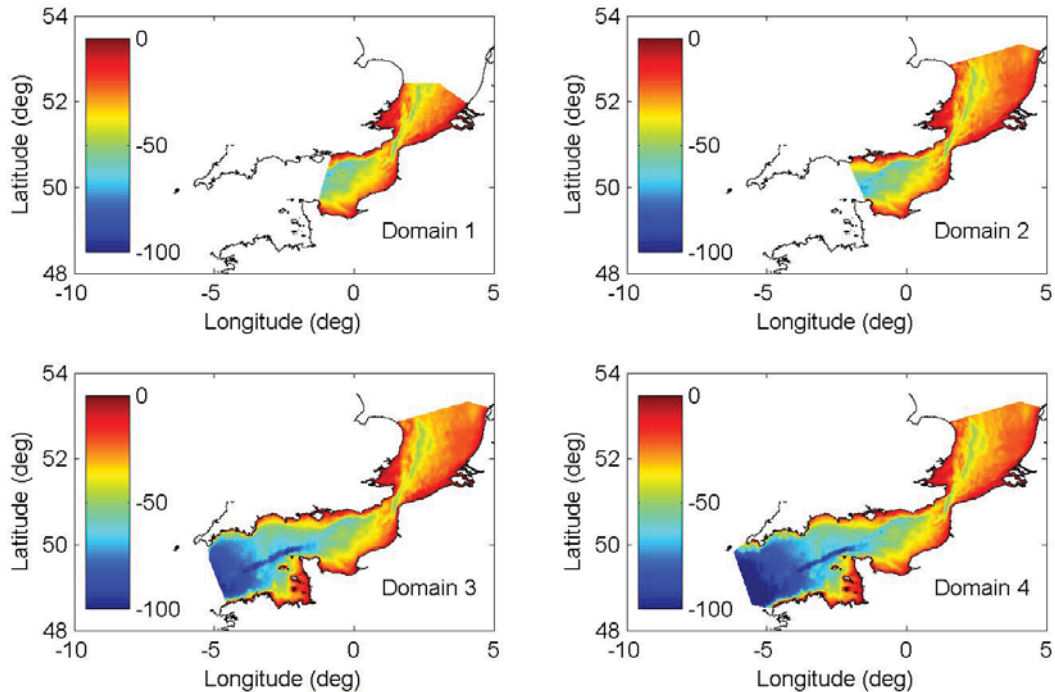


**Figure 23. The four domains tested. The colour scale indicates the depth of the seabed in meters below mean sea level. Domain 4 was chosen for use in the final model.**

During testing it was found that, in all four configurations, instantaneous current speeds and directions immediately adjacent to the open boundary were significantly magnified and that a more extensive region of distorted flow was visible in the residual flow field, associated with the open boundary. As indicated in Figure 24, distortion fields of similar size are evident, adjacent to the open boundaries of both domain 1 and domain 4. Distortion in the central Channel corresponding to the western boundary of domain 1 is not apparent in the same region of domain 4; residual flow patterns unaffected by local distortion at the boundaries are similar or the same in both domains. The boundaries used in the larger domain 4 are far enough from the regions of primary interest (the eastern and central/western parts of the English Channel) that such distortion did not extend into them. Domain 4 was therefore used in the final model.

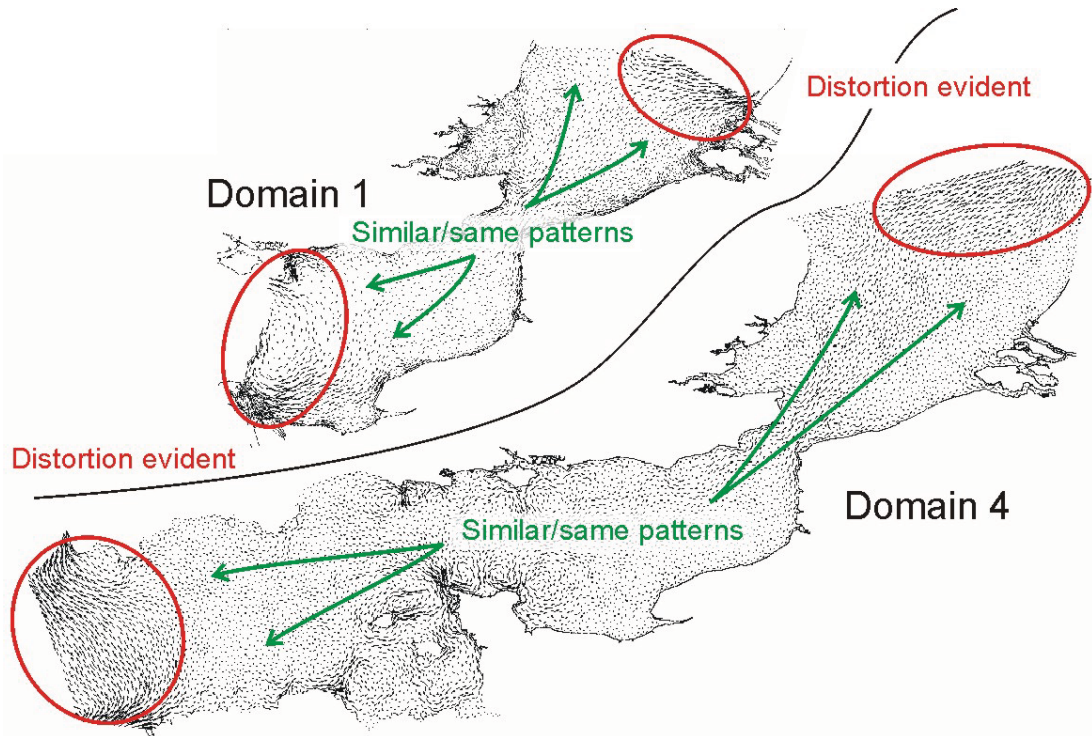


Figure 24. Distortion identified in the residual flow field, adjacent to the open boundaries of domains 1 and 4. Residual flow patterns in regions of the domain away from the open boundaries are similar to or the same as, those from other models covering the same spatial extent.

### 3.3.3.2. Land boundaries

The land boundaries were initially obtained as a high (but variable) resolution (<1000m separation) series of coordinates obtained from the digital GEBCO atlas (2000). These were converted into arcs (lines of sequentially connected points) for use in the mesh generator tool. In the study relating to optimum mesh design (Appendix C), it was found that the land boundary nodal spacing should be chosen to compliment (typically 0.8 times) the desired element length scale. A sub-optimal choice of node spacing produces irregular or smaller elements adjacent to the coast, potentially increasing overall run times but this was found to have no significant effect on the results elsewhere in the domain. The spatial resolution of the coastline boundary was therefore chosen to compliment the desired mesh resolution adjacent to that section of coastline (variable between the different meshes tested and also within the mesh in the case of the spatially refined meshes).

No testing was undertaken to establish the effect on the flow field of reducing boundary resolution, a process which necessarily results in deviation from the true shape of the coastline and sometimes the removal of estuaries and inlets. The advice from other users (DHI and Ivan Haigh, *pers comm.*) was that the detailed land boundary shape may have an effect immediately adjacent to it (hence would be important for nearshore studies), but not further offshore. The removal of estuaries and inlets may have a similar local effect, the extent of which is likely proportional to the size or volume of the feature removed.

### 3.3.3.3. Mesh resolution – English Channel

The choice of mesh resolution has several important implications for model accuracy, run time and other practical issues relating to subsequent processing of the results.

The choice of mesh resolution in all parts of the domain may affect the model results. It is typically found that the results from progressively higher mesh resolutions converge onto a single solution. Using a resolution finer than that required to obtain results close to (i.e. within acceptable error bounds of) this unique solution does not improve the accuracy of the results but does increase the run time of the model. Therefore, the optimum mesh resolution is the coarsest one that provides an acceptable result.

Predicted tidal elevation, current speed and direction were extracted from existing model runs at twenty evenly distributed offshore points in the domain (Figure 25). Data were extracted at hourly intervals over one spring-neap cycle. The models used the same configuration [domain 4, Mannings bed resistance,  $M=40$ , otherwise default values] except for meshes of varying resolution [3000m, 5000m, 7500m, 10,000m].

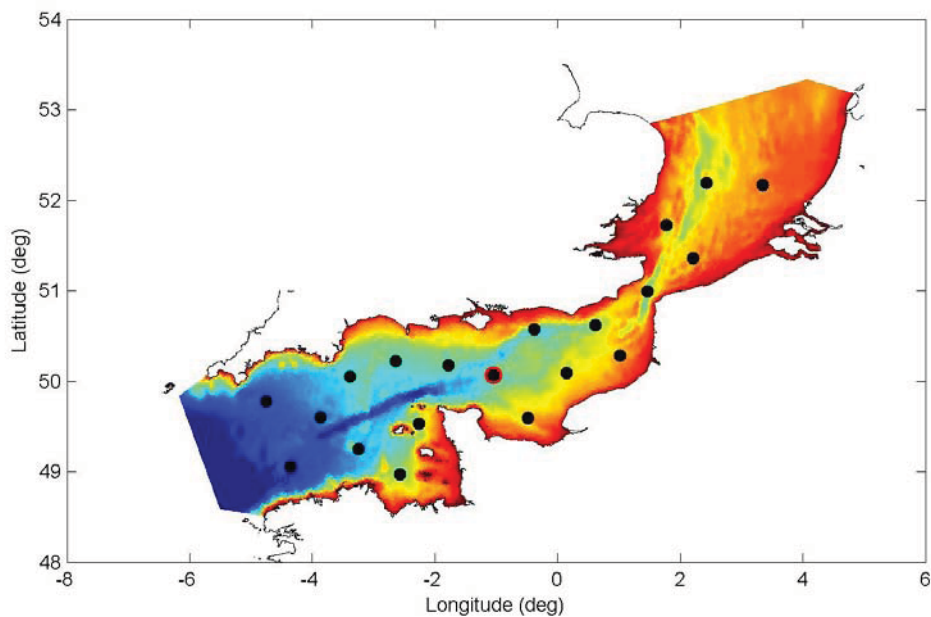


**Figure 25.** The location of the 20 data sampling points used to extract time series for comparison between different model setups. Where indicated, data shown in some other Figures are extracted from the location outlined in red.

Figure 26 shows a detailed comparison of one day of data, during spring tides, from a site in the central English Channel (indicated in Figure 25); this comparison image is typical and representative of all of the points tested. Tidal elevation, current speed and direction all demonstrate close similarity at all times; the exception is an apparent deviation in current direction when the flow rotates through North and values of, e.g.  $358^\circ$  and  $002^\circ$  appear more disparate than they actually are.

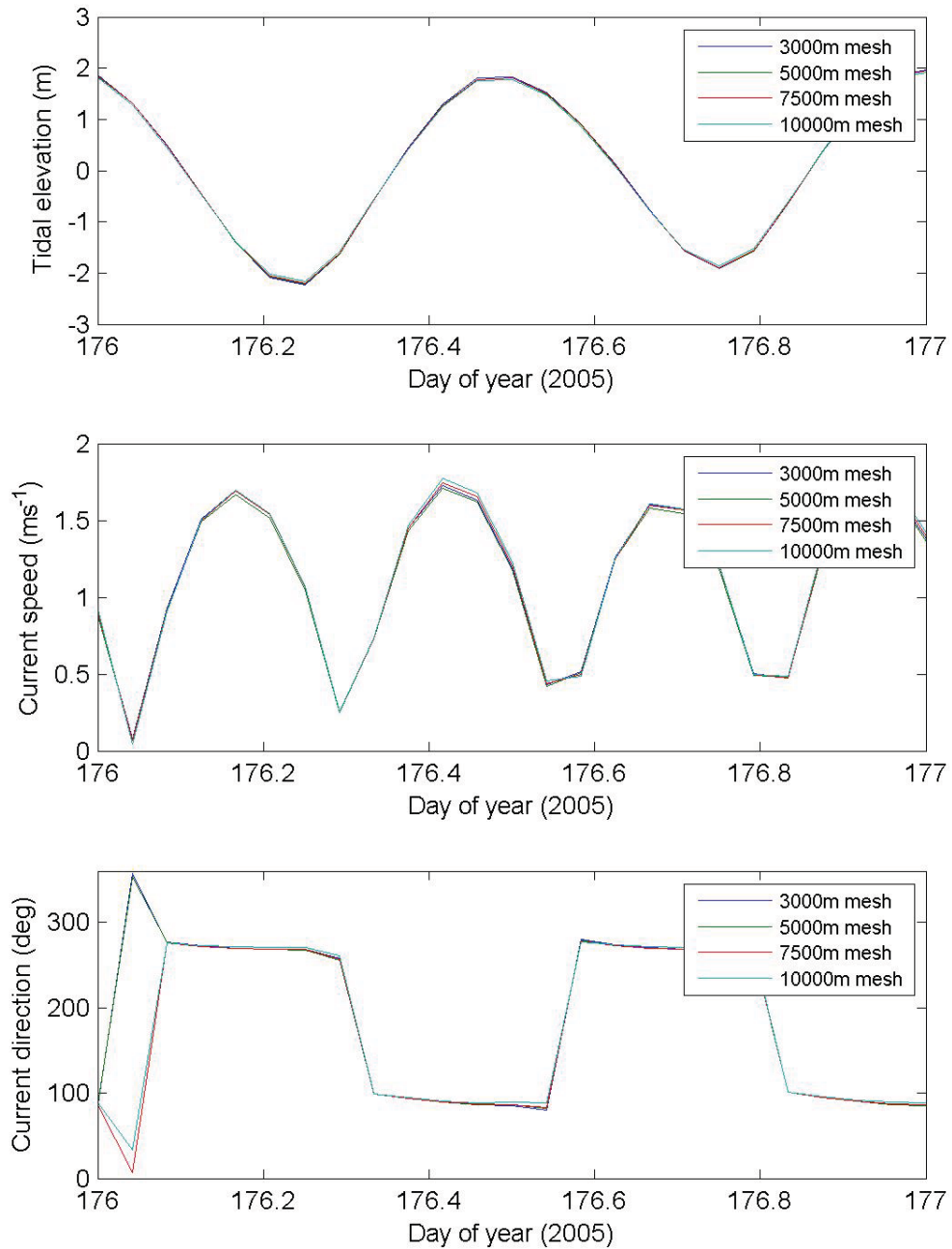


**Figure 26. Detailed comparison of tidal elevation, current speed and direction data from models using different uniform mesh resolutions. One day of data during spring tides from a site in the central English Channel (indicated in Figure 25).**

The quantitative difference between the results predicted using the finest mesh (most likely to represent the ‘true solution’) and those predicted by coarser meshes is shown in Figure 27. As expected, the mean difference tends to decrease with increasing mesh resolution. The current direction subplot indicates a relatively large standard deviation of instantaneous difference and a high mean difference at one location also; this is due to the anomalously large apparent difference in direction occasionally observed due to flow rotation

through North, as described above. In all other cases and for all three parameters the mean difference, including standard error, is relatively low in comparison to the target levels of accuracy (i.e.  $\pm 0.1\text{m}$ ,  $\pm 0.2\text{ms}^{-1}$  and  $\pm 20^\circ$  from Bartlett, 1998) and in comparison to that associated with variation in other key calibration parameters (e.g. varying bed roughness within the range  $M=20-50$  equates to  $\pm 1.5\text{m}$ ,  $\pm 0.6\text{ms}^{-1}$  and  $\pm 5^\circ$ ).

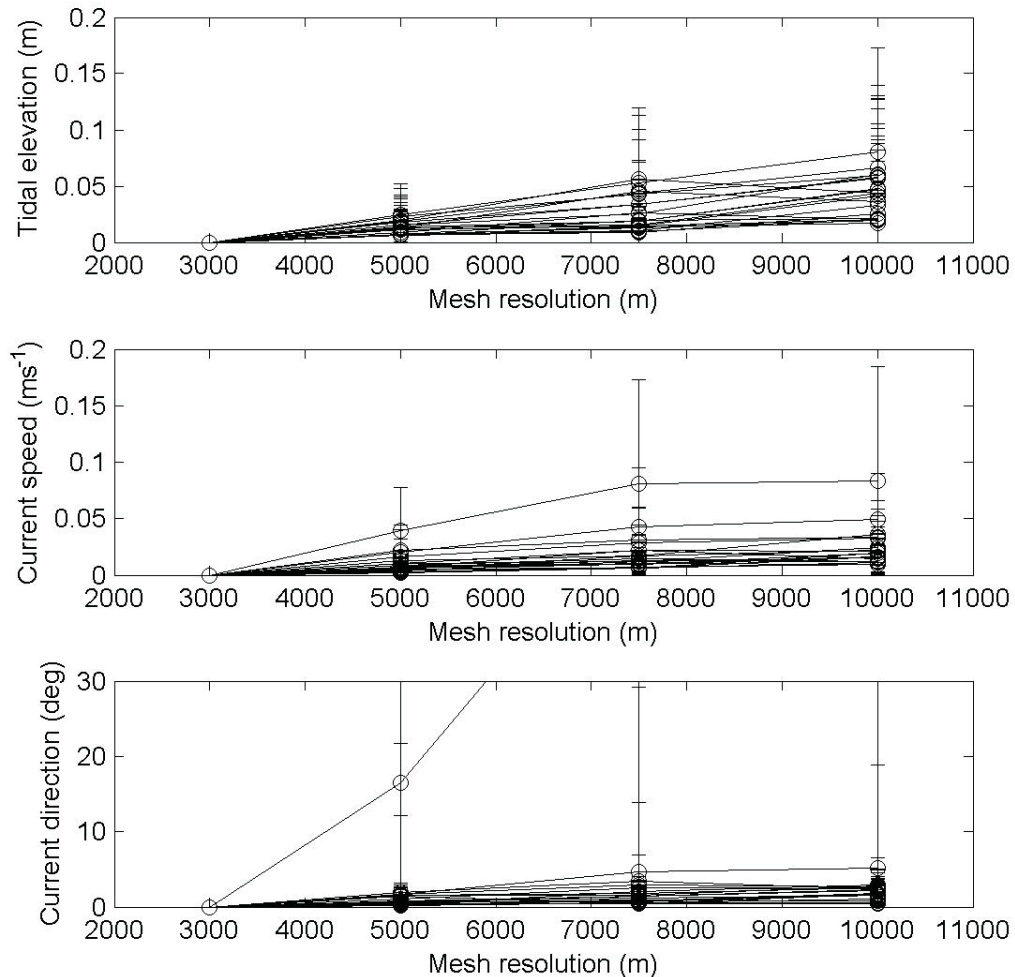


**Figure 27. The mean (absolute) difference in instantaneous tidal elevation, current speed and direction over a 14 day period at twenty locations in the English Channel and southern North Sea. Difference measured between the results of the finest mesh tested (3000m uniform resolution) and other coarser resolution meshes; error bars indicate  $\pm 1$  standard deviation.**

Another site specific mesh resolution sensitivity test was also made. Figure 28 and Figure 29 compare the current speed and direction predicted at the Hastings Shingle Bank over one spring-neap cycle, by models using meshes of varying resolution but otherwise with the same configuration [domain 4, Mannings bed resistance,  $M=40$ , otherwise default values] these are compared with the observed data. A more detailed comparison of one day of data is made in Figure 30.

Comparing only the predicted values, the Figures show that the current speed predicted using meshes with a resolution of 3000m, 5000m or 7500m are very similar. Peak current speeds at spring tides were within  $0.02-0.08\text{ms}^{-1}$  (2.3-9.1% of peak values); a greater degree of similarity was observed between the 3000m and 5000m meshes during flood tides but

between the 3000m and 7500m on ebb tides. Current speeds from the 3000m and 5000m meshes were always closely in phase whereas the 7500m and 10,000m meshes had a negative phase lag (-10 minutes and -40 minutes, respectively). Current direction was similar (within  $5^\circ$ ) between all of the meshes at all times of significant current speed. During periods of lower current speed and during flow reversal, the 3000m and 5000m meshes continued to compare closely. The 7500m mesh followed a similar phase to the finer meshes but was deviated by up to  $10^\circ$ ; the 10,000m mesh direction results consistently predict earlier flow reversal (by 40 minutes), resulting in a strong deviation in predicted current direction at these times.

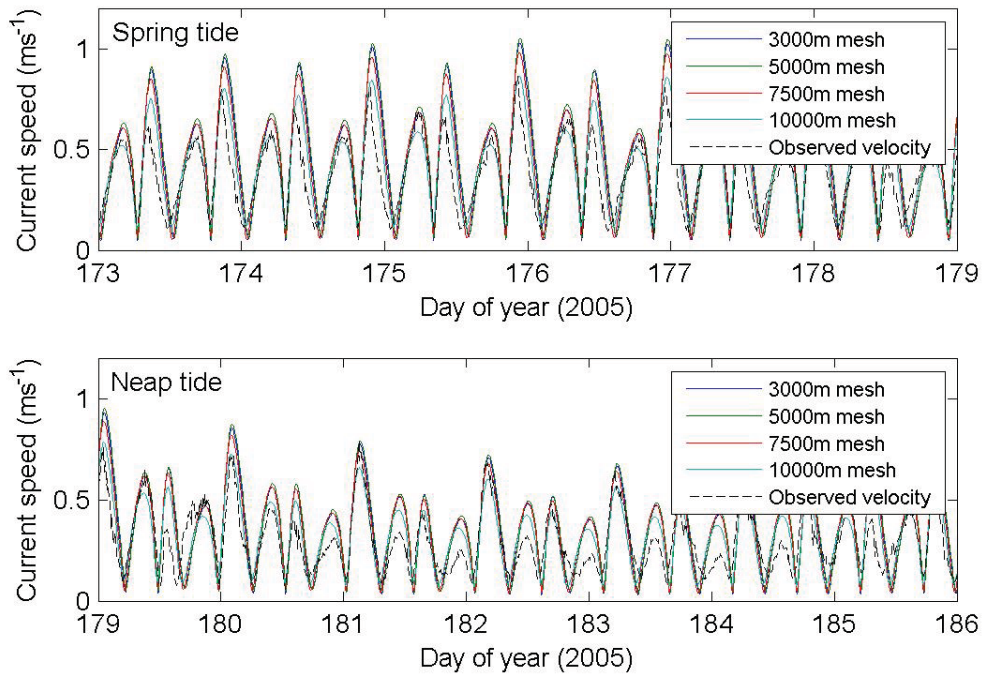


**Figure 28.** Comparison of one spring-neap cycle of observed current speed data at the Hasting Shingle Bank with that predicted by a variety of mesh resolutions.

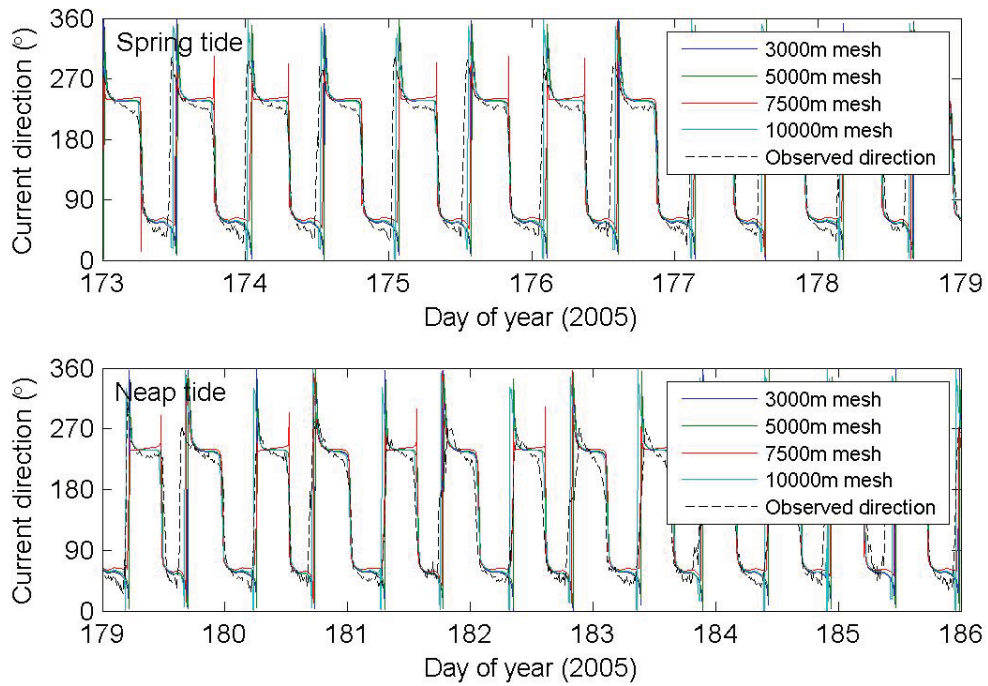


**Figure 29. Comparison of one spring-neap cycle of observed current direction data at the Hasting Shingle Bank with that predicted by a variety of mesh resolutions.**

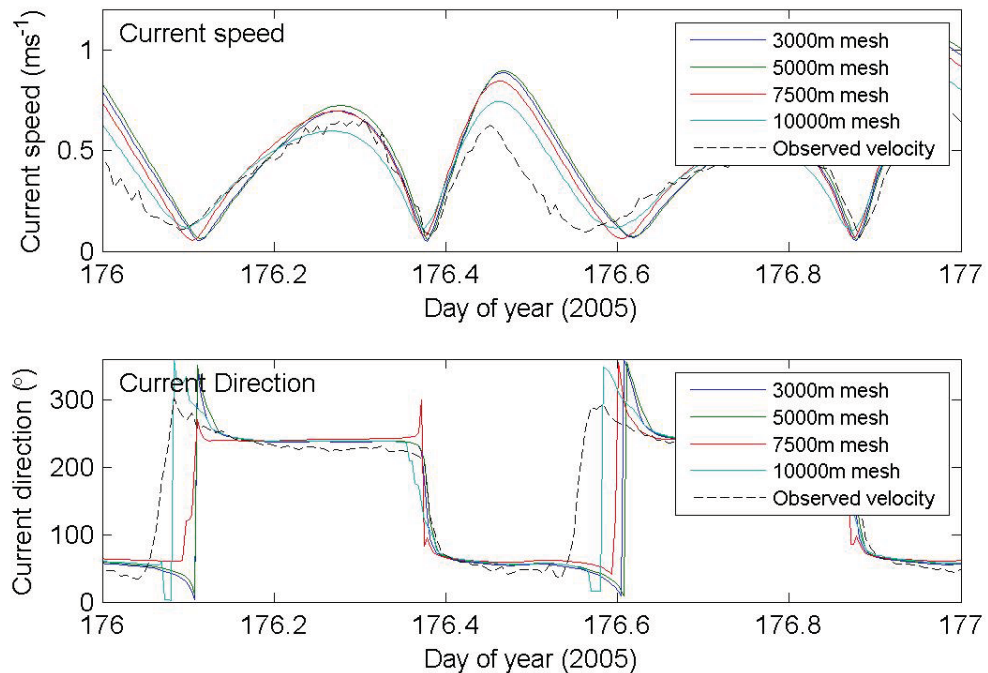


**Figure 30. Comparison of one day (during spring tides) of observed current speed and direction data at the Hasting Shingle Bank with that predicted by a variety of mesh resolutions.**

The difference between predicted and observed data is quantified in Figure 31, using the analysis technique described in Section 3.3.2.2. Given that the absolute difference is governed by other calibration parameters, i.e. bed roughness and eddy viscosity, the relative difference between predicted and observed current speed and direction over a range of peak current

speed conditions is similar for all meshes, i.e. the 10,000m mesh seems to provide the best predictions of velocity, however, the other meshes can be made to have a similarly good comparison by choosing a slightly different value of other calibration parameters, e.g. bed roughness.

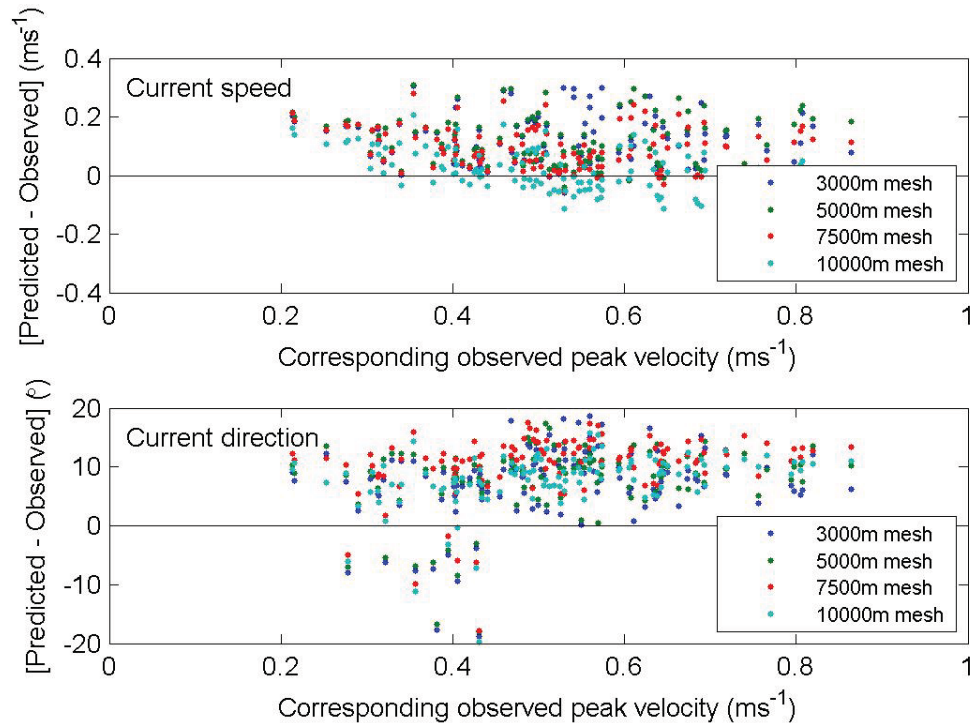


**Figure 31. Towards calibration of the mesh resolution. Difference between predicted and observed peak current speed and direction over two spring-neap cycles, plotted against the corresponding peak observed current speed. Comparison of data observed at the Hasting Shingle Bank with that predicted by a variety of mesh resolutions.**

There is apparently no way of calculating the optimum mesh resolution in advance. However, the mesh should be fine enough to resolve any important rotational or deflected flow fields, e.g. associated with flow around headlands, with at least 5-10 elements across the diameter of the feature. If such features at and below a certain scale are not important in the study, then they may be excluded from this rule-of-thumb approach. Eddies in the residual flow field associated with the Cotentin Peninsular were found to be in the order of 45-90km in diameter; a minimum resolution of 7500m was considered necessary to resolve these adequately.

The impact of mesh resolution on model run time is the subject of Appendix B which provides guidance on the choice of mesh design parameters including element size and land boundary vertex spacing.

A higher mesh resolution increases the total number of nodal points in area type output; this number, along with the number of data categories requested and the number of time steps, is proportional to the resulting file size. Beyond a certain file size (depending upon the computing power available), the file may become unmanageable and possibly even impossible to open in analysis packages other than MIKE (e.g. Matlab). A uniform mesh of 3000m resolution was found to produce output files that were almost unmanageably large, so was excluded from further use.

In conclusion, the tests show that any of the meshes tested could be used to produce equally acceptable results in offshore areas. The 3000m mesh was excluded due to the size of output files produced and the 10,000m mesh was excluded as it may not properly resolve

large flow features in some parts of the domain. The majority of sensitivity testing was then undertaken with a 7500m mesh to reduce run time, processing time and file sizes. The final whole English Channel model used a 5000m mesh to maximise resolution and detail. The final nested model meshes used a resolution of 7500m for the majority of the domain, with increasing resolution into the region of interest.

#### **3.3.3.4. Mesh resolution – Nested subregions**

Predicted tidal elevation, current speed and direction were extracted at 5 minute intervals over a 5 day period at ten evenly distributed points within the inner part of the Hastings Shingle Bank and Area 473E nested subregions. The models used the same configuration [domain 4, Mannings bed resistance,  $M=40$ , otherwise default values] except for the choice of mesh; the particular choice of Mannings number is discussed later in this Section. The finest mesh was constructed as a series of concentric zones surrounding the region of interest [200m over the region of interest, increasing through 500m, 1000m and 2500m to 7500m for the remainder of the domain]. To test the sensitivity to variable mesh resolution, the inner zones of higher resolution were progressively removed; the perimeter location of the remaining zones was unchanged. The mesh resolution quoted here refers to the resolution of the inner (finest resolution) zone.

Figure 32 and Figure 33 show detailed comparisons of one day of data from sites in the Hastings Shingle Bank and Area 473E nested subareas; these comparison images are typical and representative of all of the points tested. Tidal elevation, current speed and direction demonstrate similarity at all times in magnitude, form and phase. Small differences are observed between the results from the different meshes but do not visibly converge on a single solution with increasing local mesh resolution.

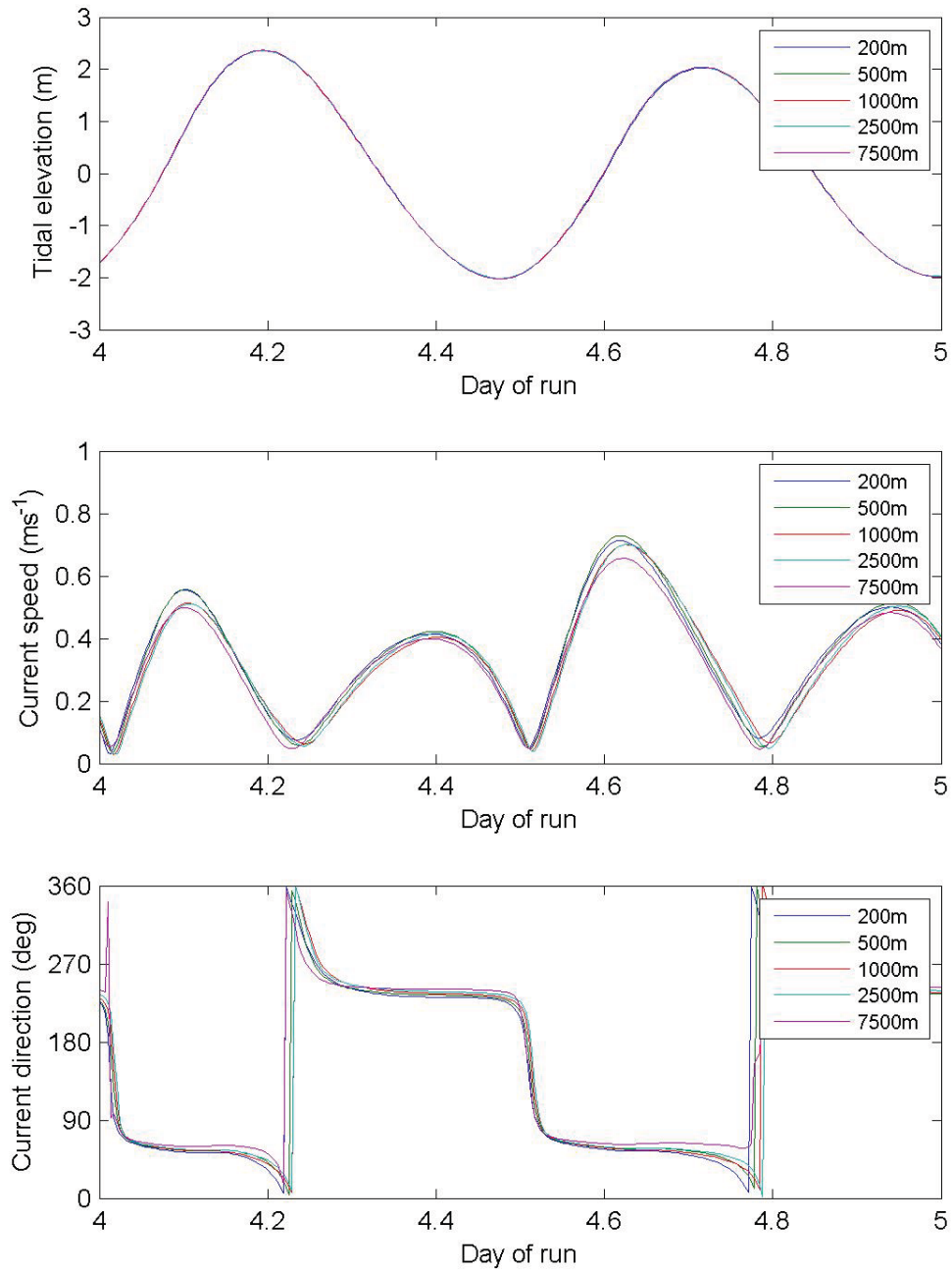


**Figure 32. Detailed comparison of tidal elevation, current speed and direction data from models using different maximum local mesh resolutions. One day of data from a representative site in the Hastings Shingle Bank subarea.**

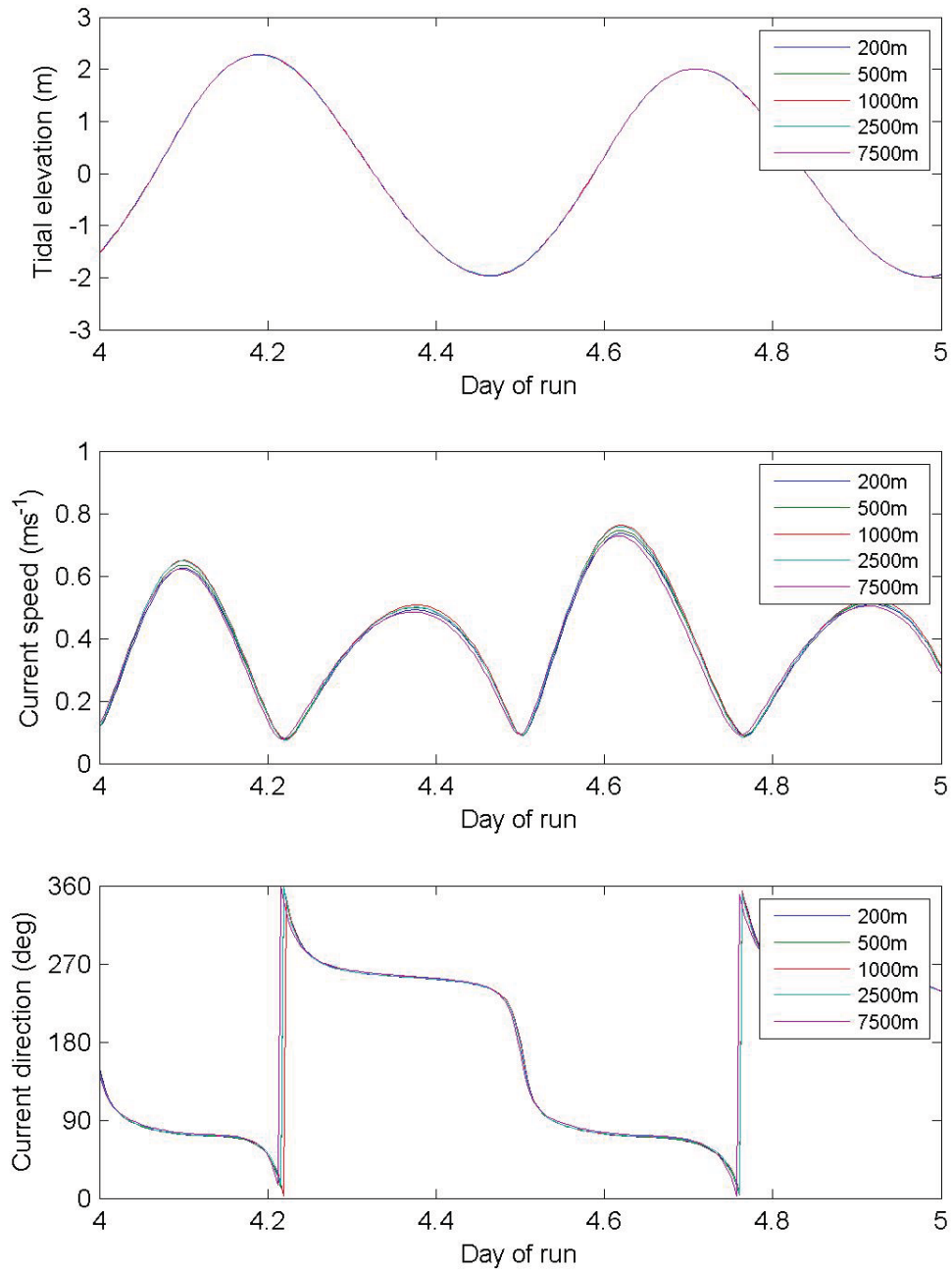


**Figure 33. Detailed comparison of tidal elevation, current speed and direction data from models using different maximum local mesh resolutions. One day of data from a representative site in the area 473E nested subarea.**

Differences between the results from different meshes over the 5 day modelling period are quantified in Figure 34 and Figure 35. With the exception of current direction at the Hastings Shingle Bank site, predictions of tidal elevation, current speed and direction did not consistently improve with increasing local mesh resolution. In all cases, the actual difference between any of the mesh resolutions was small (typically  $<0.02\text{m}$ ,  $<0.03\text{-}0.05\text{ms}^{-1}$  and  $<2\text{-}10^\circ$ ) relative to the recommended values (i.e.  $\pm 0.1\text{m}$ ,  $\pm 0.2\text{ms}^{-1}$  and  $\pm 20^\circ$  from Bartlett, 1998).

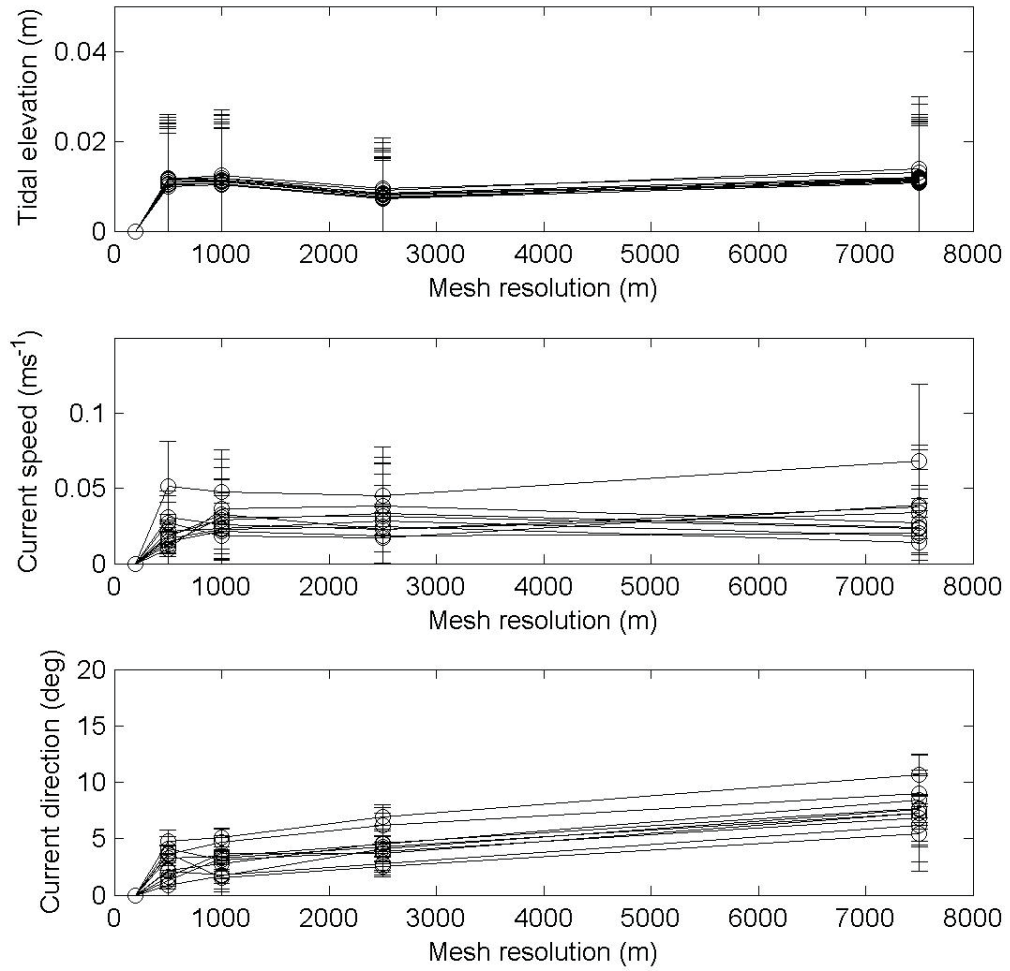


**Figure 34.** The mean (absolute) difference in instantaneous tidal elevation, current speed and direction over a five day period at ten locations in the Hastings Shingle Bank nested subregion. Difference measured between the finest mesh tested (200m local resolution) and coarser resolution meshes; error bars indicate  $\pm 1$  standard deviation.

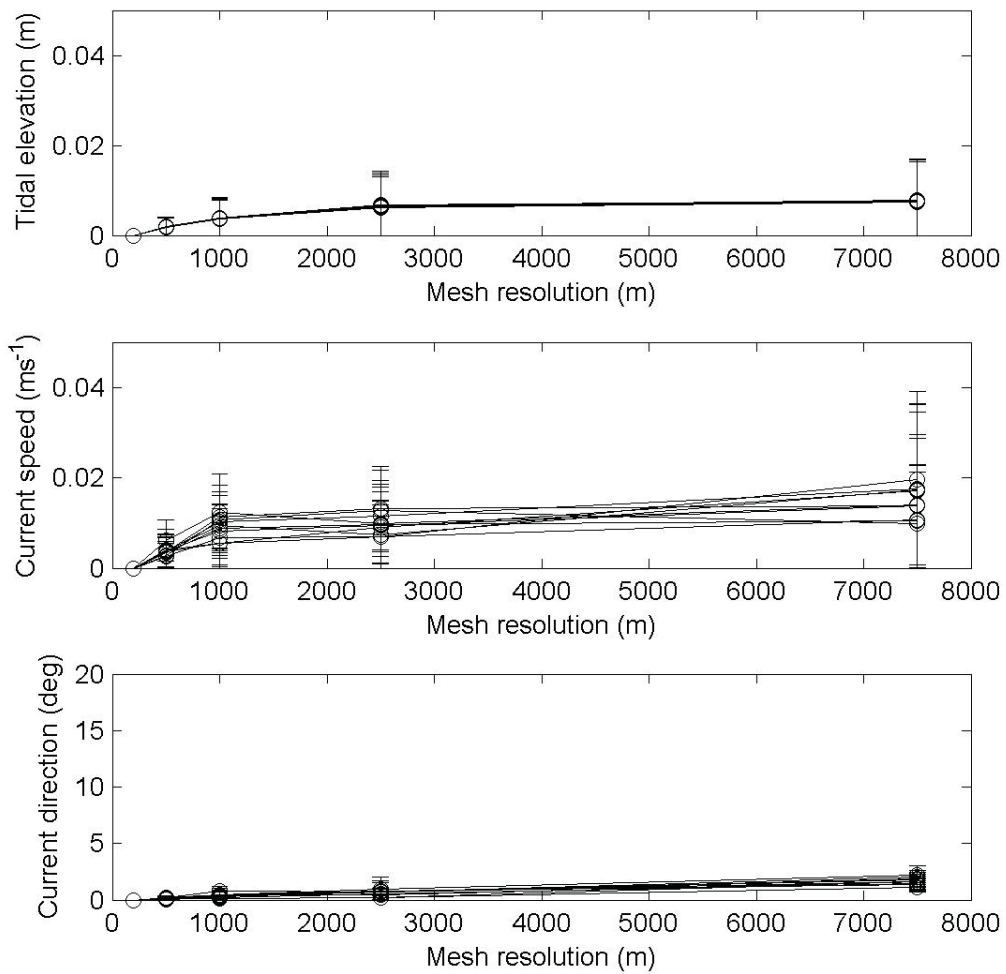


**Figure 35. The mean (absolute) difference in instantaneous tidal elevation, current speed and direction over a five day period at ten locations in the Area 473E nested subregion. Difference measured between the finest mesh tested (200m local resolution) and coarser resolution meshes; error bars indicate  $\pm 1$  standard deviation.**

These results suggest that, possibly because the nested sub areas are relatively small and located far from the coast, flow is uniform across them and the resolution at which that is modelled is less important.

### 3.3.3.5. *Solution technique*

Comparison runs were made to gauge the effect, if any, of choosing a low or high order solution scheme. All other parameters were kept the same. Fourteen day long time series' of tidal elevation, current speed and direction were sampled from the results files at the twenty sampling points shown in Figure 25. The maximum mean difference and typical standard deviation between the results of low order and high order schemes was  $0.052\text{m} \pm 0.05\text{m}$ ,  $0.053\text{ms}^{-1} \pm 0.015\text{ms}^{-1}$  and  $5.6^\circ \pm 1^\circ$ , respectively. Again, these differences are small relative to the previously published acceptable error bounds (i.e.  $\pm 0.1\text{m}$ ,  $\pm 0.2\text{ms}^{-1}$  and  $\pm 20^\circ$  from Bartlett, 1998), also to the differences in these parameters caused by varying the other key calibration parameters, e.g. bed roughness, and also compared to the natural variability observed over the domain and over semi-diurnal and spring-neap cycles.

A specific test was made to compare the predicted flow from the two model types with observed data from three locations on the Hastings Shingle Bank. The two models predict very similar current speed and direction at all times during both spring and neap tidal cycles. The observed data are not explained any better or worse by the choice of either model.

The high order model required a run time 2.3 times that of the low order model but did not significantly change the fit of the results to observed data. Therefore, a low order scheme was used in the final model runs.

#### **3.3.3.6. *Bed roughness***

The choice of bed roughness formulation (Mannings vs Chezy), the coefficient value used (of M or C) and choice of spatial distribution (uniform vs spatially varying) were tested. Bed roughness has a significant effect on tidal propagation (local tidal range, curve shape and phase) and the resulting current speed and direction with obvious, but not extensively tested, implications for prediction of sediment transport.

Figure 36 shows current speed and direction results data from models using Mannings and Chezy bed roughness formulations; this is a representative image, similar to that for other time periods and at other locations. The different colour solid curves represent different coefficient values of M or C. For both formulations, the chosen coefficient value controls primarily the magnitude and partially the shape of the current speed curve, but not the phase. The shape and phase of current speed curves of comparable magnitude, predicted using either the Mannings or Chezy formulation, are not significantly different and do not describe the observed data any better or worse than the other. In all cases, the current direction is not significantly affected by the choice of formulation.

The Mannings formulation is the recommended default setting and does not produce significantly different results from the Chezy formulation; therefore the Mannings parameterisation was used in the final model.

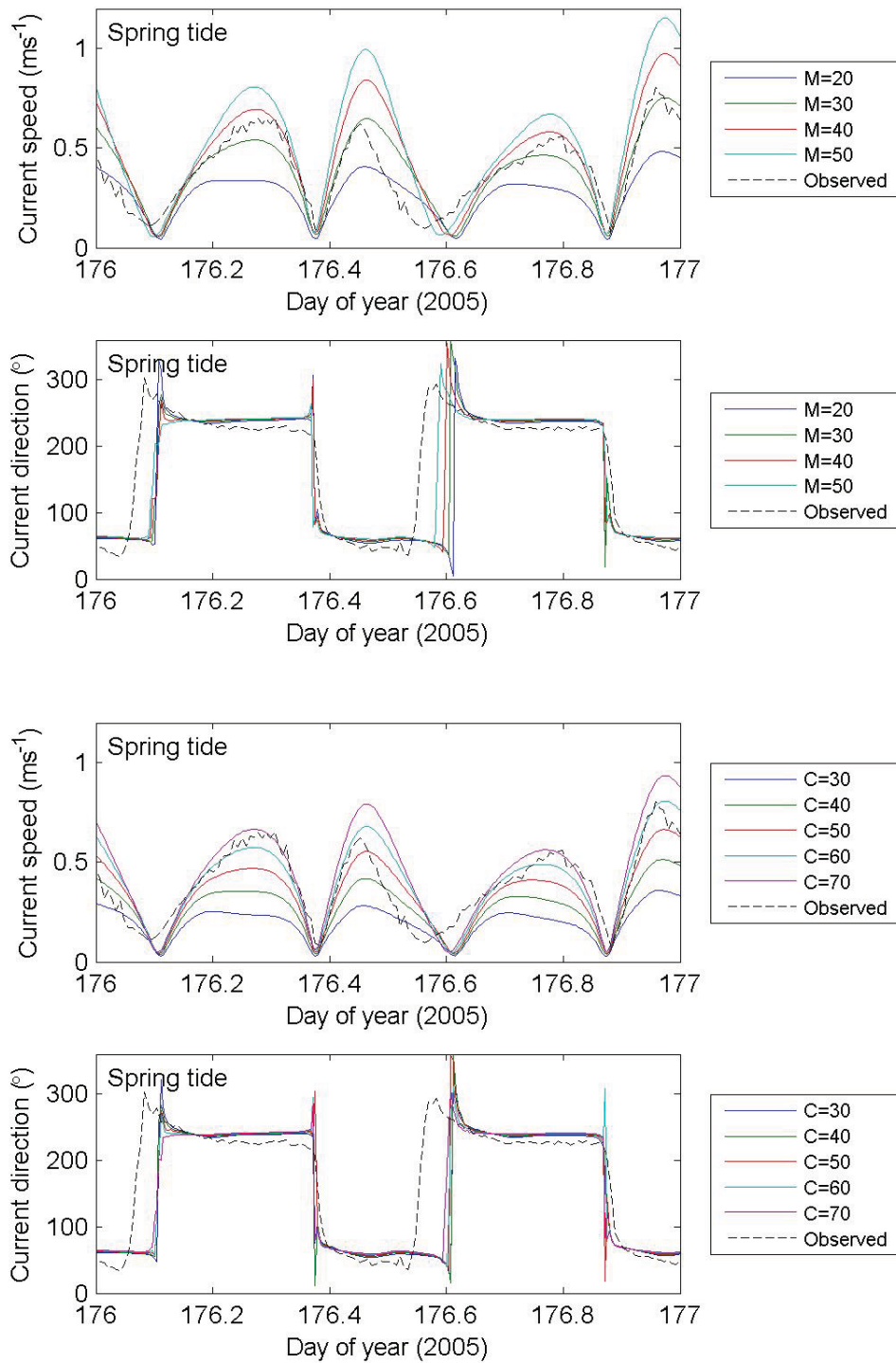


**Figure 36. Detailed comparison of current speed and direction data from models using either the Mannings (M) or Chezy (C) formulation for bed roughness. Values created using different uniform values of M or C are compared with one day of observed data from a representative site in the Hastings Shingle Bank subarea.**

In order to calibrate the final choice of Mannings coefficient, 6 sets of model results were created using a variety of values of  $M = [20, 30, 40, 50]$  to compare with the 6 identified groups (30 individual time series) of observed data. The predicted and observed data were compared quantitatively using the method outlined in Section 3.3.2.2. The difference in predicted minus observed peak current speed and direction during each individual tidal half

cycle in each time series is plotted against the corresponding observed peak current speed in Figure 37 and Figure 38, respectively.

As also shown in Figure 36 above, the difference between predicted and observed values of current speed is very sensitive to the chosen uniform value of  $M$  but the difference in current direction is much less so; this general observation was also borne out by quantitative analysis of the larger data set. Where a medium value of  $M$  (e.g.  $M=40$ ) is used, current speed is generally over-predicted at low observed peak current speeds and under-predicted at high observed peak current speeds in comparison to the observed values. Varying the value of  $M$  from this middle ground tends to reduce error at either high or low peak current speeds but at the expense of increasing error at the other. Current direction observations were typically within  $\pm 10\text{-}15^\circ$ , irrespective of the value of  $M$  used.

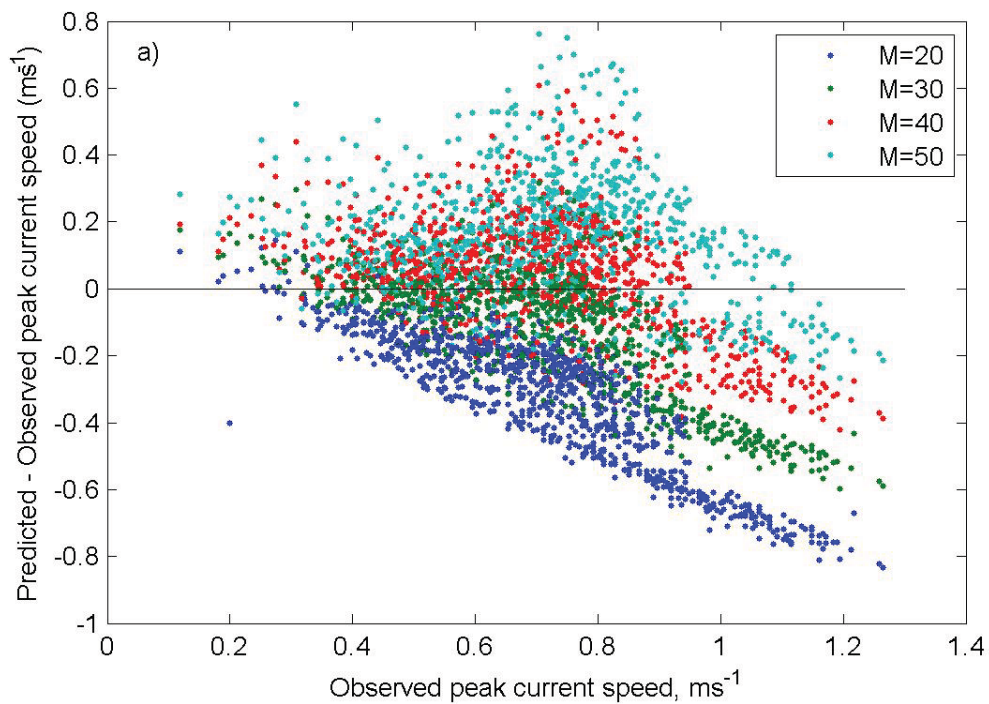


**Figure 37. Difference between the predicted and observed peak current speed plotted against the corresponding peak observed current speed, during each tidal half cycle. Data from thirty individual time series of between 7 and 40 days, representing different parts of the domain and periods of time.**

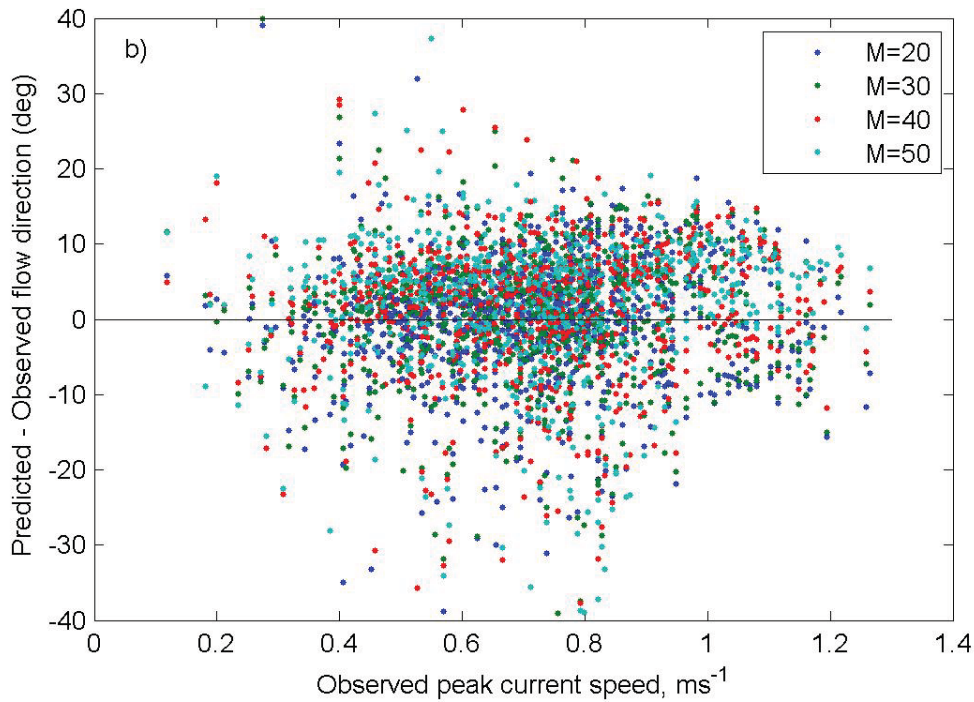


**Figure 38. Difference between the predicted and observed current direction at the point of and plotted against the corresponding peak observed current speed, during each tidal half cycle. Data from thirty individual time series of between 7 and 40 days, representing different parts of the domain and periods of time.**

The main purpose of the hydrodynamic model output is to provide a realistic as possible flow field to drive a sediment dynamics model. Sediment transport occurs only when a threshold current speed is achieved and typically then in proportion to the excess current speed cubed (e.g. Soulsby, 1997). It is therefore of particular importance that the difference between observed and predicted flow is minimised for current speeds in excess of the threshold value. Using the threshold relationship of Shields (1936) and the ‘Law of the Wall’ to convert shear stress to depth mean current speed, the threshold of motion for fine to medium quartz sands is achieved at current speeds of approximately  $0.5\text{ms}^{-1}$ . The difference data was then resampled to exclude difference values with corresponding observed peak velocities less than  $0.5\text{ms}^{-1}$ , i.e. not strong enough to induce sediment transport.

The mean difference value for the resampled data for each time series is plotted in Figure 39 against the corresponding value of  $M$ ; the standard distribution of difference is also shown. The figure shows that the mean difference between predicted and observed current speeds is minimised, depending upon the particular time series being considered, when using a value of  $M$  between 30 and 50. As the curves are evenly distributed in this range and as only a single value can reasonably be chosen for use, the central value of  $M=40$  would be an appropriate choice to optimise hydrodynamic results on the basis of peak current speed values. Considering all of the time series curves, mean difference at  $M=40$  is approximately  $\pm 0.2\text{ms}^{-1}$ ; applying a typical standard error of between  $\pm 0.1\text{--}0.2\text{ms}^{-1}$ , the typical difference between predicted and observed peak velocity for most sites would be in the range  $\pm 0.2\text{ms}^{-1}$  with some sites experiencing greater differences (up to  $\pm 0.4\text{ms}^{-1}$ ).

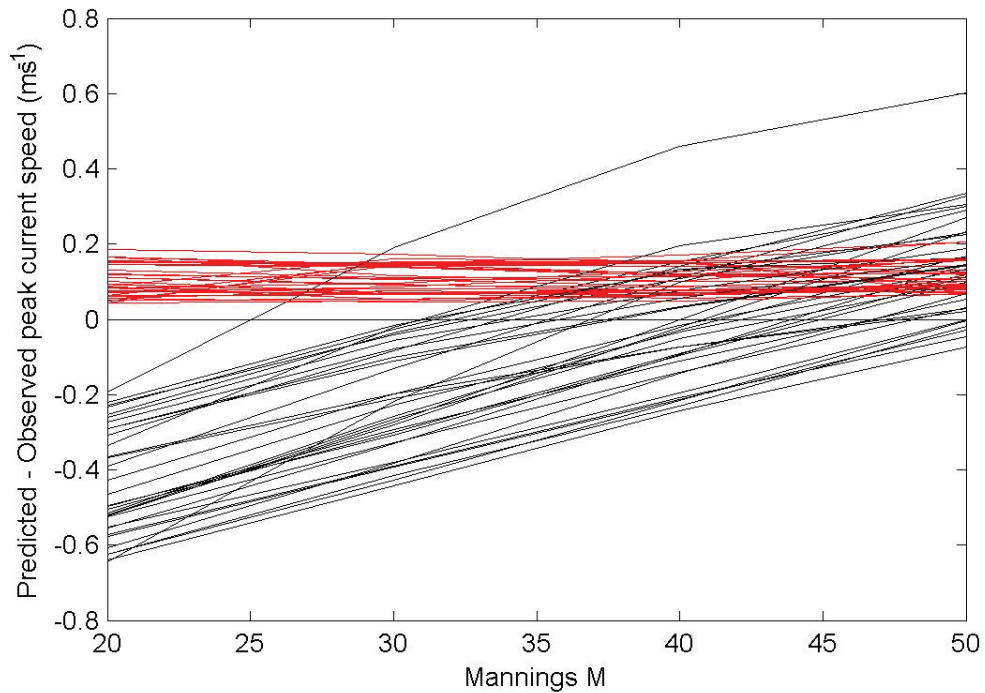


**Figure 39.** The difference between predicted and observed peak current speed for 30 time series of data from the southern North Sea, Dover Straits and south coast of UK. Key: black lines – mean value; red lines – standard deviation.

The data shown in Figure 39 were further analysed to quantifiably identify the intercept value of  $M$  for the optimal case of zero mean difference (results shown in Table 1). Before each analysis, the results were either unfiltered or filtered to exclude peak observed current speeds  $<0.5\text{ms}^{-1}$  or  $<0.75\text{ms}^{-1}$ ; results were also divided into flood and ebb cycles.

As visually discernable in Figure 39, the mean value is around  $M=40$ ; a slightly larger value ( $M+1$ ) may be more appropriate for higher overall velocities and for flood cycles but this is a relatively small difference compared to the range. When choosing a single value, it was decided that greater weight would be given to the curves and values relating to the filtered data and to data from the Hastings Shingle Bank (group 17) and Owers Bank (group 18) collected during previous ALSF project 3365. These data were collected using upwards looking flow profiling devices, more suited to making depth mean current speed measurements than the single point current meters used to collect the rest of the available data. On this basis, a value of  $M=39$  was chosen for use in the final model runs.

All current speed data			Current speed data > 0.5m/s			
Group	Flood	Ebb	Group	Flood	Ebb	
	1	38	46	1	43	51
	2	43	44	2	44	44
	4	38		4	38	
	11	37	30	11	37	30
	<b>17</b>	<b>34</b>	<b>37</b>	<b>17</b>	<b>38</b>	<b>39</b>
	<b>18</b>	<b>36</b>	<b>34</b>	<b>18</b>	<b>36</b>	<b>34</b>
Mean		38	38	Mean	39	40

Current speed data > 0.75m/s			
Group	Flood	Ebb	
	1	39	51
	2	45	45
	4	38	
	11	37	33
	<b>17</b>	<b>41</b>	<b>38</b>
	<b>18</b>	<b>36</b>	<b>35</b>
Mean		39	41

**Table 1. Intercept values of M corresponding to zero mean difference in Figure 39 between observed and predicted peak current speed. Data separated by flood or ebb tide and by calibration group.**

The effect of choosing different values of M was also explored in terms of the distribution of co-amplitude and co-phase lines throughout the domain. In Figure 40 and Figure 41, the predicted lines are compared to those previously published by Howarth (1990) for the M2 and S2 component of the tide throughout the domain. In both cases, the co-phase distribution is not strongly affected by the choice of M but the co-amplitude distribution is. The patterns of distribution (focal points and the location of amphidromes) are not strongly affected by the choice of M; the magnitude of the co-amplitude signal locally is however more affected.

These analyses agree approximately with the point data analysis that a value of M=40 provides the best fit to the published distribution of the most important, M2, constituent; the amplitude of the S2 constituent is possibly better explained by a lower value of M (=30) but also reasonably well by M=40.

It may be beneficial to future studies to pursue this calibration tool to try and improve the accurate spatial replication of the higher tidal harmonics which are largely responsible for determining local flow asymmetry, important for residual tidal and sediment transport. The fit of each tidal constituent distribution will undoubtedly prove sensitive to the location of the open boundaries and the choice of boundary condition.

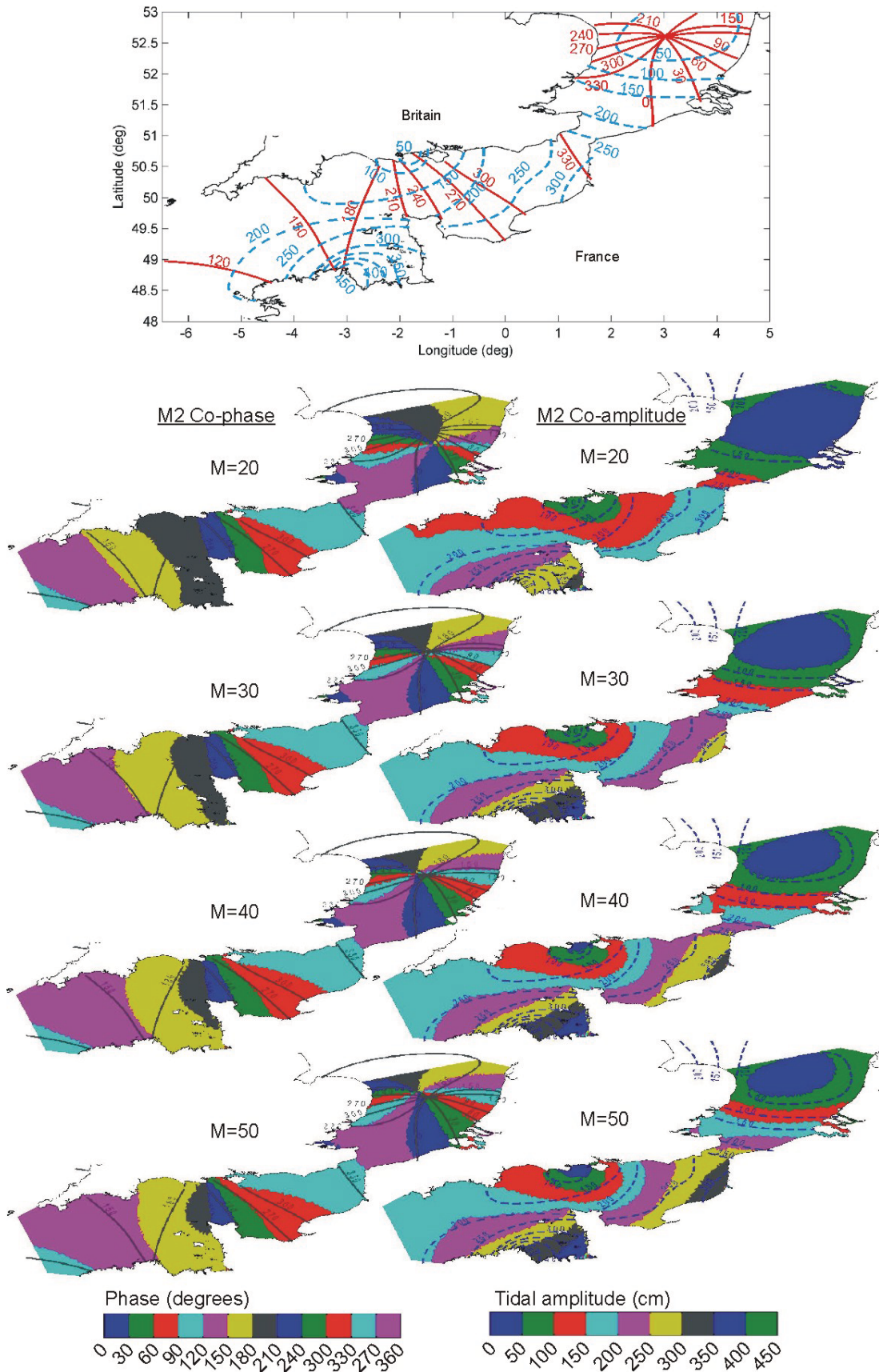


Figure 40. Co-amplitude and co-phase lines of the M2 constituent tidal elevation predicted by the model. M=40 provides the best fit to the previously published data (from Howarth, 1990).

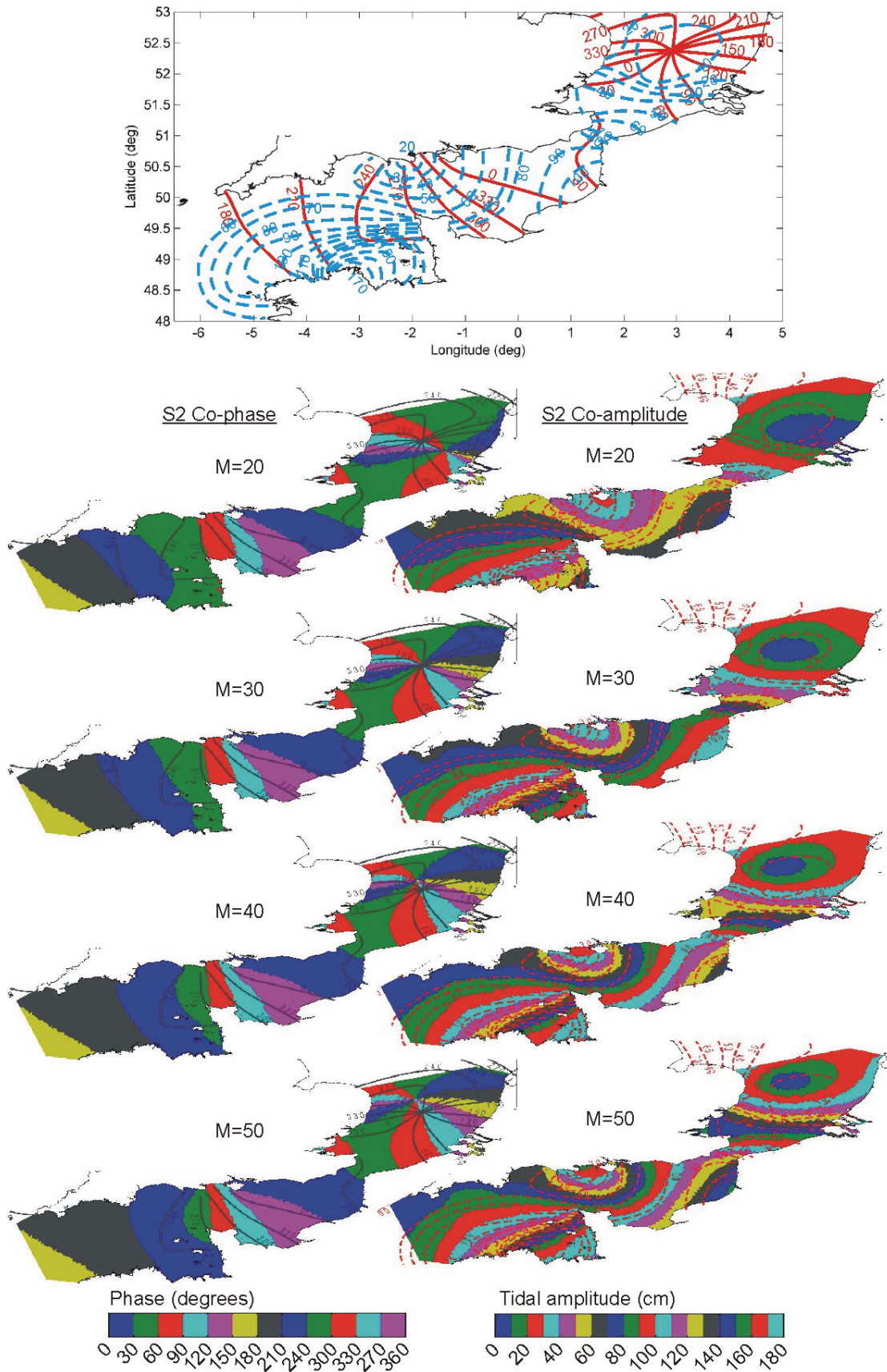
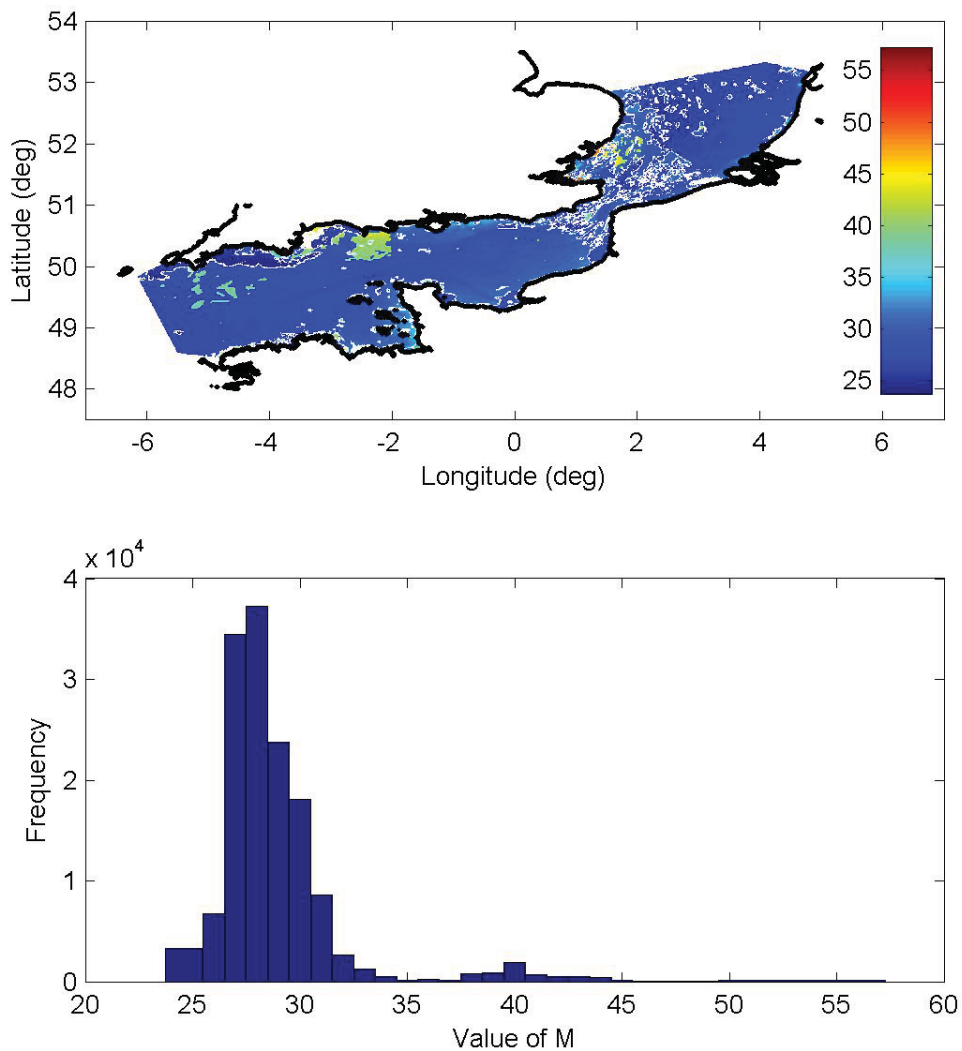


Figure 41. Co-amplitude and co-phase lines of the S2 constituent tidal elevation predicted by the model. M=30-40 provides the best fit to the previously published data (from Howarth, 1990).

In the model, the local value of  $M$  is used in conjunction with local water depth to calculate the local value of the drag coefficient  $C_d$ . The limited number of field observations of  $C_d$  associated with different seabed types were obtained from the literature and were used in conjunction with broad descriptions of seabed type distribution and the known bathymetry of the English Channel to create an idealised map of spatially variable  $M$  (see Appendix C for more details). The spatial distribution of  $M$  and a histogram of the values of  $M$  are shown in Figure 42.



**Figure 42. The calculated spatially varying distribution of  $M$ . Based on the previously published distribution of sandy, gravelly and muddy sediments (see text for more details), proposed values of the drag coefficient derived from field observations in Soulsby (1997) and the bathymetry data. Top – spatial distribution of values; bottom – histogram of values.**

The majority of points are in the range  $25 < M < 32$  and as such, the results of a model using this spatially variable bed roughness reflects most closely the results of a model using a spatially uniform value of approximately  $M=27-28$ . Local differences may be observed at locations where there are large gradients or differences in  $M$ , however, the overall effect does not improve the fit of the model results with any of the observed data. In summary, the value of the drag coefficient derived from field observations does not produce the closest fit between the model results and the observed data and the values of  $M$  previously identified by error minimisation techniques are more suitable for use in the present study.

A spatially uniform value of  $M$  ( $=39$ ) was therefore used in the final model.

### 3.3.3.7. Eddy viscosity

Different spatially constant coefficient values were tested  $c=[0.28, 0.5, 0.75, 1.0]$ , within the range suggested by DHI (0.25-1.0). This variation had a significant effect on tidal propagation (local tidal range, curve shape and phase) and the resulting current speed and direction (Figure 43) with obvious, but not extensively tested, implications for prediction of sediment transport. There was no significant effect on the phase of tidal propagation.

The coefficient  $c$  provided to the model is used to calculate the actual eddy viscosity  $N_x$ . A maximum and minimum allowable value for  $N_x$  are specified during model setup. It is evident from the results that increasing the coefficient value to  $c=0.5$  resulted in an eddy viscosity value being used that was equal to, or in excess of, the maximum value allowed, hence only the maximum value was applied. Subsequent larger coefficient values only further exceed the maximum value, so the value of  $N_x$  applied and therefore the results of all three runs using coefficients values between 0.5 and 1.0 were the same.

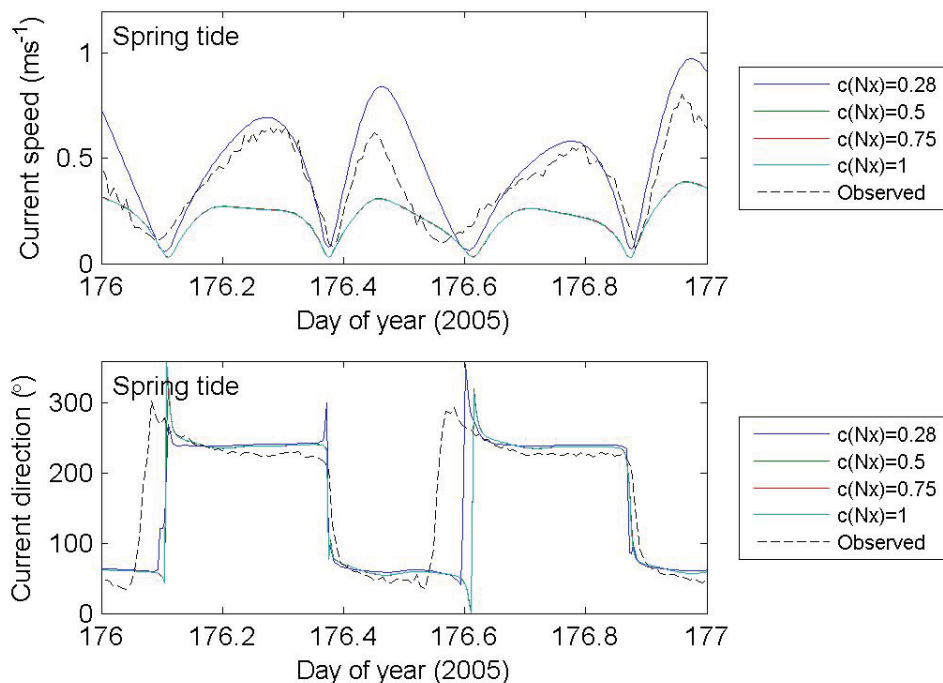


**Figure 43. Comparison of one day (during spring tides) of observed current speed and direction data at the Hasting Shingle Bank with that predicted using a variety of eddy viscosity coefficient values.**

The effect of increasing the eddy viscosity at the particular site chosen for analysis (the Hastings Shingle Bank), was to reduce the tidal range (by 40%), to reduce the peak current speed (by 60%) and to slightly deflect the flow direction (by up to  $5^\circ$ ). N.B. These degrees of change do not reflect the effect of the chosen value of  $c$ , only the maximum allowable value of  $N_x$ .

Runs using values of  $c$  larger than the default did not describe the observed data any better than the default value. The default value and setup for eddy viscosity was therefore used in the final model.

### 3.3.3.8. Decoupled timestep

When recording hydrodynamic data for later use by the sediment transport module, it is most efficient to only record (and provide) data at the largest timestep necessary to adequately resolve residual patterns. The hydrodynamic data were output at the highest possible resolution (every 5 minutes) for a period of five days modelling time (following a two day warm up period). These results were used to calculate total load transport; time series data were extracted at ten locations evenly spaced across each domain (the English Channel for the medium resolution model and over the Hastings Bank or Area 473E for the refined models). The timestep parameter in the sand transport module was varied which had the effect of manually controlling the timestep of the hydrodynamic input data and therefore the timestep of the sediment transport model. The effect on the resulting residual transport vectors was calculated for scenarios of hydrodynamic input timesteps of [5, 10, 20, 30, 45 and 60] minutes. The results for the medium resolution English Channel model are shown in Figure 44. The combined results for the Hastings Bank and Area 473E are shown in Figure 45.

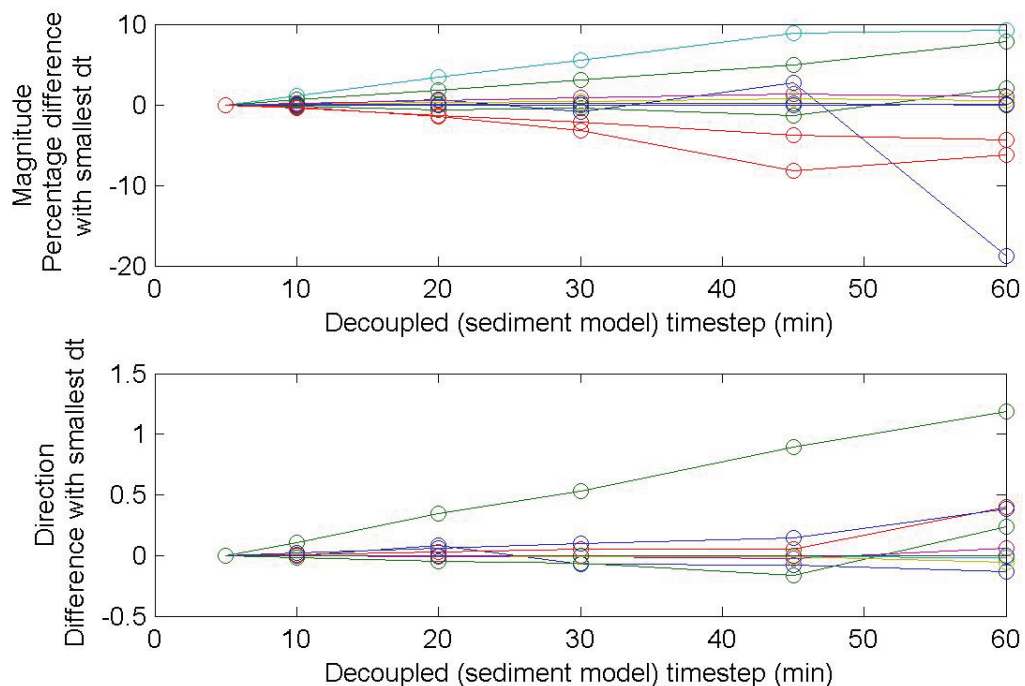


**Figure 44. Percentage difference in the magnitude and absolute difference in the direction of the calculated residual total load transport vector at ten evenly spaced locations in the English Channel domain. Effect of using different hydrodynamic input or sediment transport model timesteps. Difference calculated relative to that calculated using the smallest time step.**

Compared to results when using the smallest timestep, a 45 or 60 minute hydrodynamic input (sediment transport model) timestep for the English Channel model produces up to  $\pm 10\%$  error in the predicted magnitude of residual sediment transport; this is reduced to  $\pm 5\%$  and  $\pm 3\%$  for 30 and 20 minute timesteps, respectively. Within the range of timesteps tested, the direction of the residual transport varied by up to a typical value of  $0.5^\circ$  (maximum value  $1.15^\circ$ ); as such, direction is not a factor in the choice of timestep as it has no significant bearing on the accuracy. As file sizes and run time vary linearly with the timestep, a timestep of 30 minutes was chosen for use in the final medium resolution English Channel model.

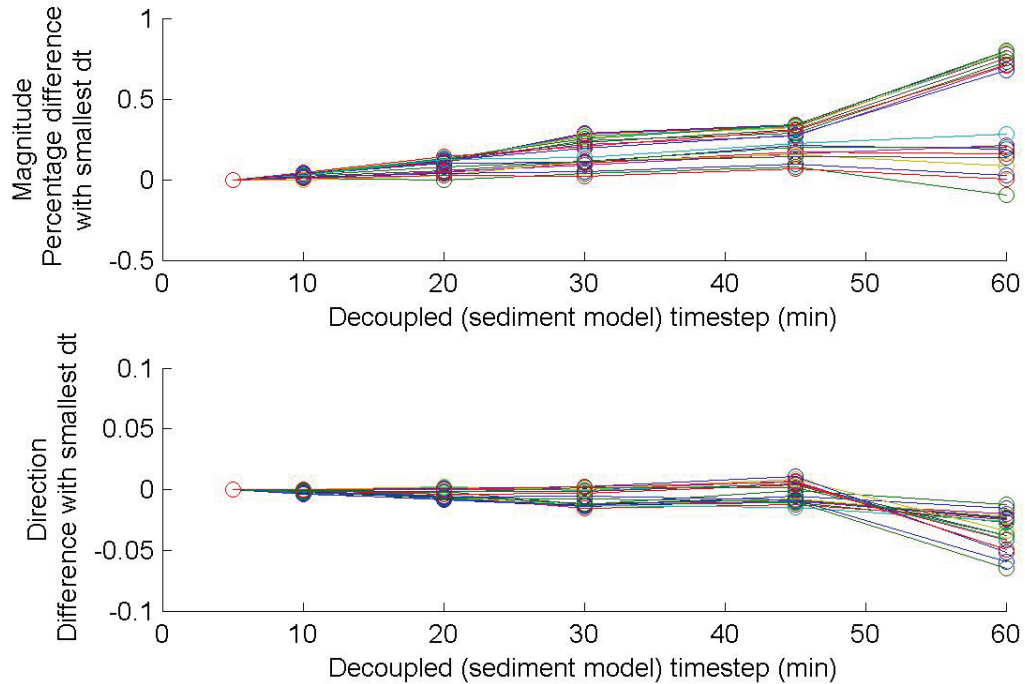


**Figure 45. Percentage difference in the magnitude and absolute difference in the direction of the calculated residual total load transport vector at ten evenly spaced locations in the Hastings Bank and Area 473E domains. Effect of using different hydrodynamic input or sediment transport model timesteps. Difference calculated relative to that calculated using the smallest time step.**

The percentage difference in magnitude and the absolute difference in direction of residual sediment transport vectors at the Hastings Bank and Area 473E is not significantly affected ( $<1\%$  and  $<0.1^\circ$ ) by the choice of timestep in the range tested. Therefore, the most efficient timestep (60 minutes) was chosen. However, only the results from the inner part of the nested area are considered in this analysis; the sensitivity of the rest of the domain was not tested.

### 3.4 Summary and final choice of model setup

As a numerical model will always be a simplification of reality and observed data will always be affected by instrument error and accuracy, local and regional weather conditions, meso- and micro-scale bathymetry, etc, it is not likely that the observed and predicted data will agree exactly in every case for a given parameter set. However, it is possible to tune a model so that it provides the best possible predictions, reproducing most accurately the important features of any observed data (magnitude, phase, curve shape) over as large an area of the domain as possible. This is the purpose of the calibration process described above.

The sensitivity of the model to different configurations of domain size, mesh resolution, bed roughness and eddy viscosity were tested. The model was calibrated by identifying the combination of these parameters that produced model results closest to observed current speed and direction data. Greater weighting in this process was given to data with current speeds in excess of  $0.5\text{ms}^{-1}$  (the approximate threshold of motion for fine to medium quartz sands) in order to ensure the most realistic conditions of sediment transport.

The literature were used where possible to predict the most realistic value of important parameters such as bed roughness, as determined by direct measurement in the field;

however, such values were found to be significantly different to the values determined from an error minimisation approach between observed and modelled data at many locations. The combination of parameters chosen for use in the final hydrodynamic model are listed below in Table 2.

Parameter	Value
Domain size	'Domain 4'
Bathymetry source	CMAP data corrected to mean sea level (& multi beam swath for refined areas)
Mesh resolution (EC)	5000m
Mesh resolution (HSB & Area 473E)	7500m, refined to 200m
Solution technique	Low order (spatial and temporal)
Flood and Dry	On
Eddy viscosity formulation	Smagorinski (default)
Eddy viscosity coefficient	0.28 (default)
Bed roughness formulation	Mannings (default)
Bed roughness distribution	Constant (default)
Bed roughness coefficient	M=39
Coriolis forcing	Varying in domain (default)
Wind forcing	Not included (default)
Ice coverage	No ice coverage (default)
Tidal potential	Not included (default)
Precipitation and Evaporation	No, No. (default)
Wave radiation	No wave radiation (default)
Sources	None (default)
Initial conditions	None (default)
Boundary conditions	KMS from MIKE zero.
Decoupling	Yes (see Table 3)
Outputs	Whole area, (see Table 3), [surface elevation, u-velocity, v-velocity.

**Table 2. Parameter choices for the final hydrodynamic model runs.**

The modelling period and timestep of each model is listed in Table 3. The three hydrodynamic models were run first of all. Area results files were recorded. The raw results of the hydrodynamic model were also recorded to decoupled output files. These were then used to efficiently provide the hydrodynamic input to the sediment transport models. The decoupled results timestep was 30 minutes for the medium resolution model but only 60 minutes for the two refined mesh models. These values were determined by sensitivity testing of the model results to the choice of decoupled timestep.

Model (mesh) name	HD model results timestep	Decoupled output timestep ST model timestep & ST model results timestep
Medium resolution	60 minutes	30 minutes
Refined HSB	60 minutes	60 minutes
Refined 473E	60 minutes	60 minutes

**Table 3. Modelling period and timestep of the final model runs.**

The combination of parameters chosen for use in the final sediment transport model setup are listed below in Table 4.

<b>Parameter</b>	<b>Value</b>
Model definition	Pure current; Equilibrium
Sediment transport formulation	Engelund and Hansen
Time parameters	Start (0); Timestep factor (1); see Table 3.
Sediment properties	Porosity (0.4); format: (variable); grainsize (variable); relative density (2.65)
Bed resistance	Constant Mannings (32) (default)
Morphology	No morphological feedback; otherwise default
Output	Bed level change; total load, x-component; total load, y-component. See Table 3.

**Table 4. Parameter choices for the final sediment transport model runs.**

## 4. Results of the numerical model

Three model sets were created using: 1) a uniform, medium (5000m) resolution mesh; and two coarser (7500m) meshes which become progressively refined to a much higher (200m) resolution over nested subareas at 2) the Hastings Shingle Bank and 3) dredging licence area 473E. The particular choice of resolutions was determined following sensitivity testing of the model setup, described in Sections 3.3.3.3 and 3.3.3.4.

Hydrodynamic models of the three areas provide predictions of tidal elevation and tidal currents over the whole domain. Sediment dynamics models then utilise these hydrodynamic results to provide predictions, over the same area and at the same resolution, of local total load transport and bed level change. The notation for these results is shown in Table 5.

Parameter	Units	Notation
<i>General</i>		
Time reference	n/a	t
Timestep	(s)	$\Delta t$
<i>Hydrodynamic results</i>		
Water depth from mean sea level	(m)	d
Tidal elevation	(m)	h
Current speed	( $\text{ms}^{-1}$ )	U
Current direction	(degrees)	$\theta$
East current vector	( $\text{ms}^{-1}$ )	u
North current vector	( $\text{ms}^{-1}$ )	v
<i>Sediment dynamics results</i>		
Total load east vector	( $\text{m}^3 \text{m}^{-1} \text{s}^{-1}$ )	$Q_{\text{TLe}}$
Total load north vector	( $\text{m}^3 \text{m}^{-1} \text{s}^{-1}$ )	$Q_{\text{TLn}}$
Bed level change	(m)	$\xi$

**Table 5. List of output parameters from the model**

The results of the hydrodynamic models were analysed for the following secondary information: 1) the distribution of tidal co-range and co-phase lines from harmonic analysis of the tidal elevation time series at each node in the mesh; 2) residual flow patterns from temporal integration of the current data at each node in the mesh.

Patterns of sediment transport and inferred morphological change were either predicted directly from the results of the sediment dynamics model or inferred from the results of the hydrodynamic model. Techniques for quantifying patterns or finding the morphological result of either bed, suspended or total load included:

Inferred bed load

- Residual vectors of the velocity cubed, *hydrodynamic model*.

Suspended load advection

- Residual vectors of velocity, *hydrodynamic model*.

Total load

- Residual vectors of total load transport, *sediment dynamic model*.

Tendency for bed level change

- Volume transport divergence analysis, *hydrodynamic model*.
- Volume transport divergence analysis, *sediment dynamic model*.
- Local bed level change, *sediment dynamic model*.

Bed load is of particular importance when considering sediment transport interacting with an obstacle, such as an archaeological site, on the seabed. Suspended load is of particular importance when considering transport of suspended material (e.g. dredge plumes) between different regions. Total load transport (the sum of bed and suspended load vectors) is of particular importance when considering the potential for bed level change.

## 4.1 Results of the hydrodynamic model

### 4.1.1. Tidal axis orientation

The orientation of the local tidal axis (calculated as the gradient of a linear fit to the predicted  $u$  and  $v$  component flow data over 14 days) is shown in Figure 46. The Figure shows that the tidal axis is approximately parallel to the coast and to the axes of the English Channel and southern North Sea. This varies smoothly in open water to remain subparallel to the orientation of adjacent coastlines. Some complexity or directional shear is observed in the vicinity of the Channel Islands and between the Dover Straits and the Thames Estuary.

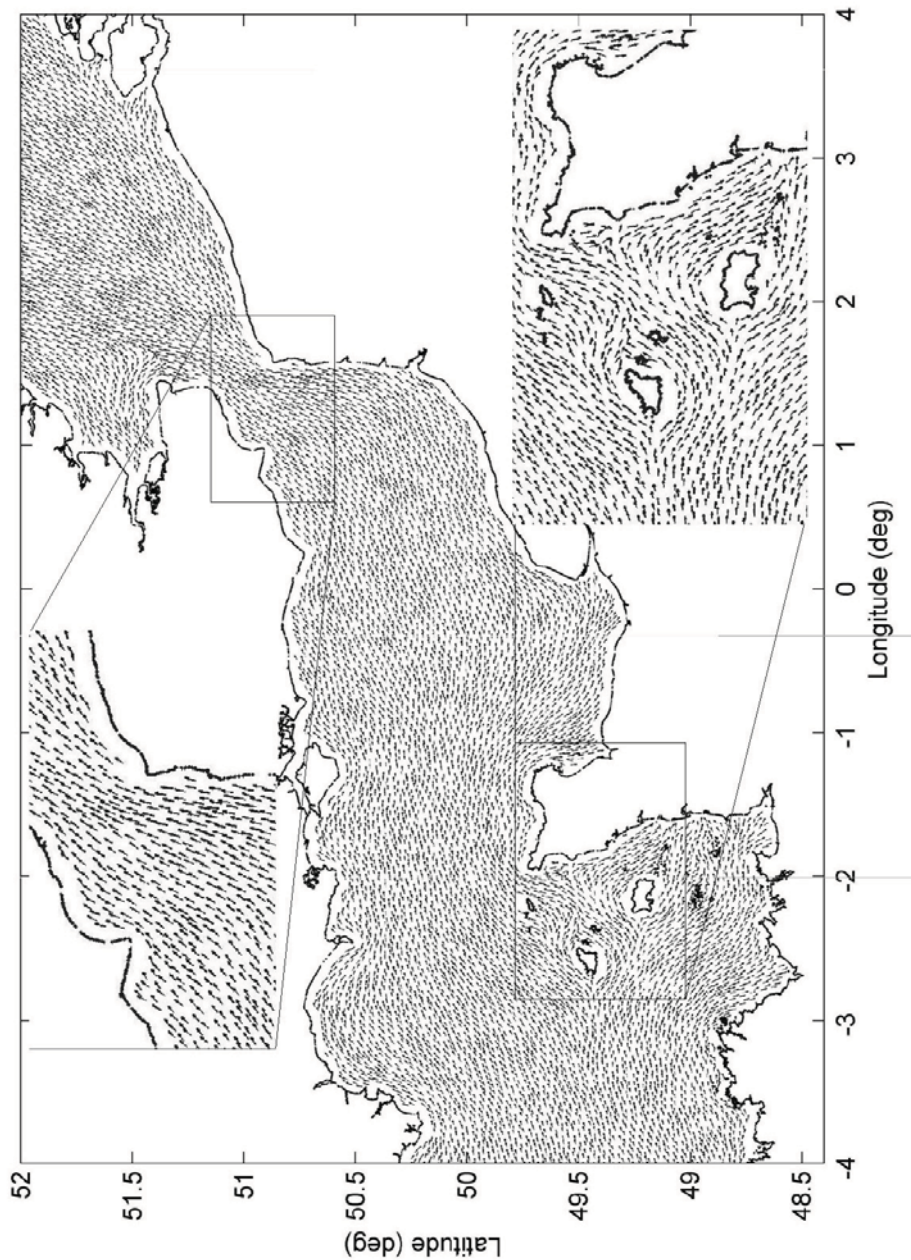


Figure 46. The orientation of the tidal axis throughout the domain. Inserts highlight tidal axes subparallel to the coast in the Dover Straits region and more complex flow in the vicinity of the Channel Islands.

#### 4.1.2. Residual flow field analysis

Residual flow field vectors  $x$  and  $y$  were calculated from time series of the  $u$  and  $v$  components of depth mean flow at each element on the mesh, using,

$$x = \sum_{t=0}^T u(t) \Delta t \quad \text{and}$$

$$y = \sum_{t=0}^T v(t) \Delta t$$

Where  $t$  is the timestep number,  $T$  is the total number of timesteps being integrated and  $\Delta t$  is the model results timestep in seconds. By tracing the location of  $x$  and  $y$  over time, a progressive vector diagram (PVD) is created; a single example PVD is shown in Figure 47. PVD's describe the residual drift of water at one location in a Eulerian sense, i.e. the curve does not trace the actual path of water flow away from the origin but rather visually represents the long term residual trend at that site. The example in Figure 47 demonstrates the typical features of residual flow data. Each flood and ebb cycle is visible as a local ellipse which varies in length over the spring-neap cycle (30km long on spring tides, 15km on neaps). The residual drift over the measurement site (the origin, shown by the black cross) is calculated as the displacement vector between the start and end of the timeseries (the black line). The residual flow is the length of the residual displacement vector divided by the time period of integration and is typically expressed here as both ( $\text{km day}^{-1}$ ) or ( $\text{ms}^{-1}$ ). To reduce bias, the start and end point of the vector must be the mean location over one tidal cycle (highlighted in blue). Results from the model are highly consistent in all locations, i.e. the direction of residual drift is not significantly sensitive to the location in the spring-neap cycle of the chosen start and end points, or to the number of days by which they are separated. The absolute magnitude does not vary linearly with time but so long as the same timeframe is used for all time series in the analysis, the difference in magnitude between any two given locations will be proportionally correct.

PVD's from twenty evenly distributed locations in the English Channel and southern North Sea are shown in Figure 48. This image is intended to demonstrate that residual displacement curves vary in form significantly over the domain but also demonstrate consistency with time. There is variety in the length of individual tidal ellipses, the length of overall residual vectors, the relative difference between spring and neap parts of the curves and the relative orientation between the tidal axis and the residual vector. These twenty chosen examples are representative of all other locations and of all other spring-neap cycles modelled; it should be noted that the pattern of residual flow is repeated over spring-neap cycle time scales and therefore that the direction and magnitude of residual flow vectors are insensitive to the choice of integration period.

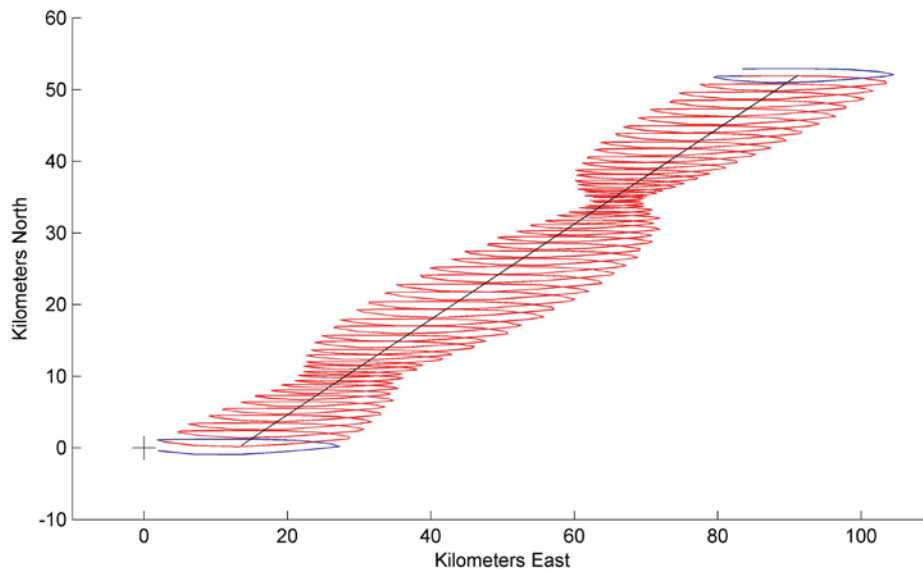


**Figure 47.** An example progressive vector diagram (red line) demonstrating the concept of residual flow from the origin (black cross) over 31 days. Data from the location indicated in Figure 25. Also shown are the data for the first and last tidal cycle of the data (blue lines) and the overall residual vector for the time series (black line).

The length and orientation of residual vectors at all mesh nodes are shown in Figure 49 to Figure 51; the colour bar scale shows the residual displacement ( $\text{km day}^{-1}$ ). The magnitude of residual flow in large parts of the domain is typically low; the modal value of all data is approximately  $0.9\text{km day}^{-1}$  ( $0.010\text{ms}^{-1}$ ), 61% of all data is  $2.5 < \text{km day}^{-1}$  ( $0.029\text{ms}^{-1}$ ), 86% of all data is  $< 5\text{km day}^{-1}$  ( $0.058\text{ms}^{-1}$ ) and 95% of all data is  $< 7.5\text{km day}^{-1}$  ( $0.087\text{ms}^{-1}$ ). Greater residual flow  $7\text{-}18\text{km day}^{-1}$  ( $0.081\text{ms}^{-1}\text{-}0.208\text{ms}^{-1}$ ) is found at the edges of large constrictions e.g. the central English Channel and Dover Straits, and to a lesser extent associated with headlands and prominences, e.g. the Isle of Wight, the Cotentin Peninsula, the Channel Islands, Portland Bill, Selsey Bill, Beachy Head and Dungeness headlands etc.

Residual flow direction in the English Channel is dominated by a strongly divergent flow pattern centred on an axis between the Isle of Wight and the Cotentin Peninsula. Strong residual flows extend outwards as broad jets in the deeper, middle part of the central Channel. Many complex and sometimes interacting residual eddy structures are observed in this region, closer to the coastline and associated with headlands, particularly strong residual eddy formation is associated with the Isle of Wight, Portland Bill, the Cotentin Peninsula and the Channel Islands. Away from the central Channel, the majority of the western Channel (offshore) experiences only relatively slight residual flows, typically in a westerly direction in British waters.

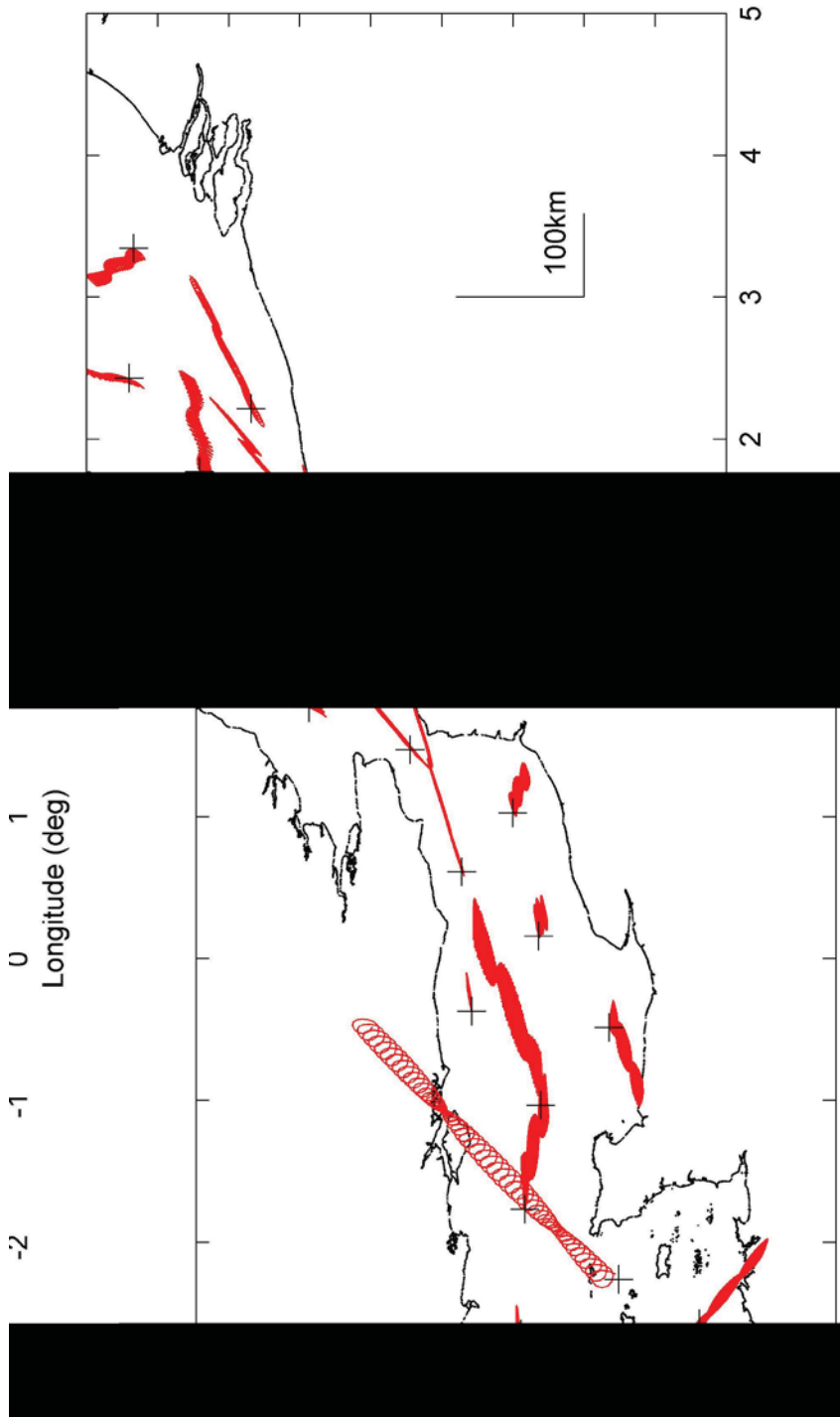


**Figure 48. Selected PVDs of residual tidal flow over 31 days, to scale, in the English Channel and southern North Sea. Data from the locations indicated in Figure 25.**

In the eastern Channel, strong easterly residual currents extend from the central Channel region, initially flowing parallel to the English coast forming a region of generally low magnitude residual flows between a point south of the Isle of Wight and Beachy Head. The jet intersects the coast between Beachy Head and Dungeness headlands, extending then to the Dover Straits. Residual currents in the southern part of the eastern Channel are generally of low magnitude and less coherent in their direction except for a region of strong northerly residual flow along the French coast between Berck and Boulogne which extends north into the Dover Straits. Strong north-easterly residual flows are predicted across the width of the Dover Straits and these extend as a jet into the southern North Sea; there is some strong

convergent interaction with south easterly residual flow from the Thames Estuary around the Margate/Ramsgate Peninsula forming a region of low residual flow around the area of the Goodwin Sands. Residual flow in the southern North Sea is generally to the north; the magnitude of residual flow is generally stronger on the British side and relatively weaker on the French/Dutch/Belgian side.

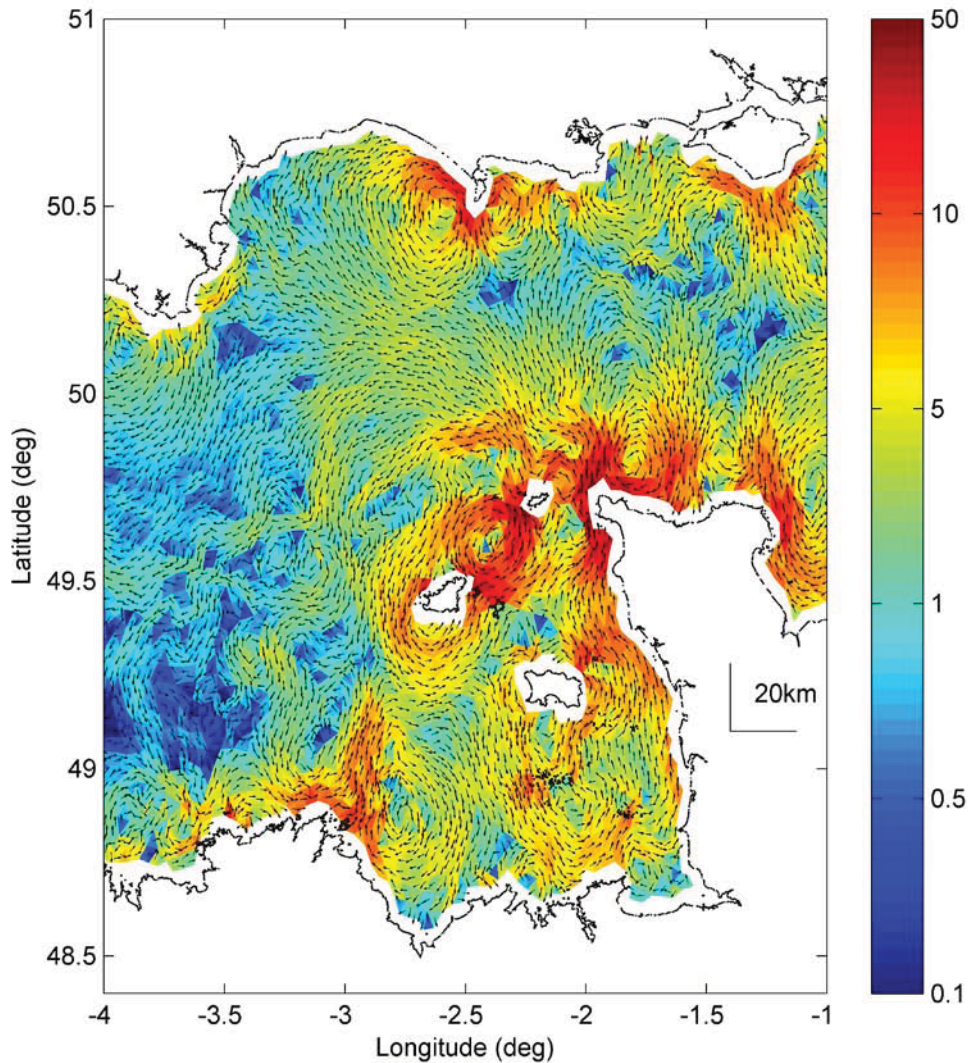


**Figure 49. Residual flow field in the Western and central Eastern English Channel. Key: colours – residual displacement length scale ( $\text{km day}^{-1}$ ); arrows - residual direction. Based on 31 days of data.**

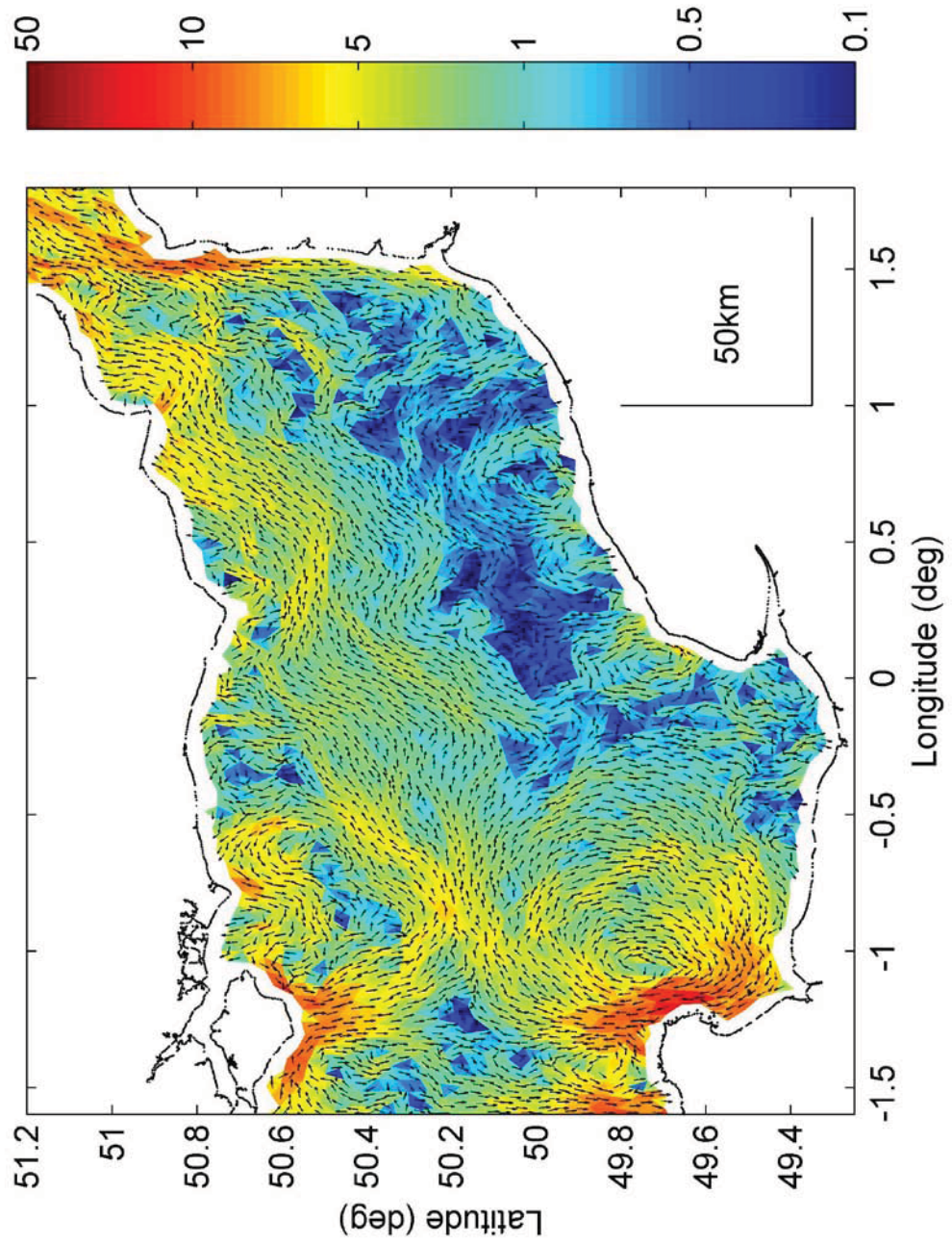
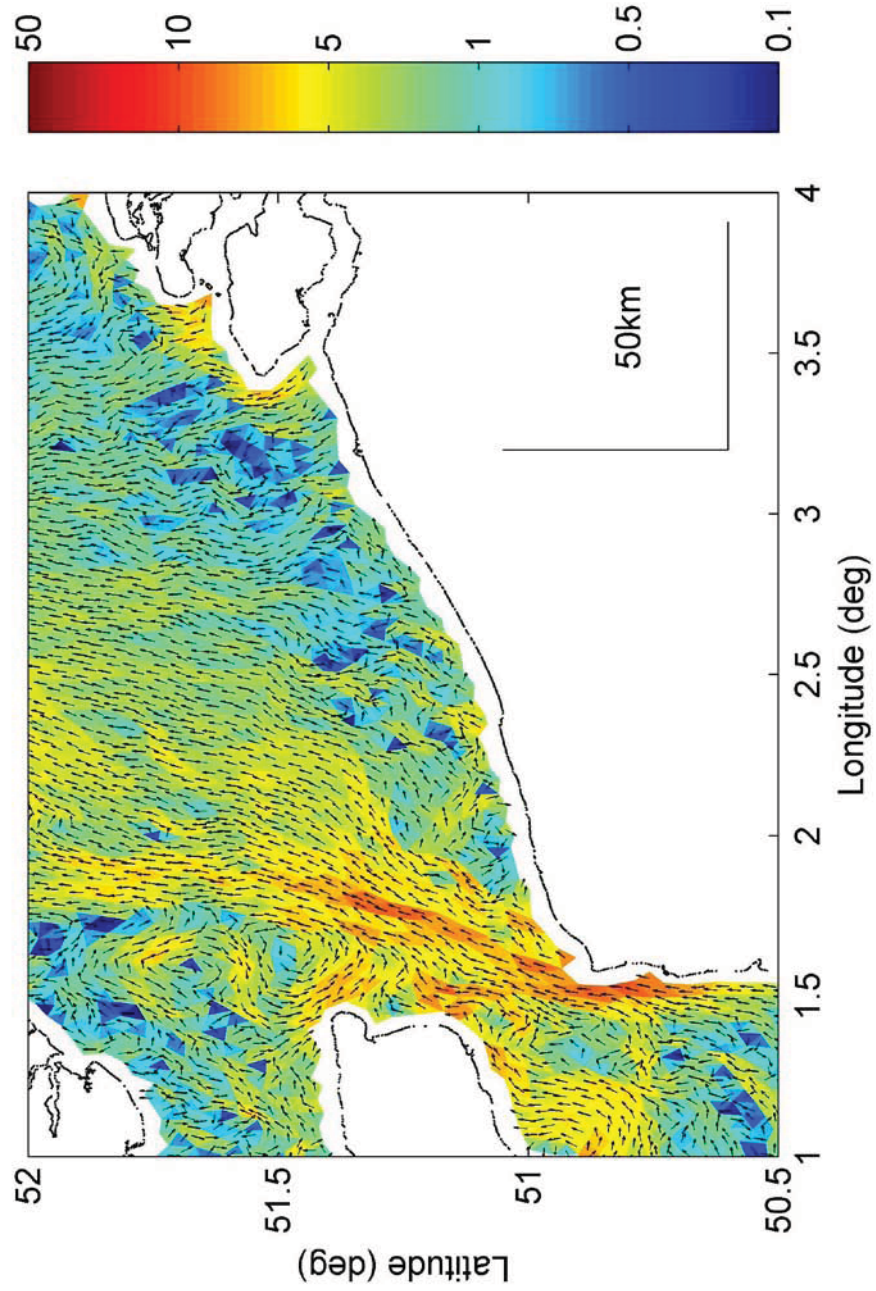


Figure 50. Residual flow field in the central and eastern English Channel. Key: colours – residual displacement length scale ( $\text{km day}^{-1}$ ); arrows - residual direction. Based on 31 days of data.



**Figure 51. Residual flow field in the Eastern English Channel and southern North Sea. Key: colours – residual displacement length scale (km day<sup>-1</sup>); arrows - residual direction. Based on 31 days of data.**

## 4.2 Results of the sediment dynamics model

### 4.2.1. The English Channel

Predictions of sediment transport over the whole domain were made for 4 scenarios of uniform sand distribution (mean grain sizes [63 $\mu\text{m}$ , 200 $\mu\text{m}$ , 500 $\mu\text{m}$  or 1000 $\mu\text{m}$ ]) using each of the three meshes, over the duration of the decoupled output (see Table 3). An additional scenario of a spatially variable distribution of grain sizes based upon an interpretation of previously published information by Stride, 1982; Evans, 1990; and Hamblin *et al.*, 1992 was tested using the medium resolution mesh.

The Engelund and Hansen (1972) formulation was used for predicting sediment transport. The rationale for this choice of formulation and more details may be found in Section 3.2.1. This formulation estimates a total load transport, which can then be divided into bed and suspended load components according to the proportions set by the user. Because of the wide range of sedimentary environments within the English Channel and southern North Sea, it was not considered appropriate to choose any one way of subdividing the total load into its component parts. Therefore, only estimates of total load from the sediment transport model will be presented and analysed as an indicator of the magnitude and direction of general sediment transport. The model also provides predictions of bed level change directly, through spatial gradients in the sediment transport budget.

The predicted sediment- and hydrodynamic data were analysed to yield:

- Residual total load sediment transport
- Local sediment mobility and transport asymmetry
- Residual bedload sediment transport inferred from current data
- Residual suspended load sediment transport inferred from current data
- Tendency for bed level change inferred from the current data
- Tendency for bed level change inferred from the sediment data
- Tendency for bed level change predicted by the model directly

#### 4.2.1.1. Residual sediment transport analysis

Residual total load transport vectors  $x$  and  $y$  were calculated from time series of the east and north vectors of transport,  $Q_{TL_e}$  and  $Q_{TL_n}$ , at each element on the mesh, using,

$$x = \sum_{t=0}^T Q_{TL_e}(t) \Delta t \quad \text{and} \quad y = \sum_{t=0}^T Q_{TL_n}(t) \Delta t$$

The overall residual vectors were calculated in the same way as described in Section 4.1.2. An example PVD using one spring-neap cycle of data is shown in Figure 52. The way in which the sediment transport data are stored restricts the number of timesteps that may be analysed to only one spring-neap cycle. However, Figure 53 shows that in the same way as for the hydrodynamic results, the direction and relative magnitude of residual sediment transport vectors were not sensitive to the particular number or choice of spring-neap cycles chosen for integration.



**Figure 52.** An example progressive vector diagram (red line) demonstrating the concept of residual sediment transport from the origin (black cross) over 14 days. Data from the location indicated in Figure 25. Also shown are the data for the first and last tidal cycle of the data (blue lines) and the overall residual vector for the time series (black line).

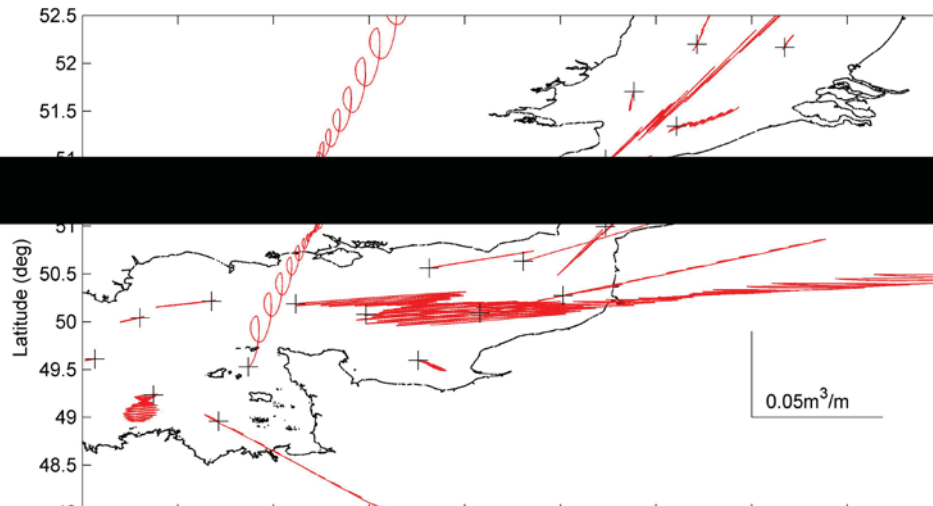


**Figure 53.** Selected PVDs of residual sediment transport over 14 days, to scale, in the English Channel and southern North Sea. Data from the locations indicated in Figure 25.

The results of all sediment models viewed together reflect the potential for sediment transport that might occur as a result of interaction between the local flow field and quartz sand of the specified grain size. Quantitative transport fields are more difficult to infer because in the absence of detailed data, no allowance can be made for the shielding or stabilising effect of mixed grain sizes (sediment sorting), the presence or absence of bedforms, or the thickness/volume of sand actually available for transport.

The direction of potential residual total load transport is shown in detail in Figure 54 to Figure 56; the magnitude shown in these Figures refers to that calculated for the spatially variable grain size distribution. For all grain sizes (spatially variable or uniform) it was found that the local direction of residual transport was not affected by the sediment grain size being modelled; only the magnitude varies. Data within one element (approximately 5km) of the coast have been removed from the plots, as this region is typically shallow water with stronger influence of wave action that is not explicitly modelled but will affect sediment transport at all timescales.

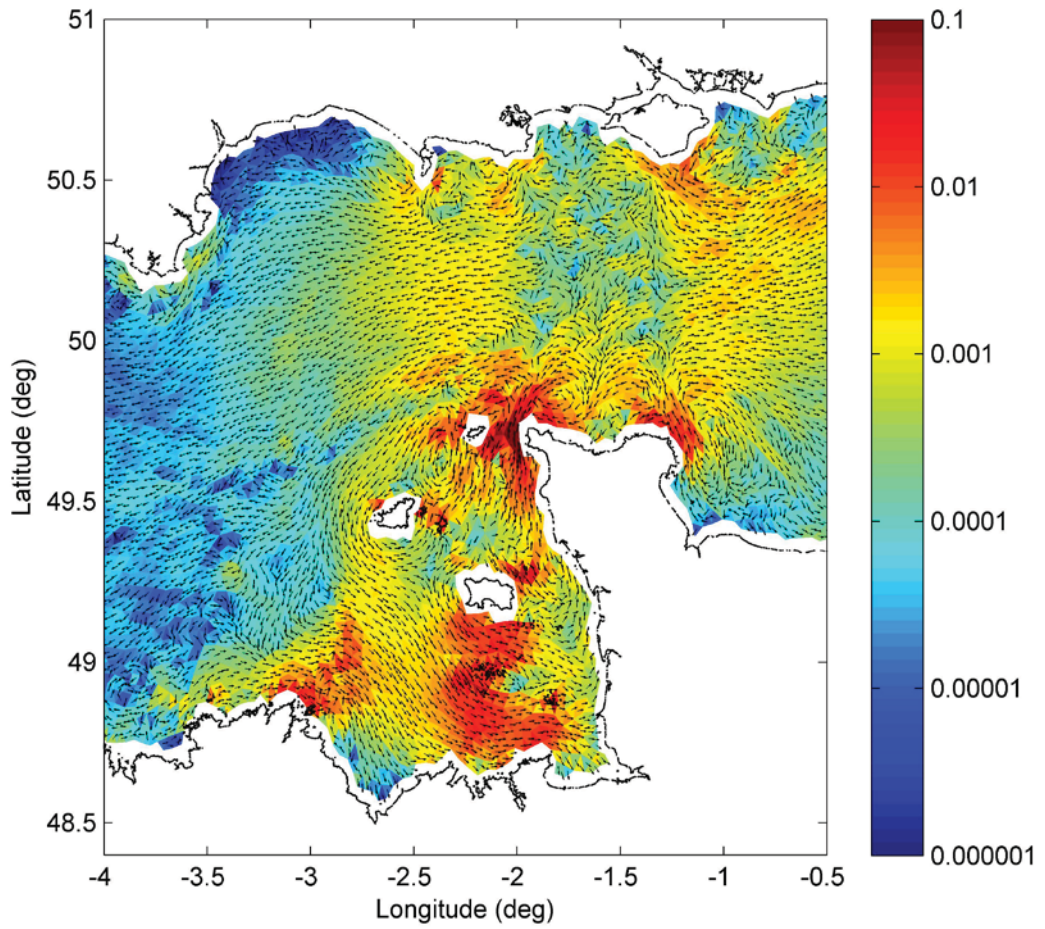


Figure 54. Residual potential total load transport of the spatially variable input grain size in the Western and central Eastern English Channel. Key: colours – residual sediment flux ( $\text{m}^3 \text{m}^{-1} \text{day}^{-1}$ ), respectively; arrows - residual direction. Based on 14 days of data.

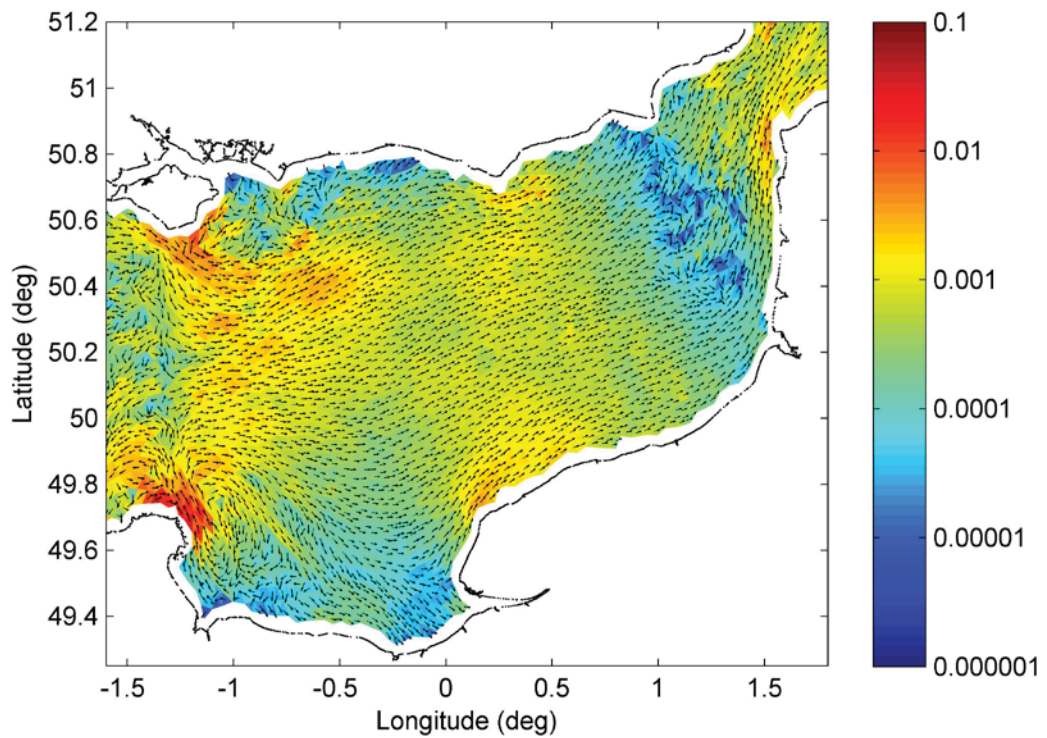


Figure 55. Residual potential total load transport of the spatially variable input grain size in the central and eastern English Channel. Key: colours – residual sediment flux ( $\text{m}^3\text{m}^{-1}\text{day}^{-1}$ ), respectively; arrows - residual direction. Based on 14 days of data.

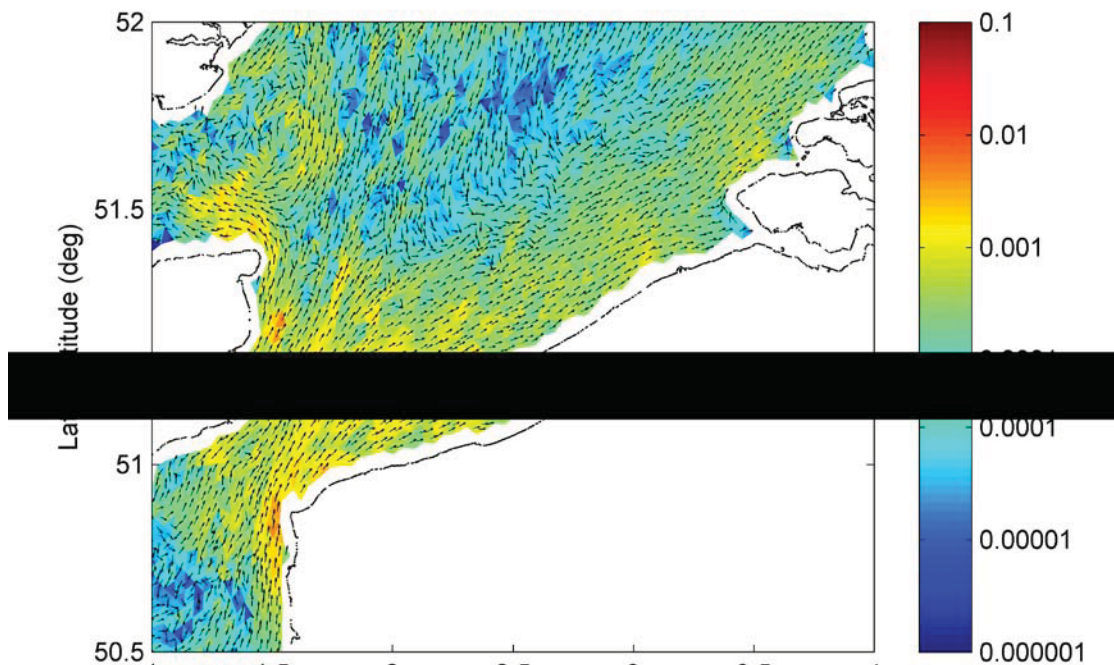


Figure 56. Residual potential total load transport of the spatially variable input grain size in the eastern English Channel and southern North Sea. Key: colours – residual sediment flux ( $\text{m}^3\text{m}^{-1}\text{day}^{-1}$ ), respectively; arrows - residual direction. Based on 14 days of data.

The residual bed load transport magnitude potential for grain sizes [63 $\mu\text{m}$ , 200 $\mu\text{m}$ , 500 $\mu\text{m}$ , 1000 $\mu\text{m}$ ] is shown in Figure 57 to Figure 60. The direction of residual transport over each area is the same as that in the more detailed Figures above.

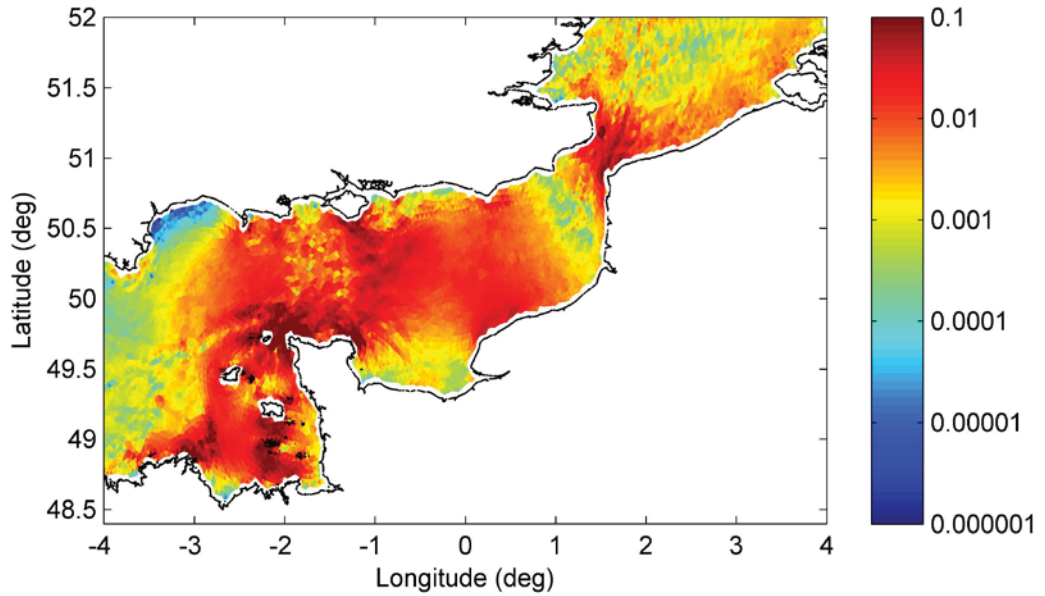


Figure 57. Residual magnitude of potential total load transport ( $\text{m}^3\text{m}^{-1}\text{day}^{-1}$ ) in the English Channel and southern North Sea for quartz sand of 63 $\mu\text{m}$  grain diameter. Based on 14 days of data.

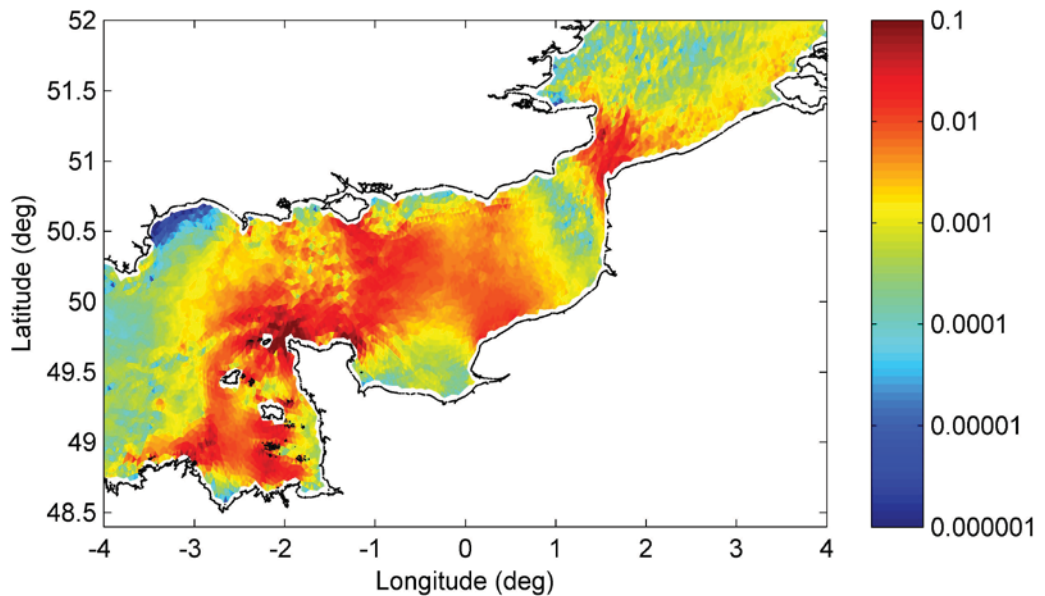


Figure 58. Residual magnitude of potential total load transport ( $\text{m}^3\text{m}^{-1}\text{day}^{-1}$ ) in the English Channel and southern North Sea for quartz sand of 200 $\mu\text{m}$  grain diameter. Based on 14 days of data.

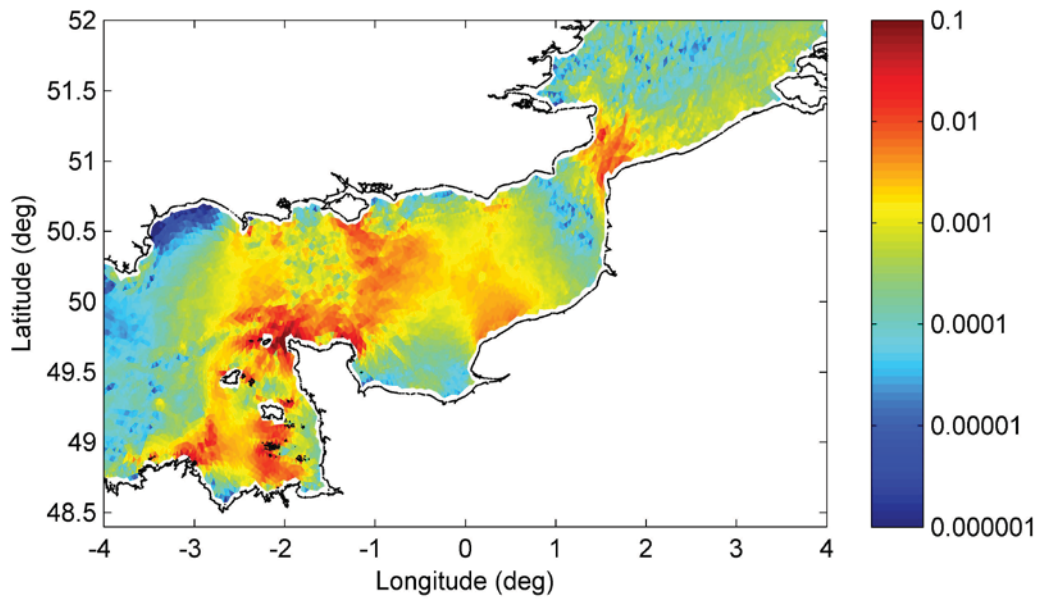


Figure 59. Residual magnitude of potential total load transport ( $\text{m}^3\text{m}^{-1}\text{day}^{-1}$ ) in the English Channel and southern North Sea for quartz sand of  $500\mu\text{m}$  grain diameter. Based on 14 days of data.

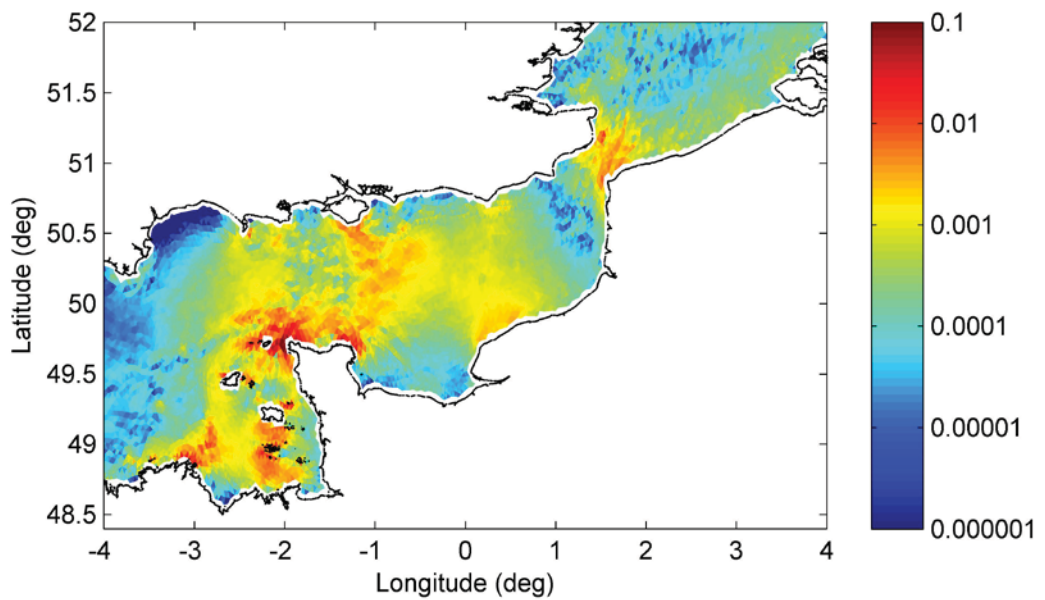


Figure 60. Residual magnitude of potential total load transport ( $\text{m}^3\text{m}^{-1}\text{day}^{-1}$ ) in the English Channel and southern North Sea for quartz sand of  $1000\mu\text{m}$  grain diameter. Based on 14 days of data.

From these series of Figures, the following observations can be drawn:

- Transport of quartz sand (<1mm diameter) by the tide can potentially occur to some degree in almost any part of the central and eastern English Channel, in the Dover Straits and large parts of the southern North Sea.
- Potential transport rates are greatest around the Cotentin Peninsula of France.
- Relatively high potential residual transport rates are also predicted: up to 100km east of the north/south axis between the Isle of Wight and the Cotentin Peninsula; in the central part of the eastern English Channel, particularly around Beachy Head and up to 50km from the French coast between Le Havre and Dieppe; in the Dover Straits; around the Channel Islands and adjacent French coastline; and up to 30-40km offshore of the French, Belgian and Dutch coastline in the southern North Sea.
- The lowest potential residual transport rates are observed in Lyme Bay.
- Relatively low potential residual transport rates are also predicted: in the western English Channel; the large embayment west of Le Havre; within 10-15km of the shore between the isle of Wight and Beachy Head; in the western approaches to the Dover Straits; in the central southern North Sea and Thames Estuary.

#### 4.2.1.2. *Local sediment mobility and transport asymmetry*

The residual potential sediment transport describes the likely transport patterns on the time scale of spring-neap cycles and greater, but does not describe how energetic the local environment is. For example, an area may have the potential for strong but symmetrical transport, resulting in a small residual transport vector; contrastingly, an area may experience only weak transport but with very strong asymmetry, yielding an apparently large residual transport rate.

The mean strength of sediment transport,  $Q_{TLmag}$  independent of direction may be calculated simply as,

$$Q_{TLmag} = \frac{\sum_{t=0}^{t=N} \sqrt{Q_{TLe}^2(t) + Q_{TLn}^2(t)}}{N}$$

The asymmetry,  $R$ , describes the proportion of mean transport towards each pole of the tidal axis, e.g. 50%:50%  $\rightarrow R=0.5$ ; 65%:35%  $\rightarrow R=0.65$ ; 85%:15%  $\rightarrow R=0.85$ , etc. and is calculated in the following manner:

1. Find the linear gradient of the scatter data  $Q_{TLe}$ ,  $Q_{TLw}$ .
2. Rotate the data so that the gradient = 0.
3. Calculate the magnitude of each vector, maintaining the sign.
4. Find  $Q_{TLmag}$  for all data  $> 0$  ( $=Q_{TLmag1}$ ) and for all data  $< 0$  ( $=Q_{TLmag2}$ ).
5. Asymmetry,  $R = Q_{TLmag1} / (Q_{TLmag1} + Q_{TLmag2})$ .
6. Filter all values, if  $R > 0.5$ ,  $R = 1 - R$ . i.e. all values must be in the range  $0.5 \leq R \leq 1.0$ .

The same ( $Q_{TLc}$  and  $Q_{TLn}$ ) data used to create the residual transport patterns (spatially varying grain size) were analysed to find the mean absolute sediment transport rate (Figure 61) and the sediment transport asymmetry (Figure 62).

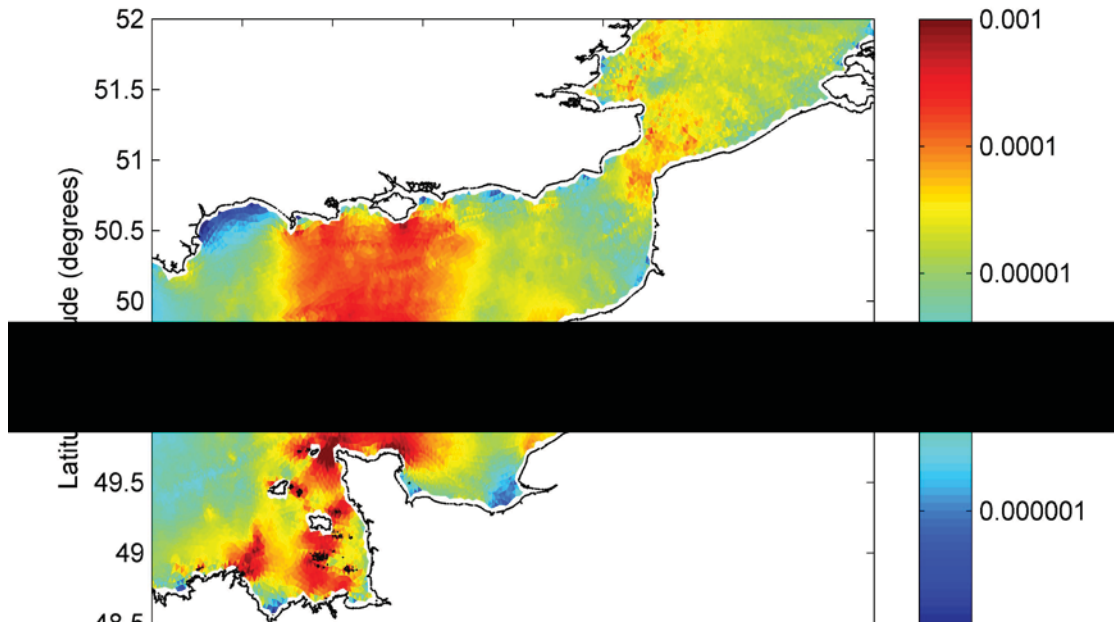


Figure 61. The mean absolute sediment transport rate of quartz sand, 200µm in diameter, as an indicator of the potential mobility/stability of sediment present locally.

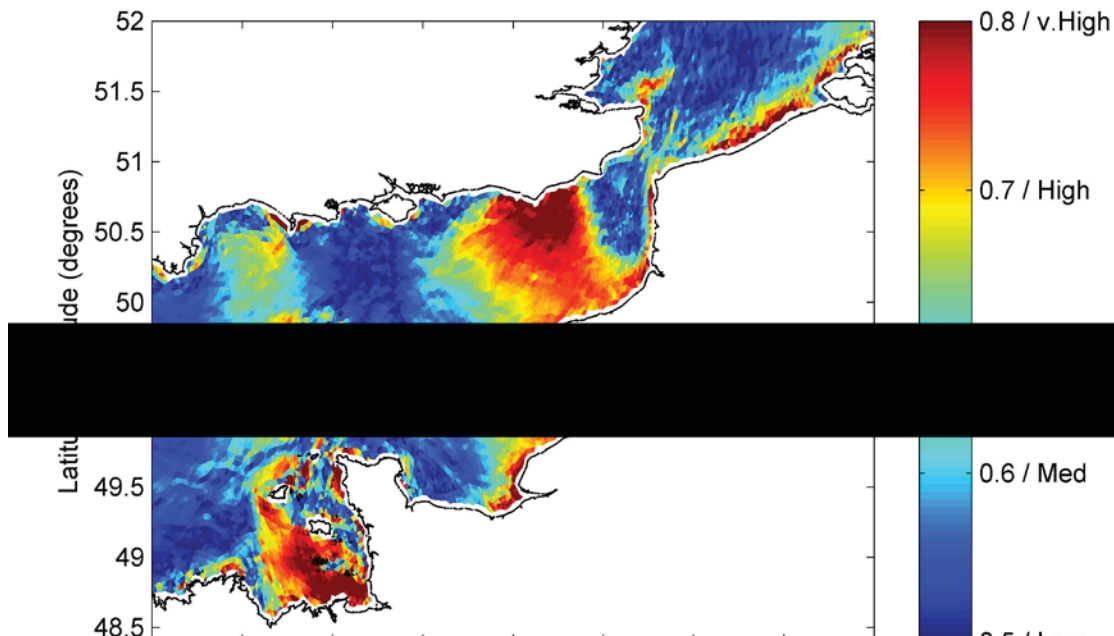


Figure 62. The transport asymmetry of 200µm diameter quartz sand.

Together, the figures reflect the patterns of potential residual sediment transport. The images show that observations of relatively high or low residual sediment transport potential over long time periods may be the result of different combinations of actual sediment mobility and transport asymmetry. A number of particular observations may be made:

- Regions identified as having particularly low magnitude residual transport potential (e.g. Lyme Bay, Selsey Bill to Beachy Head) also have low sediment mobility.
- In the central part of the English Channel, the area of apparently weak residual transport to the west of the Isle of Wight-Cotentin Peninsula axis actually experiences high sediment mobility but with low transport asymmetry.
- In the central and northern side of the Dover Straits, relatively high residual transport potential is caused by high sediment mobility but only low to medium transport asymmetry.
- In the Central part of the eastern English Channel and in a localised strip along the French coast north-east from Le Havre, through the Dover Straits and along much of the Belgian and Dutch coast, the area of apparently strong residual transport actually experiences only medium sediment mobility but with high transport asymmetry.
- Strong residual transport in the vicinity of the Channel Island and the adjacent French coastline is a product of both high sediment mobility and high transport asymmetry.
- Within approximately 10-20km of the British coastline, the mobility and asymmetry of sediment transport in regions of open coastline is spatially variable (see the Figures for more details) but both tend to be high in the vicinity of large headlands.

These figures are compared in more detail with the distribution of known sand body accumulations later in Figure 87.

#### 4.2.1.3. *Residual bedload transport inferred from tidal current data*

The divergence of a flow field is an indicator of the potential for long term net sediment erosion or accumulation. Previous studies have found that an even better correlation may be found by using the cube of the velocity (which is proportional to the sediment transport) in the form of a volume flux (i.e. local velocity<sup>3</sup> × local water depth). The particular analysis technique used may be summarised as follows:

1. Depth mean velocity vectors ( $u$  &  $v$ ) and total depth ( $h$ ) data are extracted for all elements in the mesh at every time step.

Then for every timestep:

2. Values are interpolated onto a rectilinear mesh.
3. The vectorised volume transport ( $U=u \cdot h$  and  $V=v \cdot h$ ) at each time step is calculated.
4. The value from step 3 is cubed whilst maintaining the associated sign (i.e.  $U_{vec}=U \cdot U^2$ ,  $V_{vec}=V \cdot V^2$ ).
5. The local gradient of  $U_{vec}$  and  $V_{vec}$  is calculated using a simple central differencing scheme.
6. The sum of the two gradients represents the tendency for transport divergence (positive values) or convergence (negative values).

To find the overall tendency for convergence or divergence:

7. The net result is found as the mean value over the period analysed.

The results of this analysis are sensitive to the spatial resolution at which the gradients are calculated. Gradients should be calculated over sufficiently large an area that regional scale patterns become apparent above the noise of small gradient differences between adjacent local data points. Too large a resolution will, however, remove detail and may average out important boundary lines. A spatial resolution of 0.1 degrees was chosen as it corresponds to a cell length scale of approximately 11km<sup>2</sup>, therefore integrating up to 4 data points for each cell; this choice makes the analysis representative of spatial gradients measured over a distance of approximately 22km. The result and the inferred patterns are visually summarised in Figure 63. This figure is compared in more detail with the distribution of known sand body accumulations later in Figure 87.

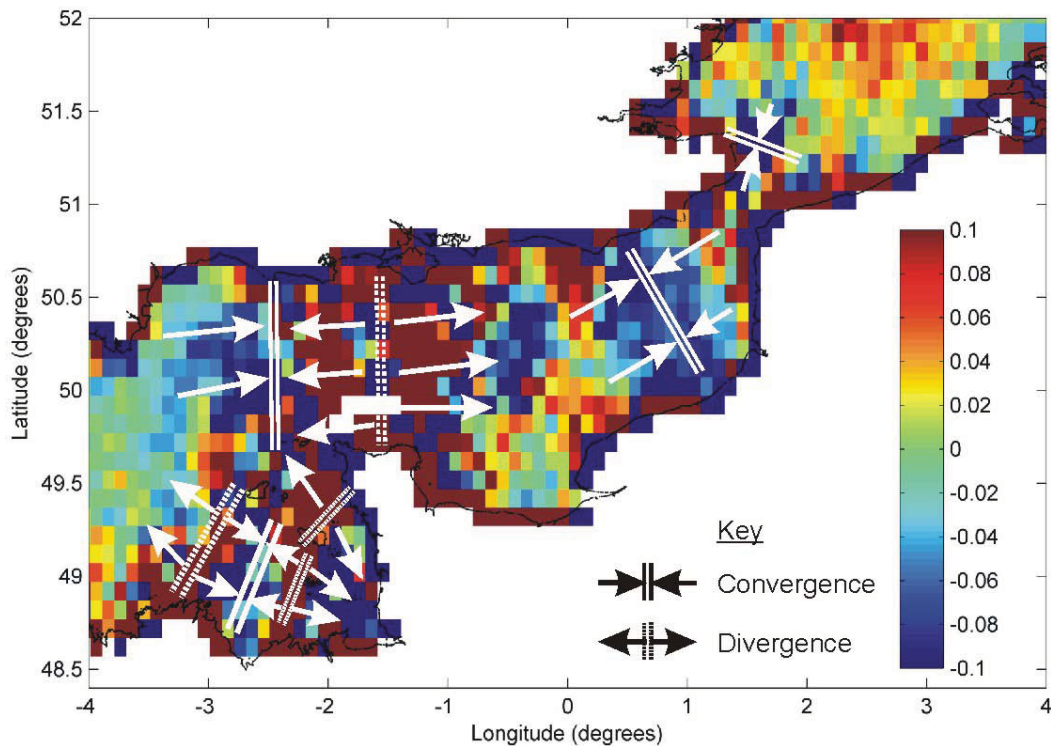


**Figure 63.** The volume transport divergence gradient based on 14 days of data. Positive values indicate a tendency for divergence of residual sediment transport vectors (erosion), negative values indicate a tendency for convergence (deposition). Arrows also indicate the tendency for convergence or divergence locally and are aligned approximately to the tidal axis (see Figure 46). Spatial resolution = 0.1degrees.

Large portions of the western English Channel, up to a line approximately between Portland Bill and the Channel Islands, have no strong tendency towards accumulation or erosion. A tendency towards net erosion is suggested around the Lizard of Cornwall and north of the Brest Peninsula.

The central and eastern English Channel are characterised by across basin banding, alternating between erosion and deposition and of varying intensity. The strongest transport divergence is centred upon an axis between the Isle of Wight and the Cotentin Peninsula, also extending south between the Channel Islands and France. The central axis of this band of

divergence reflects generally the location of the bedload divergence line identified in previous studies (e.g. Kenyon and Stride, 1970; Grochowski *et al.* 1993). This divergence is bordered by bands of apparent transport convergence, more strongly on the western side, where strong sediment transport out of the central Channel region becomes suddenly weaker. The eastern English Channel is divided almost equally in two again by another weaker divergence line predicted to run approximately south from Beachy Head to the French coast.

The mode of transport in the Dover Straits is not clear, demonstrating both relatively strong divergence and convergence at this scale. The southern North Sea basin is indicated as having a strongly divergent (erosive) residual transport field. The maximum values are observed centrally, offshore in the vicinity of the known North Sea amphidrome and may correspond to the rotational propagation pattern of the tidal wave within this amphidromic cell.

It is important to note that these patterns of tendency towards erosion or deposition are based only upon the convergence or divergence of the local velocity field (most representative of the bedload transport field) and only on 14 days of data in this example. Also importantly, the magnitude of the flow at each location relative to the threshold for sediment transport and the availability and grain size distribution of sediment at each location is not taken into account using this method.

#### 4.2.1.4. *Residual suspended load transport inferred from tidal current data*

Sediment in suspension is advected passively with the tidal current on both short and long timescales. Therefore, suspended sediment transport (from the point of suspension to the eventual point of deposition) will follow the residual displacement of the tide, as described in Section 4.1.2. In particular, suspended load transport over time periods in the order of the semi-diurnal cycle will be transported in the general orientation of the tidal axis (Figure 46) and over longer time periods in the direction of the residual flow vector (Figure 49 to Figure 51).

#### 4.2.1.5. *Bed level change*

Bed level change is the long term net result of several factors already discussed, including sediment mobility, asymmetry of transport and spatial gradients thereof. Bed level change may also be estimated directly by the model using the time integrated sediment transport budget. In simple terms, the bed level change is calculated as

$$\xi = \frac{Q_{TL(in)} - Q_{TL(out)}}{A}$$

Where  $Q_{TL(in)}$  and  $Q_{TL(out)}$  are the total sediment flux into and out of the cell, respectively, and  $A$  is the cell area. The sum of this quantity over a number of time steps yields the total bed level change from the start of the model run.

The bed level change reported by the model does not take into account the detailed spatial variability in mean grain size, local grain size distribution or erodible sediment thickness, i.e. apparent erosion of tens of metres may be reported, despite only one metre of potentially mobile sediment actually being present (DHI are working on a solution to this issue for future projects). Hence, bed level change reported here rather represents the potential for bed level change, where the magnitude and sign of the result should be interpreted in a relative sense (*erosion* or *accumulation*, *higher* or *lower* rates. Because of excessive erosion in certain areas around the Cotentin Peninsula, bed level change predicted by the model was recorded in isolation and was not allowed to feed back into the hydrodynamic model.

Time series of bed level change at twenty locations evenly distributed throughout the English Channel and southern North Sea (see Figure 25) are shown in Figure 64.

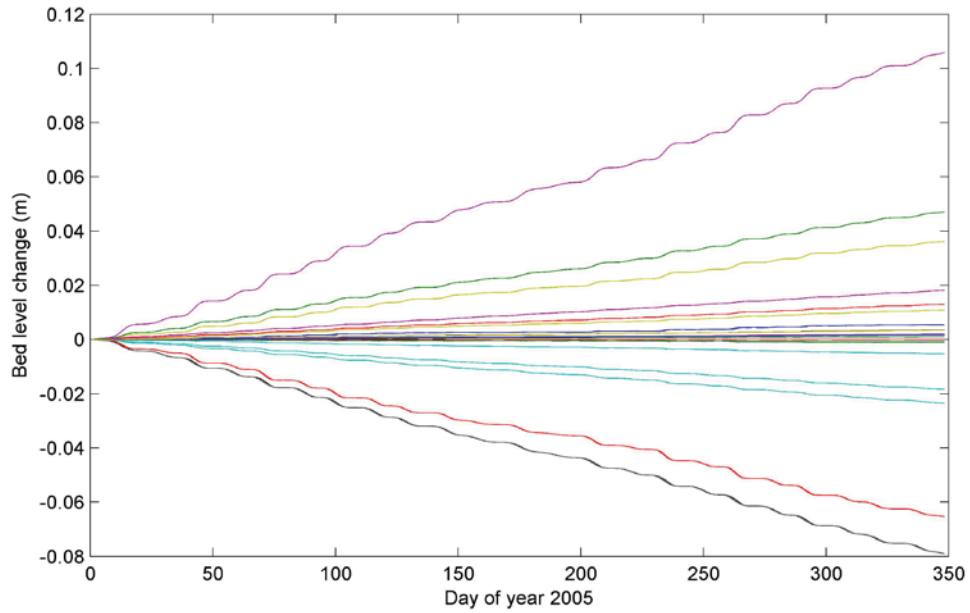


**Figure 64. Bed level change predicted by the model, over one year, at twenty evenly spaced locations throughout the English Channel and southern North Sea.**

Figure 64 shows that there is variability in the rate of bed level change throughout the domain; some sites experiencing large rates (order of centimetres per year), others very small rates (order of millimetres per year). The long term bed level change trend (rate and sign) predicted by the model at all sites is approximately linear over time periods greater than one spring neap cycle; the rate of bed level change may be slightly greater during equinoxal tides (spring and autumn) and lesser during solstice tides (summer and winter). Figure 65 shows two spring-neap cycles of change in more detail. Alternating positive and negative (sub-centimetre scale) bed level fluctuations are observed at some locations on semi-diurnal timescales; other locations may be more flood or ebb tide dominant and therefore demonstrate more consistent change. Bed level change is more active during spring tides and is typically zero at all of the sample locations during neap tides.

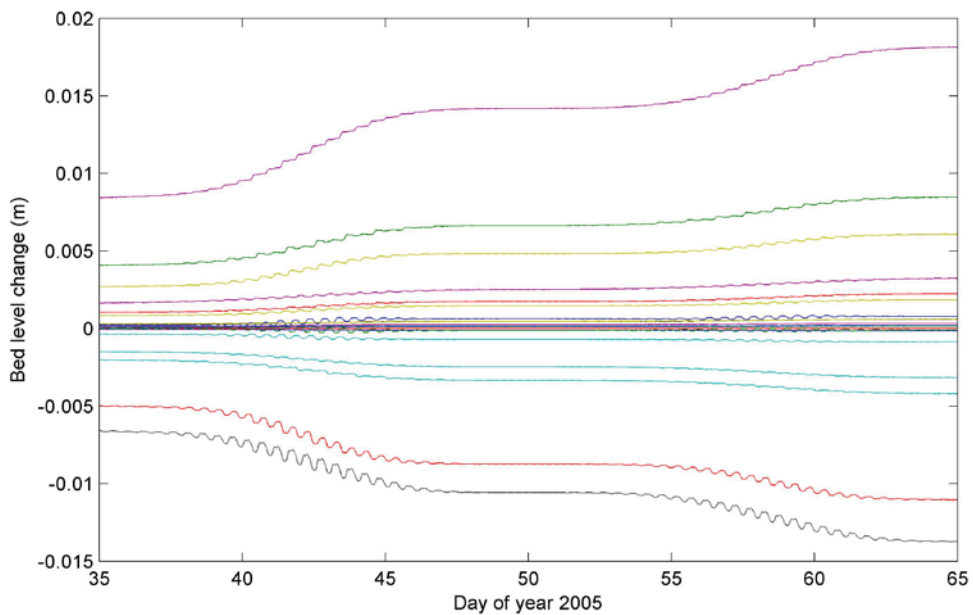


**Figure 65. Bed level change predicted by the model, over two spring-neap cycles, at twenty evenly spaced locations throughout the English Channel and southern North Sea. Exact locations indicated in Figure 25.**

Because the change is linear over time scales greater than a few spring-neap cycles, the sign and relative magnitude of bed level change will be the approximately the same, irrespective of the actual time interval chosen. In order to take into account variability on semi-diurnal, spring-neap and equinoxal time scales, bed level change data at all elements in the domain after one year were used in the following analysis. The form of bed level change (net erosion or accretion) is shown in Figure 66 and the magnitude of predicted bed level change is shown in Figure 67. The model predicts significant spatial variability in the form of bed level change; the distribution of magnitudes, however, follows similar patterns to those observed for sediment mobility. The following observations can be made:

- There is a greater potential for net bed erosion in the central English Channel (associated with the sediment transport divergence zone); the Cotentin Peninsula is also associated with particularly high potential for bed level change. However, it is known that the seabed in these regions is largely immobile (gravels and/or rocky), following the (predicted) removal of mobile sediment from these areas in the past. This provides some validation for the model results and demonstrates the need to interpret results in a potential or relative sense only.
- The Channel Islands and surrounding area have strong and spatially coherent potential for both accumulation and erosion.
- The majority of the eastern English Channel is associated with spatially consistent bed level increase (and a smaller region of bed level lowering) but only at relatively slow rates.
- The western English Channel is associated with very low potential rates of bed level change of either type, reinforced by earlier observations of low sediment mobility.
- The Dover Straits and Thames Estuary are associated with medium to high magnitude bed level change but spatially incoherent in type. These regions are therefore dynamic but with no tendency towards regional scale sediment accumulation or erosion.
- The central southern North Sea is associated with spatially variable tendencies towards erosion or accumulation and all only at relatively slow rates in either case.
- Greater potential magnitudes of bed level change (not consistent in type) are associated with headlands including Start Point, Portland, Studland, St. Catherine's point, Beachy Head and Dover.

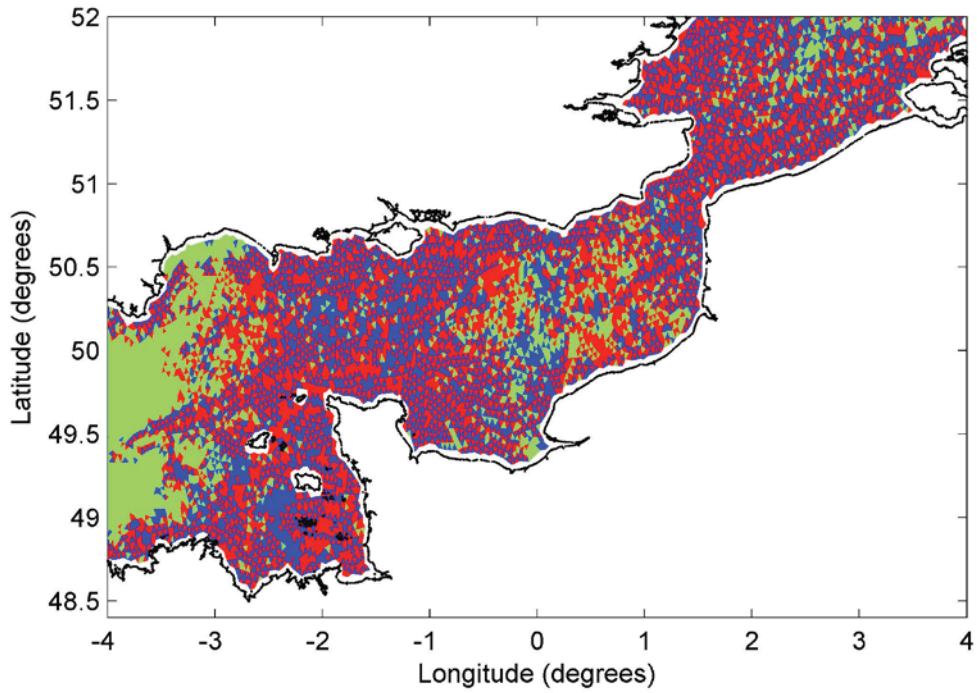


Figure 66. Predicted type of net bed level change greater than 5mm over one year in the English Channel and southern North Sea. Key: red – accumulation; blue – erosion; green – magnitude of change < 5mm.

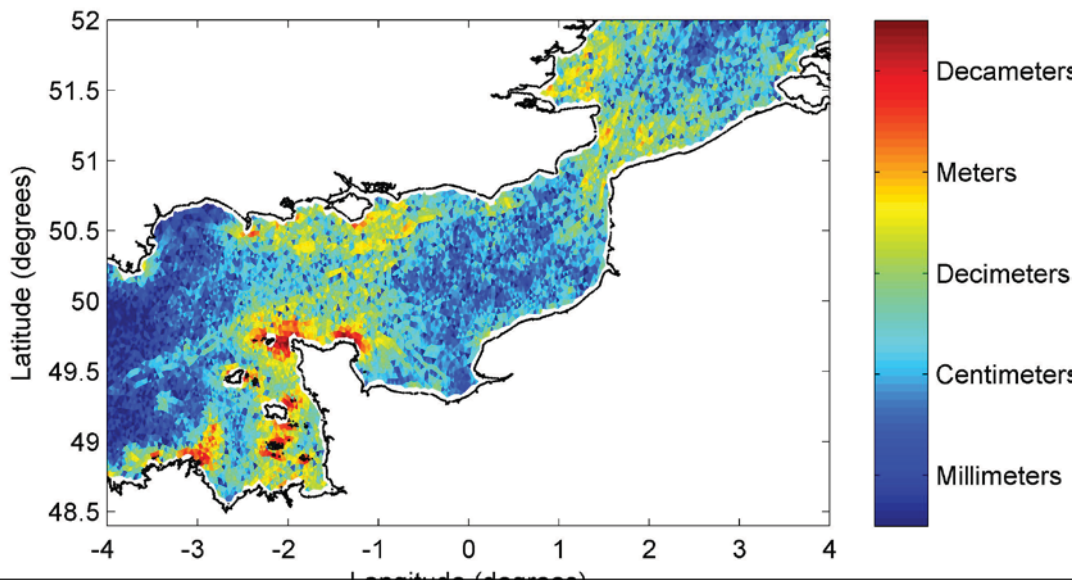
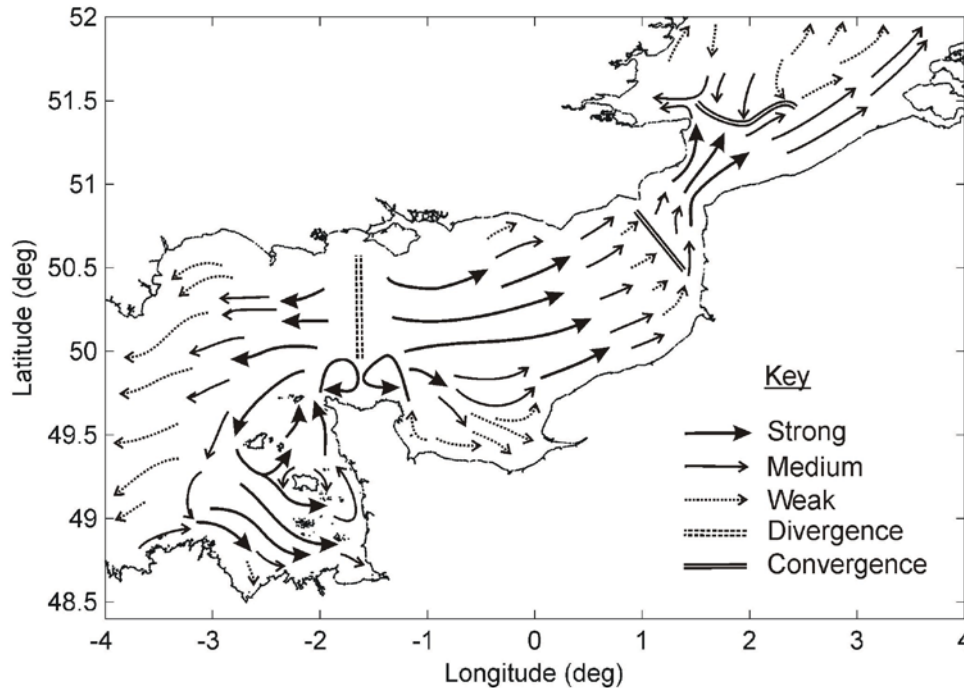


Figure 67. Predicted magnitude of net bed level change over one year in the English Channel and southern North Sea.

#### 4.2.2. Summary

The predicted potential residual transport of any given quartz sand grain size varies greatly across the domain (by 4-5 orders of magnitude). The direction of potential residual sediment transport is simple in its spatial patterning, relative to that for residual water movement. Potential sediment transport pathways, calculated using the previously reported broad spatial variability in sediment type, are shown schematically in Figure 68.



**Figure 68. Summary of potential residual sediment transport vectors.**

Figure 68 relates closely to previously published sediment transport pathway maps except for a reversal of predicted residual transport direction in the Dover Straits; the convergence zone at the English Channel entrance to the Straits is similarly located, however, it corresponds here to a convergence in magnitude, rather than a convergence of absolute transport directions. The region of northwards transport along the French coast to the north of the Dover Straits is also wider than that predicted by previous authors.

The precise location of the divergence axis in the central English Channel is not the same in all reports and is variously located: in a broad strip at an oblique angle between St Catherine's point and the west of the Cotentin Peninsula (Kenyon and Stride, 1970); a north-south line between St Catherine's point and the east of the Cotentin Peninsula (Grochowski *et al.*, 1993); and, in a north south strip between the Needles and the centre of the Cotentin Peninsula (Present Study). Although Grochowski *et al.* (1993) predict a very precise and narrow axis, the present study found the axis region to be much broader; it is unlikely that the results of Kenyon and Stride (based on interpretation of sparse geophysical data) could resolve a clear line either. As such, the accuracy of the breadth or location of the reported axis cannot be confirmed in or by any study so far.

### 4.3 Comparison with the nested subareas

In this section, model results are overlain and compared with observed (field) data from the Hastings Shingle Bank and Area 473E subregions. Spatial patterns of tidal axis orientation, residual flow orientation, residual sediment transport orientation, sediment mobility and transport asymmetry are overlain onto the bathymetry; these are then visually interpreted for potential relationships between the modelled quantities and naturally occurring patterns in the bathymetry (location of slopes, orientation of bedforms, etc).

The actual values of sediment mobility will vary with grain size but less so the asymmetry; the long term response of an area to spatial patterning of these values will likely then be grain size independent and controlled mainly by spatial gradients in sediment mobility and asymmetry. It is therefore more appropriate to present and discuss mobility and asymmetry in relative terms.

#### 4.3.1. Hastings Shingle Bank

Observed (field) data available from the Hastings Shingle Bank includes:

- Flow measurements from 3 sites using ADCPs
- Estimation of residual flow and sediment transport on the basis of the measured currents
- Detailed multi-beam swath bathymetry
- Detailed side scan sonar (bed roughness)
- Distribution of mean grain size from core samples

##### 4.3.1.1. *Comparison with flow data*

The time series' of current speed and direction observed at the Hastings Shingle Bank were compared with the model results from the same areas in Section 3.3.3.

##### 4.3.1.2. *Comparison with regional bathymetry*

Tidal axis orientation, residual tidal flow vectors and residual sediment transport vectors are overlain onto a multi-beam swath bathymetry image of the Hastings Bank region in Figure 69 to Figure 71. The edges of the data correspond to: 0.5233°E (W); 0.6685°E (E); 50.6956°N (S); 50.7586°N (N).

Tidal axis vectors are uniform in direction across the site in the refined mesh model whereas there is some deflection of the tidal axis apparent in the coarser model, associated with the top of the bank. In detail, the crest of bed features (ripples and larger sand waves where present) are orientated perpendicular to the tidal axis.

Residual flow direction from the refined mesh results is generally from S or SSW to N or NNE. Vectors respond to the presence of the bank and are deflected to be orientated more perpendicular to the bank slope; as such, they seem to follow the orientation of linear sediment accumulation and hollow features on the bank slope, especially noticeable to the south of the dredging license area. Residual flow vectors do not seem to correspond to the orientation of other repetitive bed features (ripples or sand waves) but do provide a potential mechanism by which sediment in suspension might move from more abundant sources in deeper water to the south, up onto the bank.

Residual sediment transport vectors are similar to the tidal axis vectors in orientation and uniformity across the area. There is no evidence of strong deflection in residual sediment transport associated with the local bathymetry.

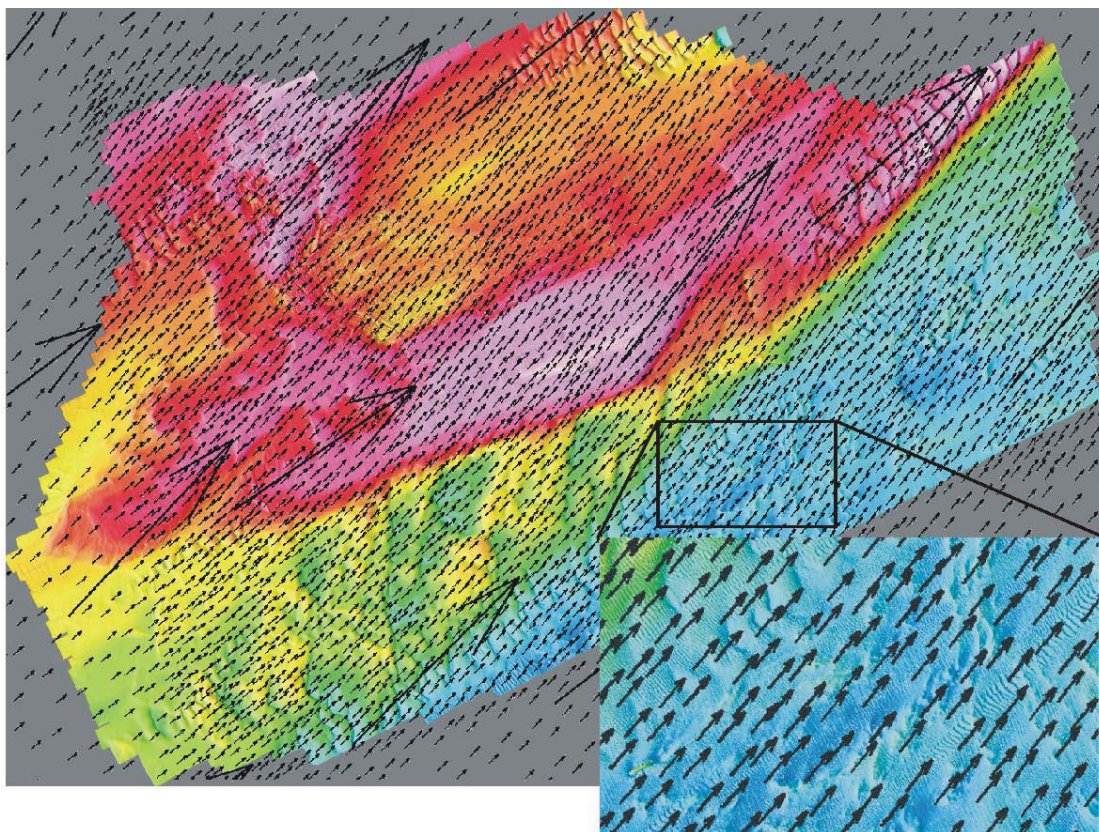


Figure 69. Orientation of the modelled tidal axis relative to multi beam swath bathymetry. Key: small arrows – data from the spatially refined model; large arrows – data from the medium resolution model. Bathymetry data courtesy of Hanson Aggregates Marine Ltd.

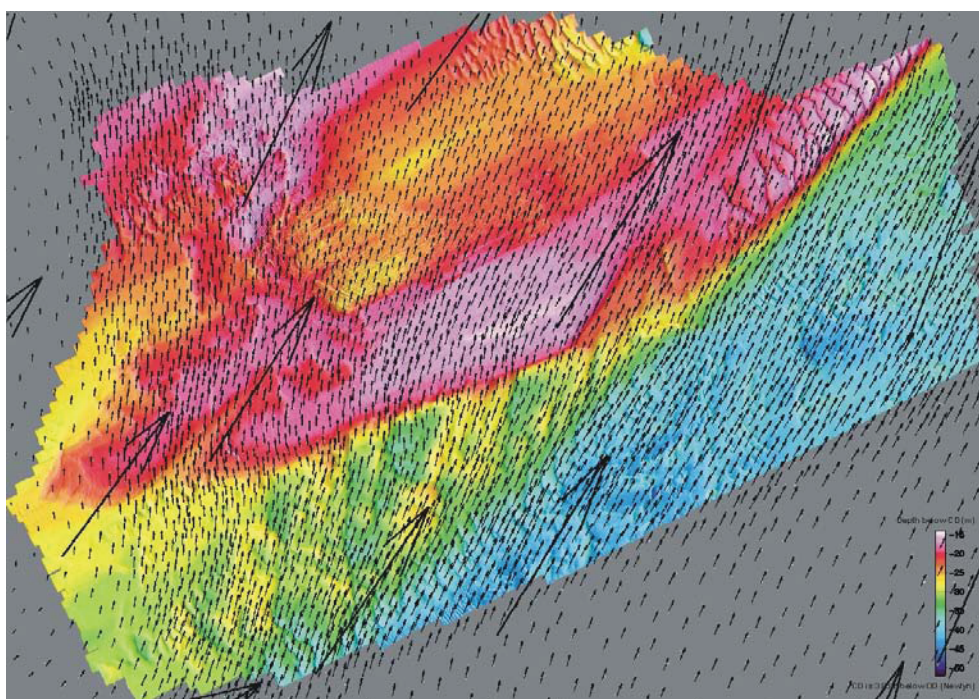
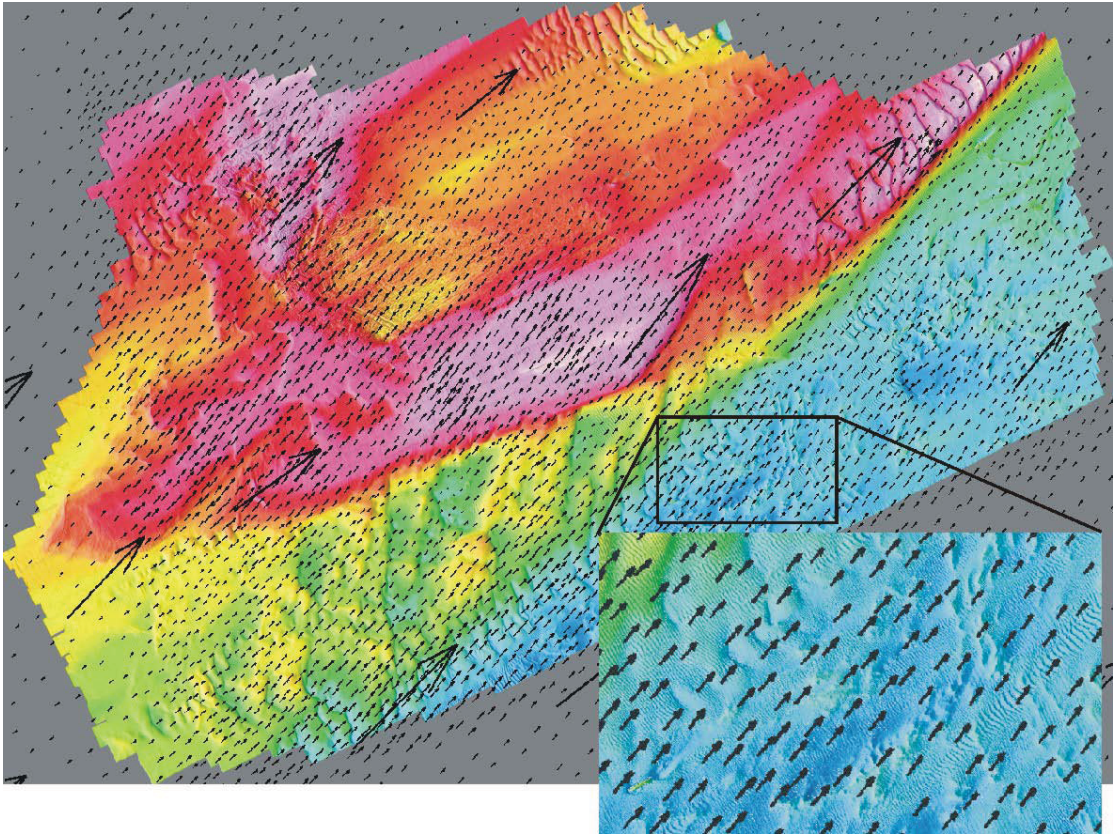
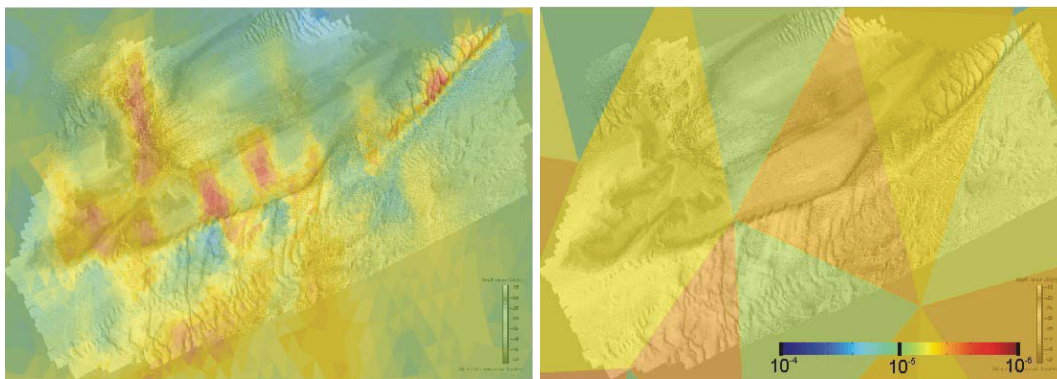


Figure 70. Orientation of residual current flow vectors relative to multi beam swath bathymetry. Key: small arrows – data from the spatially refined model; large arrows – data from the medium resolution model. Bathymetry data courtesy of Hanson Aggregates Marine Ltd.



**Figure 71. Orientation of residual sediment transport vectors relative to multi beam swath bathymetry. Key: small arrows – data from the spatially refined model; large arrows – data from the medium resolution model. Bathymetry data courtesy of Hanson Aggregates Marine Ltd.**

The spatial distribution of predicted mean absolute sediment transport and the predicted sediment transport asymmetry in relation to the bathymetry are shown in Figure 72 and Figure 73, respectively.



**Figure 72. Spatial variation of predicted mean absolute sediment transport ( $\text{m}^3 \text{m}^{-1} \text{s}^{-1}$ ) shown relative to multi beam swath bathymetry. Left – data from the spatially refined model; right – data from the medium resolution model. Bathymetry data courtesy of Hanson Aggregates Marine Ltd.**

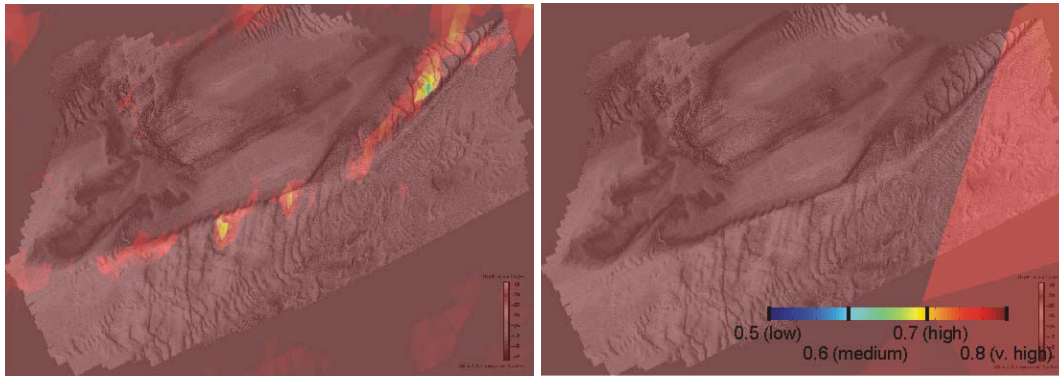


**Figure 73. Spatial variation of predicted sediment transport asymmetry shown relative to multi beam swath bathymetry. Left – data from the spatially refined model; right – data from the medium resolution model. Bathymetry data courtesy of Hanson Aggregates Marine Ltd.**

Sediment mobility is predicted to be: greatest on localised high points of the bank and along its southern slope; greater than average on the western slope of the bank and in the deeper water to the south and southeast; and, less than average in the deeper water to the north and northwest of the bank. Asymmetry of flow is predicted to be high in almost all areas by both model resolutions; the higher resolution model predicts that net sand accumulation on top of the bank is also associated with locally reduced transport asymmetry.

#### 4.3.1.3. *Comparison with predicted bed level change*

Local bed level change predicted by the model is compared here with the bathymetry of the Hastings Shingle Bank in terms of magnitude (m/6 months) in Figure 74 and in terms of sign (erosion or accumulation) in Figure 75.

In the refined model results, regions of greater bed level change are associated with the southern slope and upper plateau of the bank, similar in pattern to that observed for sediment mobility in previous Sections. The dredging license area was not associated with significant bed level change. Although banding patterns are apparent, there is no clear trend towards either bed lowering or accumulation over the bank as a whole; regions experiencing greater bed level change are typically but not always associated with bed lowering.

The coarse resolution model predicts bed level change of the same order of magnitude as the mean or typical result of the refined model but locally higher values in the refined model are obviously not resolved. Similarly for the type of bed level change, both net erosion and deposition are predicted over the region.

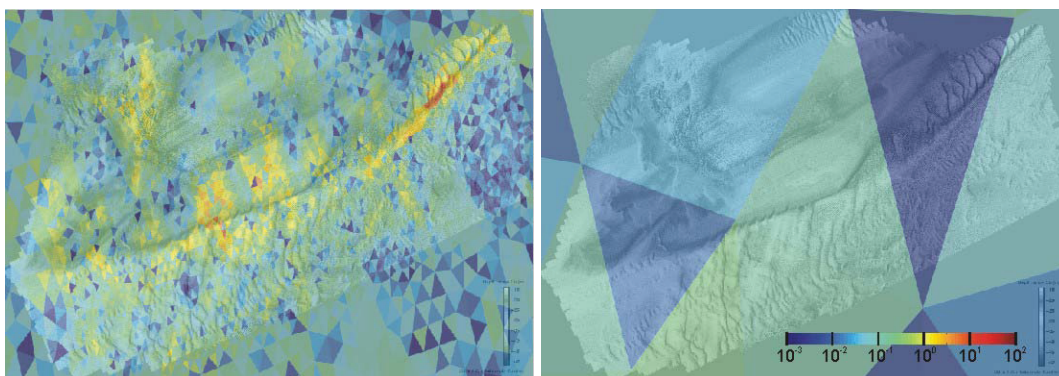


**Figure 74. Spatial variation of predicted bed level change magnitude (meters, based on 6 months of data) shown relative to multi beam swath bathymetry. Left – data from the spatially**

refined model; right – data from the medium resolution model. Bathymetry data courtesy of Hanson Aggregates Marine Ltd.

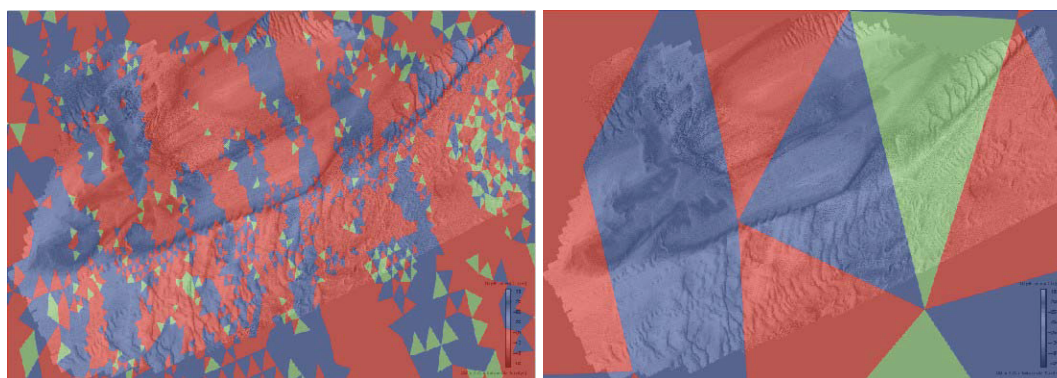


**Figure 75. Spatial variation of predicted bed level change type (Red – net accumulation; blue – net erosion; green – less than 5mm change per 6 months) shown relative to multi beam swath bathymetry. Left – data from the spatially refined model; right – data from the medium resolution model. Bathymetry data courtesy of Hanson Aggregates Marine Ltd.**

#### 4.3.1.4. Comparison with distribution of sediment grain size

A side scan sonar image of the same area as the bathymetry data coverage is shown in Figure 76 and another diagram showing mean grain size at selected locations is shown in Figure 77. The side scan tonal values may be interpreted at a basic level to indicate the roughness or mean grain size of surface seabed sediments; ground truthing of the high resolution and extensive swath is achieved using the more sparse but quantitative grab sample data. The majority of the region shown in the bathymetry data is relatively coarse (darker tones in the side scan, corresponding also to a larger mean grain size), with a mean surface sediment grain size between approximately 0.5-10mm. There is also a distinctive ribbon of finer sediment (lighter tones in the side scan, corresponding also to a smaller mean grain size) which corresponds to extensive sand waves, initially in the deeper water to the south of the bank, moving up the slope of the bank in the centre of the image and then on top of the bank towards the top right corner.

Grab samples of sediment were collected from the eastern tip of the dredging license area during the *Unknown Wreck* fieldwork in ALSF project 3365; results indicate that the sand fraction has a typical grain size of the order 0.2-0.3mm. Therefore, a larger mean gain size including all fractions indicates that gravel is present as a significant fraction of the bed material in areas of ‘coarse’ sediment.

Coarser seabed is spatially dominant and corresponds either to the area median or locally elevated sediment mobility.

The identified region of fine sediment accumulation is unusual as it is located on top of a local bathymetric high, despite being separated by the steep slope of the bank from the abundant sand found in deeper water to the south. Other large bodies of sand and sand wave fields are apparent in the image that are not apparently associated with transport conditions very different from the area mean values, but are more typically located in bathymetric low points where sediment might be expected to accumulate over very long time periods. The model results provide two types of information regarding how this feature might be controlled:

- Tidal axis and residual sediment transport vectors do not suggest that supply is occurring up the slope itself, but residual flow vectors suggest that suspended sediments may play a role over long time scales.

- Locally, this particular region also corresponds to relatively greater sediment mobility (greater mean absolute sediment transport), coinciding in some places with locally reduced transport asymmetry, all relative to typical conditions over the rest of the area.

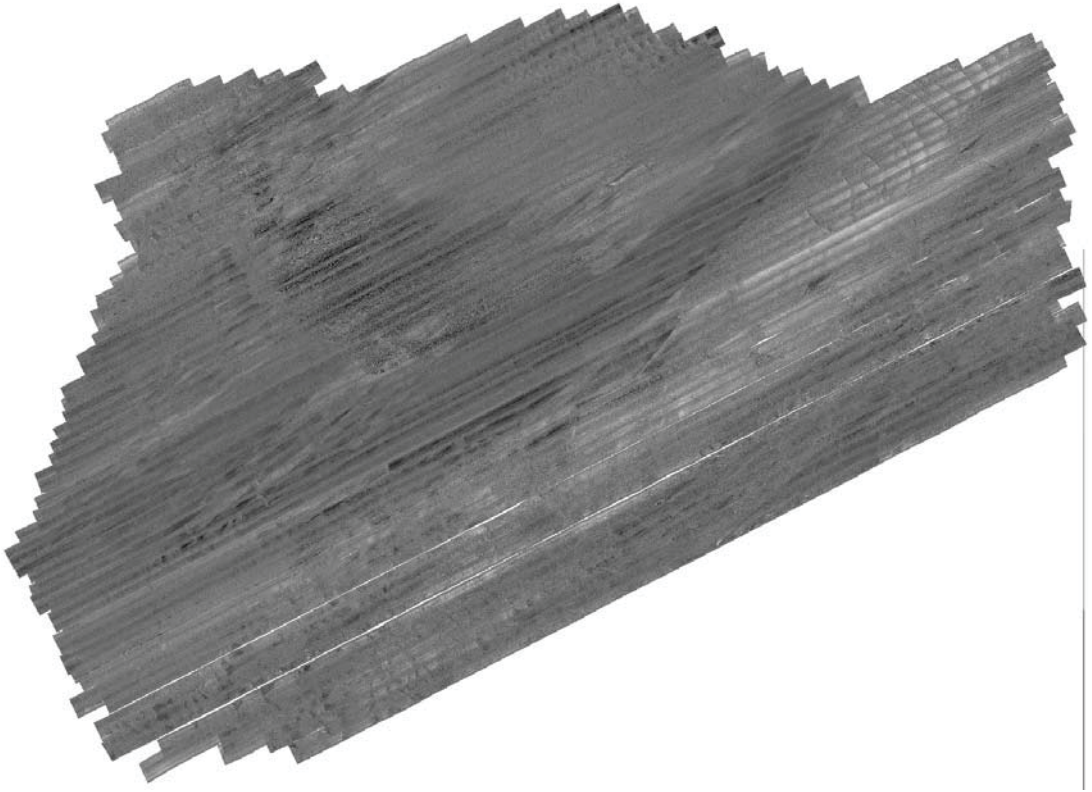


**Figure 76.** Side scan sonar mosaic of the Hastings Shingle Bank. Key: darker tones – coarser bed surface; lighter tones, smoother bed surface. Data courtesy of Hanson Aggregates Marine Ltd.

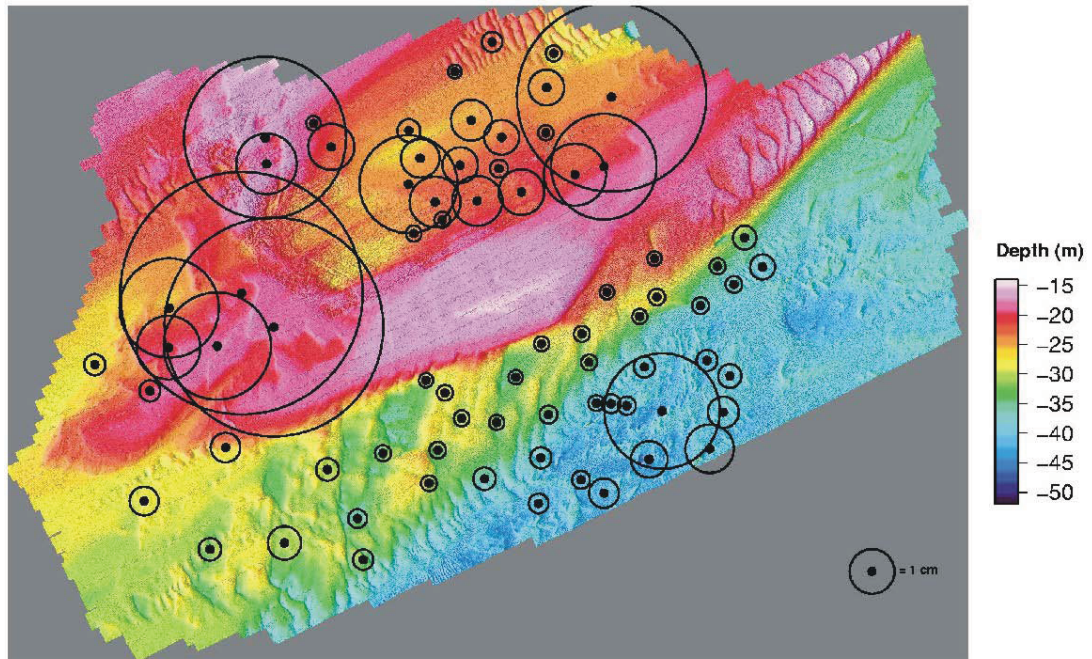


Figure 77. Mean grain size of surface sediments from grab samples over the Hastings Shingle Bank. Data courtesy of Hanson Aggregates Marine Ltd.

#### 4.3.2. Area 473E

Data available from the Area 473E license area at the time of writing only includes detailed multi-beam swath bathymetry.

##### 4.3.2.1. Comparison with regional bathymetry

Tidal axis orientation, tidal flow residual and residual sediment transport vectors are overlaid onto a multi-beam swath bathymetry image of the Area 473E license area region in Figure 78 to Figure 80.

The edges of the swath and model output data correspond to: 0.3870°E (W); 0.4668°E (E); 50.4819°N (S); 50.5161°N (N). The swath data contained significant data artefacts at the scale of typical bedforms and therefore the presence/absence and orientation of bedforms could not be established with confidence.

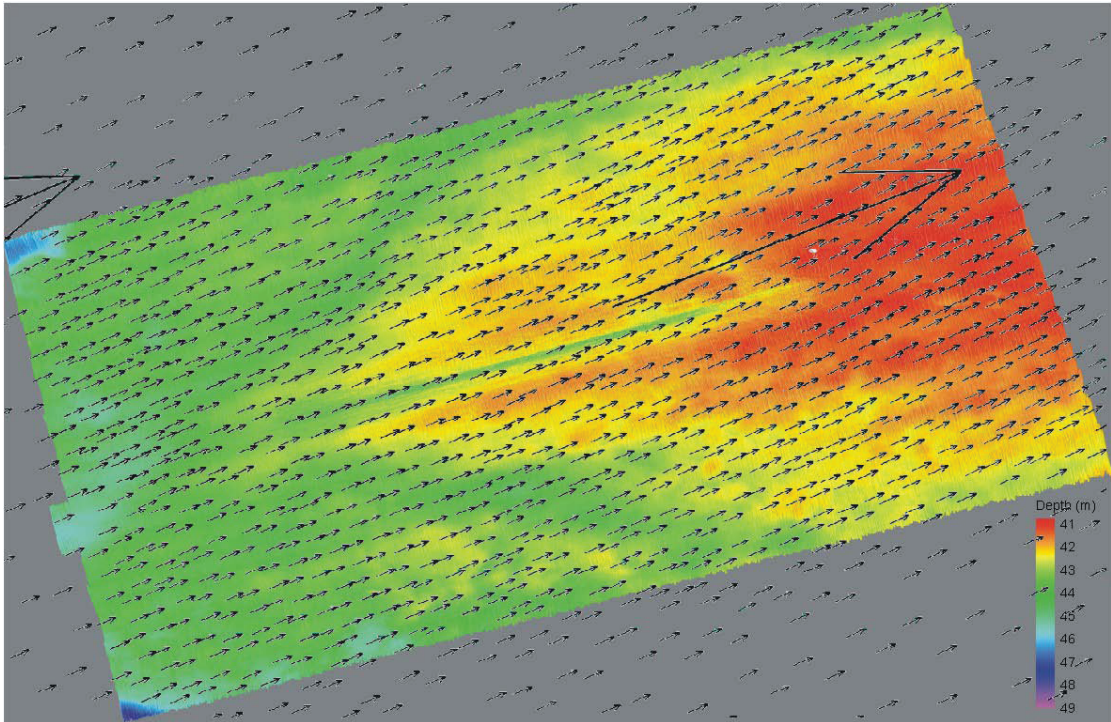


**Figure 78. Orientation of the modelled tidal axis relative to multi beam swath bathymetry. Key: small arrows – data from the spatially refined model; large arrows – data from the medium resolution model. Bathymetry data courtesy of Hanson Aggregates Marine Ltd.**

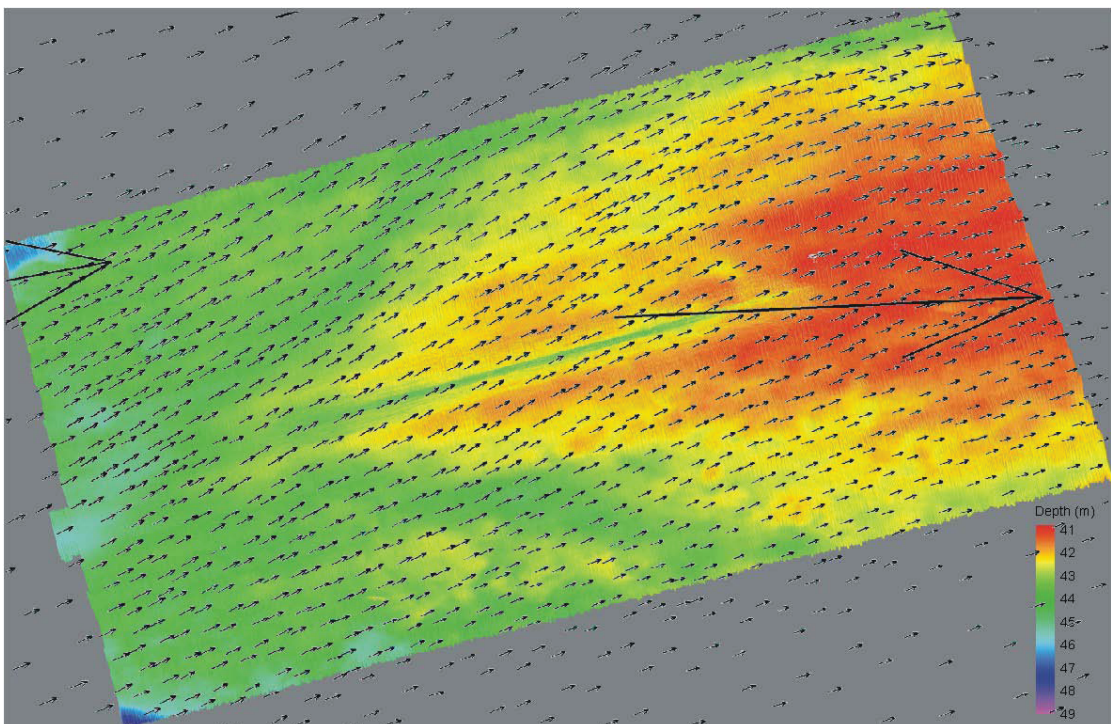


**Figure 79. Orientation of residual current flow vectors relative to multi beam swath bathymetry. Key: small arrows – data from the spatially refined model; large arrows – data from the medium resolution model. Bathymetry data courtesy of Hanson Aggregates Marine Ltd.**

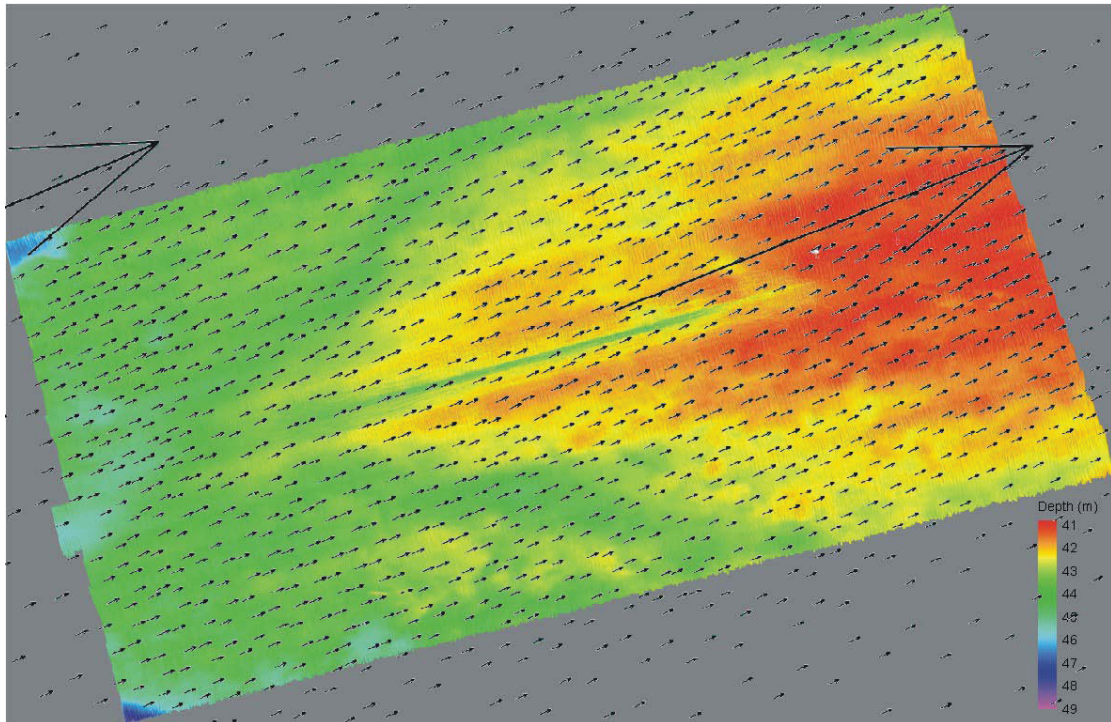


**Figure 80. Orientation of residual sediment transport vectors relative to multi beam swath bathymetry. Key: small arrows – data from the spatially refined model; large arrows – data from the medium resolution model. Bathymetry data courtesy of Hanson Aggregates Marine Ltd.**

Tidal axis vectors are uniform in direction across the site in the results from both models; the coarser model is uniform by the fact that the whole subdomain is contained in only one element and therefore has only a single result value.

Residual flow direction from the refined mesh results is generally from WSW to ENE or E. Vectors respond to the presence of the locally higher bathymetric feature and are deflected slightly in order to follow its contours around its northern side.

Residual sediment transport vectors are similar to the tidal axis vectors in orientation and uniformity across the area. There is no evidence of strong deflection in residual sediment transport associated with the local bathymetry.

The spatial distribution of predicted mean absolute sediment transport and the predicted sediment transport asymmetry in relation to the bathymetry are shown in Figure 81 and Figure 82, respectively.

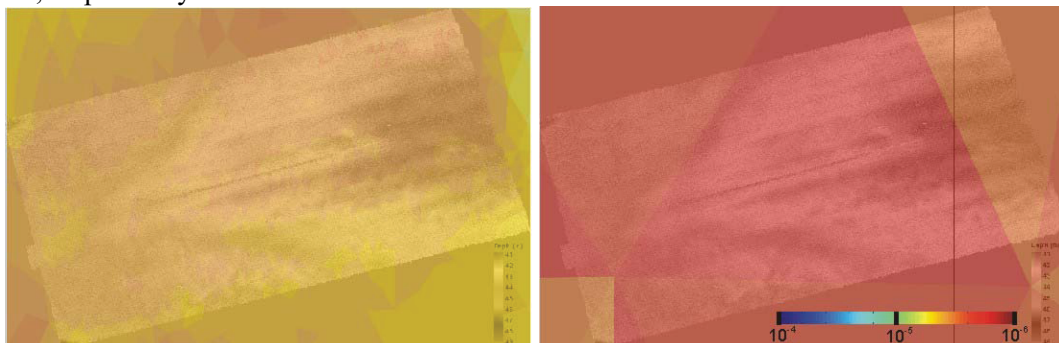


**Figure 81. Spatial variation of predicted mean absolute sediment transport ( $\text{m}^3 \text{m}^{-1} \text{s}^{-1}$ ) shown relative to multi beam swath bathymetry. Left – data from the spatially refined model; right – data from the medium resolution model. Bathymetry data courtesy of Hanson Aggregates Marine Ltd.**

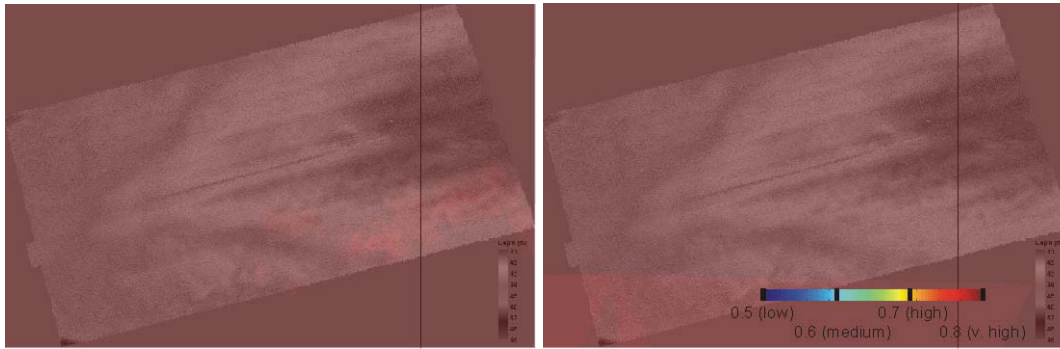


**Figure 82. Spatial variation of predicted sediment transport asymmetry shown relative to multi beam swath bathymetry. Left – data from the spatially refined model; right – data from the medium resolution model. Bathymetry data courtesy of Hanson Aggregates Marine Ltd.**

Examining firstly the results of the refined resolution model, sediment mobility is predicted to be relatively greater over and to the north of the bathymetric high; transport asymmetry is almost uniformly high except for a slight relative reduction on the southern slope of the high point. In comparison, the coarse mesh model covers almost the entire subdomain with a single element. Sediment mobility is predicted to be greater (approximately factor 2) by the coarse resolution model but asymmetry values are similarly high.

#### 4.3.2.2. *Comparison with predicted bed level change*

Local bed level change predicted by the model is compared here with the bathymetry of the Area 473E dredging license area in terms of magnitude (m/6 months) in Figure 83 and in terms of sign (erosion or accumulation) in Figure 84.

The magnitude of bed level change over the area is uniformly low in the refined model and the same order of magnitude in the coarser resolution model. The direction of bed level change is spatially variable but the median value within the license area is for bed erosion, tending towards accumulation at the edges. This is also reflected generally in the coarser resolution data.

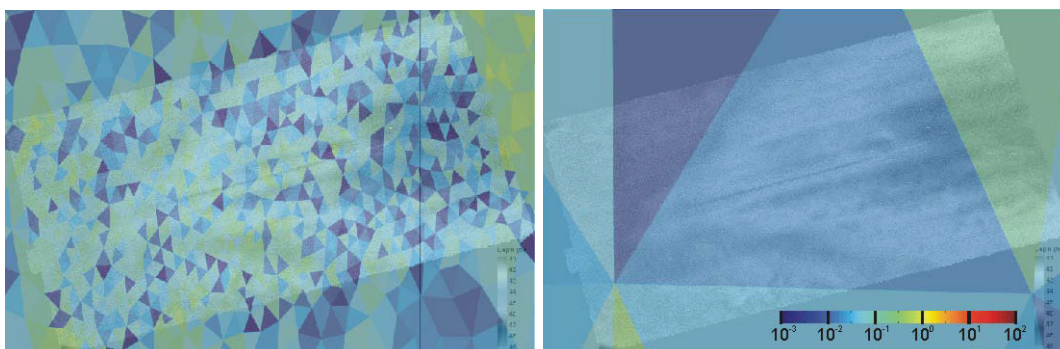


**Figure 83. Spatial variation of predicted bed level change magnitude (meters, based on 6 months of data) shown relative to multi beam swath bathymetry. Left – data from the spatially refined model; right – data from the medium resolution model. Bathymetry data courtesy of Hanson Aggregates Marine Ltd.**

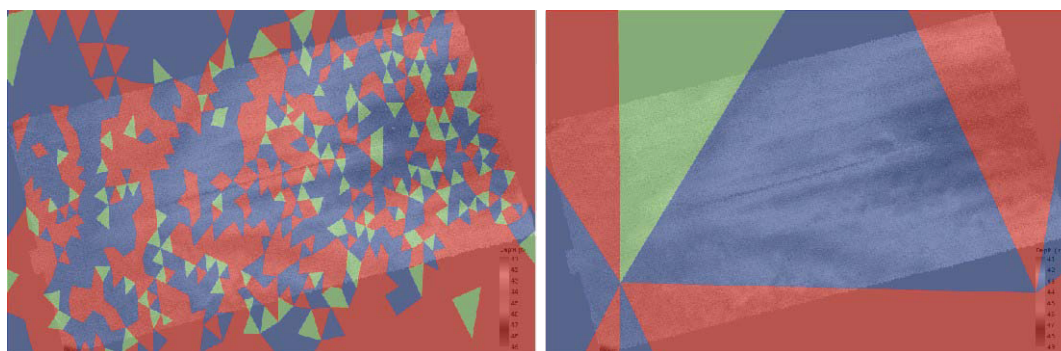


**Figure 84. Spatial variation of predicted bed level change type (Red – net accumulation; blue – net erosion; green – less than 5mm change per 6 months) shown relative to multi beam swath bathymetry. Left – data from the spatially refined model; right – data from the medium resolution model. Bathymetry data courtesy of Hanson Aggregates Marine Ltd.**

### 4.3.3. Summary

The results of the refined models are summarised below:

*At the Hastings Shingle Bank:*

- The proportion of sand in surface sediments is inversely related to the predicted local sediment mobility.
- Transport asymmetry or spatial gradients in transport asymmetry are potentially associated with local sediment (sand) accumulation.
- The crest orientation of tidally induced bed features (ripples and sand waves where present) are perpendicular to both the tidal axis and to the direction of residual sediment transport. (N.B. tidal axis orientation and residual transport vectors are not always parallel in other parts of the English Channel model results – it is more likely that smaller bedforms will align to the tidal axis whereas larger bed features will become more aligned to the residual sediment transport direction).

*At Area 473E:*

- The tidal axis and residual sediment transport direction are apparently unaffected by the local bathymetry; however, residual tidal flow is slightly deflected.
- There is uniform (medium to high) relative potential for sediment transport over the region with a strong degree of asymmetry in the residual transport direction.
- There is no strong tendency towards bed level change in this region.

When describing the orientation of tidal axis, residual flow and residual sediment transport vectors, the coarser models represented the mean orientation of the refined model closely. When describing sediment mobility, asymmetry and bed level change, the coarser resolution models represented the mean results of the higher resolution models well, with the exception of sediment mobility at 473E where the mean value was over predicted by the coarse model.

If a broad scale impression of tidal patterns or sediment mobility is required for large areas, then the results from a coarse resolution model may suffice. However, during site specific or even regional scale work (e.g. during environmental or archaeological assessments), the detail may be important as it may have local implications for a particular

wreck site or habitat identified and located within the area. The degree to which detailed patterns may differ from those obtained at a coarser resolution are site specific. In the case of Area 473E, the flat relief of the bathymetry induces uniformity of flow and transport over the site; the site is then equally well characterised by models of different resolution. The more complex, sudden relief of the Hastings Shingle Bank produces greater local detail in the results which is not adequately resolved by the coarser model. It is not possible, on the basis of these results, to specify when a higher resolution is or is not required and therefore a relatively high resolution modelling approach to any new area is recommended.

## **5. Distribution and variability of regional scale sediment mobility.**

### **5.1 Distribution of present day sediment transport patterns**

Because the published maps of sediment properties (including grain size distribution, sorting and layer thickness) are not consistent in format and typically not very high in resolution, it was not possible to assign a threshold value of residual sediment transport that corresponds to the boundary between the presence or absence of present significant sand deposits. None of the results give reason to doubt the projected eventual distribution of sandy, gravelly and muddy deposits, previously published by Johnson *et al.* (1982).

The local strength of residual sediment transport potential is a function of local sediment mobility and transport asymmetry. The relative contributions of sediment mobility and transport asymmetry to the residual sediment transport potential vary throughout the domain. The whole domain is subdivided and characterised in relative terms of these parameters in Table 6 and Figure 85; the same analysis is applied to the zone between 5 and 20km from the English coastline in Table 7 and Figure 85. It is important to emphasise again that the model does not account for wave action which is known to have a measurable effect in shallow, near coastal waters; hence, the interpretations below exclude model results less than 5km from the coast. The implications to archaeological sites of particular combinations of high/low sediment mobility and high/low transport asymmetry are discussed further in Section 6.

<b>Area</b>	<b>Ref</b>	<b>Sediment mobility</b>	<b>Transport asymmetry</b>
Western approaches to the English Channel	A	LOW	LOW
Western English Channel	B	LOW-MED	MED
Channel Islands and adjacent coast	C	MED-HIGH	HIGH
Central English Channel	D	HIGH	LOW
Eastern English Channel	E	LOW-MED	HIGH
Southern approaches to Dover Straits	F	LOW-MED	LOW
Dover Straits and northern approaches, Thames estuary	G	MED-HIGH	LOW-MED
Southern North Sea	H	MED	LOW
Adjacent to French, Belgian and Dutch coastlines.	I	MED	HIGH

**Table 6. Relative magnitude of potential sediment mobility and transport asymmetry offshore in the English Channel and southern North Sea.**

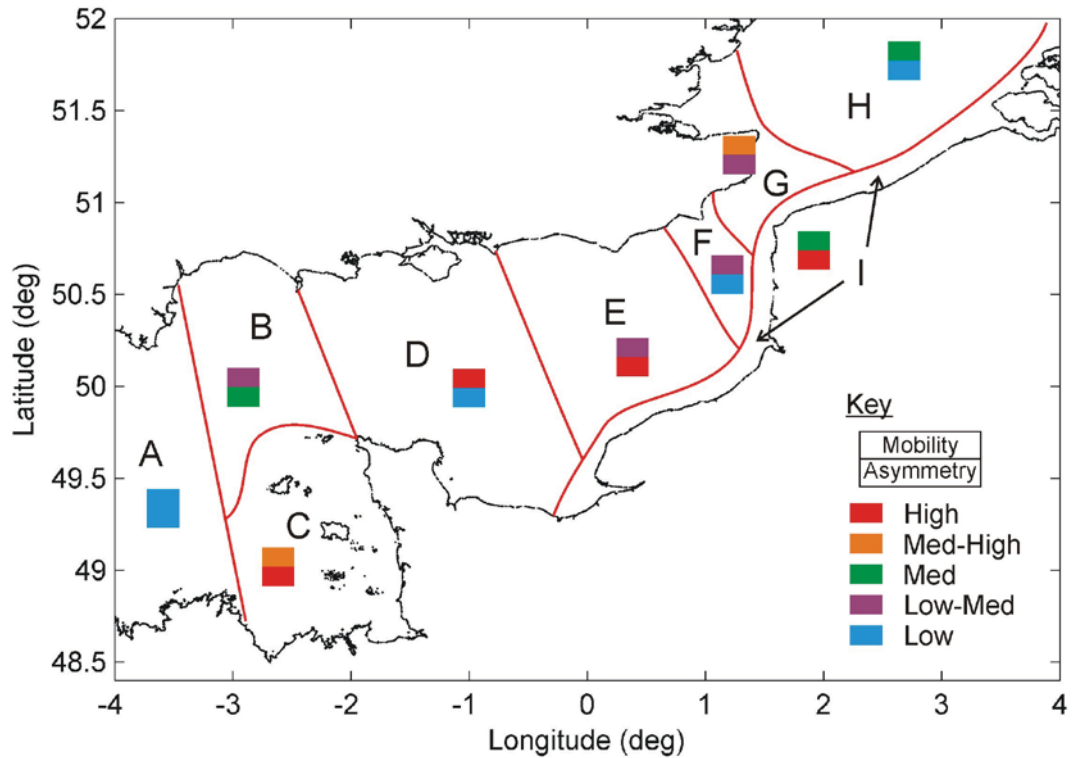
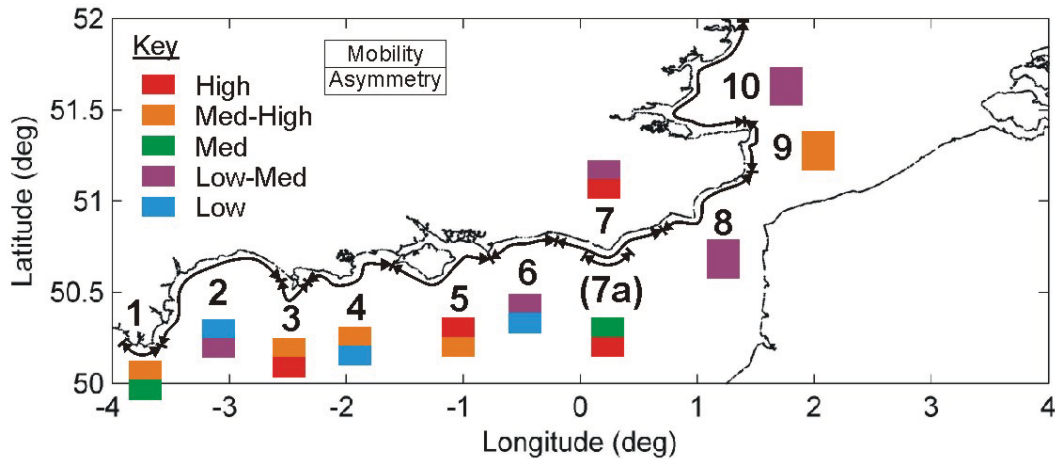


Figure 85. Relative magnitude of potential sediment mobility and transport asymmetry offshore in the English Channel and southern North Sea. See text and Table 6 for more details.

Area	Ref	Sediment mobility	Transport asymmetry
Start Point headland	1	MED	HIGH
Lyme Bay	2	LOW	LOW-MED
Portland Bill	3	MED-HIGH	HIGH
Weymouth to the Needles	4	MED-HIGH	LOW
Isle of Wight	5	HIGH	MED-HIGH
Selsey Bill to Shoreham	6	LOW-MED	LOW
Shoreham to Hastings	7	LOW-MED	HIGH
(Beachy Head)	(7a)	MED	HIGH
Hastings to Dover	8	LOW-MED	LOW-MED
Dover to Margate	9	MED-HIGH	MED-HIGH
Margate to Harwich	10	LOW-MED	LOW-MED

Table 7. Relative magnitude of potential sediment mobility and transport asymmetry near (5-20km from) the British coast of the English Channel and southern North Sea.



**Figure 86. Relative magnitude of potential sediment mobility and transport asymmetry near (5-20km from) the British coast of the English Channel and southern North Sea. See text and Table 7 for more details.**

The distribution of large sand bodies (sand waves or sheets), obtained through analysis of geophysical or other field data, has been reported in the literature (e.g. Johnson *et al.*, 1982; Evans, 1990; Cameron *et al.*, 1992; Hamblin *et al.*, 1992). A visual comparison between the results of the different analyses and the distribution of sand bodies is made in Figure 87, where it is shown that accumulations correspond to certain features or gradients in the results. The Figure shows that:

- Sand bodies in the western Channel are associated with regions of low sediment mobility; the boundary is delimited by the transition from high to low sediment mobility and the resulting convergent transport gradient.
- Sand bodies in the vicinity of the Channel Islands are associated with regions of locally reduced sediment mobility and low transport asymmetry. From Figure 54, these regions also correspond to shear or divergence in the residual transport direction.
- Sand bodies offshore between Selsey Bill and Beachy Head are associated with locally reduced sediment mobility.
- Sand bodies along the French coast between Cherbourg and Dieppe in the eastern Channel are associated with medium sediment mobility, i.e. less than that found to the north in the central Channel, but higher than that found further south in the Le Havre estuary.
- The width of the sand body is reduced locally around Dieppe. This is associated with a local increase in sediment mobility and a local divergence in transport.
- The width of the sand body then increases towards the Dover Straits, eventually spanning the full width of the Channel to the vicinity of Dungeness Headland. This region is associated with strong convergence of sediment transport and lower sediment mobility.
- Widespread sand bodies are present in the southern North Sea but are absent in a local region, north of Margate, at the entrance to the Thames Estuary. This is associated with a similarly localised region of increased transport asymmetry but reduced transport magnitude, which is then not apparent in the residual transport field.

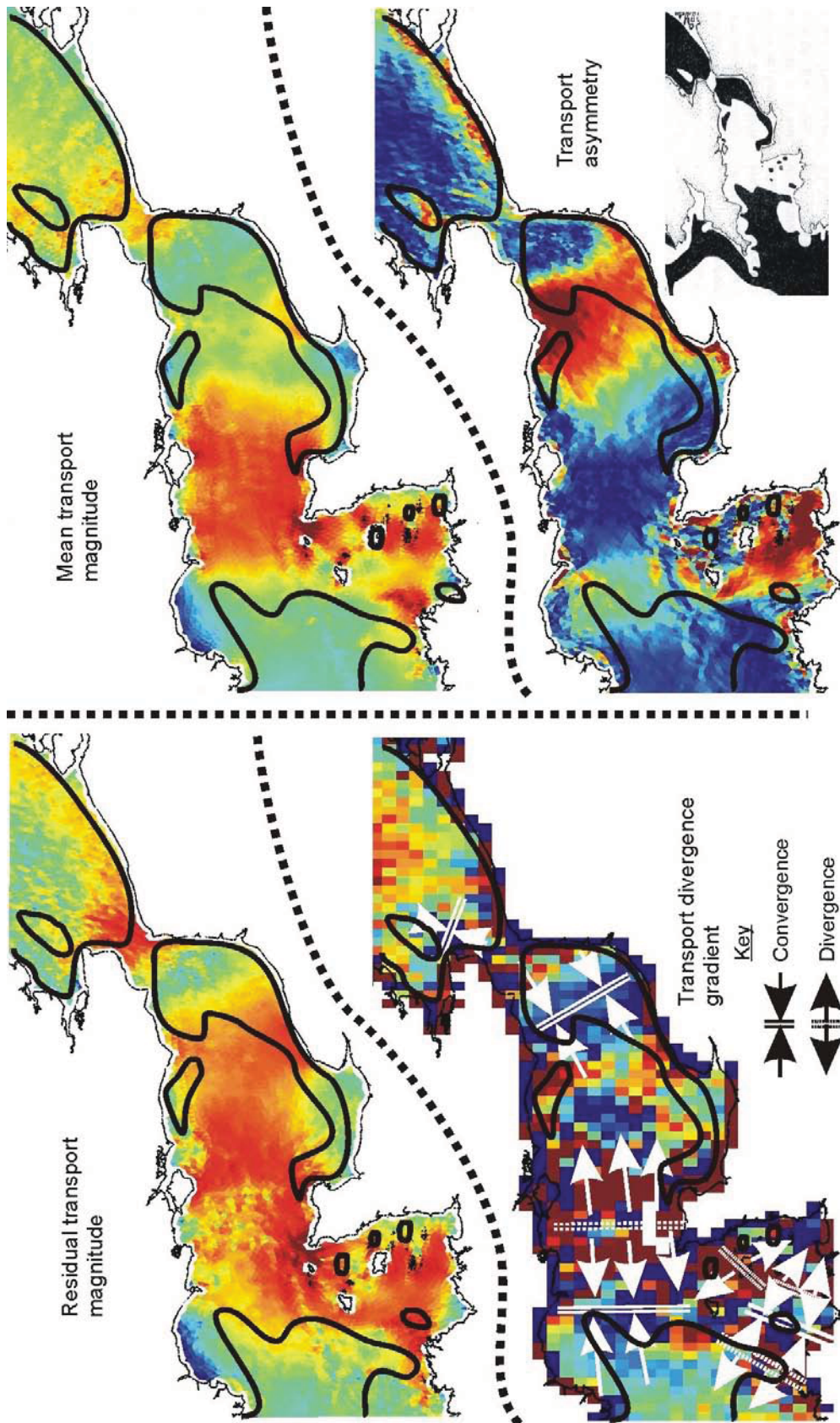


Figure 87. Various sediment transport indicators (for 200µm sand) compared with the distribution of bodies of significant sand accumulation in the English Channel and southern North Sea according to (black line, see insert bottom right) Beck *et al.* (1991), after Johnson *et al.* (1981). Key to magnitudes and asymmetry: (red – largest, green – intermediate, blue – smallest). Key to divergence: (red – divergence, green – even, blue – convergence).

Observations such as these simply relate observed sand distribution (or absence) to patterns in the modelled data. However, the particular combinations of transport magnitude, asymmetry and spatial gradients vary within the domain; there is no single condition (e.g. a threshold value of a single parameter) that describes the resulting sand distribution entirely.

There is presently insufficient field data resolution and accuracy to quantitatively express the combination of predicted conditions that will lead to actual long term sedimentary accumulation or erosion. Without this data the models cannot be fully calibrated or utilise their full predictive potential. Higher resolution data is required for the whole of the English Channel, including: bathymetry for nested model studies; detailed sediment parameter (size, sorting) distribution data; and isopach (sediment layer thickness) maps. Additional current meter and tidal gauge data from offshore in the English Channel are also required. These would allow more robust sensitivity testing and calibration to be undertaken, and would take the present study forward from a more circumstantial [observation vs. model result] interpretive approach, to a more quantitative, process driven approach to the problem.

## **5.2 Predicting regions likely to experience future changes in local sediment mobility and/or transport asymmetry**

It is known that purely tidal forcing varies most significantly on timescales of hours (semi-diurnal), weeks (spring-neap), months (equinoxal) and years (18.6 year Metonic cycles). The resulting magnitude of tidal currents, relative sediment mobility and asymmetry also then vary on those same timescales. Meteorological effects (wind stress, storm surges, etc) may add other significant spatially and temporally variable forcing.

The numerical model boundary inputs contain variability in tidal forcing only on timescales less than one year (the 18.6 year cycle is not accounted for) so no additional information can be gained by modelling for more than one year. The model used in the present study does not represent meteorological effects at all. The implications of this are that model results of potential sediment mobility or the strength of transport asymmetry will vary on the sub-annual timescales listed above, but not on annual or greater timescales. However, it has also been shown that the predicted directions and relative magnitude of mobility and asymmetry will be consistent when analysed over spring-neap cycle timescales or longer (with an associated reduction in accuracy if less than 1 year of data is used). Therefore, no long term change (on annual, decadal or longer timescales) is predicted by the model in the residual or mean patterns of sediment mobility and transport.

In the absence of single point observed data sets of 6 months (equinoxal cycles) or longer, it is not possible to say with any confidence what the changes in observed sediment mobility or transport asymmetry are over these longer timescales. There are also issues during data collection (single point versus profiling devices to obtain depth mean values; absolute accuracy of the device; and non-tidal meteorological effects) which affect the detail of the observed results which may in turn significantly affect variability of long term observed, and comparability with predicted, residual patterns.

## **5.3 Predicting regions likely to experience future net bed level change**

A number of conditions must be met conceptually in order to predict the likely occurrence of net local sediment accumulation or erosion:

## Chapter 5. Implications of the model results for regional scale sediment mobility.

### Requirements for local sediment accumulation

1. Sediment is present outside the local region.
2. The flow conditions and bed configuration (e.g. presence of bed armouring) are such that the sediment fraction in question is potentially mobile.
3. The net transport conditions are such that sediment will be transported from a source area into the deposit area.
4. The potential entry flux of sediment to the area is greater than the potential exit flux.

### Requirements for local sediment erosion

1. Sediment is present inside the region.
2. The flow conditions and bed configuration (e.g. armouring and sediment layer thickness) are such that the sediment fraction in question is potentially mobile and the thickness of potentially mobile sediment is significant.
3. The net transport conditions are such that sediment will be transported from the source area.
4. The potential exit flux of sediment to the area is greater than the potential entry flux.

Conditions 3 and 4 may be assessed for a given location or region using the results of the present study, with an associated degree of certainty. Results can be informative at a variety of spatial resolutions and the most appropriate choice of resolution depends on the spatial and temporal scale of the question being asked, e.g. information about the 'long term sediment transport trends in the eastern Channel' can be assessed using a coarse resolution model, whereas more specific information about 'local sediment transport conditions around wreck site X and the adjacent dredging license area' requires a higher resolution.

Sediment accumulation cannot occur if there is no (mobile) sediment available to move into an area; likewise, net erosion cannot occur if there is no (mobile) sediment present at the site in question. Therefore, whether conditions 1 and 2 are met is crucial, however, this is typically difficult to establish. The accurate assessment of the presence of sediment, its thickness and its potential mobility (described by the local grain size distribution, potential for bed armouring, etc.) is difficult at large scales because of the cost and difficulty of measuring, obtaining and representing such data at an appropriate scale, spatial resolution and detail. At smaller scales, data may become available as the result of regional or site specific investigation, e.g. in preparation for a dredging license application or during site assessment works for dredging or other marine engineering projects.

The distribution of regions in the English Channel experiencing significant sand accumulation or conversely, regions now devoid of significant quantities of fine sediment has been shown to be controlled by large scale spatial patterns and gradients of sediment mobility and asymmetry in Figure 87 and the associated text. The same principles have been shown to apply to regional and local scale processes in the site specific investigation of the Hastings Shingle Bank in Section 4.3.1. Although not simple, these observations provide a set of criteria by which to identify areas particularly likely to experience on going net bed level change. More work is however needed to understand the combination of values that correspond to the locations of present day sediment sink areas and to identify regions within these that are likely to experience further net sediment gain or loss.

Predictions of long term bed level change must also be made in the context of the fact that there are very few areas of the channel reported to be experiencing active or rapid bed level change. Returning to the conceptual list of conditions above, this could be due to locally limited availability of mobile sediment (only rock or gravels remain) or conversely,

insufficient tidal energy to mobilise local sediments, or immobility of sediment due to armouring. The model might accurately predict this condition if the distribution of sediment was correctly represented in great detail; however, as described above, obtaining this data presents many difficulties.

Areas known to be experiencing significant bed level change on larger scales typically include large offshore sand bank systems. Here, sediment is accumulated over long time periods due to large scale tidal current and sediment transport patterns which should be reflected in the model. Sediment volume in the bank is relatively constant on shorter timescales but may be redistributed, causing local bed level change, in response to storms and other periodic wave events interacting through the locally shallower water depths. Periodic wave action has not been included in this version of the model but its role in sandbank morphology is the subject of previous numerical modelling studies, e.g. Jones (2007) and the references contained therein. Anecdotal evidence from repeated exposure and coverage of the Sterling Castle shipwreck on the Goodwin Sands suggests that sediment redistribution can lead to a variation in bed level in the order  $\pm 2-3\text{m}$  about a mean level. In near shore areas where wave action is also more important, seasonal cross shore sand transport can lead to the formation and removal of near shore bars in the order of metres in height, a local form of bed level change on inter-annual timescales.

Where sediment supply is adequate, bed level change may be observed on smaller scales as bedforms, including ripples, dunes and sand waves (moving undulations in the seabed level). These local vertical fluctuations are a deviation from a mean bed level and are not resolved in the model of the present study. A much higher spatial resolution vertically resolved (3D) model would be required and only relatively small areas (10s-100s of metres<sup>2</sup>) could be sensibly modelled with present computing power.

## **6. Desktop evaluation of the impact to archaeological sites caused by changes in local sediment mobility.**

The results of the numerical modelling presented in earlier chapters provide an estimate of the degree of sediment mobility (where sediment is present) and the direction and asymmetry of subsequent transport. These patterns, in conjunction with the existing sediment distribution, represent the naturally occurring sediment transport with which any archaeological sites are in equilibrium. If patterns are changed, then the equilibrium state of the wreck site may change, with potentially positive or negative implications for wreck conservation and the dispersal of artefacts. Such changes might occur naturally on a variety of time scales; they may also occur in response to anthropogenic activities (potentially by e.g. marine aggregate dredging, offshore and coastal engineering, etc) either due to an effect on the flow itself or by changing the quantity of sediment available for transport locally.

The following conceptual study tries to anticipate the probable impact of altering the spatial patterning of sediment mobility and the potential effects of gross changes to the mean seabed level, on the seabed and any archaeological sites thereon.

### **6.1 Changes to the seabed potentially caused by marine aggregate dredging**

#### **6.1.1. Gravel extraction**

In areas targeted for gravel extraction, the seabed typically consists of mixed sand and gravel with a particularly high proportion of the latter. The most likely natural condition of the seabed in this case will be for mobile sediment at the sediment-water interface to be winnowed away, leaving a coarser, less mobile ‘armouring’ layer. The remaining finer, potentially mobile sediments below this layer can not interact with agents of erosion and transport and are therefore effectively immobilised. Mobile sediment transport may continue to occur in the form of a sandy veneer if there is an input of mobile sediment from outside the area.

Whilst dredging for gravel, the thickness of any armoured layer is reduced, previously buried finer sediments are brought closer to the sediment-water interface and made available for transport. This occurs through a number of processes, including:

- Mechanical removal of the armoured layer and direct exposure of mobile sediment rich sub-strata by all types of dredging process.
- Mechanical overturning of stratified near-surface sediment layers by the moving drag head in the case of trailer hopper suction dredging.
- Settlement of fine grained sediment put into suspension by the all types of dredging process at the seabed.
- Settlement of fine grained sediment returned to the water column via the dredge plume following onboard screening and loss of overspill.

Together, these processes increase the volume of potentially mobile sediment locally available for transport. Studies (e.g. those summarised in Dix *et al.* 2007 and the references contained therein) show that the majority volume of potentially mobile sediments placed onto

the seabed surface by aggregate dredging are initially deposited within a relatively small distance (order of decimetres) from the site of dredging. The supply rate of potentially mobile sediment varies according to the frequency of dredging, the character and thickness of the local sediment strata, the depth of water, the state of the tide at the time of dredging and the dredging method employed. Following re-deposition, sediment will be transported according to the transport potential for its grain size.

Local supply and subsequent transport of potentially mobile sediment through marine aggregate dredging occurs in addition to any background sediment flux originating from outside the affected area. If the background sediment flux is small and the local supply is large, then the local mode of transport may change (i.e. from transport as dispersed grains or sand ribbons to transport as sand sheets with bedforms), increasing the overall mobility and rate of transport of this sediment. If the contribution from local supply is small relative to the background flux, then the transport character and mobility of sediment may be unaffected but the overall flux may increase. Such changes in bed character and sediment mobility are linked to the relative variability and magnitude of both background flux and local supply which are both spatially and temporally variable.

Following cessation of dredging at a license area or even in a particular lane of a license area, any additional mobile sediment placed on the nearby seabed will be transported at the rate and in the direction of residual transport which may be orientated with the tidal axis over sub-spring-neap cycle timescales or at another rate and direction over longer time periods. If the long term residual transport rate is significant, then the additional sediment will be removed from the area in a net sense over time, asymptotically returning to background conditions. If the local supply is significant in volume compared to background fluxes, additional sediment will be present as a 'pulse' in the local sediment transport budget as it is moved. The duration of the pulse will likely increase but its magnitude decrease, with distance and time from the point of origin, due to dispersal.

If the remaining seabed is sufficiently gravel rich, bed armouring should naturally redevelop at the expense of further sand loss at the seabed surface (an additional source of mobile sediment following the cessation of dredging). However, if dredging has removed enough of or all sediment containing coarse armouring material and only finer, mobile sediments remain, then the seabed will continue to erode, supplying sediment to the residual transport pathway until an equilibrium is reached between the hydrodynamic conditions and seabed mobility.

### **6.1.2. Sand extraction**

In areas suited to dredging for sand, the naturally present sediment is typically relatively fine, hence mobile. Well sorted sands do not tend to form strongly armoured layers although slight armouring may occur if the hydrodynamic environment is not capable of transporting a significant proportion of the grain size distribution. Sand may become more resistant to erosion over time following initial deposition as individual grains become more closely packed in the sand-water matrix of the bed; individual grains in the matrix may also become bonded either by chemical reaction or precipitation or by organic compounds secreted by sediment infauna and epifauna.

Sandbank systems are a typical source of sand for dredging and are inherently mobile and dynamic in their morphology. The act of dredging in already uniformly sandy areas will not significantly change the grain size distribution of surface seabed sediments but may cause disturbance of the sediment and possibly change its transport characteristics through the following processes:

- Mechanical removal of any stabilised surface layers, e.g. by close packing, biological or chemical bonding or low-level armouring by larger sand grains.

## Chapter 6. Desktop evaluation of the impact to archaeological sites caused by changes in local sediment mobility.

- Mechanical overturning of stratified near-surface sediment layers by the moving drag head in the case of trailer hopper suction dredging, increasing the porosity of the sediment and its susceptibility to erosion.
- Settlement of fine grained sediment put into suspension by the all types of dredging process at the seabed or via the dredge plume following loss of overspill, increasing the porosity of surface sediment and its susceptibility to erosion.
- Modification of the local bathymetry, causing a local change in the interaction between the bed and tidal or wave forcing, with implications for local sediment mobility and transport direction.

The significance of any local effect on potential sediment mobility and transport direction by dredging should be measured in comparison to the natural range and variability in local bed level, slope angle and orientation, seabed character, etc, which may be large, observed over the rest of the sand body. The timescale required for bed readjustment to a 'natural' state is also likely to be less than that for a gravel rich site.

### **6.2 The potential impact of regional scale net seabed erosion/accretion on archaeological sites**

Adjustments to background levels of sediment transport or to the mean bed level in an area containing an archaeological site will have implications for the relative, long term exposure of the site.

Patterns of local sediment accumulation and erosion that develop around three-dimensional objects proud of the seabed (e.g. shipwrecks) in tidally dominated environments are described in Dix *et al.* (2007 'Modelling Exclusion Zones for Marine Aggregate Dredging', ALSF report 3365). Key observations include:

- As the tide flows over and around three dimensional obstacles on the seabed, predictable and highly localised regions of flow develop with increased potential to cause erosion (principally associated with elevated turbulence) or increased potential to cause deposition (principally associated with reduced mean current speed).
- If the obstacle is located upon a potentially mobile sedimentary bed, these regions are manifest as regions of net sediment erosion (scour) or as regions of net sediment accumulation.
- The extent and depth/height of the resulting sedimentary features is controlled largely by the height of the obstacle above the seabed.
- The depth/height of the resulting sedimentary features is controlled by the height of the obstacle above the seabed and the erosion potential of the sediment (in particular, the potential for development of armoured layers limiting the depth of scoured regions).
- The degree of lateral symmetry (across the tidal axis) in the morphological response and also the extent of sedimentary features (to a lesser degree) are controlled by the orientation of the obstacle to the flow.
- The degree of axial symmetry (along the tidal axis, upstream and downstream of the obstacle) in the morphological response is controlled by the relative symmetry of the local residual sediment transport.
- For each site, there will be an equilibrium maximum depth of scour (a complex function of the obstacle dimensions and orientation, the current speed and the

Chapter 6. Desktop evaluation of the impact to archaeological sites caused by changes in local sediment mobility.

resistance of the bed material); the maximum height of accumulation is approximately the top of the obstruction.

- The dimensions of the equilibrium morphological response of the sea bed are fixed by the above parameters of obstacle dimensions, orientation and seabed sediment type. The time taken to achieve this equilibrium state is a function of obstacle dimensions (which determines the volume of sediment that must be scoured or accumulated) and the local rates of erosion and accumulation.
- Prior to equilibrium, accumulation rates are a function of the input rate of sediment to the site, which may vary between sites and on semi-diurnal, spring-neap and equinoxial time scales. If sediment input rates are variably low or negligible, accumulations may be small or altogether absent and may fluctuate in volume.
- Prior to equilibrium, erosion rates are less dependant on input rates (there are however reported differences between 'clear water' and 'live bed' scour); equilibrium scour is typically achieved in the order of hours to days.

Shipwrecks of archaeological or historical importance are typically in equilibrium with the seabed on or within which they rest, i.e. equilibrium patterns of scour and accumulation are already established or the shipwreck is fully buried, posing no obstruction and therefore not modifying the seabed.

Based upon the key points above, the implications for wreck site morphology of 4 scenarios of local/regional scale sediment transport are explored in Table 8, namely:

1. High sediment mobility, high transport asymmetry, *e.g. the Channel Islands and adjacent coastline.*
2. High sediment mobility, low transport asymmetry, *e.g. central English Channel.*
3. Low sediment mobility, high transport asymmetry, *e.g. eastern English Channel*
4. Low sediment mobility, low transport asymmetry, *e.g. Lyme Bay, southern approaches to the Dover Straits, western approaches to the English Channel.*

These morphological predictions may be used by planners and managers in order to better understand sites in terms of: expected morphology prior to survey or exploration; expected local and distal distribution of artefacts separated from the wreck; potential for burial/exposure; distribution of seabed type around a wreck towards prediction of local ecological habitats, (see also the '*Wrecks on the Seabed: Ecology*' ALSF project, 2008). Conversely, the information can be used to make an informed assessment of local sediment mobility and transport asymmetry based on multi-beam swath bathymetric or even side scan sonar survey data, at previously unmonitored sites.

Changes in local sediment mobility and transport asymmetry may occur as a result of, or in conjunction with, changes in sediment mobility, asymmetry or mean bed level at a regional scale. The effect of 5 scenarios of changes in regional scale sediment transport or mean bed level are explored in Table 9, namely:

1. An increase in the input rate of sediment with no associated bed level change, *e.g. caused by additional local supply of mobile sediment by aggregate dredging upstream in the sediment transport direction.*
2. A decrease in the input rate of sediment with no associated bed level change, *e.g. caused by the cessation of aggregate dredging upstream in the sediment transport direction.*

Chapter 6. Desktop evaluation of the impact to archaeological sites caused by changes in local sediment mobility.

3. A regional scale increase in mean bed level *e.g. caused by massive mobilisation and redistribution of sand on a sand bank.*
4. A regional scale decrease in mean bed level, *e.g. caused by massive mobilisation and redistribution of sand on a sand bank.*
5. A change in the residual magnitude (symmetry) of sediment transport, *e.g. potentially occurring on equinoxal or 18.6 year timescales (but not reflected in the model results of the present study).*

These morphological predictions may be used by planners and managers in order to predict the probability of positive (providing protection through burial) or negative (increased exposure to agents of decay and dispersal through erosion) changes to particular shipwreck site bed morphology.

Scenario	Implications for site seabed morphology	Potential for artefact and debris dispersal
Scenario 1. High sediment input <sup>a</sup> , high transport asymmetry.	Maximum volume of accumulation present. Scour pits may be partially infilled or lined with finer sediment. Morphology asymmetrical along the tidal axis (accumulation on the ‘upstream’ and both scour and accumulation on the ‘downstream’ flank of the wreck relative to the residual transport direction).	There is high potential for local dispersal of artefacts and debris along the tidal axis in the short term and to be transport away from the site (artefact loss) in the direction of residual transport in the longer term.
Scenario 2. High sediment input <sup>a</sup> , low transport asymmetry.	Maximum volume of accumulation present. Scour pits may be partially infilled or lined with finer sediment. Morphology more symmetrical along the tidal axis (scour and accumulation on both flood and ebb facing flanks of the wreck)	There is high potential for local dispersal of artefacts and debris along the tidal axis in the short term but it is not so likely to be transported very far or very quickly from the general vicinity of the site.
Scenario 3. Low sediment input <sup>a</sup> , high transport asymmetry.	Possibly sub-maximal volume of sediment accumulation. Scour pits fully developed, probably lined with coarse armouring material in poorly mixed sediments. Morphology asymmetrical along the tidal axis (see Scenario 1), accumulations upstream may be absent and replaced by localised scour pits immediately adjacent to the structure.	There is low potential for short term movement and dispersal of heavier artefacts but any more mobile material may be transport slowly away from the site in the direction of residual transport.
Scenario 4. Low sediment input <sup>a</sup> , low transport asymmetry.	Scour and accumulation features may be present but site morphology will be strongly dependant on local flow conditions, sediment availability and character.	There is low potential for local dispersal and material is unlikely be transported far from the site.
a) High or low sediment input may be caused by either high/low residual transport potential or by limited mobile sediment availability in the case of the latter.		

**Table 8. Predicted implications for shipwreck site morphology and dispersal of artefacts and debris of 4 scenarios of sediment mobility and transport asymmetry.**

Scenario	Effect on site bed morphology	Potential for artefact and debris dispersal
Scenario 1. An increase in the input rate of sediment with no associated bed level change.	The volume of sub-maximal accumulations increases towards maximum. The depth of scour pits may be reduced relative to mean bed level due to partial infilling with mobile sediment.	Potential may increase for exposed items if associated with an increase in flow erosion potential or transport asymmetry. Potential may decrease for items buried by sediment accumulation.
Scenario 2. A decrease in the input rate of sediment with no associated bed level change.	The volume and height of sediment accumulations may decrease. The depth of scour pits is increased relative to mean bed level, to a maximum value at zero input rates or earlier if significant bed armouring develops.	Potential may decrease for exposed items if associated with a decrease in flow erosion potential or transport asymmetry. Potential may increase for items exposed by sediment removal.
Scenario 3. A regional scale increase in mean bed level	Short term, there is an increase in the input rate of sediment to the site (see Scenario 1). Long term, the equilibrium depth/height of scour/ accumulation features are decreased relative to mean bed level as the height of the obstacle above mean bed level increases. The extent of sedimentary features (the footprint of the site on the seabed) is decreased. Overall, more of the wreck material is buried. The smaller the exposure of the wreck above the seabed, the greater the tendency	Potential may increase for exposed items if associated with an increase in flow erosion potential or transport asymmetry. Potential may decrease for items buried by sediment accumulation.

**Table 9. Predicted implications for shipwreck site morphology and dispersal of artefacts and debris of 5 scenarios of changing sediment mobility or mean bed level.**

<b>Scenario</b>	<b>Effect on site bed morphology</b>	<b>Potential for artefact and debris dispersal</b>
Scenario 4. A regional scale decrease in mean bed level	Short term, despite a negative net transport, there must be an associate increase in sediment mobility to facilitate bed level change and therefore an increase in the input rate to the site (see Scenario 1). Long term, the equilibrium depth/height of scour/accumulation features are increased relative to mean bed level as the height of the obstacle above mean bed level increases. The extent of sedimentary features (the footprint of the site on the seabed) is increased. Overall, more of the wreck material is exposed, except where maximum accumulation heights are maintained.	Potential may decrease for exposed items if associated with a decrease in flow erosion potential or transport asymmetry. Potential may increase for items exposed by sediment removal.
Scenario 5. A change in the relative symmetry of sediment transport	See Table 8.	See Table 8.

**Table 9 cont. Predicted implications for shipwreck site morphology and dispersal of artefacts and debris of 5 scenarios of changing sediment mobility or mean bed level.**

### 6.3 Spatial and temporal scales of variability in sediment mobility and site response

Natural spatial variability in sediment mobility and asymmetry of transport associated with the tide occurs due to the shape and bathymetry of the English Channel and North sea, the distribution of sediment available for transport and the distribution of sediment grain size (although typically a mixture of grain sizes are present at any given location). Temporal variability is also naturally present due to harmonic variability of tidal currents over semi-diurnal, spring-neap, equinoxal and 18.6 year (Metonic) timescales.

The tidal and sediment model results presented here represent and include all but the 18.6 year cycle. The results of the numerical model suggest that an area may be classified as either net erosional or net accretional and that it will have an associated direction of residual transport which do not vary on these timescales; however, the magnitude of potential sediment mobility may vary on semi-diurnal, spring-neap cycle and equinoxal timescales.

Due to issues of cost, battery life and data storage, field observations of tidal current speed and direction are typically made for perhaps 30 days or less (sometimes up to 60 days). Therefore, sediment transport estimates at particular locations based on field data can not typically resolve differences at equinoxal or longer timescales. It is however

It is predicted that a shipwreck site will respond to such changes in the way outlined in Table 8 and Table 9. The rate of response will vary depending upon the rate and magnitude of the change, the new levels of sediment mobility (controlling rates of erosion) and the new rates of actual sediment input (controlling rates of accumulation). Large scale changes (i.e. significant bed level change) must be associated with significantly high sediment mobility, therefore, site response will likely be rapid and in proportion to the rate of bed level change. A decrease in sediment mobility (without a reduction in sediment supply) however, reduces the ability and increases the time needed by the site to respond.

Further additional spatial and temporal variability, not studied in detail in the present study, is associated with the contribution of wave action to sediment transport. Wave action is both sporadic and seasonal, and may be localised or regional in scale. The contribution of wave action to sediment transport depends on the water depth, relative primarily to the wavelength but also the height of the wave in question. Wave action in sufficiently shallow water may drive an additional component of sediment transport in a direction other than that described by the tidal ellipse or residual transport vector. In intermediate water depths, waves act only as a stirring mechanism, promoting sediment mobility but not affecting the transport direction. In sufficiently deep water, wave action may become absent or insignificant at the bed. Wave action therefore has a proportionally stronger effect and is more frequently a significant factor in water movement and sediment transport in shallower waters, but is considered to be less significant in water depths greater than ~15m. For this reason, model results adjacent to the coast (therefore more likely to be in shallow water) are excluded from the final report images. It is recommended that further work be undertaken to understand and quantify the contribution of wave action to the mobility and residual transport of sediment.

It is thought that climate change will cause gradual long term changes to sea level and the level of storminess. It is predicted that mean water depth in the English Channel may increase by between 0.23-0.69m by the year 2100 due to the combination of eustatic and isostatic sea level rise (Shennan and Horton, 2002 and IPCC, 2007). *The results of the present study indicate that the effect of this on tidal patterns and sediment transport pathways is negligible.* Potential changes to the frequency or intensity of storms are as yet unquantified

Chapter 6. Desktop evaluation of the impact to archaeological sites caused by changes in local sediment mobility.

but represent a potential deviation from the present day environment. Potential impacts will probably be more significant at shallow water locations.

## **7. Dissemination**

Throughout this project, the project members have sought to interact with and support other researchers, stakeholders and data end-users. To this end, the following was achieved:

### **Exchange/provision of data and GIS images**

- Olivia Merritt at Bournemouth University, in support of her MALSF project '*Refining Areas of Maritime Archaeological Potential for Shipwrecks – AMAPI*'. Ongoing.
- English Heritage and the international partners of the EU project 'MACHU', in support of ongoing collaboration created through the present study. Ongoing.
- Hanson Aggregates Marine and the RMA, support in relation to the output of previous project 3365 ('... Exclusion Zones...'). Ongoing.
- Claire Dagleish and Wessex Archaeology, in support of their round 3 MALSF project considering the spatial distribution of ecological habitats. Jan 08.

### **Talks and lectures**

- ALSF meeting 3-4/10/07.
- Lectures to MSc students at the NOCS – 'The Design of Numerical Coastal Models' 18-19/2/08.
- ALSF meeting 28/2/08.
- Abstract submitted – 'Development of Regional and Local Scale Sediment Mobility Models for Submerged Archaeological Sites'. 6<sup>th</sup> World Archaeological Congress, Ireland 29/6-4/7/08.
- Abstract submitted – 'Artefact scale physical processes in marine site formation'. 6<sup>th</sup> World Archaeological Congress, Ireland 29/6-4/7/08.

### **Other meetings attended**

- Invited attendee at the DHI user group meeting 18-19/9/07.
- Invited attendee at the DHI training day 14/10/07.
- DHI visit to NOCS 21/2/08.

### **Documents and reports**

- 'A Review of the Bed Roughness Variable in MIKE21fm HD and ST Modules' to DHI, now published through their technical website.
- 'Optimising mesh design in MIKE FM' to DHI, now published through their technical website.

## 8. References

- Anthony E J, (2002). 'Long-term marine bedload segregation, and sandy versus gravelly Holocene shorelines in the eastern English Channel.' *Marine Geology* **187**(3-4), p221-234.
- Bagnold R A, (1963). 'Mechanics of marine sedimentation'. In: *The Sea*, vol. 3, M N Hill (eds.), New York: Wiley, p. 507-528.
- Bartlett, J.M. (1998) 'Quality Control Manual for Computational Estuarine Modelling'. Environment Agency, R&D Technical Report W113, 80pp + appendix
- Beck, C., Clabaut, P., Dewez, S., Vicaire, O., Chamley, H., Augris, C., Hoslin, R. and Caillot, A. (1991) 'Sand bodies and sand transport at the English Channel-North Sea border: morphology, hydrodynamics and radioactive tracing'. *Oceanologica Acta*, special edition 11, Proceedings of the International Colloquium on the Environment of Epicontinental Seas, p111-121.
- Bricker J D, Inagaki S, and Monismith S. (2005) 'Bed drag coefficient variability under wind waves in a tidal estuary'. *Journal of Hydraulic Engineering*, 131. p497–508.
- Cameron, T D J, Crosby A, Balson P S, Jeffery D H, Lott G K, Bulat J and Harrison D J, (1992). 'The geology of the southern North Sea'. British Geological Survey UK Offshore Regional Report, HMSO, London, UK.
- Channels', *Nordic Hydrology*, 7, p293-306.
- Channon R D and Hamilton D, (1976). 'Wave and tidal sorting of the shelf sediments southwest of England'. *Sedimentology* **23**, p17-42.
- Crickmore M J, Waters C B, Price W A, (1972). 'The measurement of offshore shingle movement.' Proceedings of the 13th Coastal Engineering conference, pp 1005-1025.
- DHI (2007) '*MIKE 21: Coastal Hydraulics and Oceanography - User Guide*', DHI Water and Environment, Hørsholme, Denmark, pp204.
- DHI (2007) '*MIKE 21: Sediment Transport and Morphological Modelling - User Guide*', DHI Water and Environment, Hørsholme, Denmark, pp388.
- Dix J K, Lambkin D O, Thomas, M D and Cazenave P W, (2007) '*Modelling Exclusion Zones for Marine Aggregate Dredging*'. English Heritage ALSF project no. 3365. School of Ocean and Earth Science, University of Southampton, U.K. 421pp.
- Dix, J.K., Lambkin, D.O. and Cazenave, P.W. (In preparation) '*Development of a Regional Sediment Mobility Model for Submerged Archaeological Sites*'. University of Southampton, English Heritage ALSF Project No. 5224.
- Draper L, (1966). 'Wave Activity at the Sea Bed Around Northwestern Europe'. *Marine Geology* **5**, p133-140.
- Eisma D and Irion G, (1988). 'Suspended matter and sediment transport'. In: Salomon, J.C. (Ed.), *Pollution of the North Sea: An Assessment*. Springer, Berlin, p20-35.
- Eisma D and Kalf J, (1979). 'Distribution and particle size of suspended matter in the Southern North Sea'. *Netherlands Journal of Sea Research* **13**, p298-324.
- Eisma D and Kalf J, (1987). 'Dispersal, Concentration and Deposition of Suspended Matter in the North-Sea.' *Journal of the Geological Society* **144**, p161-178.
- Engelund, F. and Fredsøe, J. (1976) 'A sediment transport model for straight alluvial

- Engelund, F. and Hansen, E. (1972) '*A Monograph on Sediment Transport in Alluvial Streams*'. 3<sup>rd</sup> Edition. Technical Press, Copenhagen.
- Green MO and McCave IN. (1995) 'Seabed drag coefficient under tidal currents in the eastern Irish Sea'. *Journal of Geophysical Research*, 100(C8). p16,057-16,069.
- Green MO, Hewitt JE and Thrush SF. (1998) 'Seabed drag coefficient over natural beds of horse mussels (*Atrina zelandica*)'. *Journal of Marine Research*, 56. p613-637.
- Grochowski N T L and Collins M B, (1994). 'Wave Activity on the Sea-Bed of the English-Channel.' *Journal of the Marine Biological Association of the United Kingdom*, p739-742.
- Grochowski N T L, Collins M B, Boxall S R, Saloman J C, (1993a). 'Sediment Transport Predictions for the English-Channel, Using Numerical-Models.' *Journal of the Geological Society* **150**, p683-695.
- Grochowski N T L, Collins M B, Boxall S R, Saloman J C, Breton M, Lafite R, (1993b). 'Sediment Transport Pathways in the Eastern English-Channel.' *Oceanologica Acta* **16**(5-6), p531-537.
- Hamblin R J O, Crosby A, Balson P S, Jones S M, Chadwick R A, Penn I E, Arthur M J, (1992). 'The geology of the English Channel'. British Geological Survey UK Offshore Regional Report, HMSO, London, UK.
- Harris P T, Pattiarachi C B, Collins M B, Dalrymple R W, (1995). 'What is bedload parting?' In: Flemming B W and Bartholoma A (eds.) *Tidal signatures in modern and ancient sediments*. Oxford: Blackwell Science, p3-18.
- Howarth M J, (1990). 'Atlas of tidal elevations and currents around the British Isles'. Offshore Technology Report by the Proudman Oceanographic Laboratory for the Department of Energy, HMSO, London, UK. 44pp.
- IPCC, 2007: *Climate Change 2007: The Physical Science Basis*. Contribution of Working Group I to the Fourth Assessment Report of the Intergovernmental Panel on Climate Change [Solomon, S., D. Qin, M. Manning, Z. Chen, M. Marquis, K.B. Averyt, M. Tignor and H.L. Miller (eds.)]. Cambridge University Press, Cambridge, United Kingdom and New York, NY, USA, 996 pp.
- Johnson, M.A., Kenyon, N.H., Belderson, R.H. and Stride, A.H. (1982) 'Sand Transport'. Chapter 4, p 58-94 In: 'Offshore Tidal Sands: Processes and Deposits' Stride A.H. (Ed) Chapman and Hall, London. 222pp.
- Jones, O. (2007) 'Modelling Headland Sandbank Processes' PhD Thesis, University College London, 247pp.
- Jones, S., Jago, C.F., Prandle, D., Flatt, D., (1994). 'Suspended sediment dynamics: Measurements and modelling in the Dover Strait'. In: Beven, K.J., Chatwin, P.C., Millbank, J.H. (Eds.), 'Mixing and Transport in the Environment'. Wiley, New York, pp. 183-201.
- Ke X, Collins MB and Poulos SE. (1994) 'Velocity structure and sea bed roughness associated with intertidal (sand and mud) flats and saltmarshes of the Wash, U.K.' *Journal of Coastal Research*, 10(3). p702-715.
- Kenyon N H and Stride A H, (1970). 'The tide-swept continental shelf sediment between the Shetlands Isles and France'. *Sedimentology* **14**, p159 - 173.
- Kenyon, N.H. and Stride, A.H. (1970) 'The tide-swept continental shelf sediments between the Shetland Isles and France'. *Sedimentology*, 14, p159-173.
- Kenyon, N.H., Belderson, R.H., Stride, A.H. and Johnson, M.A. (1981) 'Offshore tidal sandbanks as indicators of net sand transport and as potential deposits'. In: 'Holocene Marine

- Sedimentation in the North Sea Basin'. Special Publication 5 of the International Association of Sedimentologists. Nio, S.D., Shüttenhelm, R.T.E. and van Weering, Tj.C.E. (Eds).
- Lafite, R., Shimwell, S.J., Grochowski, N.T.L., Dupont, J.P., Nash, L., Salomon, J.C., Gabioch, L., Collins, M.B., Gao S., (1999). 'Suspended Particulate Matter fluxes through the Strait of Dover', *Oceanologica Acta*. **23**(6), p687-700.
- Lambkin, D.O. (2007) '*A Review of the Bed Roughness Variable in MIKE21fm HD and ST Modules*'. DHI Website – FAQ, and In: Dix, Lambkin and Cazenave (In prep).
- Larsonneur C, Bouysse P and Auffret J-P, (1982). 'The superficial sediments of the English Channel and its Western Approaches'. *Sedimentology* **29**, p851-864.
- Mauvais J L (1991). 'The role of hydrodynamics in environmental studies. The case of tidal seas.' *Oceanologica Acta* **11**, p29-45.
- McManus, J.P., Prandle, D., (1997). 'Development of a model to reproduce observed suspended sediment distributions in the southern North Sea using Principal Component Analysis and Multiple Linear Regression'. *Continental Shelf Research* **17**, 761-778.
- Meyer-Peter, E. and Muller, R. (1948) 'Formulas for bed-load transport. Report 2<sup>nd</sup> meeting of the International Association Hydraulic Structural Research. Stockholm, p39-64.
- Newell R C, Seiderer L J, Hitchcock D R, (1998). 'The impact of dredging works in coastal waters: a review of the sensitivity to disturbance and subsequent recovery of biological resources on the seabed.' *Oceanography and Marine Biology Annual Review* **36**, p127-178.
- Ole Baltazar Andersen (1995) 'Global ocean tides from ERS 1 and TOPEX/POSEIDON altimetry' *Journal of Geophysical Research*, 100, C12, p25249-25260.
- Pingree R D and Griffiths D K, (1979). 'Sand Transport Paths around the British-Isles Resulting from M2 and M4 Tidal Interactions.' *Journal of the Marine Biological Association of the United Kingdom* **59**(2), p497-513.
- Pingree R D, (1980). 'Physical Oceanography of the Celtic Sea and English Channel'. In: Banner F T, Collins M B and Massie K S. (eds.) *The north-west European shelf seas: the sea bed and the sea in motion. II. Physical and chemical oceanography, and physical resources. Oceanography Series 24B*, Elsevier, p415-465.
- Pohlmann, T., Puls, W., (1994). 'Currents and transport in water'. In: Sundermann, J. (Ed.), *Circulation and Contaminant Fluxes in the North Sea*. Springer, New York, pp. 345-402.
- Posford Haskoning, (2002). 'Regional Environmental Impact Assessment'. Report prepared for the East Channel Association.
- Postma, H., (1990). 'Transport of water and sediment in the Strait of Dover'. In: Ittekkot, V., Kempe, S., Michaelis, W., Spitzky, A. (Eds.), *Facets of Modern Biogeochemistry*. Springer, Berlin, pp. 147-154.
- Rubin D M and Hunter R E, (1987). 'Bedform alignment in directionally varying flows'. *Science* **237**, p276 - 278.
- Rubin D M and Ikeda H, (1990). 'Flume experiments on the alignment of transverse, oblique, and longitudinal dunes in directionally varying flows'. *Sedimentology* **37**, p673-684.
- Salomon, J-C. and Breton, M. (1991) 'Courants résiduels de marée dans la Manche'. *Oceanologica Acta*, special edition 11, Proceedings of the International Colloquium on the Environment of Epicontinental Seas, p47-53.
- Sentchev A and Korotenko K, (2005). 'Dispersion processes and transport pattern in the ROM system of the eastern English Channel derived from a particle-tracking model.' *Continental Shelf Research* **25**(18), p2294-2308.

- Shennan, I. and Horton, B. (2002) Holocene land- and sea-level changes in Great Britain. *Journal of Quaternary Science*, 17, p511-526.
- Smith A J, Curry D and Boillot G, (1975). 'The Structure and Geological Evolution of the English Channel [and Discussion]'. *Philosophical Transactions of the Royal Society of London. Series A, Mathematical and Physical Sciences* **279**, p3-20.
- Soulsby (1997) '*Dynamics of Marine Sands*', Thomas Telford, London, pp249.
- Soulsby R.(1997) *Dynamics of marine sands*. Thomas Telford, pp249.
- Sternberg RW. (1968) 'Friction factors in tidal channels with differing bed roughness'. *Marine Geology*, 6. p243–260.
- Stride A H, Belderson R H, Kenyon N H, and Johnson M A, (1982). 'Offshore tidal deposits: sand sheet and sand bank facies'. In: Stride A H (ed.) *Offshore tidal sands: processes and deposits*, London: Chapman and Hall, p95-124.
- Stride, A.H. (1963) 'Current swept sea floors near the southern half of Great Britain. *Quaternary Journal of the Geological Society of London*, 119, p175-199.
- Van Rijn, L.C. (1984) 'Sediment Transport: part I: bed load transport; part II: suspended load transport; part III: bed forms and alluvial roughness. *Journal of the Hydraulic Division, proceedings of the ASCE*, 110 (HY10), 1431-56; (HY11), 1613-41; (HY12), 1733-53.
- Velegrakis A F, Gao S, Lafite R, Dupont J P, Huault M F, Nash L A, Collins M B, (1997). 'Resuspension and advection processes affecting suspended particulate matter concentrations in the central English Channel.' *Journal of Sea Research* **38**(1-2), p17-34.
- Velegrakis, A. F., D. Michel, Collins M B, Lafite R, Oikonomou E K, Dupont J P, Huault M F, Lecouturier M, Salomon J C, Bishop C, (1999). 'Sources, sinks and resuspension of suspended particulate matter in the eastern English Channel.' *Continental Shelf Research* **19**(15-16), p1933-1957.

## **9. Appendix A – Basic variables in MIKE**

The basic input variables for a MIKE21 flexible mesh hydrodynamic model are listed in Section 3.1. A short study is shown here that describes the very basic effect of spatial gradients in the variables of bathymetry, bed roughness, eddy viscosity and the presence of obstacles and headlands.

### **9.1 Method**

A simple channel domain was created, 8km long x 4km wide x 10m deep. Flow in the domain was induced by adding water at the entry boundary and removing water at the exit boundary, at a rate equal to a flow of  $1\text{ms}^{-1}$  over the boundary cross section area, e.g.  $4,000\text{m} \times 10\text{m} \rightarrow 40,000\text{m}^3\text{s}^{-1}$ . The model was then allowed to come to equilibrium. The resulting spatial distribution of current velocity and direction within the domain is then controlled in the model by the interaction between the flow and other variables including boundary shape, bathymetry, bed roughness, eddy viscosity and wind stress.

Unless otherwise specified, tests used the default channel shape, depth and flow rate (described above), default settings for bed roughness (Manning formulation,  $M = 32\text{m}^{1/3}\text{s}^{-1}$ ) and eddy viscosity (Smagorinsky formulation, constant = 0.28) and no wind stress were applied.

The following scenarios were tested, changing parameters individually from the basic set to observe the general effect.

Bathymetry – [uniform depth, transverse bed slope, channelised pit]

Bed roughness – [uniform value, transverse gradient in value, no resistance]

Eddy viscosity – [uniform value, transverse gradient in value]

Obstacles – [central island, twin piers from lateral boundaries]

Wind – [ $10\text{ms}^{-1}$  from the NE]

Differences in the resulting flow field may appear large on the colour scales used but may be small in absolute terms.

### **9.2 Results**

#### **9.2.1. Bathymetry**

The scenarios tested and the resulting flow patterns are shown in Figure 88.

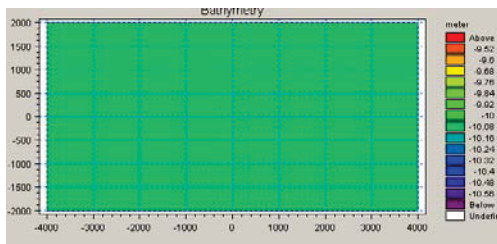
A flat, uniform bathymetry results in smooth, undeflected flow throughout the domain. Current velocities vary slightly (between  $0.97 - 1.01\text{ms}^{-1}$ ) along the domain as a result of friction with the bed and the corresponding development of a longitudinal slope in the water surface.

A cross-flow slope in the bathymetry results in relatively lower velocities in shallower water and relatively higher velocities in deeper water. This is potentially caused by choosing to use the Mannings number parameterisation for bed roughness, which increases friction in shallower water.

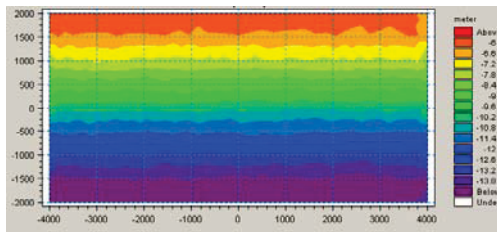
An isolated pit in the centre of the domain causes local flow velocity modification. Velocity is reduced as flow enters the pit and velocity is increased where flow in the pit is constricted and where flow must rise up and out of the pit at the downstream end. There is also a localised acceleration of flow upstream of the pit. There is evidence of slight flow deflection ( $<5^\circ$ ) in locations at the edge of the pit.

Although flow direction was not significantly affected by bed slopes in the three cases tested, it is possible that more flow deflection might be observed if the lateral slopes were made steeper, or if the local pit were deeper relative to the water depth.

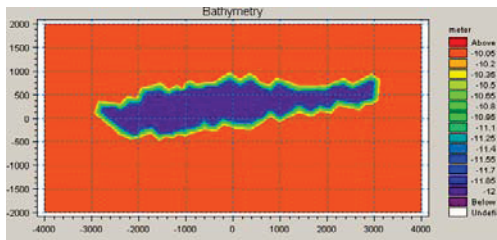
**Bathymetry**



Case 1 – Uniform bathymetry



Case 2 – Laterally sloped bathymetry



Case 3 – Central pit in bathymetry

**Resulting current velocity and direction**

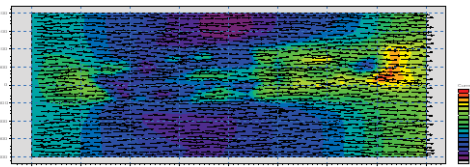
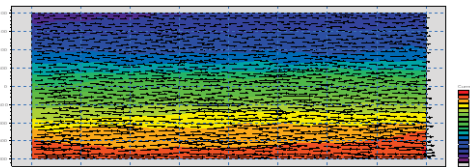
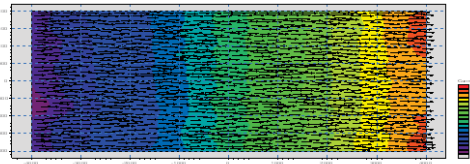


**Figure 88. The effect of spatially variable bathymetry on current velocity and direction in the domain.**

**9.2.2. Bed Roughness**

The scenarios tested and the resulting flow patterns are shown in Figure 89.

A uniform bed roughness results in smooth, undeflected flow throughout the domain. Current velocities vary slightly (between  $0.97 - 1.01\text{ms}^{-1}$ ) along the domain as a result of friction with the bed and the corresponding development of a longitudinal slope in the water surface.

An absence of any bed roughness (‘no resistance’) also results in smooth, undeflected flow throughout the domain. Due to the absence of friction, longitudinal slopes in the water surface are not set up and flow velocities are uniform over the domain ( $1.00\text{ms}^{-1}$ ).

Two distributions of bed roughness were tested. The first was an asymmetrical lateral gradient in bed roughness, specifically a smooth variation in  $M$  from 140 (low resistance) along the south boundary to  $M=32$  (the default value) in the central part to  $M=5$  (high resistance) along the northern boundary. Current velocity is clearly increased in regions of lower bed resistance; this was observed mainly away from the boundaries where water is being added and removed evenly across the boundary cross-section irrespective of local bed roughness. A strong deflection of the flow was also observed as a larger proportion of flow volume is naturally diverted to the faster flowing lower resistance areas.

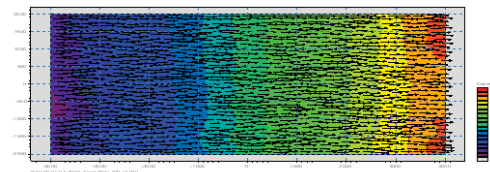
The second distribution of bed roughness provided a symmetrical lateral gradient from low resistance ( $M=45$ ) at the north and south boundaries to higher resistance ( $M=28$ ) in the central part. As in the previous case, current velocity is increased locally over regions of low resistance and decreased over regions of high resistance. Likely as a result of the smaller contrast in bed roughness, a smaller degree of flow deflection was observed in this example.

It was found in more complex experiments, described in Section 3.3.3.6, that variation in the uniform bed roughness value has the effect of increasing or decreasing the predicted range of tidal elevation and the magnitude of current speed; current direction is not significantly affected by the use of different but uniform values.

Manning's number distribution

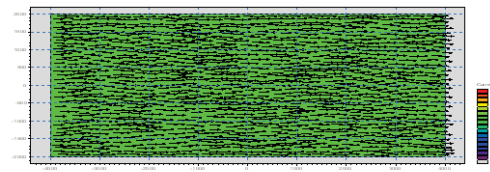
Resulting current velocity and direction

$M=32$

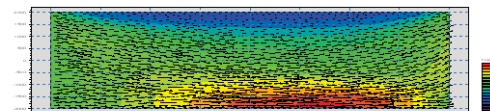
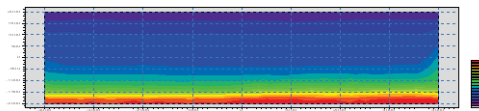


Case 1 – Uniform value

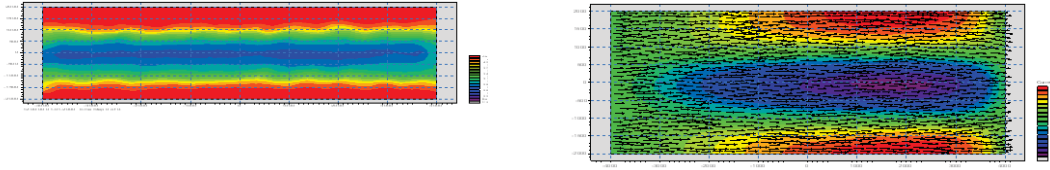
None



Case 2 – No resistance



Case 3 – Lateral roughness gradient 1



Case 4 – Lateral roughness gradient 2

**Figure 89. The effect of spatially variable bed roughness (Mannings formulation) on current velocity and direction in the domain.**

### 9.2.3. Eddy viscosity

The scenarios tested and the resulting flow patterns are shown in Figure 90.

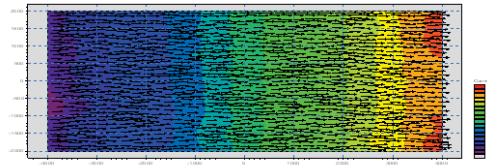
An asymmetric lateral gradient in the eddy viscosity coefficient produces only a slight distortion of the current velocity contours, suggesting that flow along the southern boundary (where the eddy viscosity constant is increased) is accelerated relatively more than in the uniform value case. In general, no significant difference was observed in the resulting flow field, compared to that made using a uniform value.

It was found in more complex experiments, described in Section 3.3.3.7, that variation in the uniform eddy viscosity coefficient can have a similar effect to altering the uniform value of bed roughness, i.e. increasing or decreasing range of tidal elevation or the magnitude of current speed; current direction is not significantly affected by the use of different but uniform values.

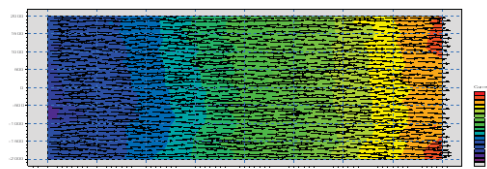
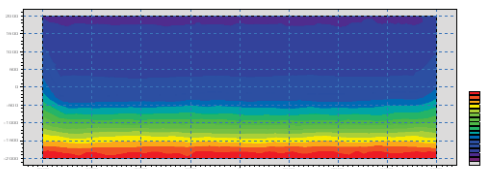
#### Eddy viscosity constant distribution

C=0.28

#### Resulting current velocity and direction



#### Case 1 – Uniform value



#### Case 2 – Lateral gradient

**Figure 90. The effect of spatially variable eddy viscosity (Smagorinsky formulation) on current velocity and direction in the domain.**

### 9.2.4. Wind

The scenarios tested and the resulting flow patterns are shown in Figure 91. Cases 1 and 2 were conducted in with equilibrium input and exit flows so that no flow was actively applied but the wind stress was allowed to develop a flow field within the domain.

In the absence of any flow across the boundaries or wind stress, the model produces zero flow across the domain.

Applying a wind stress to the domain creates a flow of water (approximately  $0.2\text{ms}^{-1}$  in this example) in the direction of the stress (towards  $225^\circ$ ). This flow meets the impermeable southern boundary and is deflected to the west. Current velocities become greater with increasing fetch and are increased along the southern boundary due to secondary flows developing as the set up of water is redirected. The very short fetch for areas under the northern boundary creates the smallest current velocities.

The effect of adding the same wind stress to the basic flow model is a slight reduction in the current velocity along the southern boundary. The pattern of distortion is best described as a summation of the results from model runs with flow only (Case 3) and wind only (Case 2).

#### Wind field distribution

No flow, no wind  
Case 1 – No flow, no wind

No flow,  $10\text{ms}^{-1}$  from  $45^\circ$

Case 2 – No flow, uniform wind field

Flow, no wind

Case 3 – Uniform flow field, no wind

Flow,  $10\text{ms}^{-1}$  from  $45^\circ$

Case 4 – Uniform flow field, uniform wind field

#### Resulting current velocity and direction

No flow

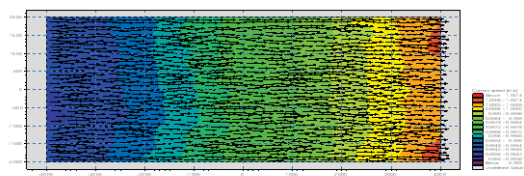
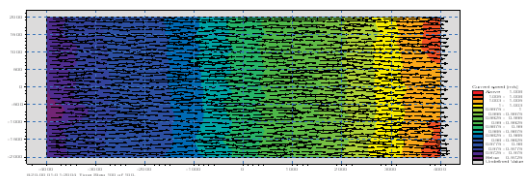
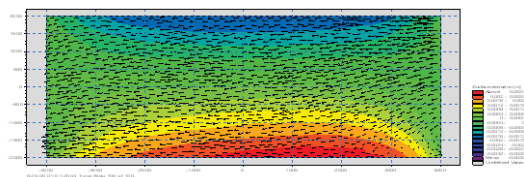


**Figure 91. The distribution of current velocity and direction resulting from application of a uniform wind stress.**

**9.2.5. Obstacles**

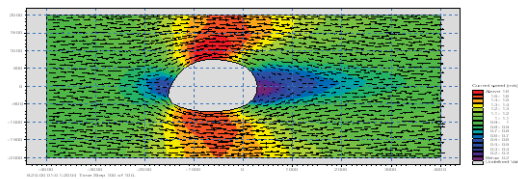
The scenarios tested and the resulting flow patterns are shown in Figure 92.

An island in the domain causes flow to diverge upstream of the obstacle, then following the shape of the island and converging on the lee side. Current velocity is reduced immediately upstream of the island and in the downstream wake. Constriction of the streamlines either side of the island causes flow acceleration. This pattern of flow is similar to what might be expected when observing flow around any such low Reynolds number flow system.

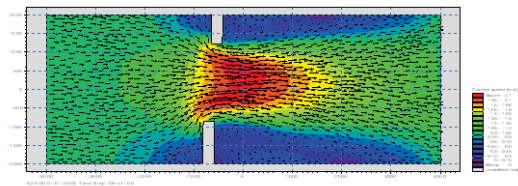
A constriction in the channel flow also causes localised acceleration of flow through the gap. Regions of low velocity flow and back eddies develop in the lee of the piers.

**Obstacles to the flow**

**Resulting current velocity and direction**



**Case 1 – An island**



**Case 2 – Pier constriction**

**Figure 92. The effect of obstacles and constrictions on current velocity and direction in the domain.**

**9.3 Summary and conclusions.**

This small number of tests represents part of the learning and familiarisation tests that were undertaken by the project in order to understand the general effect of the many model variables available.

These tests are presented only to provide some indication of the general effect of slopes, gradients and obstructions in the model domain. The range of values tested and presented here are not exhaustive as there are infinite combinations and further complexity when jointly varying these variables in a ‘real world’ scenario model. The general effects described by these few examples are typically exaggerated by increasing the gradients of the variable being described.

## **10. Appendix B – Optimising Mesh Design in MIKE FM**

### **10.1 Rationale**

This study explores the impact of the choices made during mesh design on the total model run time. A poor choice of mesh can result in an inefficient model where a minority of small elements in the domain induces longer run times without improving data quality. Conversely, unnecessarily large mesh elements may be considered sub-optimal as a greater spatial resolution could be relatively efficiently achieved; meshes that are too coarse are also known to affect the propagation speed of tidal features through the domain. Through better understanding of the tools used to create meshes, the actual result when an area of ‘uniform’ mesh is created and the implications of co-varying element properties, an optimum mesh may be designed before it is created. A mesh may be optimised for certain spatial or temporal resolutions or it may be optimised purely in terms of run time.

The frequency of time stepping in the model (when a calculation set is made for every element in the whole mesh) is dynamically controlled within the 2007 and later releases of MIKE software. The time step is determined by the MIKE engine, using the CFL Courant number which considers local parameters of water depth, flow velocity and length scale for each element in the modelling domain. Even a single poorly optimised element in the domain can result in (unnecessary) additional time steps having to be calculated, significantly increasing the overall run time of a model.

By identifying the temporal or spatial scale of the processes considered to be important in a model, the most efficient element length scale for a given water depth can be calculated. Through simple geometric relationships, the identified length scale may be translated into an equivalent element area to be used when creating the mesh. Users will often deliberately apply higher mesh resolution near to areas of interest or to resolve complex bathymetry and it is these areas that will then control the efficiency of the model overall. It is therefore particularly important to understand the implications of mesh design in these areas.

This study was specifically aimed at the use of flexible meshes in MIKE21 FM, but the same principles should apply to ST, SW and other modules.

### **10.2 Introduction**

When numerical models are used for commercial consultation, and to a lesser extent in academic research, there is usually a certain time frame within which the study must be completed. Because computing resources are finite, this limits somewhat the total number of calculations that can be made in the time available. The number of models or scenarios that can be tested is then a function of the number of mesh elements, the number of time steps per run and the setup choices made (high vs low order formulations, wave or sediment transport modules, etc). By optimizing the design of the mesh (which in turn controls the number of time steps required), the total model run time may be optimized also. This study will provide general guidelines for the design of an efficient mesh and a method by which to calculate and apply the optimum ‘maximum element area’.

In comparison to rectilinear or curvilinear mesh designs, the concept and use of a flexible mesh allows model domains to be constructed that: 1) describe the model boundaries more accurately; 2) are of variable (user controlled) resolution across their extent. The second is particularly important and useful when the model domain contains a large range of water

depths, has regions of complex flow (e.g. constrictions or deflected flows) or when a nested approach is required.

The Courant-Friedrich-Levy (CFL number) describes the rate at which information moves through the domain (elements/timestep). For the shallow water hydrodynamic (HD) equations in Cartesian coordinates, the CFL number is defined as

$$\text{Eq. 1} \quad CFL_{HD} = \left(\sqrt{gh} + |u|\right) \frac{\Delta t}{\Delta x} + \left(\sqrt{gh} + |v|\right) \frac{\Delta t}{\Delta y}$$

where h is the total water depth, u and v are the velocity components in the x and y direction, g is the acceleration due to gravity, Δx and Δy are a characteristic length scale in the x and y direction for an element and Δt is the time step interval. It is a requirement for stability of the explicit numerical scheme used by the model that the CFL number is less than 1.

For the transport advection and dispersion (AD) equations (e.g. for sediment) in Cartesian coordinates the CFL number is defined instead as

$$\text{Eq. 2} \quad CFL_{AD} = |u| \frac{\Delta t}{\Delta x} + |v| \frac{\Delta t}{\Delta y}$$

where |u| and |v| are the transport vectors in the x and y directions. As it excludes the wave celerity term, stability requirements for the transport equations are usually less restrictive than the CFL number for the shallow water equations.

Some Mike21 modules (e.g. FM, ST and SW) in the 2007 release and later, use a ‘dynamic time step’ mechanism whereby the actual timestep is calculated in order to ensure numerical stability, using a (user defined) maximum CFL number. During model setup, a minimum and maximum time step is defined by the user and the model then adjusts the time step to satisfy these limits but will only output results at the time steps requested by the user. If the required time step falls outside of the user defined range, the model run is automatically terminated.

The dynamic time step is chosen on the basis of the largest CFL value in the domain and can therefore be sensitive to single isolated small elements which produce anomalously high CFL values compared to the majority of the elements.

For the purposes of this exercise, the assumption is made that the shallow water CFL number is the most important and that all of the flow is in the x direction. A simplified CFL number may therefore be considered

$$\text{Eq. 3} \quad CFL = \left(\sqrt{gh} + |u|\right) \frac{\Delta t}{\Delta x}$$

In practice, the representative length scale is calculated in MIKE software as the smallest length of the three element sides. Information about local water depth is contained in each of the three mesh nodes that define each element but for purposes of the CFL number calculation, this quantity (and the velocity) are evaluated at element centre (MIKE21 HD manual, p 112). It is assumed that the mean depth value is used.

### 10.3 Parametric sensitivity testing

The CFL number controls the dynamic time step as an implicit function of the local water depth, flow velocity, the length of the smallest element side and the user defined limiting CFL number (taken to be 1 in this study). In order to understand the basic effect of the CFL number on controlling Δt, a number of simple sensitivity studies were undertaken

using example parametric combinations and are presented below. In each case the curves shown in the Figures are calculated by rearranging Eq. 3, constant values are assigned to the parameter set (as indicated in the caption). The effect of positive/negative variation in one other parameter is also indicated.

### 10.3.1. Effect of local water depth

$\Delta t$  is proportional to  $\sqrt{h}$ , as shown in Figure 93. If a mesh of uniform element area is used over a domain with a range of water depths, the number of time steps required will be determined by the CFL number calculated in the deepest water depths. This is because the wave celerity is greater in deeper water and a greater number of time steps must be used to resolve its progress at the same spatial resolution. The relative effect on the maximum time step is large in comparison to that of other parameters (max. CFL,  $\Delta x$ ,  $|u|$ ).

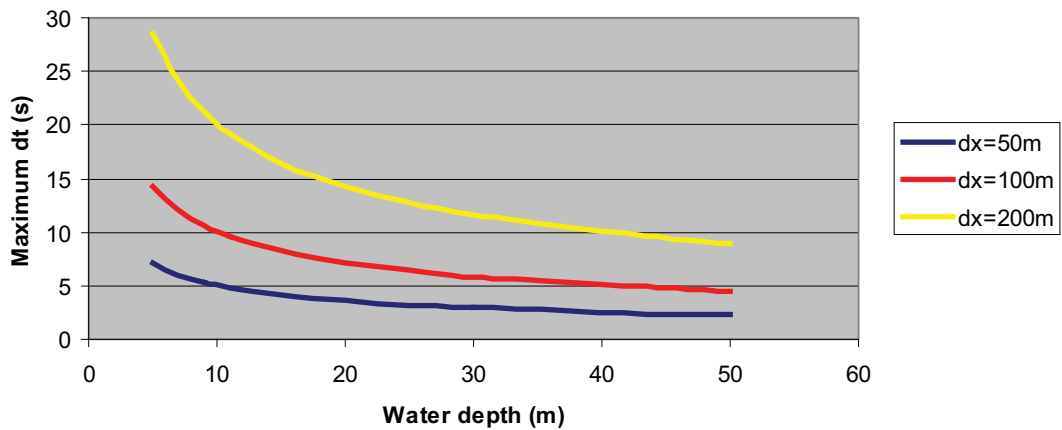
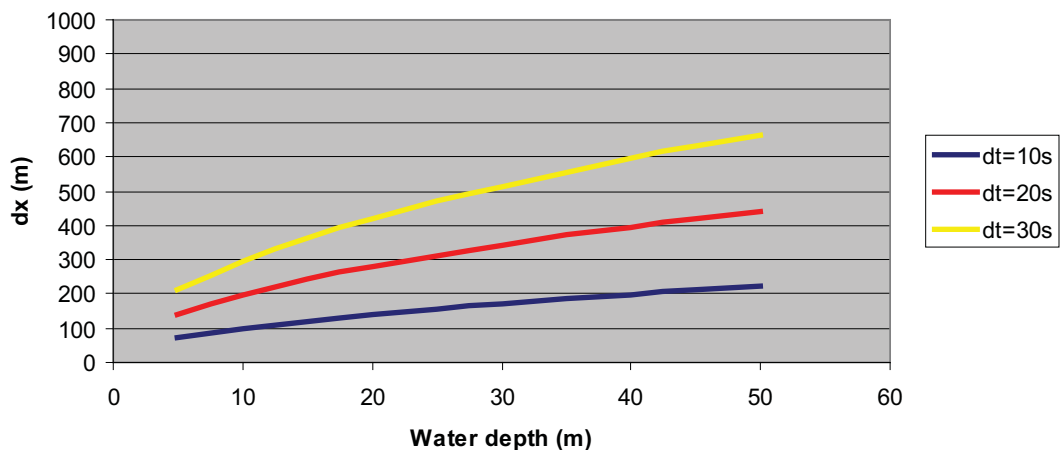


Figure 93. The effect of variable water depth on  $\Delta t$  calculated using Eq. 3, for example values of  $\Delta x$  and for fixed parameter set [CFL=1,  $|u|=0 \text{ ms}^{-1}$ ].

As water depth is considered to be a particularly important controlling variable, its effect on  $\Delta x$  is also shown in Figure 94. In the Figure,  $\Delta x$  is instead proportional to  $1/\sqrt{h}$ . If a mesh is created for a domain containing a range of water depths, the size of each element should be chosen on the basis of the local water depth and target time step. A larger element size is needed in deeper water to harmonise the time step required by elements in all water depths. This is because wave celerity is greater in deeper water and larger mesh spacing must be used to allow its stable progress at the same temporal resolution.



**Figure 94.** The effect of variable water depth on  $\Delta x$  calculated using Eq. 3, for example values of  $\Delta t$  and for fixed parameter set [CFL=1,  $|u|=0 \text{ ms}^{-1}$ ].

**10.3.2. Effect of local velocity magnitude**

In an area of uniform element area and water depth,  $\Delta t$  is inversely proportional to  $|u|$ , as shown in Figure 95. If a mesh of uniform element area is used in an area of uniform water depth but with spatially varying local flow velocity, the number of time steps required will be determined by the CFL number calculated in the area with the strongest flows. In this simple case, this limiting effect can be offset by increasing element area in regions of strong flow. However, it is also shown in Figure 95 and in Figure 96 that the relative importance of  $|u|$  depends upon the water depth (which controls the magnitude of the wave celerity term). In relatively deep water ( $\sim >5\text{m}$ ) the relative effect of  $|u|$  on the maximum time step is small in comparison to that of the other parameters ( $h$ ,  $\Delta x$ , max CFL) but becomes progressively greater in shallower water depths. Given that the smallest elements tend to be created in the shallowest water depths,  $|u|$  is potentially a very important factor in determining the limiting time step. Values of  $|u|$  may be estimated but are not known until the model is actually run.

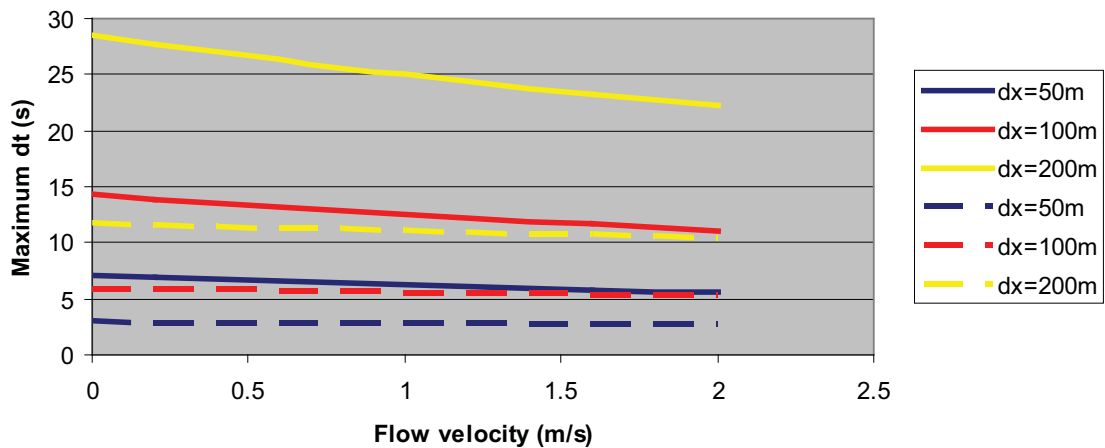


**Figure 95.** The effect of variable local flow velocity on  $\Delta t$  calculated using Eq. 3, for example values of  $\Delta x$  and for fixed parameter set: solid lines [CFL=1,  $h=5 \text{ m}$ ]; dashed lines [CFL=1,  $h=30 \text{ m}$ ].

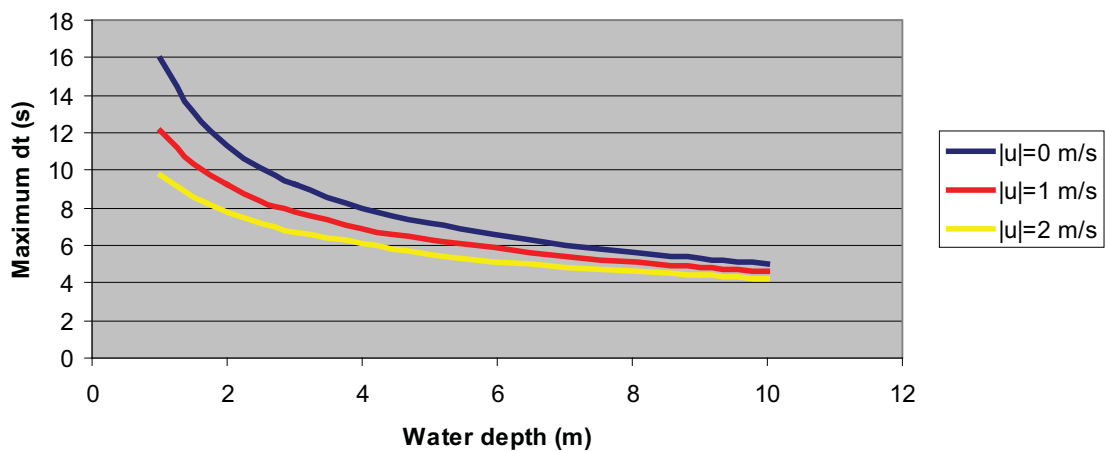


**Figure 96.** The effect of variable local water depth on  $\Delta t$  calculated using Eq. 3, for example values of  $|u|$  and for fixed parameter set [ $\Delta x = 50 \text{ m}$ , CFL=1].

### 10.3.3. Effect of element size

$\Delta t$  is linearly proportional to  $\Delta x$ , as shown in Figure 97, whereby halving the value of  $\Delta x$  will halve the maximum permissible time step. If a mesh of spatially varying element shapes and sizes are used to model a domain with uniform water depth and flow velocity, the number of time steps required will be determined by the CFL number of the element with the smallest value of  $\Delta x$ . The relative effect on the maximum time step is large in comparison to that of the other parameters ( $h$ ,  $|u|$ , max CFL).

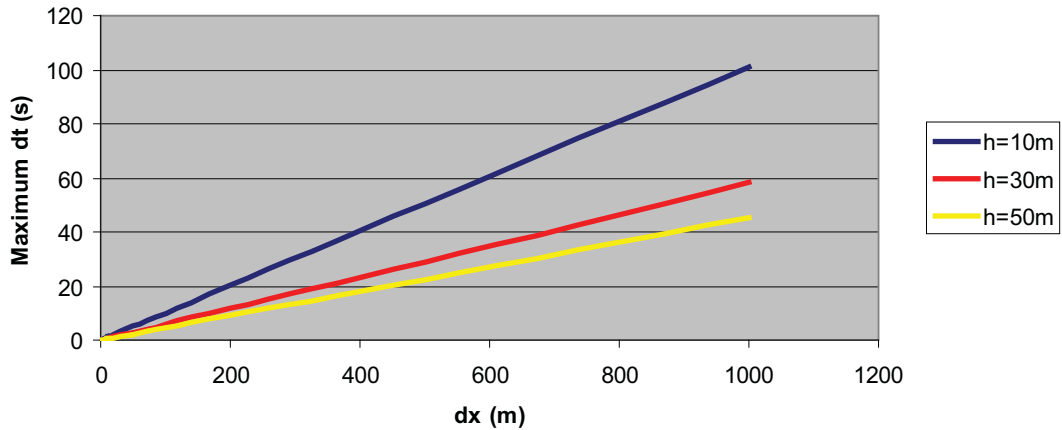


Figure 97. The effect of variable element size,  $\Delta x$ , on  $\Delta t$  calculated using Eq. 3, for example values of  $h$  and for fixed parameter set [CFL=1,  $u=0 \text{ ms}^{-1}$ ].

### 10.3.4. Effect of the chosen maximum allowable CFL number

$\Delta t$  is proportional to the chosen maximum allowable CFL number, as shown in Figure 98. If a mesh of uniform element area is used to model a domain of uniform depth and flow velocity, the number of time steps required will be minimised by choosing the highest possible CFL number ( $\rightarrow 1$ ). As the choice of CFL number is likely to lie between the recommended value of 0.8, and the maximum value of 1, the relative effect on the maximum time step is also small in comparison to that of the other parameters ( $\Delta x$ ,  $h$ ,  $|u|$ ).

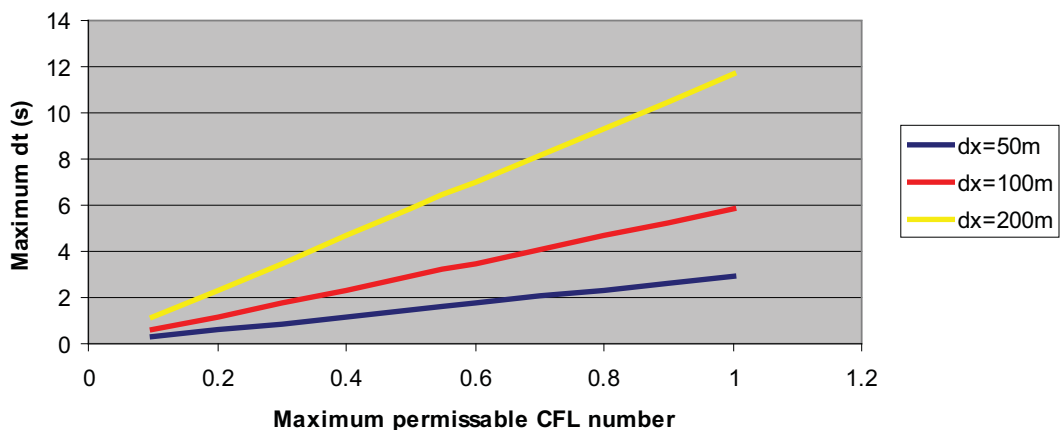


Figure 98. The effect of varying the chosen maximum allowable CFL number on  $\Delta t$  calculated using Eq. 3, for example values of  $\Delta x$  and for fixed parameter set [ $h=30 \text{ m}$ ,  $|u|=0 \text{ ms}^{-1}$ ].

## 10.4 The distribution of $\Delta x$ and $\Delta t$ in a mesh of ‘uniform’ element area

### 10.4.1. Relating $\Delta x$ to the area of triangular flexible mesh elements

When using the mesh generation tool in MIKE zero, the software allows the user to define the maximum element area, the smallest allowable angle and the maximum number of elements. A method is therefore needed to relate a desired value of  $\Delta x$  to the area specified.

The shape of triangular elements may be equilateral (three sides of equal length and three equal internal angles =  $60^\circ$ ), isosceles (two sides of equal length and two equal internal angles  $> 60^\circ$ ) or scalene (all sides and internal angles are different). Simple observation of a number of meshes indicates that practically all elements are scalene but that the vast majority are close to isosceles or equilateral in shape.

In the model, the characteristic length scale ( $\Delta x$ ) is approximated by the length of the smallest side for each element (MIKE21 HD manual, p 112). The smallest side of an isosceles triangle is located opposite the vertex with the smallest internal angle ( $\theta$ ). The value of  $\Delta x$  used to calculate the CFL number for elements isosceles or equilateral in shape can therefore be related to the element area ( $A$ ), using the simple geometric relationship shown in Figure 99.

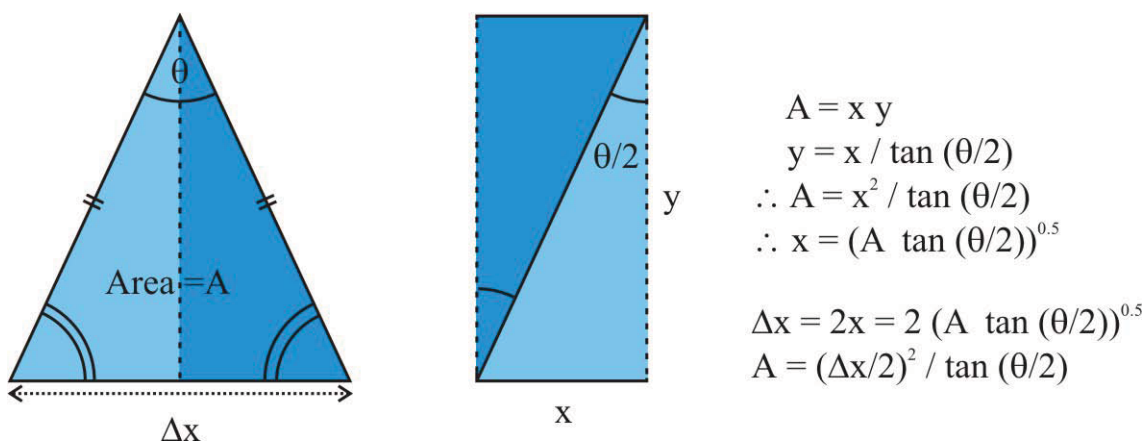


Figure 99. The geometric relationship between the area of a triangular element, the smallest internal angle,  $\theta$ , and the length of the smallest side,  $\Delta x$ .

#### 10.4.1.1. Testing methodology

In most cases, a simple rectangular domain ( $4000\text{m} \times 2000\text{m}$ ) using Cartesian coordinates was used; the Oresund Sound land boundary outline was also used to test a more complex domain shape. The chosen domain was populated with triangular elements using the flexible mesh generation tool in MIKE zero. The default smallest allowable angle ( $26^\circ$ ) was maintained and the maximum number of elements was large enough to not limit the mesh creation process. From Figure 99, the theoretical maximum element area and  $\Delta x$  are related by the smallest internal angle as

$$\text{Eq. 4} \quad A = \left(\frac{\Delta x}{2}\right)^2 / \tan(\theta/2)$$

and

$$\text{Eq. 5} \quad \Delta x = 2\sqrt{A \cdot \tan(\theta/2)}$$

The maximum element size applied in the mesh generator tool was calculated using Eq. 4 on the basis of a desired value of  $\Delta x$  and a fixed value of  $\theta=60^\circ$ . The resulting mesh files were analysed in Matlab, using the DFS manager (2007 edition) tools to read in the mesh and additional code (shown in Appendix A) was written to obtain, for each element, the area, the length of each side and the size of each internal angle. By prescribing a maximum CFL number of 1, a uniform depth of  $h=20\text{m}$  and a flow velocity  $|u| = 0\text{ms}^{-1}$ , Eq. 3 can be rearranged and used to calculate the corresponding value of  $\Delta t$  for each element as

$$\text{Eq. 6} \quad \Delta t = \frac{\Delta x \cdot CFL_{\max}}{\sqrt{gh + u}}$$

If  $\Delta x$  is variable within the domain, there is also a corresponding distribution of CFL numbers which may be calculated using Eq. 3, where  $\Delta t$  is set to the minimum value in the domain.

Through this analysis, the distribution of  $A$ ,  $\Delta x$ ,  $\theta$ ,  $\Delta t$  and CFL reflect the variability in element shape and size, and the corresponding efficiency of the generated mesh, in comparison to the idealized, initial, single, user defined value.

#### 10.4.2. Raw meshes and the effect of mesh smoothening

A series of meshes were created in the rectangular domain with desired  $\Delta x = [25\text{m}, 37\text{m}, 50\text{m}, 75\text{m}, 100\text{m}]$ , producing meshes with between 46,443 and 2944 elements. In each case the boundary vertex spacing was set to the desired value of  $\Delta x$ . Mesh smoothening was applied to the basic mesh with a gradually increasing number of iterations [5, 10, 25, 50, 100, 150, 200]. Histograms of the resulting distribution of  $A$ ,  $\Delta x$ ,  $\theta$ ,  $\Delta t$  and CFL in the raw mesh and following 50 iterations of smoothening are shown in Figure 100 for the case  $\Delta x=50\text{m}$ .

The distribution curves for the other cases (values of  $\Delta x$ ) tested are very similar both qualitatively and quantitatively. The location of mean, modal and minimum values in Figure 100 are described in more detail below, normalized to the desired value of  $\Delta x$  or element area. These normalised values describe equally well all of the cases tested. This suggests that the mesh seeding and smoothening method employed by the mesh generator tool is not sensitive to the number or area of elements being generated and the results can be applied to any uniform area of flexible mesh.

##### 10.4.2.1. No Smoothening

As shown in Figure 100, the initial raw mesh (with no smoothening) contains no elements larger than the maximum area specified. There is however a broad and somewhat skewed distribution of element sizes smaller than this value: the peak or modal value is consistently 0.55-0.58, and the minimum value is consistently 0.30 of the specified maximum  $A$  for all values of  $\Delta x$  tested. Without smoothening, the smallest internal angles of most elements are between  $40^\circ$ - $60^\circ$  and are approximately equally likely to have any value in this range. Angles smaller than  $40^\circ$  become progressively less likely and there are no internal angles smaller than the value specified ( $26^\circ$  in this case).

The smallest element lengths (values of  $\Delta x$ ) are all less than the desired value (50m in the Figure). There are a gradually increasing number of smaller elements, up to a peak or modal  $\Delta x$  which is consistently 0.63-0.69 of the desired value, followed by a sudden truncation of the curve at 0.57 to 0.59 of desired  $\Delta x$ . Mean  $\Delta x$  is 0.74 of the desired value. In this case there is also an isolated peak at a smaller value of  $\Delta x$  equal to [the boundary vertex spacing / 2]. This occurs where  $\Delta x$  is typically smaller than the desired value and therefore the boundary vertex spacing. The mesh generator tool intermittently then creates two elements instead of one between some pairs of boundary vertices, thus forming a well defined sub-

population of elements with this particular length scale. The appropriate spacing of boundary vertices is discussed further in Section 10.7.

By assuming uniform depth and flow speed over the domain, the resulting distribution of  $\Delta t$  mirrors the distribution of  $\Delta x$ , including the same scaling values and isolated peaks. At this stage, the smallest time step (controlling the maximum time step of the model) is related to the double boundary elements. The distribution of the CFL number, as would be calculated by MIKE, is also broad. The boundary elements are again visible as a well defined sub-population at CFL=1. The mean CFL number is 0.71 with a standard deviation of 0.09 to 0.11, indicating that the majority of elements are running at only 60-80% efficiency.

As a simple example of the principles of mesh optimisation, the smallest values of  $\Delta x$  and  $\Delta t$  in this domain are those associated with the double boundary elements. These have a length scale [ $\Delta x = 0.5 \times \text{desired } \Delta x$ ] whereas the next smallest elements have [ $\Delta x = 0.57-0.59 \times \text{desired } \Delta x$ ]. By adjusting the spacing of the boundary vertices (as described in Section 10.7), the double elements could be eliminated. The run time of models using the ‘optimised’ mesh would be reduced to 0.85-0.88 of that required by the original, arguably without any significant change in the spatial resolution.

Appendix B – Optimising Mesh Design in MIKE FM

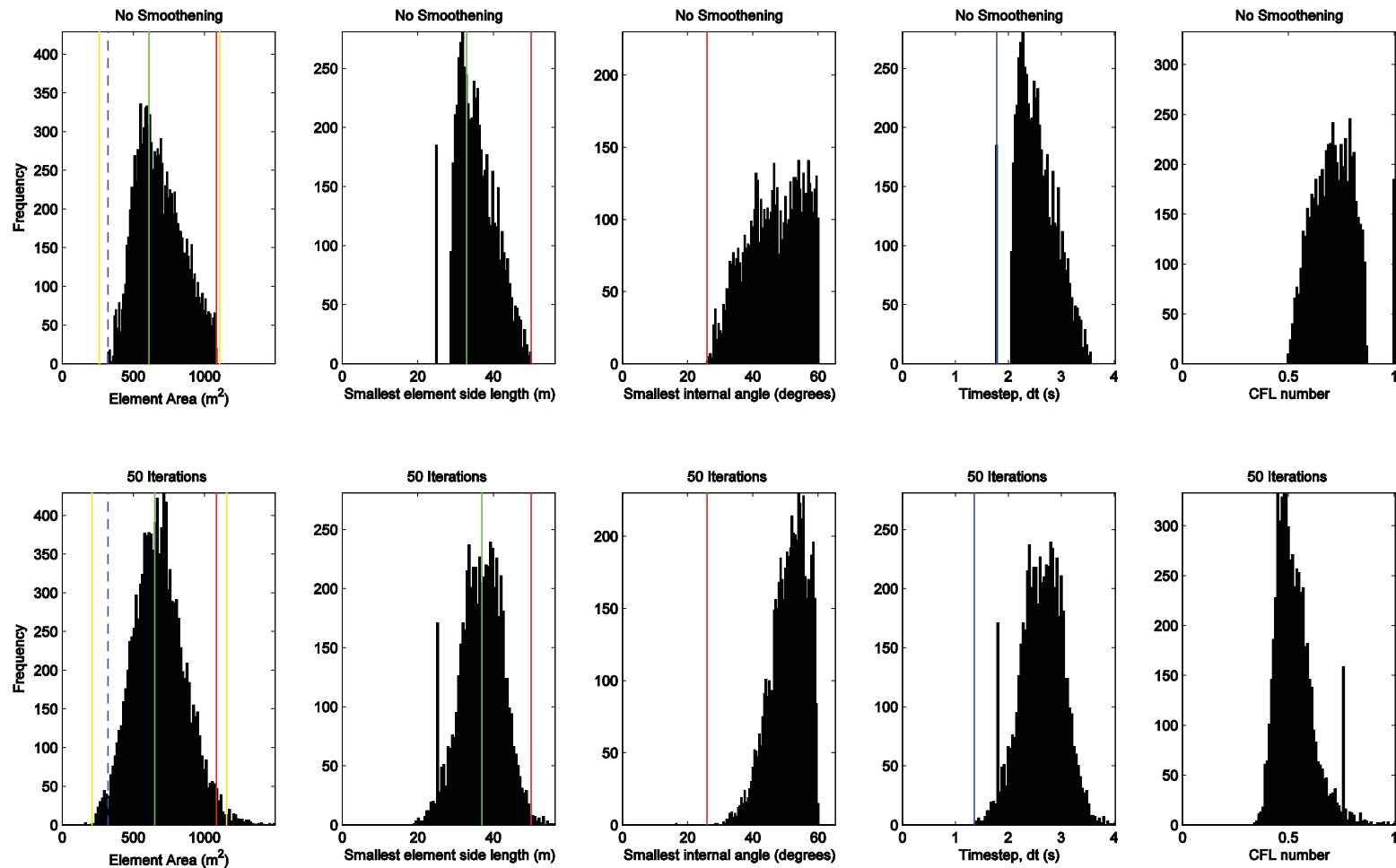


Figure 100. The actual distribution of  $A$ ,  $\Delta x$ ,  $\theta$ ,  $\Delta t$  and CFL in a mesh created by the MIKE mesh generator. Raw mesh (No smoothing) and following 50 iterations of smoothing. Desired  $\Delta x = 50\text{m}$ ,  $A = 1082.5\text{m}$ , minimum internal angle =  $26^\circ$ , boundary vertex spacing =  $50\text{m}$ . Key to lines: red – specified or desired values when creating the mesh; blue solid – minimum values; blue dotted – minimum value in the raw mesh; green – peak or modal value (mean of top ten values); yellow – 99% confidence limits based on a Gaussian distribution.

#### 10.4.2.2. *With Smoothing*

The smooth mesh tool in the mesh generator is used with the intention and effect of increasing spatial uniformity in the mesh. It does not have any effect on the efficiency of the vast majority of elements. However, in order to homogenize the shape of the majority of the elements, a minority of elements become smaller or more elongate (isosceles or scalene in shape) to fill awkward gaps between or within the textural clusters that are formed. This has the unintended consequence of reducing the efficiency of the mesh as a whole by creating a small number of elements with smaller  $\Delta x$  and therefore  $\Delta t$ .

Progressively smoothing each of the test meshes causes the distribution of  $A$ ,  $\Delta x$ ,  $\theta$ ,  $\Delta t$  and CFL to converge on a different set of characteristic parameter distributions (described below). There is no significant measurable change in the distribution of the mesh parameters after 50 iterations of smoothing. Testing shows that it makes no difference to the final result whether the 50 iterations are applied all at once or in smaller steps, e.g.  $10 \times 5$  iterations. The rate of convergence with the 50 iterations mesh is initially high (67% convergence after 5 iterations), becoming slower (89% and 98% after 10 and 25 iterations, respectively). Again, the distribution curves for other test cases using other values of desired  $\Delta x$  are very similar both qualitatively and quantitatively.

As shown in Figure 100, following 50 smoothing iterations, elements are formed within the domain that are both larger than the prescribed maximum area during initial triangulation and smaller than the previous minimum value. The distribution of  $A$  becomes less skewed and closer to Gaussian in shape. The mean value of  $A$  (equivalent to the peak or modal value) is consistently 0.63 of the desired value. The smallest value of  $A$ , obtained as the lower 99% confidence interval, is consistently 0.18-0.21 of the desired value. The majority of elements become closer to equilateral in shape both visually and as shown by the increasing skew of the distribution of  $\theta \rightarrow 60^\circ$ . In most cases the smallest of all internal angles increased only slightly (by 5%, less than  $1^\circ$ ); however, in one case the smallest angle in the domain as a result of smoothing was reduced to  $16^\circ$  (from  $26^\circ$ ).

There are a greater number of elements with smaller sides (values of  $\Delta x$ ). The smallest values are consistently 0.33-0.38 of the desired value (compared to 0.5 for double boundary elements or 0.57-0.59 for normally created elements in the un-smoothed mesh). The mean value of  $\Delta x$  however does not change with smoothing and is constant and consistent at 0.74 of the desired value.

The creation of elements with  $\Delta x$  smaller than the previous minimum value means that the smallest and limiting values of  $\Delta t$  in the various test cases are also smaller (by a factor 0.67-0.76) compared to meshes with no smoothing. Smoothing therefore increases the run time of these test meshes by a factor 1.31-1.50.

As a second simple example of mesh optimisation, by removing or enlarging less than 50 of the smallest elements in the smoothed mesh (as described in Section 10.9), then the run time of models using the optimised mesh would be reduced to 0.80 of the original (becoming then limited by the double boundary elements). Removing the double boundary elements prior to initial mesh triangulation, as described in the previous Section, would further reduce the run time.

#### 10.4.3. Complex domains

The above method was also applied to the Oresund Sound domain, using only the land boundary files to provide a more complex domain outline. The depth was again assumed to be constant (20m) and three values of  $\Delta x$  were tested = [500m, 750m, 1000m], producing domains with between 29,581 and 7,781 elements. The boundary spacing was equal to  $\Delta x$ . Meshes with no smoothing and 50 iterations of smoothing were tested for each case.

The two finer meshes followed the same distribution patterns as described in Sections 10.6.1 and 10.6.2 for raw and smoothed meshes. The coarser mesh contained a very small minority (less than 10) of particularly small elements which further reduced the minimum element area and  $\Delta x$  values, however, the vast majority of elements followed the same distribution as the other test cases described so far.

## 10.5 Choice of vertex spacing for describing boundaries and structures

Meshes are created within domains or polygons delimited by user defined boundaries. Nodes (default - blue squares) represent the terminal points of individual arcs which are shaped by vertices (default – red circles). During initial triangulation, whatever the user specified maximum element area, the mesh generator will force elements to be created that use all of the nodes and vertices. A poor choice of boundary vertex spacing that does not match the desired element resolution may cause unnecessarily small elements to be created, reducing the efficiency of the model. Problems are mainly caused when the spacing is less than, similar to or in small multiples of the desired value of  $\Delta x$ .

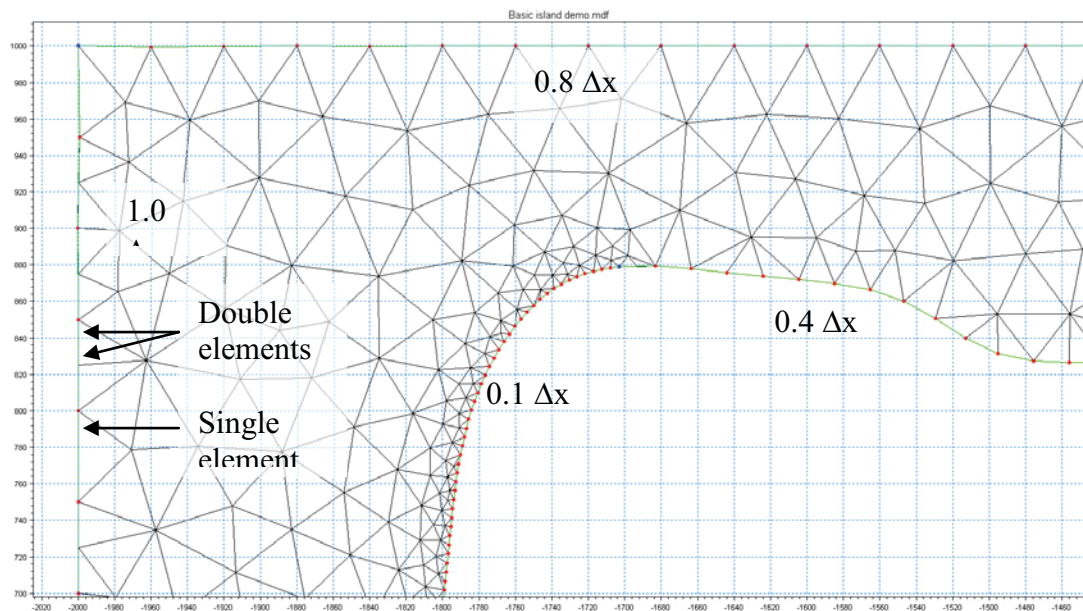


**Figure 101. Examples of optimised and non-optimised boundaries: (top) optimal broad spacing for the desired element area ( $=0.8 \Delta x$ , calculated using Eq. 5); (middle right) optimal reduced spacing ( $=0.4 \Delta x$ ); (left) sub-optimal, too large spacing ( $=\Delta x$ ) causes double elements to be intermittently formed between pairs of vertices; (bottom middle) poorly optimised spacing ( $=0.1 \Delta x$ ) resulting in a sharp transition between elements of different size and a large number of very small element lengths, increasing overall run times.**

If the vertices are more closely spaced than the equivalent length scale of the requested maximum element area (e.g. calculated using Eq. 5) then elements of smaller area will be created at the boundary, larger elements representative of the desired value will be created away from the boundary and a steep gradient of element size will be applied between the two. An example of this is shown in Figure 101.

If the boundary spacing is larger than the length scale of the majority of the elements being initially triangulated, the mesh generator may force two or more elements to be created between two adjacent boundary vertices (Figure 101, labelled as ‘ $1.0\Delta x$ ’). These elements will equally divide the space between the boundary vertex pair and may result in relatively small values of  $\Delta x$  and  $\Delta t$ . It was shown in Section 10.6.1 without smoothing, these elements are likely to be the smallest in the domain, thus controlling the time step of the

model and reducing its efficiency; however, following smoothening, even less efficient elements are created and double boundary elements become less important. In addition to reducing efficiency, occasional double boundary elements also create less uniform element spacing at the boundary.

It was found that double elements at the boundaries could be avoided or at least discouraged by applying boundary vertex spacing at least 20% smaller than the desired value of  $\Delta x$ . The mesh generator has less problems creating single elements at this spacing as it is approximately similar to the mean value of  $\Delta x$  (0.74 of desired  $\Delta x$ ) for the open part of the area being triangulated. Following this logic, the minimum boundary spacing that can be applied without unnecessarily reducing efficiency is equivalent to the smallest values of  $\Delta x$  created in an open mesh, which (from Section 10.6.2) is conservatively 0.40 of desired  $\Delta x$  following smoothening (see Figure 101).

As illustrated in Figure 102, it is therefore recommended that the boundary vertex spacing be between 0.40 and 0.80 of the desired value of  $\Delta x$  (or the value of  $\Delta x$  implied by Eq. 5 for the desired local element area). The higher value should be used if the detailed boundary shape is not considered important to the overall solution or if a structure is being added that will be later removed, preferably without altering the local mesh. The lower (or some intermediate) value can be used if additional detail is required. If boundary data is only available at a coarse resolution, boundary vertex spacing of 1.2-1.7  $\Delta x$  can also be used as the mesh generator will consistently create pairs of elements with efficient length scales between each pair of vertices. Using larger multiples of  $\Delta x$  causes unpredictable numbers of elements to be created, thus introducing smaller edges and heterogeneity into the mesh. Open boundaries should contain only enough nodes and vertices to describe the shape of the boundary (preferably a straight arc with two nodes and no vertices).

If the user wishes to have higher resolution at the boundary (typically with progressively shallower water depths) then it is better to manually apply a more gradual increase in mesh resolution by using the mesh refinement tool (see Section 10.8.1) or a series of manually created nested polygons (see Section 10.8.2). The typical recommendation is that the area of elements in adjacent polygons or regions should differ by a maximum factor of approximately 2 (*Pers. Comm.* Henrick Kofoed-Hansen, 9<sup>th</sup> DHI User Group Meeting 2007). Through analysis of Eq. 4,  $A \propto \Delta x^2$ , thus, reducing the area by a factor of 2 causes the representative length scale of elements to decrease by a factor 1.41 (becoming 0.71 the size of the larger elements); if the area is reduced instead by a factor of 4, the element length scale is decreased by a factor 2.

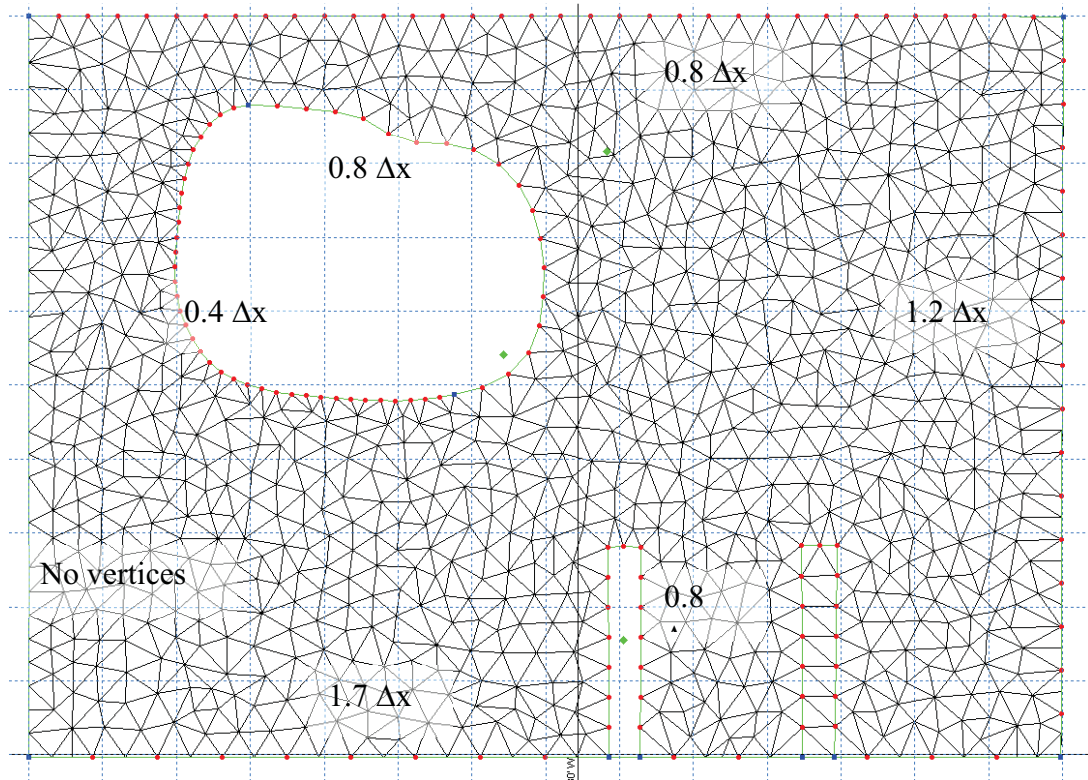


Figure 102. Examples of optimised boundaries: (top and right of island) optimal spacing ( $=0.8 \Delta x$ , calculated using Eq. 5) with best control for the applied maximum element area; (left of island) optimal reduced spacing ( $=0.4 \Delta x$ ); (right) finest optimal spacing for coarse boundary data ( $=1.2 \Delta x$ ); (bottom) coarsest optimal spacing for coarse boundary data ( $=1.7 \Delta x$ ); (left) spacing applied by the mesh generator at an open boundary (no vertices). Also shown (extending from the bottom boundary) is the effect of using one of these optimal spacings to create a structure that may be switched ‘on’ (the right side) and ‘off’ (the left side) without significantly altering locally the mesh resolution.

## 10.6 Refining a mesh using local water depth

### 10.6.1. The refine mesh tool in MIKE zero

#### 10.6.1.1. Basic functionality and best practice

The mesh generator tool applies a spatially variable distribution of maximum element area, determined by the local water depth, to the mesh (see the appropriate DHI user guide). The intention of this tool is to optimise the co-variation of water depth and element area (therefore  $\Delta x$  and therefore  $\Delta t$  and CFL). Essentially, elements in deeper water remain large and elements in shallow water are made smaller. Before the refine mesh tool may be used, at least one polygon must be present in the domain, an initial mesh must be created and the bathymetry data must be interpolated.

The general layout of the ‘Mesh Refinement’ GUI is shown in Figure 103. For the purposes of this study, the minimum and maximum depth coefficients are referred to herein as  $h_{\min}$  and  $h_{\max}$ , the corresponding element area values are referred to as  $A_{\min}$  and  $A_{\max}$ . In normal use, a linear variation (indicated by a straight line curve from corner to corner of the small set of axes) in local maximum element size is specified between  $h_{\min}$  and  $h_{\max}$  (the default setting is the range of water depths in the mesh file). The user may also choose to apply a non-linear variation by clicking on and dragging the curve. It is important to note that

the refinement process will only reduce the size of elements from the initial mesh created – existing elements will not be enlarged. When first opened, the plotted curve may not be a straight line between the axis corners (as shown in the Figure). In this case, it is important to simply click once on the curve which should rectify or reset the curve shape.

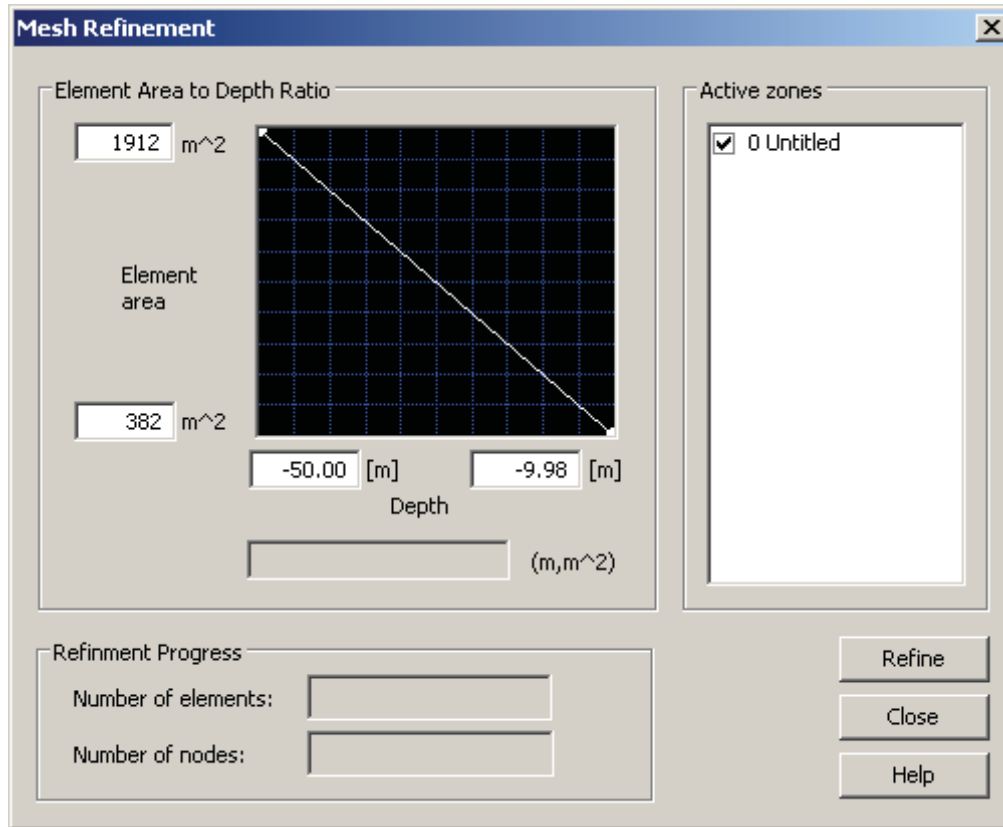


**Figure 103. The GUI of the Mesh Refinement tool in Mike zero (2007 release).**

The optimal area for any given element is related primarily to the water depth through Eq. 3 and Eq. 4, as shown in Section 10.3.2; the local flow velocity is of secondary importance under most circumstances as it is likely to be small in comparison to the depth controlled wave celerity term (typically  $31\text{-}157\text{ms}^{-1}$  for 10-50m water depth). As shown in Figure 104, the form of the optimal relationship between water depth, element area and  $\Delta t$  is linear. It is therefore appropriate to refine the mesh according to a linear relationship between depth and element area. However, although an optimal value may be calculated, it has been shown in Section 10.6 that prescribing a particular value of  $A$  does not result in a uniform distribution of elements of that area, but rather a broad but predictable distribution of smaller elements. Therefore, if a mesh of variable element area is applied to a domain with spatially varying water depth, it is expected that there will be broad distributions of  $\Delta t$  and CFL due to both the variation in depth and in actual element size.

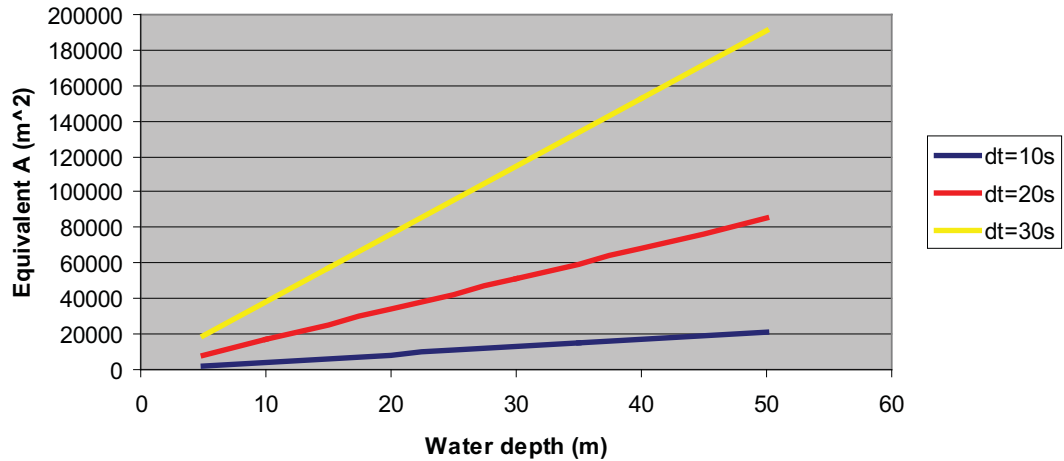


**Figure 104.** The general relationship between water depth, equivalent element area and  $\Delta t$ . Calculated using Eq. 3 and Eq. 4. for fixed parameter set [CFL=1,  $|u|=0$ ,  $\theta=60^\circ$ ].

Following mesh refinement, it is expected that the controlled co-variation of element area and local water depth will result in a more closely constrained final distribution of  $\Delta t$ , as shown schematically in Figure 105. In the initial uniform mesh, elements in deeper water are less efficient than those in shallower water and control the smallest (limiting) time step; the majority of elements in shallower water are relatively inefficient as they could be made smaller and run faster without requiring a shorter time step. Following refinement, there is a relative increase in the number of elements in shallower water depths as elements are made individually smaller but must cover the same area. Smaller elements become more efficient (closer to the limiting value of  $\Delta t$ ) and the resolution of the mesh is improved without adding additional time steps.

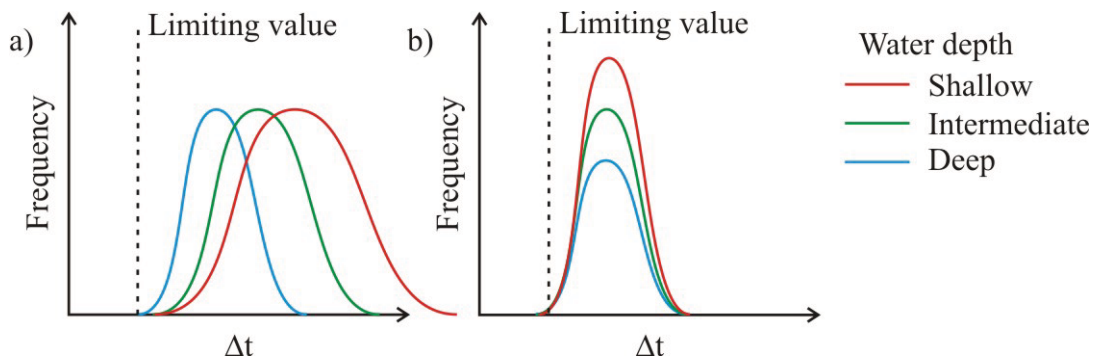


**Figure 105.** The conceptual effect of refining a mesh according to depth. Schematic distribution of  $\Delta t$ : a) with a uniform mesh spanning a range of water depths; b) following mesh refinement.

A simple test was set up using the rectangular test domain. An initial uniform coarse grid was created, smoothed by 50 iterations and a scatter data set interpolated to form a deep pool (-50m) in the centre of the domain, the depth decreasing linearly to -5m at the edges (Figure 106). The mesh was then refined within the range of depths present, using the refinement coefficient listed in Table 10, smoothed (by 50 iterations) and then re-interpolated. The resulting distribution of  $A$ ,  $\Delta x$ ,  $\theta$ ,  $\Delta t$  and CFL are shown in Figure 108. The Figure indicates the extent to which the distribution of  $\Delta t$  and CFL are compressed, thus optimising the majority of the mesh, however, the majority of elements have a CFL number of 0.25-0.5, suggesting that if a small minority of elements could be eliminated, then run times could be improved by approximately a factor 2. When element subpopulations are

identified independently by water depth, the distribution of values of  $\Delta t$  (Figure 107) follow generally the patterns described in Figure 105.

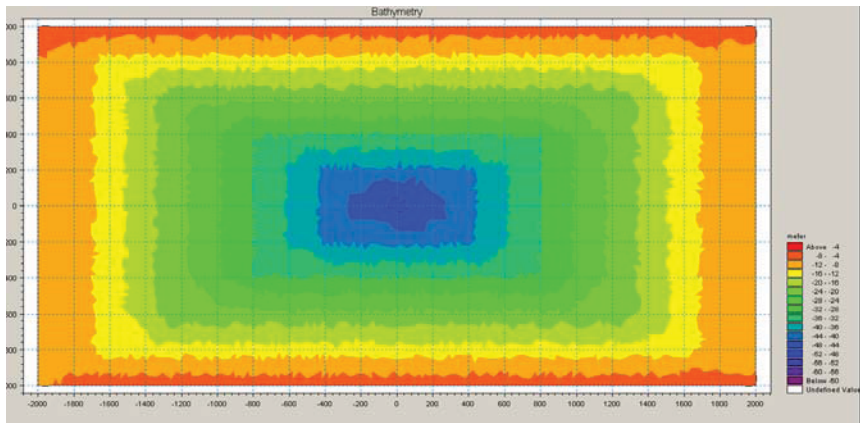


Figure 106. Simple domain with variable depth (-50m in the centre to -5m at the edges) for use in testing the effect of the refine mesh tool.

	Deep	Shallow
CFL <sub>max</sub>	1	1
u	0	0
<b>Depth</b>	<b>50</b>	<b>5</b>
Desired dx	50	15.8 <i>Eq. 3</i>
resultant dt	2.3	<i>Eq. 6</i>
<b>Equivalent A (m)</b>	<b>1082.5</b>	<b>108.3</b> <i>Eq. 4</i>

Table 10. Refining coefficients for the test case. The values of CFL<sub>max</sub>, |u| and desired  $\Delta x$  in deep water are fixed and all other values are derived from those for a chosen shallower depth of 5m.

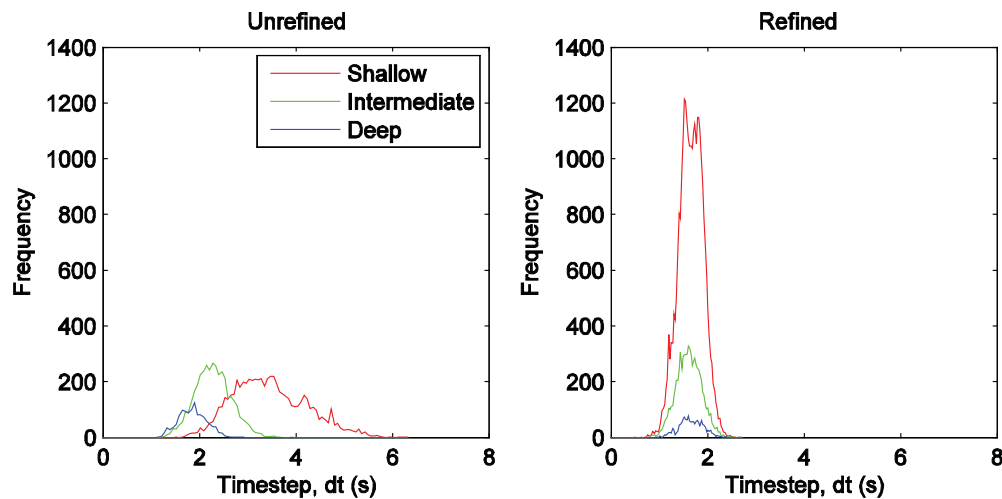


Figure 107. Distribution of  $\Delta t$  for elements in a simple uniform and depth refined mesh. Deep  $-50\text{m} < h < -35\text{m}$ ; intermediate  $-35\text{m} < h < -20\text{m}$ ; shallow  $h > -20\text{m}$ .

Appendix B – Optimising Mesh Design in MIKE FM

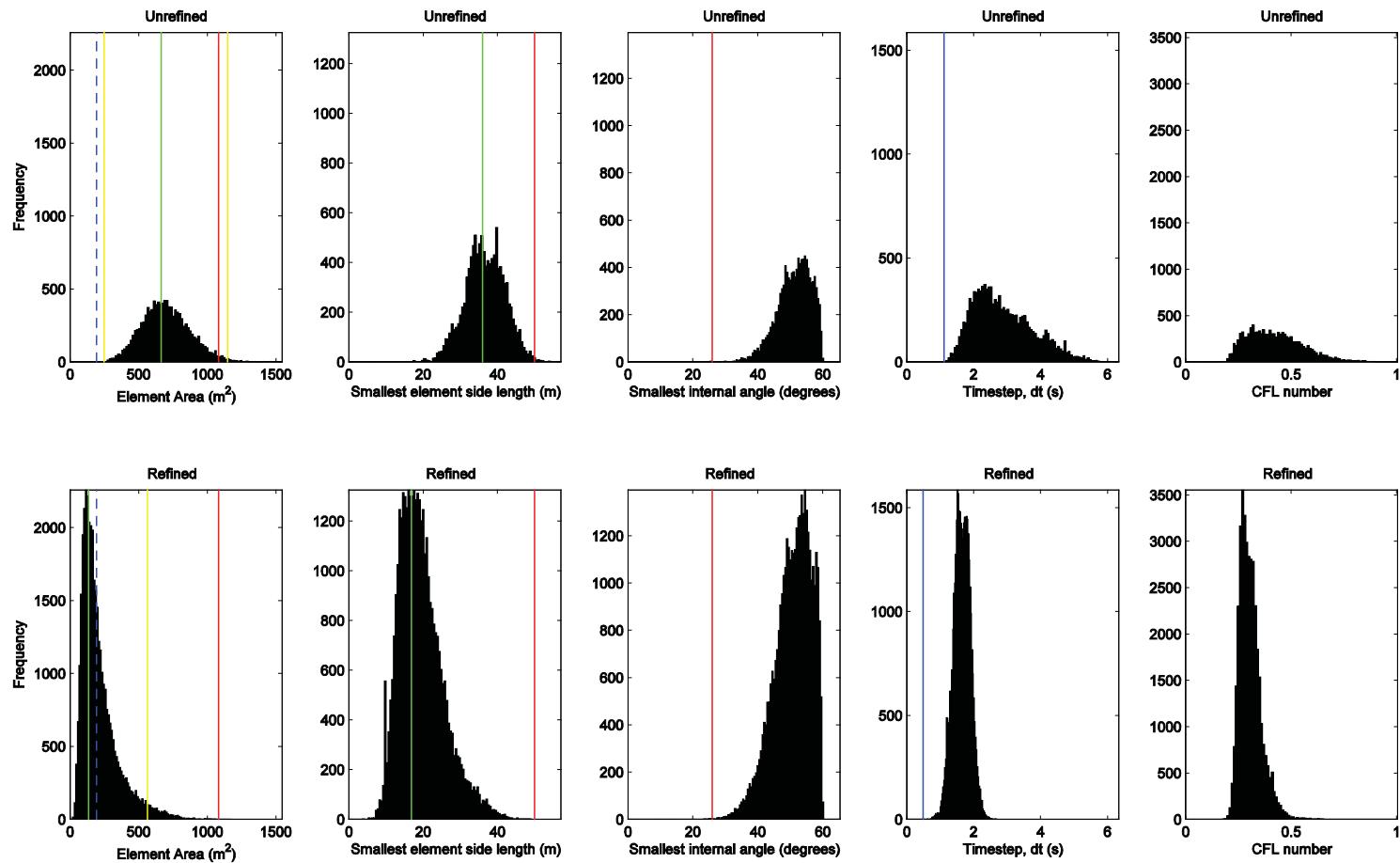


Figure 108. The actual distribution of  $A$ ,  $\Delta x$ ,  $\theta$ ,  $\Delta t$  and CFL in meshes created by the MIKE mesh generator. Uniform unrefined mesh and mesh following refinement according to depth. Key to lines: red – specified or desired values when creating the mesh; blue solid – minimum values; blue dotted – minimum value in the raw mesh; green – peak or modal value (mean of top ten values); yellow – 99% confidence limits based on a Gaussian distribution.

The best choice of mesh refinement is largely dependant upon the requirements of the user. If a certain value of  $\Delta x$  is required in a region of interest within the model (perhaps contractually or based on previous experience), then the maximum element area of the initial mesh, the boundary vertex spacing and the mesh refinement parameters can be calculated by the user, using the principles described in the present study.

### 10.6.1.2. *Optimisation of the refine mesh procedure*

A refined mesh has a higher resolution in shallower water and a larger total number of elements. By using the simple method described in the previous Section to calculate the refinement coefficients, the minimum time step does tend to be reduced from that of the uniform mesh and, in conjunction with the increased number of elements, the total number of calculations that must be made and therefore the real run time of the model, is increased (by a factor of 5.3 in the example used).

When refining a mesh, the total number of elements will always be increased but it is possible to reduce any unnecessary reduction in the limiting value of minimum  $\Delta t$ . Figure 107 indicates that the reduction in minimum  $\Delta t$  is primarily caused by the distribution curves for elements in shallow and intermediate water depths (the red and green lines) extending further left into smaller values of  $\Delta t$  following refinement. During the refinement process, the largest element areas in the deepest water depths are set during the initial triangulation. The area of these elements is not affected during the refinement process (unless a value of  $A_{\max}$  smaller than the initial triangulation area is specified); the distribution of  $\Delta t$  for elements in deep water (the blue line) is not shifted and therefore do not contribute to the reduction in efficiency.

The position of the curves for shallower and intermediate water depths can be controlled by adjusting the value of  $A_{\min}$  from that calculated directly using Eq. 4. As shown in Figure 109, increasing  $A_{\min}$  has the effect of moving the curves for shallower and intermediate water depths to the right causing the minimum value of  $\Delta t$  to be controlled instead by the deep water curve which does not move as a result of mesh refinement. Conversely, reducing  $A_{\min}$  has the effect of moving those curves to the left, thus further reducing the minimum, limiting value of  $\Delta t$  and the efficiency of the mesh. The left hand slope of the three curves approximately line up in this example when using  $[A_{\min} \times 2.0]$ . Note that the total number of elements (the area under the curves) decreases as a larger adjustment value is applied.

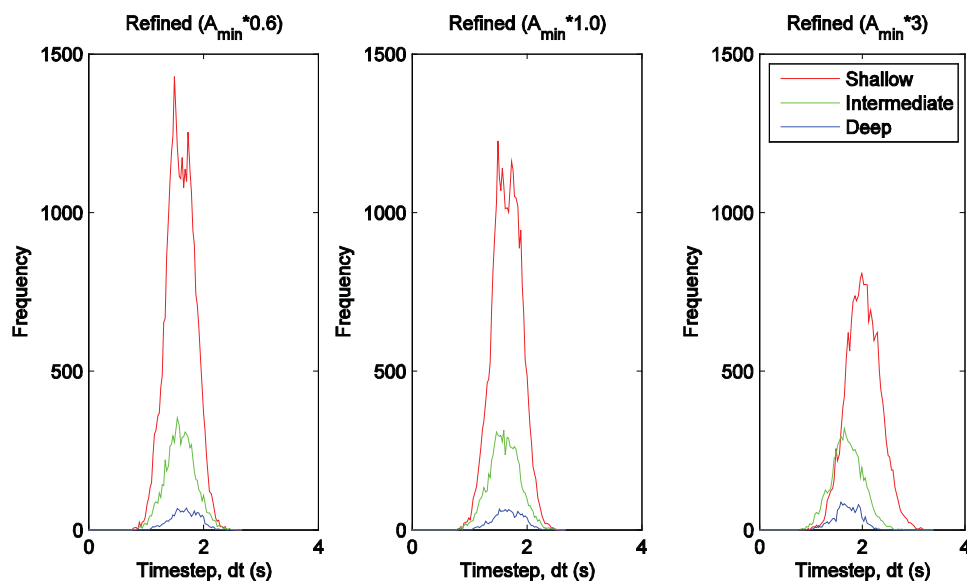


**Figure 109. The effect of modifying  $A_{\min}$  in the distribution of  $\Delta t$  for elements in different water depths. Deep  $-50\text{m} < h < -35\text{m}$ ; intermediate  $-35\text{m} < h < -20\text{m}$ ; shallow  $h > -20\text{m}$ .**

Figure 110 summarises the effect of using a modified value of  $A_{\min}$  on the minimum value of  $\Delta t$  and the overall model run time; the effect of removing a certain small number (10 or 20) of the smallest limiting elements from the mesh is also shown. By increasing the value of  $A_{\min}$  (making the smaller elements in shallower water larger), the total number of elements decreases and the minimum limiting value of  $\Delta t$  is gradually improved but becomes constant beyond a modification factor of 2. This corresponds to the point at which the distribution of  $\Delta t$  for elements in shallow water moves to the right of the curve for elements in deep water. As expected, there is a corresponding decrease in the overall model run time, the rate of decrease is greatest between modification factors of 1 and 2 (as  $\Delta t$  increases); the rate of improvement becomes smaller but is still significant at factors  $>2$ . If  $A_{\min}$  is instead decreased, there is a non linear increase in model run time.

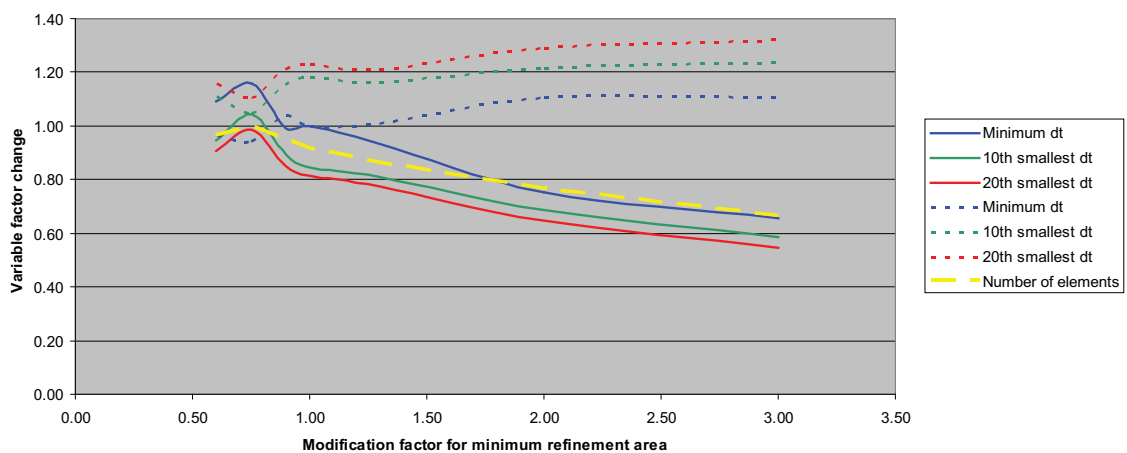


**Figure 110. The effect of modifying  $A_{\min}$  on model run time (solid lines) minimum  $\Delta t$  (dotted lines) and the number of mesh elements. Values normalised to the value of minimum  $\Delta t$  at nil modification (factor =1.0).**

The study of mesh refinement described here not take into account the potentially important effect of significant flow velocities in shallow water depths, nor the variability in actual local water depth due to tidal fluctuation during the model run.

### 10.6.1.3. *Effect of mesh resolution on tidal propagation rates*

There is also a commonly held rule of thumb that there is an upper limit to the largest element size that should be applied in deeper water. This effect is observed during traditional sensitivity testing of mesh resolution – by starting with a coarse mesh and progressively increasing resolution, time series of results from selected points or transects converge upon a more consistent result. The chosen mesh is the coarsest one to not benefit significantly from further refinement.

This point was discussed at the 9<sup>th</sup> UK DHI User Group Meeting (2007). It was generally proposed that the problems associated with a too coarse mesh resolution is caused by water volume entering an element which is then instantaneously dispersed through the whole element. If the element is ‘too large’, fluid may be able to propagate more quickly through the domain as a result. The underlying cause of the problem is evidently not well understood but the method for correction is as described in the previous paragraph.

In the context of the present study as a whole, one theoretical cause of this problem may be as follows. The time step of a model is controlled by the single mesh element with the

smallest time step. Due to the desire to maintain high resolution boundary vertex spacing or mesh resolution near to boundaries, this element is often located at the boundary or in shallow water. All other elements are therefore suboptimal in comparison; specifically, the single optimised element allows the tidal wave to propagate  $1.0\Delta x$  every  $\Delta t$  whereas the tidal wave can only propagate some fraction of  $\Delta x$  through every other element. The model does not spatially resolve the passage of the information over sub-element scales and instead averages it over the entire area of the element. Some of that information is then passed on to other adjacent elements at the next time step, effectively increasing the velocity of the tidal wave.

This concept is described schematically using rectilinear grids for simplicity in Figure 111 and Figure 112. Figure 111 shows that in the simple case of a truly uniform mesh, using  $CFL=1$ , the crest of the tidal wave (shown as the red line) can propagate fully and correctly  $1.0\Delta x$  each  $\Delta t$  (an implicit result of using the CFL number to calculate a dynamic time step). However, if a smaller value of CFL (e.g. 0.8) is used, the tidal wave crest can only propagate  $0.8\Delta x$  each  $\Delta t$ . Because the model does not resolve the partial transfer of the location of the crest, the model allows ‘leakage’ of information into the next element at subsequent time steps, i.e. at  $i=3$  there is an increase in the water level in elements  $j=3$ , despite the crest not having reached those elements yet.

This concept applies to grids of variable element area also, where larger elements in deeper water are ‘too large’ (Figure 112). The Figure shows that in shallow water (typified by smaller elements), the time step is suitable that the tidal wave propagating at  $\sqrt{gh}$  will travel approximately  $1.0\Delta x$  in  $\Delta t$ . However, in deeper water the value of  $\Delta t$  is not large enough to allow full translation of the information and leakage occurs (i.e. at  $i=3$ , there is an increase in the water level in the third element, despite the crest not having reached that element yet), thus erroneously speeding up the passage of information.

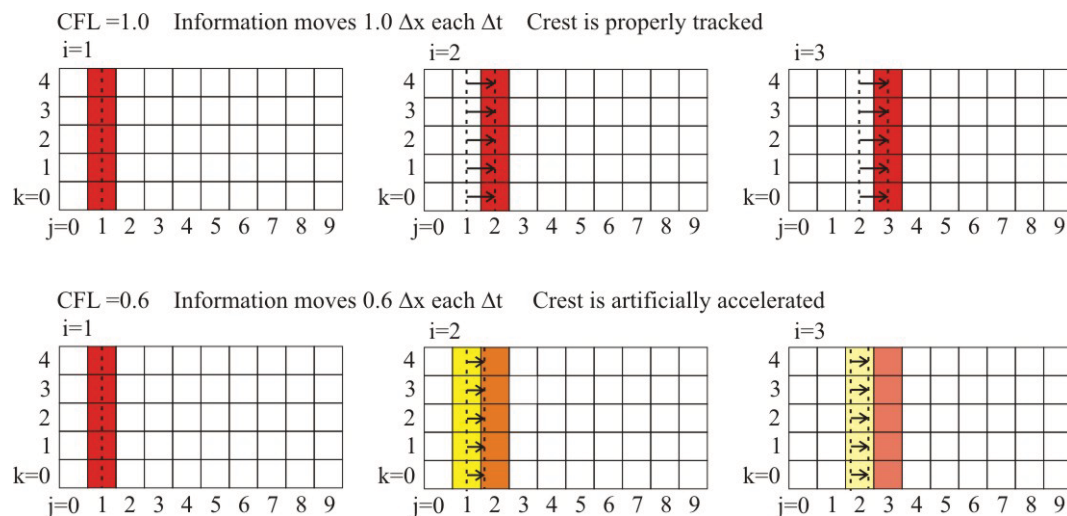


**Figure 111. Example of how non-optimised element size can artificially increase the propagation rate of the tidal wave. Example of uniform rectilinear mesh. The ‘true’ position of the wave crest is indicated by the dashed line; arrows indicate the actual distance covered by the tidal wave each  $\Delta t$ ; depth of colour indicate the local water elevation.**

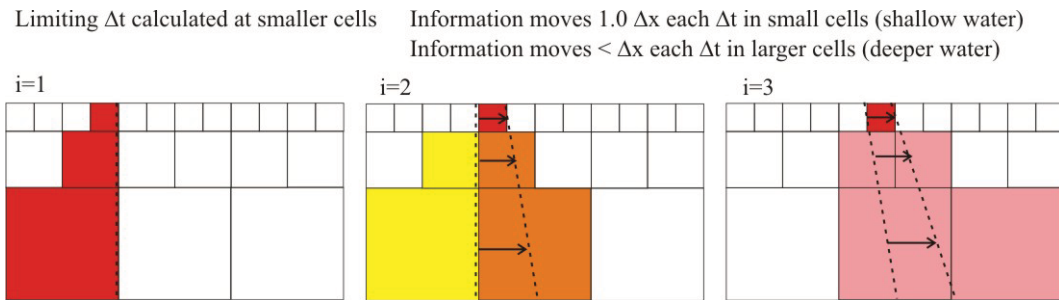


**Figure 112. Example of how non-optimised element size can artificially increase the propagation rate of the tidal wave. Example of non-uniform rectilinear mesh. The ‘true’ position of the wave crest is indicated by the dashed line; arrows indicate the actual distance covered by the tidal wave each  $\Delta t$ ; depth of colour indicates the local water elevation.**

If the above explanation is correct, the solution is therefore to ensure (as far as possible) that all elements in all water depths are optimised such that information can travel approximately  $1.0\Delta x$  in each  $\Delta t$ , i.e. that  $\Delta x \approx \Delta t \times \sqrt{gh}$ . Another solution would be to increase the bed resistance at elements in deeper water to slow down the propagation rate. Traditionally both of these actions may be applied for other reasons: during ‘mesh resolution sensitivity/convergence testing’ the resolution of the mesh is reduced until it is optimised experimentally; separately, as a standard calibration tool, it has been reported that some users increase bed resistance in deeper water by progressively lowering the value of the Mannings number (see Lambkin 2007 ‘*A Review of the Bed Roughness Variable in MIKE21fm HD and ST Modules*’). The methods described in this study (up to and including mesh refinement) provide the means to calculate directly the appropriate choice of element area to ensure that  $\Delta x$  is matched as closely as possible to  $\Delta t$  for all elements in all parts of the mesh. On this basis it also seems all the more important to use the maximum value of CFL ( $=1.0$ ) and to undertake removal of the small number of limiting elements (see Section 10.9) which could potentially cause all elements to incorrectly model the speed of tidal wave propagation. When refining a mesh, it would still be appropriate to positively adjust the value of  $A_{\min}$  as this brings more elements closer to the limiting value of  $\Delta t$  or CFL.

### 10.6.2. Manual mesh refinement

It is also not unusual to refine a mesh manually by creating polygons (user defined sub areas) within the domain and manually specifying the maximum element area for each polygon prior to basic triangulation and smoothing. Sub-areas are typically defined in order to provide: high resolution (for detail and accuracy) at the area of interest; lower resolution (for efficiency) in deeper water and away from the area of interest; bands of intermediate resolutions to provide a gradual transition between the former two general regions; and, higher resolution in areas of complex bathymetry or boundary shape where it is considered important for overall accuracy or stability of the model.

No specific experiments were carried out as part of the present study to examine the best way of manually refining a mesh in this way. However, the key points from Section 10.8.1 may be applied in the following ways:

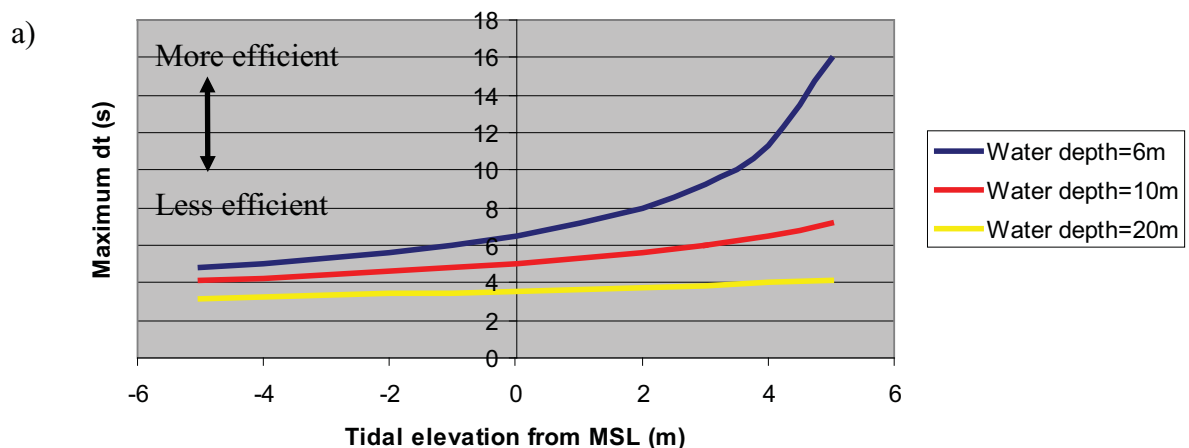
1. The maximum element area chosen for each polygon should be calculated on the basis of the maximum water depth in that polygon. Given that water depth typically increases from the shore and that the shore is the area of interest, it is therefore more efficient to have thinner (in a cross shore direction) polygons which span a smaller range of water depths.
2. As a first approach, the recommended step in specified area between two polygons should be no more than a factor of 2. (*Pers. Comm.* Henrik Kofoed-Hansen, 9<sup>th</sup> DHI User Group Meeting 2007).

3. As the elements in shallow water are likely to control the time step of the model, it is useful to know what is the smallest element area that can be applied offshore (in deeper, open water) without reducing efficiency. Once the finest resolution has been set, the smallest value for area specified in the polygon containing the deepest water should be approximately 0.5 times that calculated on the basis of Eq. 3 and Eq. 4. This value may be increased (if the user feels that the resulting resolution in deeper water is still unnecessarily fine) thus reducing the number of elements and therefore the run time of the model. However, see also point number 4 below. Using a smaller value than that calculated is likely to increase run times more substantially.
4. If a relatively fine resolution is used in shallower waters or at the boundary, then elements in deeper water should not be made too coarse (see Section 10.8.1.3). If elements are made too large, then the speed and form of the tidal wave propagation through the domain can be anomalously affected.

## 10.7 Dealing with individual small elements

It has been shown that meshes, created using the software tools provided, contain a broad distribution of sizes and shapes in comparison to the single value specified. There are typically a small number of limiting elements that, because of their combination of shape, size and local water depth, require a much smaller time step for stability than the majority of elements. Either through the dynamic time stepping function or as a simple requirement for stability, these smaller elements then control the time step of the model as a whole.

As shown in Figure 113, the least efficient state (time step) of individual elements is that calculated using Eq. 3 for the chosen value of maximum CFL, the greatest anticipated local water depth = [initial water depth to Mean Sea Level + the maximum tidal elevation] and the largest anticipated value of  $|u|$ .



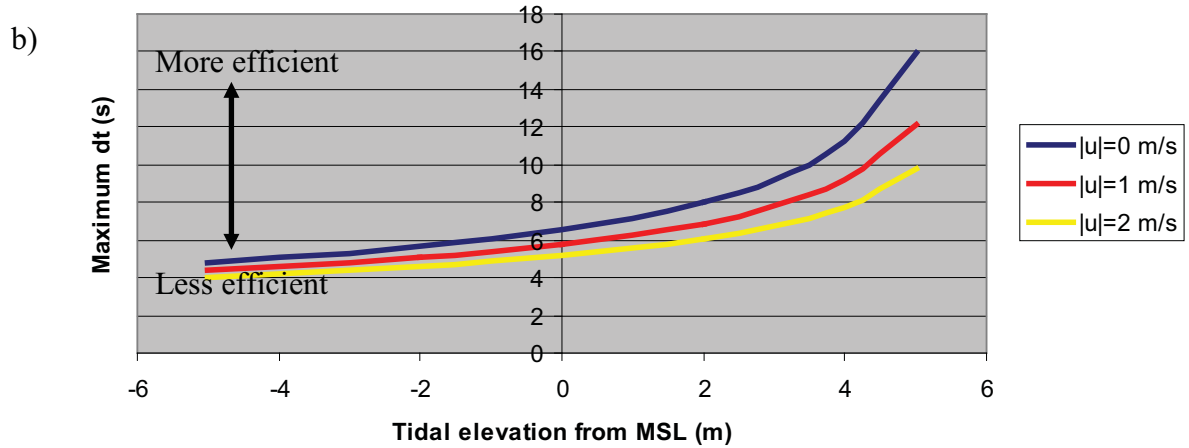


Figure 113. The effect of (a) variable water depth measured to MSL ( $|u|=0 \text{ ms}^{-1}$ ) and (b) variable  $|u|$  for fixed water depth=6m, on  $\Delta t$  calculated using Eq. 3, for fixed parameter set [CFL=1,  $\Delta x=50\text{m}$ ].

All of the test meshes used in the present study (123 meshes) were re-analysed to show the effect on model run time if the least efficient elements were ‘fixed’, i.e. if the smallest length of those elements were to be manually removed or made larger. Figure 114 shows that the majority of meshes would benefit from fixing of up to 100 small elements (a very small proportion of the total number), reducing run times significantly by a factor between 0.85 and 0.65, depending upon the mesh. The meshes that benefited most from fixing the first 100 elements were the more complex domains containing narrow and constricted boundaries (e.g. Oresund Sound) and simple domains (with both uniform and refined mesh area) where a relatively large element area (i.e. a small total number of elements) was specified.

The majority of the benefit is gained by fixing the first 50 elements and this is also likely to be a practicable limit to the number of elements that can be manipulated manually within the time constraints of a commercial project. The Figure also shows the proportion of benefit gained from fixing less than, but up to, the first 50 elements. Typically, more than 50 -60% of the potential benefit can be gained from fixing only the first 20 elements.

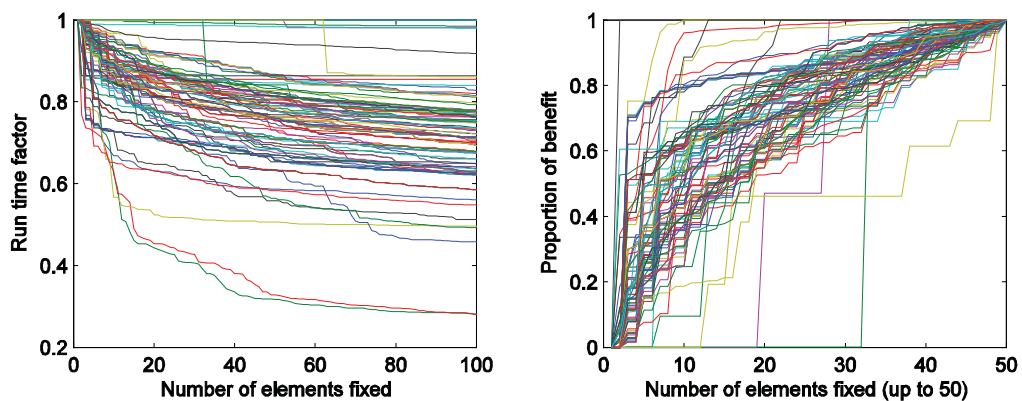


Figure 114. The effect of ‘fixing’ (removing or enlarging) the smallest elements in a mesh. Results for all meshes used in the present study. Effect on overall model run time (left) and the proportion of benefit gained by fixing up to the first 50 elements (right).

The knowledge that a small number of elements need to be changed is not useful unless a method exists by which to fix them. Traditional methods used to deal with small elements at the land boundaries include moving, adding or deleting vertices from the boundary. Small elements away from the boundary may be enlarged by specifying a larger (or slightly different) element area within than polygon when creating the initial mesh, however, this will

be to the detriment of the efficiency of the other elements in that polygon. The model will then become limited by the minority of elements in another polygon which could also be usefully fixed.

Matlab code is provided in Appendix B for the purposes of manually manipulating the size and shape of individual elements in an existing mesh. The best use of this tool has not yet been tested but it is provided here with the intention that users may experiment with it and report back to the community as a whole.

## 10.8 Summary of findings

### 10.8.1. Summary of sensitivity studies

If it is found that a model has inefficient run times due to dynamic time stepping more frequent than the time step theoretically required, the following rules of thumb may be used to decrease run times.

- Increase element area generally.
- Increase element area in deeper water depths.
- Increase element area in regions with stronger flows.
- Increase the maximum permissible CFL number.

In order to choose which of these changes to apply, the user should create a map of CFL numbers (a standard user defined output of the model), identifying those regions where generally high CFL numbers are located and applying the appropriate rules of thumb to that area.

In addition, it may be calculated that the element resolution can be increased in certain regions (increasing the run time only linearly in proportion to the total number of elements) without causing more substantial non-linear increases in total run times by forcing additional (dynamic) time steps to be introduced.

This sensitivity study has demonstrated that:

- To encourage efficient model run times, the value of  $\Delta x$  should be chosen carefully with consideration for the expected parameters ranges of  $h$  and  $|u|$ , and with a view to matching the resulting value of  $\Delta t$  with a desired value, based on knowledge of the system being investigated.
- There needs to be a method by which to apply the identified or desired value of  $\Delta x$  through the mesh generator tool where only the triangular element area and minimum internal angle can be specified.
- The accuracy of the mesh generator tool must be tested in order to be confident in the resulting distribution of  $\Delta x$  by choosing a particular maximum element area.

### 10.8.2. Summary of uniform mesh studies

When used to populate a domain or polygon with elements of a specified area, the flexible mesh generator tool actually creates elements with a broad but predictable distribution of element areas. The uniformity of element shape, described by the uniformity of internal angles, and the resulting smallest triangle side length are also broadly but predictably distributed. The statistical distribution is apparently independent of the absolute size of the elements, the number of elements being created and the shape of the model domain or

polygon boundaries. Exceptions may include meshes with a relatively small total number of elements, e.g. <3-5000, or, in domains where significantly narrow constrictions (approximately less than  $2-3\Delta x$  wide) are formed. The expected distribution of element areas and  $\Delta x$  are summarised in Table 11.

	No smoothening	50 Iterations
<b>Area</b>		
Mean	0.63	0.63
Min*	0.3	0.18 - 0.21
Peak**	0.55 - 0.58	
<b>dx</b>		
Mean	0.74	0.74
Min*	0.57 - 0.59	0.33 - 0.38
Peak**	0.63 - 0.69	

**Table 11. Summary of the statistical distribution of element area and smallest side length in uniform meshes created by the MIKE zero mesh generator tool. Values indicate the proportion of the desired value, calculated using Eq. 4 or Eq. 5 using  $\theta=60^\circ$ . \* Lower 99% confidence interval; \*\* Peak or modal value (mean of 10 highest frequencies).**

Smoothening the mesh changes the statistical distribution of these parameters, also in a predictable and consistent manner. The majority of change occurs in the first 5 iterations of smoothening and there is no significant difference between meshes smoothened by more than 50 iterations. It makes no difference to the final result whether the 50 iterations are applied all at once or in smaller steps, e.g.  $10 \times 5$  iterations. Smoothening does create a more uniform mesh overall, however, it also creates a small number of even smaller elements that increase overall run times.

In order that the mesh blends smoothly with the boundary, the boundary vertex spacing should be  $[0.4-0.8 \times \Delta x]$  where  $\Delta x$  is calculated using Eq. 5, for the value of A specified for that area or polygon, or the expected element area in that water depth following mesh refinement. Using 0.8 or a multiple of 0.8 (1.6, 2.4) maintains approximately the same element area at the boundary, as found further away in the same polygon. Using 0.4 or some intermediate value will tend to increase resolution at the boundary slightly whilst maintaining uniformity. Using intermediately larger values (1.0-1.4) will result in non-uniformity of element size at the boundary. Using values smaller than 0.4 will significantly increase overall model run times without any improvement in accuracy.

### 10.8.3. Summary of mesh refinement studies

During mesh refinement, the resolution of the mesh is varied across the domain in order to provide: sufficient resolution in areas of interest or in regions of complex flow; reduced (more efficient) resolution in areas where a higher resolution is simply not required. Mesh refinement may be undertaken semi-automatically using the mesh refinement tool in the mesh generator, or manually by the creation of polygons with user specified element area prior to initial triangulation.

The effect of mesh refinement using either method is to cause the distribution of  $\Delta t$  to become more focused. Elements in shallow water with initially large elements are capable of large time steps but the time step of the model as a whole is limited by elements in deeper water. By reducing the size of elements in shallower water the spatial resolution in shallow water is increased and the new mesh is overall (hopefully) more efficient than before.

If a large proportion of the total number of elements in the refined mesh are located in shallow water, the particular algorithms used by the mesh refinement tool may produce a minority of elements with  $\Delta t$  smaller than the previous smallest value, thus reducing the

overall efficiency of the mesh. It is possible to reduce or avoid this effect by making the elements in shallower water slightly larger than would be predicted using the simple method described above. By increasing the value of  $A_{\min}$  by a factor of 2, the smallest time step in the model is not changed significantly from the unrefined mesh but the overall run time is decreased from the original refined mesh due to the smaller total number of elements. This does however also have the effect of increasing the representative length scale of elements in shallow water by approximately 40%. If it is more important to have a particular area or distribution of  $\Delta x$  in the shallower water, then the initial mesh area (equivalent to  $A_{\max}$ ) should be made smaller by factor 2 and the desired value used for  $A_{\min}$ .

If the dynamic time step is controlled by much smaller elements at the boundary or in shallow water, the passage of large scale tidal information (moving at velocity  $\sqrt{gh}$ ) may be incorrectly resolved in deeper water by using elements that are ‘too large’ where local  $\Delta x \ll \Delta t \times \sqrt{gh}$ . In this case, tidal elevation potential is ‘leaked’ into adjacent cells allowing the tidal wave to propagate faster and also potentially reducing the amplitude of the wave in the domain. The solutions are: to optimise the size all elements to the expected minimum value of  $\Delta t$  using the guidance provided in this study; or, to use larger than recommended elements in deeper water but to then increase bed roughness in these areas to counter the increased propagation speed.

When manually refining a mesh, the calculation of the element area to apply should be made on the basis of the maximum depth in that polygon. Therefore, it is more efficient to draw polygons parallel to depth contours if possible. If a large proportion of elements are in relatively shallow water then the same principles (described above) for modifying the calculated ideal area should apply; the user will have to make appropriate calculations as to the degree of modification to apply to polygons in intermediate water depths.

#### 10.8.4. Fixing local problems

Using the guidance and information above, a mesh may be created that has a resolution acceptable to the user with good efficiency, i.e. a tight distribution of potential  $\Delta t$  for all elements. However, it will always be the case that a small minority of elements will present values of  $\Delta t$  significantly smaller than the majority. It was found that the test models would run in 0.65-0.85 of the ‘optimised’ time by adjusting 100 elements or by 0.75-0.9 of the time by adjusting only 20 elements.

Using software such as Matlab (code provided in Appendix B), the mesh nodes that define the three corners of individual problem elements can be individually identified and manipulated manually in order to improve the least efficient elements in the mesh. The least efficient state (time step) of individual elements is estimated using Eq. 3 for the chosen value of maximum CFL, the greatest anticipated local water depth = [initial water depth to Mean Sea Level + the maximum tidal elevation] and the largest anticipated value of  $|u|$ . It is recommended that these values are estimated for the domain as a whole on the basis of the background research or a very simple first approach model run. A map of more accurate, spatially variable values could be derived by making initial model runs, but unless a very large number of scenarios will be run with the resulting mesh the time saved in total run time of the actual scenarios may not be worth the additional time spent in optimisation.

### 10.9 Choosing the appropriate mesh resolution

When choosing the appropriate mesh resolution for an area, particularly areas of special interest or areas of complex or constricted flow, there are several design approaches that may be adopted:

1. Design through iteration. An initial coarse mesh is chosen and a series of short runs are made using progressively higher spatial resolution. Point or line data time series are extracted and compared. Results will tend to converge on a stable solution at finer resolutions. The chosen mesh is the coarsest one to not benefit significantly from further refinement.
2. Design through experience. Based on the results of previous studies using approach (1), a 'best' value of  $A$  or  $\Delta x$  is anticipated. This may be an explicit value known to resolve certain process that occur at well defined length scales or it may be a more qualitative choice whereby the mesh is deemed to 'look right'. This approach relies on significant modelling experience and an understanding of the hydro/sediment dynamics processes considered important in the model being constructed.
3. Design constrained by previous agreement. In some cases, the client may specify the mesh length scale in certain parts of the model, typically in the regions of special interest. The rest of the mesh should then be designed to compliment the region of fixed resolution.

## **11. Appendix C – A Review of the Bed Roughness Variable in MIKE21fm HD and ST Modules**

Bed roughness is considered a primary calibration variable within the MIKE21 HD module and is also essential for the correct modelling of other process such as sediment transport and wave attenuation. Whatever the chosen method for defining bed roughness in the model, values are typically manipulated iteratively by the user within the suggested ranges as part of the calibration process, commonly using variables of water depth or seabed type. The short study below explores the theoretical relationship between flow, water depth and choice of coefficient. It also compares the range of values recommended for calibration and used by previous modelling studies with suggested values from previous field studies. This study is intended to compliment existing calibration tables but also to provide a starting point for those without the benefit of such experience.

Summarising from the MIKE21 HD manual: in the model the bottom shear stress ( $\tau_b$ ) is determined by a quadratic friction law:

$$\text{Eq. 1)} \quad \tau_b = C_d \rho \bar{U}^2$$

Where  $C_d$  is a drag coefficient,  $\rho$  is the density of the fluid medium (typically  $1027 \text{ kgm}^{-3}$ ) in seawater and  $\bar{U}$  is the depth averaged velocity.

The shear stress experienced at the bed therefore increases with the velocity squared but is scaled by the drag coefficient. The value of  $C_d$  thus allows parameterization of the effect of varying bed roughness. The value of  $C_d$  may be specified for a particular height above the bed (corresponding to the height at which the velocity measurement is made) or as a depth averaged value (for use with depth averaged velocity as is the case in the various MIKE21 modules).

In MIKE21, the value of  $C_d$  is specified in one of three different ways:

1. No bed resistance
2. Manning number (M)
3. Chezy number (C)

Where

$$\text{Eq. 2)} \quad C_d = \frac{g}{(Mh^{1/6})^2}$$

Or

$$\text{Eq. 3)} \quad C_d = \frac{g}{C^2}$$

Where  $h$  is the total water depth and  $g$  is the acceleration due to gravity ( $9.81 \text{ ms}^{-2}$ ). Using these methods of formulation, a larger bed roughness value (M or C) implies a smaller bed friction for the same flow velocity and water depth.

According to the MIKE21 manual, the relationship between the Manning number and the Nikuradse roughness length,  $k_s$  can be estimated using

Appendix C – A Review of the Bed Roughness Variable in MIKE21fm HD and ST Modules

$$\text{Eq. 4)} \quad M = \frac{25.4}{k_s^{1/6}}$$

Using one of the several relationships recommended in Soulsby (1997), over flat beds of sediment  $k_s$  is related to the median grain diameter ( $D_{50}$ ) as approximately

$$\text{Eq. 5)} \quad k_s = 2.5D_{50}$$

By combining and rearranging these simple relationships, the suggested value for the Manning number ( $M=32$ ) in the MIKE21 manual therefore corresponds to a flat bed of median grain size  $D_{50} = 0.1\text{m}$ ; the suggested range  $20 < M < 40$  corresponds to flat beds of median grain size  $0.025\text{m} < D_{50} < 1\text{m}$ . Such a flat but very coarse bed is of course not representative of most natural marine environments and the additional friction suggested by the recommended values may instead accounted for by the form drag of naturally occurring bedforms (e.g. sand ripples) in otherwise finer sediment.

Values of the drag coefficient for different seabed sediment grainsizes (flat beds) and similar but ‘with bedform’ scenarios have been empirically derived from field and laboratory data in previous studies. Values of  $C_{100}$  (i.e. for use with velocity data collected at 1m above the bed) suggested by various authors are shown below in Table 12. In the reports, bed roughness was typically presented as either: the bed roughness length ( $z_0$ ), defined as the height above the bed at which the current speed becomes zero; or, the drag coefficient ( $C_D$ ) referenced to 1m above the bed ( $C_{100}$ ). Where only  $z_0$  was given, equivalent values of  $d_{50}$  have been calculated using the following relationship between  $d_{50}$  and  $z_0$  in hydrodynamically rough flows:

$$z_0 = \frac{d_{50}}{12}$$

Where grain diameter was only given in units of phi ( $\Phi$ ), these were converted to millimetres using the relationship:

$$d_{50} = 2^{-\phi}$$

where  $d_{50}$  is the particle size in millimetres.

Appendix C – A Review of the Bed Roughness Variable in MIKE21fm HD and ST Modules

Author	Bottom type	$z_0$ (mm)	$C_{100}$	$d_{50}$ (mm)	Notes
Sternberg, 1968 †	Rock/gravel	0.02	0.0022	0.824	
	Shell/gravel	0.17	0.0039	1.087	
	Nondistinct	0.04	0.0026	0.332	
	Small ripples	0.03	0.0023	0.301	
	Nondistinct	0.2	0.004	0.095	
Ke et al., 1994 *‡	Sandflat	0.49	0.00521	5.88	
	Mudflat	1.65	0.00898	19.8	
	Arenicola sandflat	0.32	0.00465	3.84	
	Saltmarsh	3.88	0.02594	46.56	
Green and McCave, 1995 *	Noncohesive, silty sand: 37% silt plus clay (grain size <0.063mm) and 63% sand	0.33	0.0025	3.96	Coastal (26m depth) eastern Irish Sea. highly variable $C_{100}$ (0.0008 - 0.01) and $z_0$ (0.001 - 0.2).
Soulsby, 1997 *	Mud	0.2	0.0022	2.4	
	Mud/sand	0.7	0.003	8.4	
	Silt/sand	0.05	0.0016	0.6	
	Sand (unrippled)	0.4	0.0026	4.8	
	Sand (rippled)	6	0.0061	72	
	Sand/shell	0.3	0.0024	3.6	
	Sand/gravel	0.3	0.0024	3.6	
	Mud/sand/gravel	0.3	0.0024	3.6	
Green et al., 1998 *	Gravel	3	0.0047	36	
	Horse mussels	11	0.0082	132	Estuarine setting
	Horse mussels	15	0.0096	180	Estuarine setting
	Horse mussels	22	0.0115	264	Estuarine setting
Bricker et al., 2005 ‡	Cockle shells, seaweed and crab burrows	4	0.0055	48	Estuarine setting
	Silt/fine sand	0.01	0.0025	0.022	

**Table 12.** Values of  $C_D$  for different seabed types derived from a variety of marine field studies. \*  $d_{50}$  was calculated from  $z_0$  using  $z_0 = d_{50}/12$ . †  $d_{50}$  was calculated from  $\Phi$  using  $d_{50} = 2^{-\Phi}$  ‡ Experiment undertaken in the intertidal zone of The Wash.

The values of  $C_d$  listed in Table 12 are plotted against grain size in Figure 115. It is shown that for muddy beds, flat sandy beds and even flat beds of small gravel (equivalent  $d_{50} < 10\text{mm}$ ), the drag coefficient is almost consistent, mean value 0.0023, with variability of the order  $\pm 0.0015$ . Rougher beds (rippled sands, very coarse biogenic surfaces) in deep water have a progressively larger associated value of  $C_{d100}$ , up to a maximum value 0.01. Even

Appendix C – A Review of the Bed Roughness Variable in MIKE21fm HD and ST Modules

higher values were observed in measurements made over horse mussel beds on mudflats (i.e. in very shallow water or in the littoral zone); these results are not considered to be representative of the range that might be applied in deeper water because the height of the roughness elements are so large compared to the water depth and are therefore excluded from the trend line.

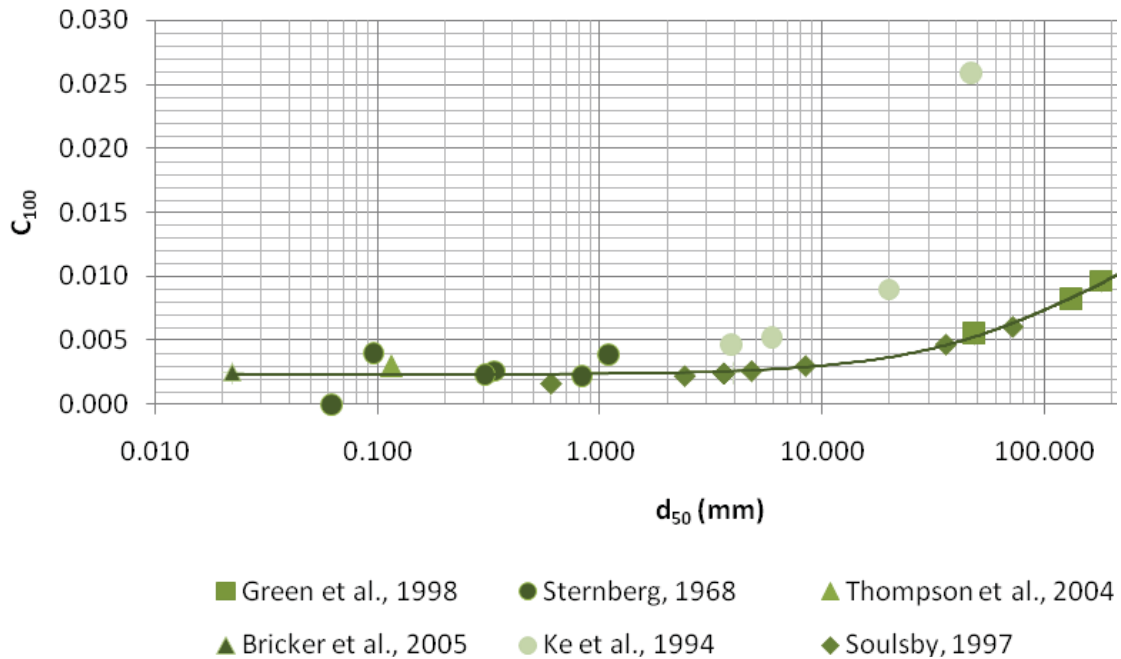


Figure 115 Plot of extant literature  $C_{100}$  and  $d_{50}$  values for sites around the UK. Solid line indicates the polynomial trend through all data except the intertidal values from Ke *et al.*, 1994.

Before use within a depth averaged 2D model, the suggested values of  $C_{100}$  must first be converted to equivalent values of depth averaged  $C_d$ . A relatively simple method is described as follows. The quadratic relationship for both vertically resolved and depth integrated cases are equivalent, i.e. Eq. 1 may also be written as

$$\text{Eq. 6) } \tau_b = C_{100} \rho U_{100}^2 = C_d \rho \bar{U}^2$$

Which may be simplified and rearranged to,

$$\text{Eq. 7) } C_{100} U_{100}^2 = C_d \bar{U}^2 \quad \text{and} \quad \frac{C_{100}}{C_d} = \frac{\bar{U}}{U_{100}}$$

As a first order approximation, the velocity profile in the bottom half of the water column may be estimated using the empirical formulae given by Soulsby (1990):

$$\text{Eq. 8) } U_z = \left( \frac{z}{0.32h} \right)^{1/7} \bar{U} \quad \text{for } 0 < z < 0.5h$$

Where  $z$  is the height of the reference velocity  $U_z$  (i.e.  $U_z = U_{100}$  and  $z=1\text{m}$  in this case). Rearranging eq. 8 and substituting for the velocity quotient in eq.7 yields the depth dependant conversion

$$\text{Eq. 9) } C_d = \left( \frac{1}{0.32h} \right)^{1/7} C_{100}$$

Using equations 2, 3 and 9, the values in Table 1 may now be interpreted to yield equivalent Mannings and Chezy numbers for different seabed types, the former will also vary

Appendix C – A Review of the Bed Roughness Variable in MIKE21fm HD and ST Modules

with water depth as shown in Figure 116. From the Figure, the suggested single value ( $M=32$ ) and range ( $M=20-40$ ) of the Manning number in the MIKE21 manual compare most closely with the equivalent calculated values for rippled sand ( $M=32$  in shallow water to  $M=24$  in deeper water) and gravels ( $M=35$  in shallow water to  $M=26$  in deep water). The range also encompasses smooth sandy beds in deep water ( $>40m$ ). Also shown in the Figure are the values of  $M$  determined by iterative calibration of MIKE21 hydrodynamic model studies of an undisclosed region in Malaysia and another in the Bristol Channel, UK. The chosen values suggest that the Malaysian study region was dominated by smoother (flatter) beds than those in the (highly energetic) Bristol Channel.

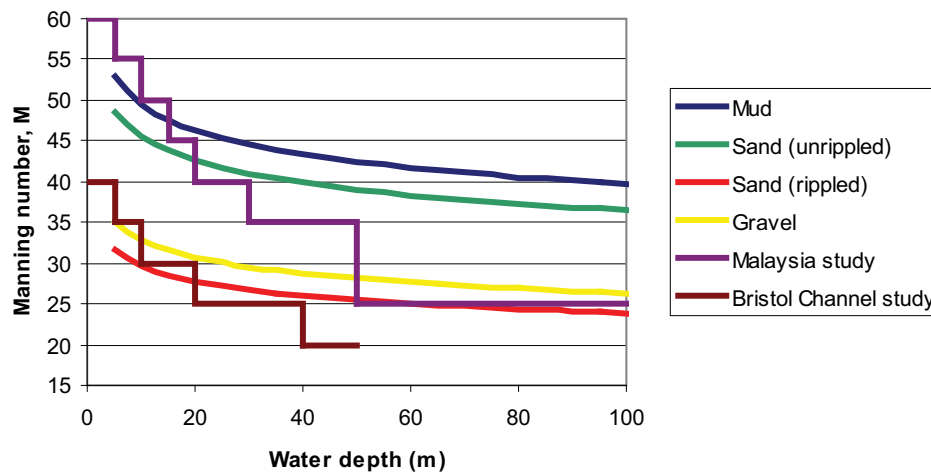


**Figure 116. Variation in the Manning number calculated for varying water depth and seabed type (based on values from Soulsby, 1997). Also, the suggested values from calibrated MIKE21 studies in order to properly simulate local hydrodynamic processes.**

Values of the Chezy number also calculated from the suggested values of Soulsby (1997) are shown in Figure 117. Values of  $C$  also vary with depth due to the depth dependant conversion of  $C_{100}$  to  $C_d$ . In opposition to the Manning number, the Chezy number suggests that the same depth mean velocity produces higher  $\tau_b$  in shallower water depths. However, this assumes that  $C_{100}$  for a given bed type remains constant with changing water depth. The range suggested by the manual for the Chezy number ( $C=30-50$ ) generally underestimates the suggested values for ‘real beds’, therefore representing a bed of generally higher resistance. From the Figure, better similarity with the suggested range for the Manning number might be achieved by using a range of  $C=40-60$ .

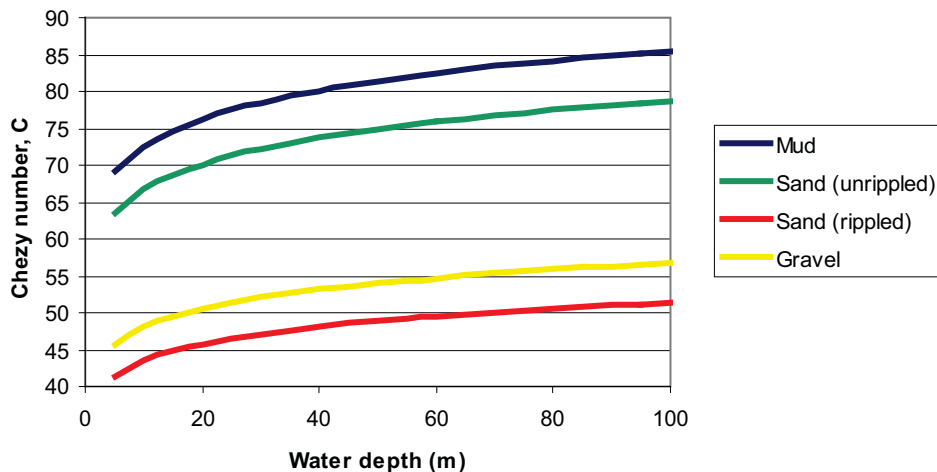


**Figure 117. Variation in the Chezy number calculated from values of Soulsby (1997) for varying water depth and seabed type.**

The depth mean drag coefficient resulting from the use of the suggested range of M or C in the Manual is shown in Figure 118. The ranges of values of M and C suggested by the manual and indicated in the Figure are relatively large compared to the range for field conditions ( $C_d = 0.0015-0.0040$ ) suggested by Soulsby (1997). This has the effect of causing the model to predict higher bed shear stresses than might be observed in the field. This may not be so important in the HD module where the primary aim is to calibrate the model results but is more important in the ST model as it also affects predicted sediment transport rates. These errors become larger at higher flow speeds (especially flows in excess of the threshold of sediment motion) as  $\tau_b \propto U^2$  and sediment transport  $\propto U^3$  (approximately!). This is especially important given the uncertainty in the sediment transport relationships (see notes below).

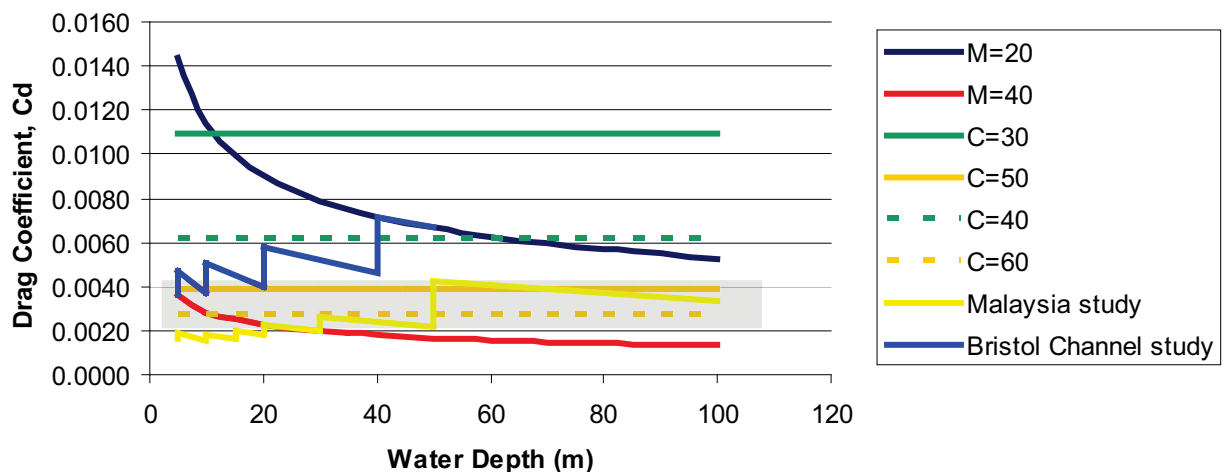


**Figure 118. Values of  $C_d$  resulting from the maximum and minimum suggested values of the Manning and Chezy number in the manual and the alternative Chezy range suggested in the text. The grey box represents the approximate range of  $C_d$  (0.0015-0.0040) suggested by Soulsby (1997) for a variety of seabed types.**

It is particularly interesting to note that although the definition of M (Eq. 2) intends to increase the value of  $C_d$  in shallower water depths (see below for further discussion), calibration studies suggest that better hydrodynamic calibration is achieved by using an

## Appendix C – A Review of the Bed Roughness Variable in MIKE21fm HD and ST Modules

almost constant value of  $C_d$  (more akin to the intentions of  $C$ , Eq. 3) or even reversing this effect (i.e. decreasing  $C_d$  in shallower water depths). The calibration tables from the two studies shown typically alter  $M$  in somewhat arbitrary steps of 5 units and the corresponding depth interval in also somewhat arbitrary steps of 5-10m. Further analysis of the two tables show that a practically uniform value of  $C_d$  could be achieved by making subtle changes of only  $\pm 1-7M$  (typically less than the calibration iteration step) to each depth interval.

This prompts the obvious question - how should the value of  $C_d$  vary with water depth in the field? As a first order theoretical approach, consider the situation of a shallower and a deeper water location with the same depth mean velocity and similar (rippled sand) seabed type. Assuming Eq. 8 applies in both cases, for the same depth averaged velocity, the velocity gradient near to the bed and thus the shear stress should be greater in the shallower water case. An additional factor is that the rippled bed poses a larger roughness in proportion to the water depth, also potentially increasing shear stress at the bed through form drag. Using Eq. 1, such an increase in shear stress in shallower water is accounted for by increasing the value of  $C_d$ . This is the basic premise of the Manning number. However, in the literature, values of  $C_d$  quoted from field or laboratory studies are not described as varying with depth (e.g. those of Soulsby, 1997) but this might result from such values being based upon many disparate observations, representative of only a certain range of water depths or containing significant scatter.

### In practice...

The model requires values of bed resistance for each element when calculating the hydrodynamic and sediment dynamic components of output; these bed resistance maps are provided separately to the HD and ST modules during model setup. From the ST manual p46 – “The specification of bed resistance must be consistent with the specification used in the [associated HD]... [the user should check precisely the type and values of bed resistance used in the HD for use in the ST]. However, simple trials show that the model will run without errors if different bed roughness maps are specified in each module during a simultaneous HD/ST run. Therefore, it may be preferable to form a map of seabed roughness using one method to correctly reproduce (to calibrate) flow patterns and then using a second method in order to properly scale sediment transport.

### Brief notes on estimating sediment transport (from Soulsby, 1997)

Most of the well accepted relationships for current only flows (e.g. Engelund and Hansen, 1972; Ackers and White, 1973; Van Rijn, 1984) were designed for or are stochastically based upon sediment transport in rivers (strictly unidirectional flow) where large bedforms are in equilibrium with the flow. This is not the case in tidal environments.

“The accuracy of sediment transport formulae is not high. In rivers, the best formulae give predictions which are within a factor of 2 of the observed values in no better than 70% of samples. In the sea the position is worse – probably no better than a factor of 5 in 70% of samples. The accuracy can be improved significantly by making site specific measurements and calibrating the formulae to match.”